BULGARIAN CHEMICAL COMMUNICATIONS

Some endocrine disrupting compounds in the environment and possibilities for their removal / degradation

R. P. Kralchevska, M. M. Milanova, I. L. Hristova, D. S. Todorovsky*

University of Sofia, Faculty of Chemistry and Pharmacy, 1, J. Bourchier Blvd., Sofia 1164, Bulgaria

The paper presents a review of literature data on the occurrence of endocrine disruption compounds in the effluents from wastewaters treatment plants, surface, underground and drinking waters and sediments. General data concerning their action on the living organisms (mainly fish) are given. The peculiarities of the methods for removal/degradation of the pollutants *via* adsorption, ozonation, biodegradation, photolysis and photocatalysis are considered.

1. INTRODUCTION

The steroids of concern for the aquatic environment due to their endocrine disruption potential are mainly estrogens and contraceptives, which include 17β-estradiol (E2, a), 17α-ethinylestradiol (EE2, b), bisphenol A (BPA, c), estrone (E1, d) and estriol (E3, e) (Fig. 1). A major source of hormone steroids is livestock (sheep, cattle, pigs, poultry, etc.) waste [1]. Steroid drugs are also frequently used in cattle as well as in other livestock to control the oestrous cycle, treat reproductive disorders and induce abortion [2]. This could greatly increase the generation of hormone steroids in urine of livestock [3]. Both natural and synthetic estrogens enter the aquatic environment via effluents of wastewater treatment plants or untreated discharges and reach concentrations (normally in the ng/l range) sufficient to exert estrogenic responses. Human-used contraceptives pills are the other source of such compounds entering the environment.

The order of aqueous solubility observed was consistent with the increasing polarities of the estrogens, firstly E2 (two hydroxy groups) and then EE2 (added ethinyl group at 17R position on the D ring). At pH=7, temperature 25.0 ± 0.5 °C the solubility in Milli-Q reagent grade water (Millipore) reported for E2 is 1.51 ± 0.04 mg/l and for EE2 – 9.20 ± 0.09 mg/l [4].

Among endocrine disrupting compounds, EE2 and BPA are the two compounds most frequently studied in environmental research [5]. EE2 is
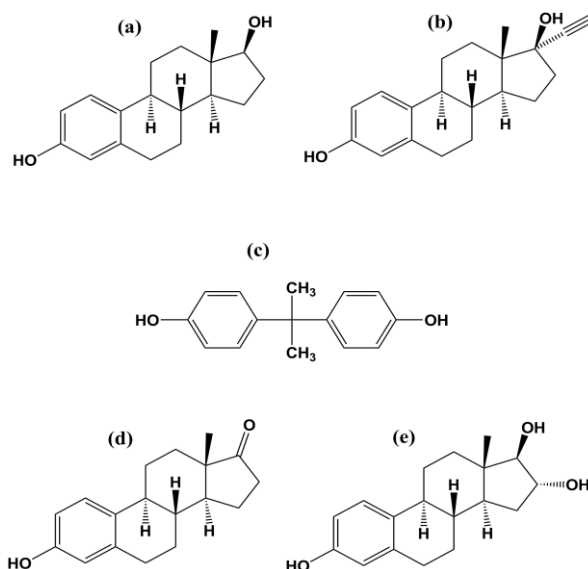

Fig. 1. Molecular structures of 17β-estradiol (E2, a), 17α-ethinylestradiol (EE2, b), bisphenol A (BPA, c), estrone (E1, d) and estriol (E3, e).

widely used as an oral contraceptive, its low removal was observed [6] and its toxicity is higher by a factor of 10-50 than that of estrone (El) and E2 [7]. Thus, reduction/elimination of EE2 could have the strongest single impact on the estrogenicity of the effluents [8].

2. ESTROGEN DISRUPTING COMPOUNDS (EDCS) IN THE ENVIRONMENT

2.1. EDCs in sewage-treatment works effluents (STWE)

In 1970 Tabak *et al*. [9] reported concentrations of 2000 ng EE2/l, 25 ng E1/l, 60 ng E3/l, and 10 ng E2/l (parent compounds plus conjugates) in STWE

---

* To whom all correspondence should be sent:
E-mail: nhdt@wmail.chem.uni-sofia.bg

from the USA [10]. Effluents from UK wastewater treatment works (WwTWs) were first reported to be estrogenic to fish in 1994 [11] and since then estrogenic contaminants have shown to be widespread in effluents discharging into rivers in England and Wales as well as in Europe and the USA [12–15]. The major estrogenic components in WwTWs effluents have been identified as the natural estrogens E2 and E1 and the synthetic EE2 [16]. Using an immunoassay procedure, EE2 was tentatively detected in STWE, river water, and potable water in Britain at concentrations in the low ng/l range and below [10, 17].

Concentrations of up to 20 ng of E2/l and up to 62 ng of EE2/l in effluents were reported in a German study (1998, employing sophisticated modern techniques) [10, 18]. Steroidal estrogens have been surveyed extensively in influents and effluents from WwTWs of different countries and their concentrations generally ranged from 10 to 200 ng /l [19–25]. The median concentration of EE2 in sewage effluents in Germany, England, The Netherlands and the USA reported by several authors [10, 19, 26–33] are rather low - between 1 and 3 ng/l. Analysis of a water sample from the Tiber river (Italy) downstream of small towns whose sewages are treated by percolating filter or directly discharged into the river revealed the presence of EE2 at 0.04 ng/l [34]. Concentrations of E2 up to 20 ng/l were reported in STWE [10, 18].

A suite of 30 primarily estrogenic organic wastewater contaminants was measured in several influent/effluent wastewater samples from four municipal WwTWs and effluents from one bleached kraft pulp mill. 17α-Ethinylestradiol was the more frequently detected synthetic estrogen/progesterone in the effluents occurring at or below 5 ng/l with sporadic occurrences up to 178 ng/l. The highest levels of steroidal estrogens in municipal effluents were for E1>E2>E3, all <20 ng/l [35].

In [36] data are summarized on the attempts to evaluate the estrogens emission in the environment resulting from the use of contraceptives by humans. Johnson and Williams [37] assume that 17 % of women are taking 26 μg EE2/day (the main estrogenic component of a combined oral contraceptive pill); if excreting 40 % of it are accepted, this would suggest a per capita normalized discharge of 890 ng/day. Of course this percentage does vary a little between countries, but there is a continuing trend to lower the EE2 dose in many contraceptive products. A typical wastewater discharge per capita value is 200 l/day (although often more, particularly where industrial waste streams also enter the sewage), which would suggest that 4 ng/l EE2 would be found in a raw sewage influent stream, and 0.8 ng/l EE2 in the effluent if 80 % removal takes place through sewage treatment. So if the receiving stream was composed entirely of effluent this would give only 0.8 ng/l EE2 in the receiving water, or 4 ng/l EE2 if sewage treatment had failed to remove any EE2 from the waste stream. Therefore, it is surprising to find reports of EE2 being detected at concentrations up to 178 ng/l in sewage effluent [35], up to 273 ng/l in some USA streams [38], 5 ng/l in a river estuary [39], and even 2 ng/l in drinking water [40], by researchers using GC/MS equipment [36].

Generalized data on the estrogens content in STWE effluents in a number of countries are reported in [41]. Detected concentrations vary within the limits (ng/l) 1 – 5400 (E1), 0.2 – 1500 (E2), 0.1 – 3000 (E3) and 0.9 – 210 (EE2).

Despite the mentioned rather high concentrations of EE2, its common concentrations in effluents are rather close to the present detection limits of most analytical techniques causing serious difficulties in its analysis [8]. That is why one can suppose that although EE2 was not always detected, it may still be present in some effluent samples [10].

2.2. EDCs in surface and underground waters

Although natural and synthetic estrogenic compounds can be biologically degraded, they cannot be completely removed in WwWTPs, thus, they are often discharged into surface waters [23, 42–44]. These estrogenic compounds are usually detected in WwWTP effluents and receiving surface waters at concentrations at the ng/l levels [35, 41, 45–51] According to Williams [52], estradiol was frequently detected (<0.4–4.3 ng/l), but ethinylestradiol was infrequently detected (<0.4–3.4 ng/l) in the River Nene and the River Lea (U.K.), upstream and downstream of sewage treatment works.

In 1998 EE2 was occasionally detected at levels below 5 ng/l in river water in Germany [10, 18]. Adler *et al.* [31] reported several positive detections of EE2 in ground- and drinking water in Germany. They determined EE2 in groundwater and in raw and purified drinking water at concentrations up to 2.4 ng/l [53]. Ethinylestradiol and 17β-estradiol were reported at concentrations ranging from 0.2 to 2.6 ng/l [54]. Lopez de Alda *et al.* [55] reported a maximum concentration of 22.8 ng/g for EE2 and 11.9 ng/g for E1 from two rivers in the North-East

of Spain. It was shown that the higher levels of estrogens from the two drainage rivers in China could be due to untreated wastewater discharge [25]. Kolpin *et al*. [38] reported E2, EE2 and testosterone to be present in surface water at an average of 9, 73 and 116 ng/l, respectively [54].

The concentrations of E2 and EE2 in Taihu Lake (2334 km^2, in a rapid economic development and urbanization area of China) were determined using a high-pressure liquid chromatography method [56].

Data from drinking, waste, and surface water in South Korea offer the possibility to evaluate the ratio of concentrations for some types of pollutants emitted by STWE, as well as in surface and drinking waters (Table 1) [54].

Table 1. Mean values (ng/l) of some pollutants in waters

Pollutant type	Water type		
	From STWE	Surface	Drinking
Farmaceuticals	2800	390	100
Hormones	17	2	
Miscelaneius	430	88	20

The generalized data show that when EE2 is detectable, the ratio of E2 to EE2 in rivers is 9:1. This means that the concentration of EE2 was probably 0.6 ng/l, with a median concentration around half this value. These values agree well with measurements taken in The Netherlands, which reported concentrations in river water of 0.3 ng of EE2/l (5-fold lower than in drinking water) [10].

2.3 EDCs in sediments

Given the relatively low polarity of these compounds, which are characterized by octanol–water partition coefficients mostly between 3 and 6, sorption to bed sediments appears a quite likely cumulative process. Laboratory experiments carried out to study the behavior of estrogens in the aquatic environment, predict that bed sediments act as environmental reservoirs from where both estrogens and progestogens (compounds also used in birth-control pills) can eventually become bioavailable [57]. These compounds could affect wildlife and human health by disrupting their normal endocrine systems.

Concentrations above 30 ng/g for both E2 and EE2 have been found in China river sediments due to the untreated wastewater discharge, but the common concentrations are much below such values. Average concentrations of E2 equal to 8.69, 10.3 and 7.26 ng/l in water and 5.28, 4.40 and 3.34

ng/l in the respective sediments have been found for three rivers in Tianjin area. Concerning the EE2 average concentrations, the following values are reported for the same rivers: 10.0, 9.45 and 3.54 ng/l in water and 5.09, 4.02 and 2.75 ng/l in the sediments [25]. The partitioning of estrogens between water and sediment was found to be influenced by the organic content of the sediment [25].

Data for estrogens content in rivers, estuaries and ocean sediments in a number of countries are reported in [25]. Table 2 presents data from the literature available for estrogens content in waters and sediments. 3. Action of EDCs on living organisms

The action of EDCs on living organisms is of general concern and is a significant research subject. Their presence in the environment is likely to disturb the ecosystems and to affect human health. The epidemiological data give evidence of a possible relationship between chemical exposure and observed harmful effects of endocrine disruption in the living beings [58]. Thus, the need for developing reliable detection methods, analysis tools, and adapted wastewater treatment processes is now the subject of significant interest.

Both natural and synthetic estrogens that end up in the environment have been shown to produce deleterious effects in aquatic organisms, such as feminization and hermaphroditism. The synthetic estrogenic compounds, EE2 and diethylstilbestrol (DES) have the ability to interfere with the functions of hormone systems [41].The presence of ethinylestradiol, the most potent synthetic estrogen known, in a river sediment has been associated with a striking incidence of carp species with macroscopically developed both male and female reproductive organs, and distinct high levels of plasma vitellogenin (egg yolk protein usually associated with adult females) in male fish [59]. These compounds can be extremely potent even at low concentrations; for instance, less than 1 ng/l EE2 can induce vitellogenin production in male rainbow trout [11, 60] and 4 ng/l caused male fathead minnows to fail to develop normal secondary sexual characteristics [52, 61]. Significant effect of concentrations below 1 ng/l is confirmed in [62], and sex reversal is possible in male fish at 3 ng/l [63]. "*In vitro*' studies [11] have shown that exposure of fishes to only 0.1 ng/l of EE2 may provoke feminization in some species of male wild fishes.

Table 2. Estrogens concentration (ng/l) in waters and sediments.

Sample type	Estrogen	Values reported, sample origin, reference	
		Minimal	Maximal
STWE	E2	0.477, USA [118]	3.66, USA [118]
		3.2, Japan [117]	55, Japan [117]
		2.7, UK [10]	48, UK [10]
	EE2	0.10, Germany [119]	8.9, Germany [119]
		0.2, Netherlands [26]	7.5, Netherlands [26]
	E1	2.5 Italy[20]	82.1, Italy[20]
		1.4, UK [10]	76, UK [10]
	E3	0.43, Italy[20]	18, Italy[20]
Rivers	E2	0.11, Italy [20]	33.9, Taiwan[113]
	EE2	0.04, Italy [20]	27.4, Taiwan [113]
	E1	0.1, The Netherlands [26]	66.2, Taiwan [113]
	E3	0.33, Italy [20]	73.6, Taiwan [113]
Sediments from rivers	E2	0.71, China [25]	9.7,China [25]
	EE2	0.93, China [25]	22.8, Spain [55]
	E1	0.2, Germany [114]	21.6, China [25]
	E3		7.29, China [25]
Sediments from sea/ocean	E2	0.22, Australia [116]	2.48, Australia [116]
	EE2		0.5, Australia [116]
	E1	0.05, Japan [115]	3.6, Japan [115]
	E3	Not determined	
Drinking waters	E2	0.20, Southern Germany [119]	2.1, Southern Germany [119]
	EE2	>LOD [31]	2.4 [36,53,120]
		0.15, Southern Germany [119]	0.50, Southern Germany [119]
	E1	0.20, Southern Germany [119]	0.60, Southern Germany [119]
	E3	Data not found	Data not found

A 7-year whole lake experiment conducted at the Experimental Lakes Area in northwestern Ontario, Canada showed that chronic exposure of fathead minnow (*Pimephales promelas*) to low concentrations (5–6 ng/l) of the potent 17α-ethinylestradiol led to feminization of males through the production of vitellogenin in RNA and protein, impacts on gonadal development as evidenced by intersex in males and altered oogenesis in females, and, ultimately, a near extinction of this species from the lake. These observations demonstrate that the concentrations of estrogens and their mimics observed in freshwaters can impact on the sustainability of wild fish populations [64].

In humans and animals, estrogens undergo various transformations mainly in the liver. EE2 is mainly eliminated as conjugates. Therefore, estrogens are excreted mainly as inactive conjugates of sulphuric and glucuronic acids [1]. Prolonged exposure of target tissues or cells to excessive mitogenic stimulation by natural or synthetic estrogens has long been considered an important etiological factor for the induction of estrogen-associated diseases of the endometrium, such as endometrial cancer and endometriosis [65, 66]. Although steroid conjugates do not possess direct biological activity, they can act as precursors of hormone reservoirs able to be reconverted to free steroids by bacteria in the environment. Due to the presence of microorganisms in raw sewage and sewage treatment plants, these inactive conjugates of estrogenic steroids are cleaved, and active estrogenic steroids are released to the environment [1, 19, 20].

4. EDCS REMOVAL/DEGRADATION

Most important processes that play a role in the removal of estrogens are: adsorption, aerobic or anaerobic degradation, anoxic biodegradation and photolytic degradation. In general, anaerobic conditions result in longer half-lives than aerobic conditions. EE2 shows far more persistence; therefore its estrogenic effect *in vitro* is about 2-3-fold higher compared to E2 [67]. Conventional treatment techniques, including coagulation, precipitation and activated sludge processes, may not be highly effective in removing EDCs, while advanced treatment options, such as granular activated carbon, membranes and advanced oxidation processes have shown satisfactory results. Such processes allow a high removal of recalcitrant compounds, however many by-products are released and could have an estrogenic activity higher than their precursors [58].

4.1 Sorption on activated sludge biomass

The process is an important mechanism for removal of EE2 in biological wastewater treatment [68]. Current wastewater treatment plants were normally designed for carbon, nitrogen, and phosphorus removal but partial EDCs removal is often simultaneously achieved [58]. Very few data on EDCs, and in particular on estrogens fate in STWPs processes are available in the literature [19, 58, 69, 70]. Literature data concerning this possibility are more or less contradictory probably due to variation in the ability of the bacterial populations in biosolids to degrade estrogens. Recent studies on the effectiveness of conventional wastewater treatment processes show that the STWPs are a significant EDCs point source, particularly for surface water and underground water. Therefore, future research priorities should include optimization of wastewater treatment plants to increase EDCs removal [58].

Ternes *et al.* [19] reported that 99.9 % of the E2, 83 % of the estrone and 78 % of the EE2 were removed from raw sewage in an aerator tank at a WTP in Brazil. However, in another study [71], 70–80 % of the added E2 was mineralized to CO_2 within 24 h by biosolids from wastewater treatment plants, whereas the mineralization of EE2 was lower by a factor of 25–75.

In batch experiments with activated sludge, the contraceptive EE2 was principally persistent under selected aerobic conditions, where mestranol was rapidly eliminated and small portions of EE2 were formed by demethylation. EE2 was also reported to be degraded completely within 6 days by nitrifying activated sludge and resulted in the formation of hydrophilic compounds [72]. E2 could also be degraded when incubated with aerobic and anaerobic riverbed sediments. Compared to E2, EE2 was much more resistant to biodegradation in water from English rivers [73]. Reports from laboratory biodegradation studies indicated that EE2 was highly stable and persistent in activated sludge, with no detectable degradation occurring after 120 h of treatment as compared with gestagens, which were completely metabolized within 48 h of treatment [74]. The solubility of EE2 in pure water and sewage-treatment water was reported to be 4.2 and 4.7 mg/l, respectively, which was 3 times less than the solubility of natural steroidal estrogens [9, 74]. This fact is believed to contribute to the increased resistance of EE2 to biodegradation, as compared with natural steroidal estrogens [10].

Mastrup *et al.* [75] estimated that less than 10 % of natural and synthetic estrogens are removed *via* biodegradation process, and although a considerable amount is adsorbed to the sludge, the majority of the compounds remain soluble in the effluent. Johnson *et al.* [29] could not determine whether biodegradation or sorption is the most important removal mechanism of these compounds [58].

4.2 Aquifer storage and recovery (ASR)

This is an emerging and effective management technique in reclaiming and reusing waste water. During ASR, attenuation processes such as sorption and degradation may play an important role in removing trace organic contaminants from injected waste water. E2 showed a rapid biodegradation with a DT_{50} value (time for 50 % loss) of ~2 days under aerobic conditions [76].

4.3 Adsorption on activated carbon, fullerenes and carbon nanotubes

Satisfactory results using granular activated carbon, membranes and advanced oxidation processes are shown in [77]. Adsorption of BPA, E2 and EE2 on powdered activated carbons (PAC) is feasible for their >99 % removal from raw drinking waters at initial concentrations of 500 ng/l and higher. The rank order from highest to lowest compound removal by PAC (measured by lg K_{ow}, where K_{ow} - octanol/water partition coefficients of estrogens, values given in parentheses) is: E2 (3.1–4.0) > EE2 (3.7–3.9) > BPA (3.3) [78].

Carbon nanomaterials have also shown high adsorption capacity for polyaromatic hydrocarbons [79], pesticides [80 natural organic matter [81], heavy metals [82], and fluorides [83].

Rather high adsorption capacity for EE2 was observed for fullerenes and single-wall carbon nanotubes (SWCNTs), which have the smallest diameters. Multi-wall carbon nanotubes (MWCNTs) with outer diameters of 8-15, 20-30 and 30-50 nm exhibit similar adsorption capacity towards both EE2 and BPA, but their activity decreased with diameter enhancement. Apparently, in case of SWCNTs the adsorption capacity depends on the nature of the pollutant. In the presence of EE2, SWCNTs adsorption ability is two times lower than in presence of BPA [42].

4.4 Ozonation

Conventional ozonation of Lake Zurich water was shown to degrade ethinylestradiol by > 99 % [84, 85]. Doses of ozone typically applied for the

disinfection of drinking waters were sufficient to reduce estrogenicity by a factor of more than 200. However, it proved impossible to completely remove estrogenic activity due to the slow reappearance of 0.1-0.2 % of the initial EE2 concentration after ozonation. The oxidation products formed during ozonation of EE2 were identified by LC-MS/MS and GC/MS using model compounds. Oxidation products of the natural steroid hormones E2 had significantly altered chemical structures as compared to the parent compounds, explaining the diminished estrogenic activity after ozonation [86].

4.5 Molecularly imprinted polymers (MIP).

The feasibility of removing estrogenic compounds from environmental water by the MIP was demonstrated using lake water spiked with α-estradiol. In addition, the MIP reusability without any deterioration in performance was demonstrated for at least five repeated cycles [87].

4.6 Enzymatic waste treatment and biodegradation.

Several oxidoreductase enzymes (*e.g.* peroxidases, polyphenol oxidases) have been shown to be effective for the removal of aromatic compounds, such as phenols, nonylphenol, and bisphenol A (BPA). Technical feasibility of laccase-catalyzed treatment of municipal wastewater contaminated by steroid estrogens (E1, E2, E3, and EE2) is reported in [88]. The municipal waste water used in the study, contained 25.3 ng/l of E2 and 6.25 ng/l of EE2. The results showed that pH has a significant influence on laccase-catalyzed treatment efficiency. The experimental results showed that 20 U/ml (1 U = 1 μmol/min) of initial laccase activity was required to completely remove each estrogen from synthetic water within a 1 h treatment period and 15 U/ml was required to achieve 100 % removal of EE2 [88].

The possibilities for biodegradation of estrogens and some of their conjugates are also tested. The study of Blánquez demonstrates the feasibility of estrogenic compounds biodegradation by suspended fungal biomass (white-rot fungi) using a continuous bioreactor. The feasibility of E2 and EE2 removal by *Trametes versicolor* was demonstrated in batch and continuous cultures. In batch, E2 and EE2 initially supplied at 10 mg/l were removed by more than 97 % in 24 h, which corresponds to volumetric removal rates of 0.43 and 0.44 mg/(l.h), respectively [89].

4.7 Mn(III) as an oxidizing agent.

The authors [90] structurally identify the oxidation products of EE2. From HPLC analysis of the reaction products, a single compound with a molecular mass of 294 was found to be predominant. As the molecular mass of EE2 is 296, it is believed that this compound has been formed by the removal of two hydrogen atoms from EE2. Due to the formed double bond the resulting compound is believed to be more easily oxidized or hydrolyzed in the further treatment (e.g. activated sludge) than the parent one.

4.8 Photolysis

Photolysis reactions have been extensively studied for estrogens removal from aqueous environment [91-94]. It is shown that the photolysis (under high-pressure mercury lamp, $\lambda \geq 365$ nm, 125 W [94]) of both estrogens causes breakage and oxidation of benzene rings to produce compounds containing carbonyl groups [58]. However, according to [95], while EE2 underwent photodegradation in aqueous solutions under irradiation with UV disinfection lamp ($\lambda = 254$ nm, 30 W), no photodegradation was observed under high pressure mercury lamp ($\lambda \geq 365$ nm, 250 W). The photodegradation of EE2 induced by high-pressure mercury lamp ($\lambda \geq 313$ nm, 250 W) in aqueous solution was investigated in [96] and it was shown that the process could be accelerated by Fe^{3+}. Ferric ions can promote the photodegradation of EE2 in aqueous solutions at a pH value of 2.0–5.0 [97].

The phototransformation of E2 and EE2 in dilute non buffered aqueous solution (pH 5.5–6.0) occurs with a quite low quantum yield of about 0.06 upon polychromatic ($\lambda > 290$ nm) or at 254 nm irradiation [95]. Increasing the initial concentration of EE2 lowers the photodegradation rate. The latter reached its lowest value at a pH about 5.0; higher pH values of 6.0 – 8.0 benefited the process [97].

The photodegradation of 1.6–20.0 mg/l EE2 in aqueous solutions at a given initial pH value of 6.8 is a pseudo-first order reaction. The pseudo-first order law is also found for the photolysis reaction of E2 in aqueous solutions (3.0–20 mg/l) [94].

According to Rosenfeldt [98], EDCs are more effectively degraded utilizing UV/H_2O_2 advanced oxidation as compared to direct UV photolysis treatment. However, mineralization of the pollutant would require extended UV treatment times. The breakdown products, as compared to their parent compounds, must be assessed through toxicological testing.

The relationship between degradation of E2 and EE2 and the removal of their estrogenic activity as measured by an *in vitro* estrogen activity assay, using UV photolysis and UV/H$_2$O$_2$ advanced oxidation processes, is examined [99].

Survey of the treatability of endocrine disruptors in water by advanced oxidation processes is made by Gültekin *et al.* [100].

4.9 Photocatalytic degradation
Photocatalysis vs. *photolysis*

Photocatalytic degradation of 17β-estradiol on immobilised TiO$_2$ was first reported by Coleman *et al.* [91]. The wavelength of light emitted from the lamp used includes the UVB (medium wave-range 280-315 nm; λ$_{max}$ = 290 nm) and UVC (short wave or germicidal-range between 200 nm and 280 nm; λ$_{max}$=254 nm) regions of the spectrum. So, experiments with TiO$_2$ are therefore photolysis and photocatalysis. The same group reported [101, 102] that photocatalysis coupled with photolysis is much more effective in degrading estrogens than photolysis alone caused by a 125 W medium pressure mercury lamp emitting radiation in the UVA (longwave or blackwave range between 315-400 nm; λ$_{max}$ = 365 nm), UVB and UVC regions of the spectrum. The photocatalytic treatment of E2 and EE2 completely removes the estrogenic activity in less than 60 min, compared to the photolytic process which requires 2-3 times longer treatment for EE2 and 8-9 times for E2 [101]. Other groups also reported that photocatalytic oxidation is much more efficient than direct photolysis in the degradation of E2, EE2 and E1 [101, 102, 103].

Photocatalytic reaction order

The authors [91] modeled the degradation kinetics using an apparent first order Langmuir-Hinshelwood kinetic rate equation. With the increase of E2 initial concentration, the rate of the reaction increases proportionally for both photocatalysis and photolysis, confirming that the reactions are first order [104]. First order kinetics is proven or accepted in practically all of the studies on this subject.

Photocatalytic reactors and irradiation sources

A quartz coil reactor and Hanovia 125 W medium pressure mercury lamp (emitting in UVB and UVC spectral regions) is used by Coleman *et al.* [104]; the TiO$_2$ is immobilized onto a quartz coil. Degussa P25 TiO$_2$, immobilized on a Ti-6Al-4V alloy film illuminated by 150 W xenon lamp is applied in [91]. Photocatalytic decomposition of

17-β-estradiol (E2) on TiO$_2$ immobilized on polytetrafluoroethylene mesh sheets is presented in [105]. The latter group reported results obtained in two kinds of reactors with different efficiency.

A quartz water-jacketed reactor with titanium dioxide immobilized on titanium alloy with a 125 W Philips high-pressure mercury lamp placed 3 cm from the reactor was used by Coleman *et al.* [101] for removal of estrogenic activity of several estrogens. Rate constants of UVA photolysis of the steroid substrates were 0.011 min^{-1} for E2 and 0.035min^{-1} for EE2 and the photocatalytic values - 0.106 min^{-1} for E2 and 0.086 min^{-1} for EE2.

A borosilicate glass spiral reactor (volume 85 ml) with TiO$_2$ immobilized onto the inside wall of the reactor was used in [106]. A black light blue fluorescent lamp (NEC, 15 W, emission range 300–400 nm with maximum at ~350 nm,) was fitted through the centre of the coil.

Zhang [107] also suggests that photocatalysis using P25-TiO$_2$ can be a very effective method of rapid removal of certain EDCs including E2 from water in two UV-photo-reactors. The water solutions were stirred with a magnetic stirrer for 30 min before TiO$_2$ was added at a concentration of 1 g/l. In reactor 1 (150 W UV-lamp), 97 % of the compounds were degraded within 4 h of irradiation. Even more rapid degradation was observed in reactor 2 (15 W-lamp), where 98 % of both compounds disappeared within 1 h due to the shorter wavelength of UV-light in this reactor (fixed at 253 nm) than in reactor 1 (238–579 nm) [107].

Influence of TiO$_2$ and pollutant concentrations on the estrogen removal efficiency

It was found that the efficiency of photocatalytic degradation of E2 in aqueous medium mediated with Degussa P25-TiO$_2$ increases with increasing concentration of TiO$_2$ but decreases for TiO$_2$ concentrations higher than 0.5 g/l due to light scattering [108]. The influence of the pollutant concentration on the photocatalytic process rate is seen from the data in Table 3 [104].

Table 3. Influence of the pollutant concentration on the rate constant and degradation rate of E2 by photolysis and photocatalytic process

E2, µmol/l	Rate constant, k.10^{-3} min^{-1} [104]		Degradation rate, r.10^{-3} µmol/l.min [104]	
	Photo-lysis	Photo-catalysis	Photo-lysis	Photo-catalysis
0,1	125	86	12	9
3	134	174	402	522

Estrogenic activity removal

Degradation of E2 in water by Degussa P25-TiO$_2$ photocatalysis has been investigated by Ohko *et al.* They showed experimentally and theoretically that the estrogenic activity of E2 is lost in the first step of the photocatalytic reactions. Thus, the authors conclude that TiO$_2$ photocatalysis could be applied to water treatment as a method for efficient removal of natural and synthetic estrogens without generating biologically active intermediates [92].

Ohko *et al.* [92] concluded in their study on E2 degradation by TiO$_2$ photocatalysis that the phenol moiety of the E2 molecule should be the starting point of the photocatalytic oxidation. In addition, since the intermediate products do not have a phenol ring, the authors presumed that their estrogenic activities are negligible [58, 92]. The association of the oxidative degradation of some EDCs with the aromatic moieties in their structure is accepted in [77], as well.

Nevertheless, the degradation of estrogen conjugates is also a rather important problem and their photocatalytic destruction had been an object of investigations. Estradiol and its conjugates estradiol-3-glucuronide and estradiol-17-glucuronide were subjected to photodegradation using TiO$_2$ immobilized on glass beads as a catalyst. Estradiol and its 17-glucuronide were almost completely degraded in presence of UV irradiation (4 W, λ_{max}=365 nm) in 4 h [109].

Estrogen susceptibility to degradation

The quantum yield of estrogen solutions degradation under UVA radiation in the absence of catalyst follows the sequence E1 > E3 > E2 > EE2, reflecting the much higher rate of decomposition of E1 compared to other estrogens. In the presence of TiO$_2$, the quantum yield follows the sequence E3 > EE2 > E1 > E2, although the difference among the estrogens is not significant [102].

In the presence of the illuminated (150 W xenon lamp) Degussa P25 TiO$_2$, E2 (0.05–3 μmol/dm^3) was 50 % degraded in 40 min and 98 % degraded in 3.5 h [91]. Photocatalytic decomposition of E2 over TiO$_2$ immobilized on polytetrafluoroethylene mesh sheets is performed in two types of reactors [103]. In the first one E2 concentration was decreased by 85 % in the dark (no UV illumination) after reaching absorption equilibrium for 1 h. UV illumination applied for 1 h after the dark period lead to decomposition of 98 % of the initial E2, with first-order rate constant of the photocatalytic decomposition of 0.033 min^{-1}. In the second reactor, 90 % of E2 disappeared after 20 min (first-order rate decomposition constant of 0.050 min^{-1}) [103]. More recently, the same group reported a first-order rate constant of 0.15 min^{-1} obtained for E2 under relatively weak UV illumination (1.2 mW/cm^2) [105].

A recombinant yeast assay to measure estrogenic activity, which provided detection limits within the reactor of 53 ng/l for E2 and EE2, and 100 ng/l for estrone is used for the study of the efficiency of the photocatalytic degradation of hormones. Pseudo-first-order kinetic data showed that photocatalysis over immobilized TiO$_2$ was equally effective at removing the estrogenic activity of all three steroid substrates in aqueous solutions (initial concentrations of 10 mg/l) with a 50 % reduction in estrogenicity within 10 min and 100 % within 1 h. In control experiments without TiO$_2$ catalyst, the rate of UVA photolysis of the steroid substrates varied, but was most effective with EE2 followed by estrone, and was least effective with E2 (0.42, 0.2 and <0.1 times the rate achieved with photocatalysis, respectively). The application of photocatalysis for the removal of steroid compounds within STW effluent released into the aquatic environment is discussed [101].

An interesting cross-relation between the irradiation light wavelength and the chemical nature of the estrogen is reported by Li Puma *et al.* [102] studying the degradation of multicomponent mixtures of E1, E2, EE2 and E3 in a slurry with P25-TiO$_2$ The E3 was low sensitive to a process under UVA irradiation, however, E1, E2 and EE2 were removed reaching 49, 20 and 25 % conversion, respectively, after 180 min of irradiation. Under UVC irradiation the conversions of E2, EE2 and E3 after 180 min were 60 %, but the reaction was much faster for E1, which was almost completely (98 %) degraded.

The research of Karpova *et al.* concerns the competitive photocatalytic oxidation and adsorption of steroid estrogens on TiO$_2$ in the presence of ethanol and urea. Degussa P25 TiO$_2$ under near-UV irradiation (1.1 mW/cm^2, 365 nm) was used as a photocatalyst. The presence of urea had a negligible effect on the oxidation of EE2 and a moderate one on E2 destruction. The process with E2 in the presence of urea proceeded a little faster than in its absence at pH 7–10, but the effect was moderate as well [110].

The comparison of some main parameters (rate constant, degradation rate and time for degradation of a part of the pollutant) for the photolysis and photocatalytic process is seen from the data in Table 4 [101, 104].

Table 4. Rate constants, degradation rates and time for pollutant removal resulted in photolysis and photocatalysis

Estrogen	Rate constant, k.10⁻³ min⁻¹		Degradation rate, r. 10⁻³ μmol/l.min [104]		Time (min) for removal (%) of the pollutant [101]					
					50		90		100	
	Photo-lysis	Photo-catalysis	Photo-lysis	Photo-catalysis	Photo-lysis*	Photo-catalysis	Photo-lysis*	Photo-catalysis	Photo-lysis*	Photo-catalysis
E2	134[104]; 11[101]	174[104]; 106[101]; 33 [103]; 50 [103]	402	522	195	10	248	24	485	55
EE2	195[104]; 35[101]	231[104]; 86[101]	585	694	23	8	72	28	120	50
Estriol	93[104]	156[104]	280	468						
Estrone	12[101]	86[101]			68	7	195	18	360	60

* Under UVA irradiation.

The great differences in the photocatalytic process conditions explain the differences in the mentioned parameters, so the cited values can be used for general evaluation of the process. Data summarized in [111] show variation in the rate constant ($n.10^{-3}$ min^{-1}) from 14 to 174 for E2 and from 86 to 231 reaching (in the cited paper) 399 for E2 at 365 nm-irradiation and 315 and full destruction for 15 min at UVC irradiation.

Doping as a tool for increasing TiO2 efficiency

It was found that the addition of silver or platinum to TiO_2 (doping by photodeposition) has no effect on the photocatalytic degradation or mineralization of all EDCs at the concentrations found in water. This was attributed to the high concentration of holes and hydroxyl radicals in the system compared to the low amount of organic matters to be degraded [106].

For the first time data on the effect of TiO_2 modification by N-doping or MWCNT, are obtained in [111]. The sorption ability and photocatalytic activity (measured by degradation rate constant and percentage of the pollutant conversion) of the catalysts under UV (150 W, emission maximum at 365 nm) illumination are determined. The commercial product TiO_2 P25 showed significant degradation efficiency for both estrogens under UV irradiation. However, in some cases the activity of the commercial product declines after the first 15-30 min of illumination and plateau trends are registered at longer irradiation times. That is why, as a final result, the catalysts TiO_2-MWCNTs and TiO_2-N show similar or better efficiency despite the fact that their main component - pure sol-gel synthesized TiO_2 - is much less effective than the Degussa TiO_2 P25.

The sorption and photocatalytic performance of the commercial product Degussa P25, the sol-gel prepared TiO_2 calcined at different temperatures and the same doped with carbon nanotubes against the estrogen EE2 under UVC irradiation is studied in [112]. It is found that the commercial product TiO_2 P25 shows significant degradation efficiency for EE2 providing its full destruction for 30 min. The pure TiO_2 sol-gel synthesized at 700 ºC is ~6-fold less effective than the Degussa P25. Higher rutile content, larger morphological grains and other surface properties (acidity, hydrophobicity, etc.) seem to be among the factors responsible for this effect. The addition of carbon nanotubes to a similar (produced at lower temperature) TiO_2 has

no significant positive influence at the applied photocatalytic test conditions.

Estrogens degradation under visible light illumination

For the first time the photocatalytic destruction of E2 and EE2 under visible light irradiation (150 W halogen lamp) is tested in [111]. The observed rather high efficiency of Degussa TiO_2 P25 under these conditions suggests that the measured band-gap energy value can not be regarded as a direct response to the level of photocatalytic activity. Full destruction of E2 and >99.7 % of EE2 is reached after 2 h irradiation with visible light.

5 CONCLUSION

The literature review shows that both natural and synthetic estrogens are a common pollutant of surface waters, sediments and even drinking waters. Extremely important sources of estrogens found in the environment are the not treated wastewaters, such as effluents from livestock farms. Despite the occasionally reported rather high concentrations, the normal presence of endocrine disrupting compounds ranges from 0.1 to dozen of nanograms per liter. The laboratory tests, as well as the environmental monitoring unambiguously show that their presence in the environment even at such low concentrations is likely to disturb the ecosystems and to affect human health. Thus, the need for developing reliable detection methods, analysis tools, and adapted wastewater treatment processes is now a subject of significant interest. The advanced oxidation processes and especially photocatalysis gained approval as a prospective method for degradation of these emerging environmental contaminants.

The data for the photocatalytic degradation rate constants and the time for degradation of different estrogens vary within rather wide limits, depending on the type of catalyst, irradiation conditions and chemical nature of the estrogen. Full destruction of EE2 can be ensured for 15 min at UVC irradiation and for 1 h in presence of E2 or EE2 under UVA treatment. The recent investigations show that full destruction of E2 and >99.7 % of EE2 can be reached after 2 h irradiation with visible light.

REFERENCES

1. G.-G. Ying, R. S. Kookana, Y.-J. Ru, *Environ. Int.,* **28,** 545 (2002).
2. O. Refsdal, *Anim. Reprod. Sci.,* **60–61**, 109 (2000).
3. M. R. Callantine, M. Stob, F.N. Andrews, *Am J Vet Res.,* **22**, 462 (1961).
4. Shareef, M. J. Angove, J. D. Wells, B. B. Johnson, *J. Chem. Eng. Data.,* **51**, 879 (2006).
5. Pan, D. Lin, H. Mashayekhi, B. Xing, *Environ. Sci. Technol.*, **42**, 5480 (2008).
6. O. Braga, G. A. Smythe, A. I. Schafer, A. J. Feitz, *Environ. Sci. Technol.*, **39**, 3351 (2005).
7. H. Segner, J. M. Navas, C. Schafers, A. Wenzel, *Ecotoxicol. Environ. Saf.*, **54**, 315 (2003).
8. C. Johnson, J. P. Sumpter, *Environ. Sci. Technol.*, **35**, 4697, (2001).
9. H. H. Tabak; R. N. Bloomhuff; R. L. Bunch, *Dev. Ind. Microbiol.*, **11**, 497 (1970).
10. C. Desbrow, E. J. Routledge, G. C. Brighty, J. P. Sumpter, M. Waldock, *Environ. Sci. Technol.,* **32**, 1549 (1998).
11. C. E. Purdom, P. A. Hardiman, V. J. Bye, N. C. Eno, C. R. Tyler, J. P. Sumpter, *Chem. Ecol.*, **8**, 275 (1994).
12. J. F. Harries, D. A. Sheahan, S. Jobling, P. Matthiessen, M. Neall, E. J. Routledge, R. Rycroft, J. P. Sumpter, T. Taylor, *Environ. Toxicol. Chem.*, **15**, 1993 (1996).
13. J. F. Harries, D. A. Sheahan, S. Jobling, P. Matthiessen, M. Neall, J. P. Sumpter, T. Taylor, N. Zaman, *Environ. Toxicol. Chem.*, **16**, 534 (1997).
14. S. Pawlowski, T. Ternes, M. Bonerz, T. Kluczka, B. van der Burg, H. Nau, L. Erdinger, T. Braunbeck, *Toxicol. Sci.*, **75**, 57 (2003).
15. S. A. Snyder, D. L. Villeneuve, E. M. Snyder, J. P. Giesy, *Environ. Sci. Technol.*, **35**, 3620 (2001).
16. R. Gibson, C. R. Tyler, E. M. Hill, *J. Chromatogr., A*, **1066**, 33 (2005).
17. G. W. Aherne; R.Briggs, *J. Pharm. Pharmacol.*, **41**, 735 (1989).
18. M. Stumpf, T. A. Ternes, K.Iiaberer; W. Baumann, *VomWasser.*, **87**, 251 (1996).
19. T. A Ternes, M. Stumpf, J. Mueller, K. Haberer, R.-D. Wilken, M. Servo, *Sci. Total Environ.*, **225**, 81 (1999).
20. Ch. Baronti, R. Curini, G. D'Ascenzo, A. Di Corcia, A. Gentili, R. Samperi, *Environ. Sci. Technol.*, **34**, 5059 (2000).
21. H. Andersen, H. Siegrist, B. Halling-Sørensen,T. A. Ternes, *Environ. Sci. Technol.*, **37**, 4021 (2003).
22. P. Labadie, H. Budzinski, *Environ. Sci. Technol.* **39**, 5113 (2005).
23. M. Esperanza, M. T. Suidan, R. Marfil-Vega, C. Gonzalez, G. A. Sorial, P. McCauley, R. Brenner, *Chemosphere* **66**, 1535 (2007).
24. Y. P. Zhang, J. L. Zhou, *Chemosphere* **73**, 848 (2008).
25. B. Lei, Sh. Huang, Y. Zhou, D. Wang, Z. Wang, *Chemosphere* **76**, 36 (2009).
26. C. Belfroid, A. Van der Horst, A. D. Vethaak, A. J. Schäfer, G. B. J. Rijs, J. Wegener, W. P. Cofino, *Sci. Total Environ.*, **225**, 101 (1999)
27. P. Spengler, W. Körner, J. W. Metzger, *Vom Wasser*, **93**, 141 (1999).
28. H. M. Kuch, K. Ballschmiter, *Fresenius J. Anal. Chem.* **366**, 392 (2000).
29. A.C. Johnson, A. C. Belfroid, A. di Corcia, *Sci. Total Environ.*, **256**, 163 (2000).
30. H. Huang, D. L. Sedlak, *Environ. Toxicol. Chem.,* **20**, 133 (2001).
31. P. Adler, Th. Steger-Hartmann, W. Kalbfus, *Acta Hydrochim. Hydrobiol.*, **29**, 227 (2001).
32. X.-Y. Xiao, D. V. McCalley, J. McEvoy,. *J. Chromatogr., A*, **923**, 195 (2001).
33. Th. Heberer, *J. Hydrol.,* (in press).
34. C. Baronti, R. Curini, G. d'Ascenzo, A. Di Corcia, A. Gentili, R. Samperi, *Sci. Technol.,* **34**, 5059 (2000).
35. M. P. Fernandez, M. G. Ikonomou, I. Buchanan, *Sci Total Environ.,* **373,** 250 (2007)
36. C. Johnson, T. Ternes, R. J. Williams , J. P . Sumpter, *Environ. Sci. Technol.,***42**, 5390 (2008).
37. C. Johnson, R. J. Williams, *Environ. Sci. Technol.*, **38**, 3649 (2004).
38. D. W. Kolpin, E. T. Furlong, M. T. Meyer, E. M. Thurman, S. D. Zaugg, L. B. Barber, H. T. Buxton, *Environ. Sci. Technol.*, **36**, 1202 (2002).
39. Y. Zuo, K. Zhang, Y. Deng, *Chemosphere*, **63**, 1583 (2006).
40. G. Morteani, P. Moller, A. Fuganti, T. Paces, *Environ. Geochem. and Health*, **28**, 257 (2006).
41. H.-Ch. Chen, H.-W. Kuo, W.-H. Ding, *Chemosphere,* **74**, 508 (2009).
42. D. Bila, A. F. Montalväo, D. A. Azevedo, M. Dezotti, *Chemosphere*, **69**, 736 (2007).
43. J. Lee, B. C. Lee, J. S. Ra, J. Cho, I. S. Kim, N. I. Chang, H. K. Kim, S. D. Kim, *Chemosphere*, **71**, 1582 (2008).
44. M. Auriol, Y. Filali- Meknassi, C. D. Adams, R. D. Tyagi, T.-N. Noguerol, B. Pica, *Chemosphere*, **70**, 445 (2008).
45. T. de Mes, G. Zeeman, G. Lettinga, *Rev. Environ. Sci. Biotechnol.,* **4**, 275 (2005).
46. G. Campbell, S. E. Borglin, F. Bailey Green, A. Grayson, E. Wozei, W. T. Stringfellow, *Chemosphere*, **65**, 1265 (2006).
47. W. Cui, S. L. Ji, H. Y. Ren, *Environ. Monit. Assess.*, **121**, 409 (2006).
48. S. R. Hutchins, M. V. White, F. M.Hudson, D. D. Fine, *Environ. Sci. Technol.*, **41**, 738 (2007).
49. J. Nelson, F. Bishay, A. van Roodselaar, M. Ikonomou, F. C. P. Law, *Sci. Total Environ.*, **374**, 80 (2007).
50. Salvador, C. Moretton, A. Piram, R. Faure, *J. Chromatogr., A*, **1145**, 102 (2007).
51. L. L. Tan, D. W. Hawker, J. F. Müller, F. D. L. Leusch, L. A. Tremblay, H. F. Chapman, *Aust. Environ. Int.,* **33**, 654 (2007).

52. R. J. Williams ,A. C. Johnson ,J. J. Smith ,R. Kanda, *Environ Sci Technol.,* **37**,1744 (2003).

53. T. Heberer, *Toxicol. Lett.*, **131**, 5 (2002).

54. S. D. Kim, J. Cho, I. S. Kim, Br. J. Vanderford , Sh. A. Snyder, *Water Res.,* **41**, 1013 (2007)

55. M. J. Lopez de Alda, A. Gil, E. Paz, D. Barcelo, *Analyst,* **127**, 1299 (2002).

56. J.H Shen, B Gutendorf , H.H Vahl, L Shen, J Westendorf, *Toxicology*, **166**, 71 (2001).

57. M. Petrovicè, E. Eljarrat, M. J. Loèpez de Alda, D. Barceloè, *TrAC, Trends Anal. Chem.*, **20**, 637 (2001).

58. M. Auriol, Y. Filali-Meknassi, R. D. Tyagi, C. D. Adams, R. Y. Surampalli, *Process. Biochem.*, **41**, 525 (2006)

59. M. J. López de Alda, D. Barceló, *TrAC, Trends Anal. Chem.,* **22**, 340 (2003)

60. S. Jobling, D. Sheahan, J. A. Osborne, P. Matthiessen, J. P. Sumpter, *Environ. Toxicol. Chem.*, **15**, 194 (1996)

61. R. Länge, T. H. Hutchinson, C. P. Croudace, F. Siegmund, *Environ. Toxicol. Chem.*, **20**, 1216 (2001)

62. K. L. Thorpe, R. I. Cummings, T. H. Hutchinson, M. Scholz, G. Brighty, J. P. Sumpter, C. R. Tyler, *Environ. Sci. Technol.*, **37**, 1142 (2003)

63. M. Fenske, G. Maack, C. Schafers, H. Segner, *Environ. Toxicol. Chem.*, **24**, 1088 (2005)

64. K. A. Kidd, P. J. Blanchfield, K. H. Mills, V. P. Palace, R. E. Evans, J. M. Lazorchak, R. W. Flick, *Proc. National Acad. Sci. USA*, **104**, 8897 (2005)

65. G. S. Dizerega, D. L. Barber, G. D. Hodgen, *Fertil. Steril.* **33**, 649 (1980)

66. B. Delvoux, B. Husen, Y. Aldenhoff, L. Koole, G. Dunselman, H. Thole, P. Groothuis, *J. Steroid Biochem. Mol. Biol.,* **104**, 246 (2007)

67. T. de Mes, G. Zeeman, G. Lettinga, *Rev. in Environ. Sci. Biotechnol.*, **4**, 275 (2005)

68. K. Xu, W. F. Harper Jr, D. Zhao, *Water Res.,* **42,** 3146 (2008)

69. Danish Environmental Protection Agency (DEPA). Feminisation of fish— the effect of estrogenic compounds and their fate in sewage treatment plants and nature. Environmental Project No. 729. Danish Environmental Protection Agency, Danish Ministry of the Environment; 2002.

70. Danish Environmental Protection Agency (DEPA). Evaluation of analytical chemical methods for detection of estrogens in the environment. Working Report No. 44. Danish Environmental Protection Agency, Danish Ministry of the Environment; 2003.

71. C. Layton, B. W. Gregory, J. R. Seward, T. W. Schultz, G. S. Sayler, *Environ. Sci. Technol.*, **34**, 3925 (2000)

72. J. S. Vader, C. G. van Ginkel, F. M. G. M. Sperling, J. de Jong, W. de Boer, J. S. de Graaf, M. van der Most, P. G. W. Stokman, *Chemosphere*, **41,** 1239 (2000)

73. M. D. Jürgens, K. I. E. Holthaus, A. C. Johnson, J. J. L. Smith, M. Hetheridge, R. J. Williams, *Environ. Toxicol. Chem.* **21**, 480 (2002)

74. M. Rathner, M. Sonneborn, *Forum Städte-Hygiene*, **30**, 45 (1979) (in German)

75. M. Mastrup, R. L. Jensen, A. I. Schäfer, S. Khan, in: Recent advances in water recycling technologies, A. I. Schäfer, P. Sherman, T. D. Waite (eds.), Australia, Brisbane, 2001, p. 103

76. G-G. Ying, R. S. Kookana, P. Dillon, *Ground Water Monit. Remed.*, **24**, 102 (2004)

77. H-S. Chang, K-H. Choo, B. Lee, S-J. Choi, *J. Hazard. Mater.*, **172**, 1, (2009)

78. Y. Yoon, P. Westerhoff, Sh. A. Snyder, M. Esparza, *Water Res.*, **37**, 3530 (2003)

79. K. Yang, L. Z. Zhu, B. S. Xing, *Environ. Sci. Technol.*, **40**, 1855 (2006)

80. K. Pyrzynska, A. Stafiej, M. Biesaga, *Microchim. Acta*, **159**, 293 (2007)

81. F. S. Su, C. S. Lu, *J. Environ. Sci. Health. Part A: Toxic/Hazard. Subst. Environ. Eng*. **42**, 1543 (2007)

82. Y. H. Li, S. G. Wang, J. Q. Wei, X. F. Zhang, C. L. Xu, Z. K. Luan, D. H. Wu, B. Q. Wei, *Chem. Phys. Lett.* **357**, 263 (2002)

83. Y. H. Li, S. G. Wang, X. F. Zhang, J. Q. Wei, C. L. Xu, Z. K. Luan, D. H. Wu, *Mater. Res. Bull.,* **38,** 469 (2003)

84. Salhi, U. von Gunten, *Water Res.*, **33**, 3239 (1999)

85. M. M. Huber, S. Canonica, G-Y. Park, U. von Gunten, *Environ. Sci. Technol.*, **37**, 1016 (2003)

86. M. M . Huber , T. A . Ternes , U. von Gunten, *Environ. Sci. Technol*., **38**, 5177 (2004)

87. Z. Meng, W. Chen, A. Mulchandani, *Environ. Sci. Technol.*, **39**, 8958 (2005)

88. M. Auriol, Y. Filali-Meknassi, R. D. Tyagi, Cr. D. Adams, *Water Res.,* **41**, 3281 (2007)

89. P. Blánquez, B. Guieysse, *J. Hazard. Mater.*, **150**, 459 (2008)

90. S. Hwang, D.-I. Lee, Ch.-H. Lee, I.-S. Ahn, *J. Hazard. Mater.*, **155**, 334 (2008)

91. H. M. Coleman, B. R. Eggins, J. A. Byrne, F. L. Palmer, E. King, *Appl. Catal., B*, **24**, L1 (2000)

92. Y. Ohko, K-I. Iuchi, C. Niwa, T. Tatsuma, T. Nakashima, T. Iguchi, Y. Kubota, A. Fujishima, *Environ Sci Technol.,* **36**, 4175 (2002)

93. B. E. Segmuller, B. L Armstrong, R. Dunphy, A.R. Oyler, *J. Pharm. Biomed. Anal.*, **23**, 927 (2000)

94. B. Liu, X. Liu, *Sci Total Environ*, **320**, 269 (2004)

95. P. Mazellier, L. Meite, J. De Laat, *Chemosphere*, **73**, 1216 (2008)

96. X. L. Liu, F. Wu, N. S. Deng, *Environ. Pollut.*, **126**, 393 (2003)

97. B. Liu, F. Wu, N. S. Deng, *J. Hazard. Mater.*, 311 (2003)

98. J. Rosenfeldt, K. G. Linden, *Environ. Sci. Technol*., **38**, 5476 (2004)

99. J. Rosenfeldt, P. J. Chen, S. Kullman, K. G. Linden, *Sci Total Environ.*, **377**, 105 (2007)

100. Gültekin, N. H. Ince, *J. Environ. Manage*., **85**, 816 (2007)
101. M. Coleman, E. J. Routledge, J. P. Sumpter, B. R. Eggins, J. A. Byrne, *Water Res.*, **38**, 3233 (2004)
102. Li Puma, V. Puddu, H. K. Tsang, Al. Gora, B. Toepfer, *Appl. Catal., B*, **99**, 388 (2010)
103. T. Nakashima, Y. Ohko, D. A. Tryk, A. Fujishima, *J. Photochem. Photobiol., A,* **151**, 207 (2002)
104. M. Coleman, M. I. Abdullah, B. R. Eggins, F. L. Palmer, *Appl. Catal B*., **55**, 23 (2005)
105. T. Nakashima, Y. Ohko, Y. Kubota, A. Fujishima, *J. Photochem. Photobiol., A*, **160**, 115 (2003)
106. H. M. Coleman, K. Chiang, R. Amal, *Chem. Eng. J*., **113**, 65 (2005)
107. Y. Zhang, J. L. Zhou, B. Ning, *Water Res.,* **41,** 19 (2007)
108. Mai, W. Sun, L. Xiong, Y. Liu, J. Ni, *Chemosphere*, **73**, 600 (2008)
109. K. Mitamura, H. Narukawa, T. Mizuguchi, K. Shimada, *Anal. Sci.* **20**, 3 (2004)
110. T. Karpova, S. Preis, J. Kallas, *J. Hazard. Mater.*, **146**, 465 (2007)
111. R. Kralchevska, M. Milanova, M. Bistan, A. Pintar, D. Todorovsky, *Reac Kinet Mech Cat.* DOI 10.1007/s11144-013-0567-0 (2013)
112. R. Kralchevska, M. Milanova, M. Bistan, A. Pintar, D. Todorovsky, *Centr. Europ. J. Chem.,* **10**, 1137 (2012)
113. C. Y. Chen, T. Y. Wen, G. S. Wang, H. W. Cheng, Y. H. Lin, G. W. Lien, *Sci. Total Environ*., **378**, 352 (2007)
114. T. A. Ternes, H. Andersen, D. Gilberg, M. Bonerz, *Anal. Chem.*, **74**, 3498 (2002)
115. T. Isobe, S. Serizawa, T. Horiguchi, Y. Shibata, S. Managaki, H. Takada, M.Morita, H. Shiraishi, *Environ. Pollut*., **144**, 632 (2006)
116. O. Braga, G. A. Smythe, A. I. Schäfer, A. J. Feitz, *Chemosphere*, **61**, 827 (2005)
117. N. Nasu, M. Goto, H. Kato, Y. Oshima, H.Tanaka, *Water Sci. Technol.*, **43**, 101 (2000)
118. S. A. Snyder, T. L. Keith, D. A. Verbrugge, E. M. Snyder, T. S. Gross, K. Kannan, J.P. Giesy, *Environ. Sci. Technol.,* **33**, 2814 (1999)
119. H. M. Kuch, K. Ballschmitter, *Environ. Sci. Technol.,* 35, 3201 (2001)
120. G. Morteani, P. Moller, A. Fuganti, T. Paces, *Environ. Geochem. Health,* **28**, 257 (2006).

НЯКОИ СЪЕДИНЕНИЯ С ЕНДОКРИННО ВЪЗДЕЙСТВИЕ В ОКОЛНАТА СРЕДА И ВЪЗМОЖНОСТИТЕ ЗА ТЯХНОТО ОТСТРАНЯВАНЕ/РАЗГРАЖДАНЕ

Р. П. Кралчевска, М. М. Миланова, Ил. Л. Христова, Д. Ст. Тодоровски

Софийски университет, Факултет по химия и фармация, бул. Дж. Баучър 1, София 1164

(Резюме)

Работата представя преглед на литературните данни за присъствието на съединения с ендокринно въздействие в изходните води от пречиствателните станции за отпадни води, повърхностни, подземни и питейни води и седименти. Дадени са общи данни за тяхното въздействие върху живите организми (главно риба). Разгледана е спецификата на методите за отстраняването/разграждането на замърсителите чрез адсорбция, озониране, биоразграждане, фотолиза и фотокатализ.

Investigation of electrode reactions in hydrogen peroxide alkaline medium onto Pt and Au electrodes by cyclic voltammetry - Part I

V. Stefanova[1], Ts. Dobrovolska[2], R. Miletiev[3], M. Georgiev[1], I. Simeonov[3]

[1]*University of Chemical Technology and Metallurgy 8 Kl. Ohridski blvd, 1756 Sofia, Bulgaria*
[2] *Institute of Physical Chemistry, Bulgarian Academy of Sciences Acad. G. Bonchev st. bl 11, 1113, Sofia, Bulgaria*
[3] *Technical University, 9 Kl. Ohridski blvd, 1756 Sofia, Bulgaria*

In the present paper, the effect of electrolyte convection on the electrode reactions taking place on Pt and Au electrodes in alkaline H_2O_2 solution is investigated by cyclic voltammetry (CV). The electrochemical behavior of H_2O_2 obtained by hydrolysis of calcium peroxide (CaO_2) in the presence of potassium hydrogen carbonate ($KHCO_3$) is also studied with a view to its use as a reagent (fuel and oxidant) for hydrogen peroxide fuel cells (HPFC).

The first cathodic reaction taking place on a Pt electrode is the reduction of the perhydroxyl ion (HO_2^-). At more negative potentials current oscillations are observed. Based on the analogy to acidic medium it is supposed that the reaction continues with formation of a hydroxide passive film and only after that by recombination of the hydrogen atoms to the evolution of hydrogen. The electrode processes take place in conditions of stationary diffusion and the reaction rate is determined solely by the concentration of reagent.

On solid gold, as well as on an electrodeposited gold coating onto a nickel substrate, the reactions of reduction, as well as of oxidation take place with high catalytic activity. The morphology of the gold coating onto nickel foam does not disintegrate after the electrochemical treatment in alkaline H_2O_2 solution. The trends of CV curves (respectively, the electrode reactions) of synthesized and stabilized alkaline solution of H_2O_2 are analogous. This result leads to the conclusion that hydrogen peroxide obtained by hydrolysis of CaO_2 can be used directly as a reagent (fuel or oxidant) for HPFC.

Keywords: cyclic voltammetry, platinum, gold, electrode, hydrogen peroxide, calcium peroxide

INTRODUCTION

The search for energy sources alternative to the traditional carbon-based fuels is a task of primary importance nowadays. The use of hydrogen peroxide in the fuel cells (HPFC) is determined by the chemical nature of this reagent to be both oxidant and reducer. The feasibility of transforming its chemical energy into electrical through electrochemical reactions makes it competitive to other ecological energy sources such as hydrogen, methanol, etc., especially where oxygen is not easily available [1, 2]. Some of the main problems that still hinder the wide use of H_2O_2 for HPFC are difficulties related to its storage, low stability, and generation of large quantities of water upon decomposition. One of the possible solutions is production of H_2O_2 by hydrolysis of peroxides of alkaline and alkali earth metals (BaO_2, SrO_2CaO_2 etc.) [3]. Of these, CaO_2 is considered the most promising due to its low price, non-toxicity and affordability.

In the course of our previous research [4] a new method was developed for obtaining H_2O_2 by hydrolysis of CaO_2 in the presence of sodium (potassium or ammonium) hydrogen carbonate, the chemistry of which can be described by the following summary reaction:

$$CaO_2 + MeHCO_3 + H_2O = H_2O_2 + CaCO_3 + MeOH \quad (1)$$
$$\text{where } Me^+ \rightarrow Na^+, K^+, NH_4^+$$
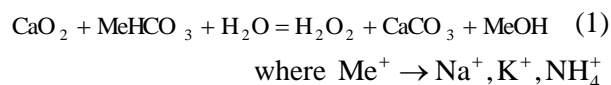
It was found that the process runs at a high rate, while the concentration of H_2O_2 in the solution can be controlled by variation of the pH, temperature, density of the pulp and manner of mixing the reagents.

According to [5–7] the electrode processes taking place on Pt and Au electrodes in neutral and alkaline hydrogen peroxide solutions are comparatively well studied. It is known that both precious metals are good catalysts of the electrode reactions taking place in alkaline hydrogen peroxide solution. There is lack of information in the literature about the effect of *H_2O_2* concentration on the course of the electrode reactions, as well as

the influence of the natural and forced convection on them. Both parameters are of great significance for improving the efficiency of HPFC operation.

At the same time, taking into account that platinum and gold electrodes can be considered as model ones in terms of catalytic capabilities with respect to the electrode reactions taking place in alkaline solution of H_2O_2, it would be interesting to compare the run of electrode reactions of hydrogen peroxide obtained by hydrolysis of CaO_2 in the presence of $KHCO_3$ (called briefly „non-stabilized") with data about stabilized hydrogen peroxide in analogous conditions.

The objectives of this paper are: to determine the influence of convection on the electrode processes taking place on Pt and Au electrodes in alkaline hydrogen peroxide medium (a vertical electrode for determination of the natural convection and a rotating disc electrode (RDE) providing forced convection in conditions of stationary diffusion) and to assess the behavior of synthesized H_2O_2 on platinum and gold, with a view to its direct use as a reagent (fuel and oxidant) for hydrogen peroxide fuel cells.

EXPERIMENT

The following solutions were prepared for the CV experiments: basic electrolyte with concentration 1 M KOH, solution A - 0.1÷0.15 M H_2O_2 in 1M KOH; solution B – 0.2÷0.25 M H_2O_2 in 1M KOH; solution C - 0.4÷0.45 M H_2O_2 in 1M KOH. Solutions A, B and C were prepared using a 30% solution of H_2O_2, potassium hydroxide with purity *pro analysis* and distilled water. Solution D was prepared before each experiment by hydrolysis of CaO_2 in the following conditions: temperature 298K, 50% excess of $KHCO_3$, solid:liquid ratio = 1:10, contact time 5 min. The variations in the molar concentration of H_2O_2 in the examined solutions are due to low stability of the peroxide. Its concentration in the solution was determined before and after each experiment by a method proposed by Solvay [8].

The method of cyclic voltammetry that permits comparatively easy determination of the thermodynamic (reaction potential) and kinetic (current density) parameters of reactions taking place in the system [9] was used to investigate the efficiency of electrode reactions taking place on platinum and gold electrodes.

The experiments were carried out in a glass three-electrode Gamry cell with volume of 200 cm³ at room temperature. The working electrodes made of solid platinum and gold had areas between 1 and

2 cm². The area of the rotary disc electrode was 0.0707 cm². A platinum counter-electrode with area ~2 cm² was used in all experiments. A calomel reference electrode (Hg/Hg₂Cl₂) was used. Its potential, compared to a normal hydrogen electrode, is $E_{SCE} = 0.244$ V. During the experiment it was placed in a separate cell filled up with 3M solution of KCl. Its connection to the electrolytic cell was made by a Haber-Lugin capillary through an electrolyte bridge filled with 3M KCl on one side, and with the working electrolyte on the other side. The experiments were carried out with a computer-controlled potentiostat-galvanostat Model G 300/ZRA made by GAMRY Instruments. GAMRY FRAMEWORK PHE 200 software was used for processing the experimental data.

The scan rate during cyclic voltammetry experiments was 0.1 V s⁻¹. In most cases scanning started from 0 V compared to the potential of the comparator calomel electrode and continued up to – 2.0 V, a potential sufficiently negative to trigger the reaction of hydrogen release. After that the scanning direction was reversed and scanning was carried out up to a potential of +1.2 V in the anode region. Before each experiment, the cathode surface was cleaned and pickled.

RESULTS AND DISCUSSION

Effect of convection on the electrode processes

Figures 1a to 1d present cyclic voltammetry curves obtained in solutions A, B and C onto a Pt working electrode. As mentioned above, platinum is one of the best catalysts for cathodic reduction of hydrogen peroxide [10]. One major drawback of using platinum is the occurrence of a random reaction of destruction manifested by covering the electrode surface with bubbles of oxygen immediately after its immersion in hydrogen peroxide solution.

The CV curves obtained with a working rotating disc electrode (RDE) without rotation are presented in Fig.1a. In this case the natural convection is severely suppressed. The difficulties met by the electrolyte flow in ascending are due to absence of microconvection along the electrode/solution interface. In consequence, the new reagent flow is not delivered uniformly to the electrode surface, in case of non reacted hydrogen peroxide. During the experiments, a gas bubble occupying a large part of the electrode can be observed, which grows with scanning to more negative potentials. According to Littauer and Tsai [11], in strongly alkaline solution,
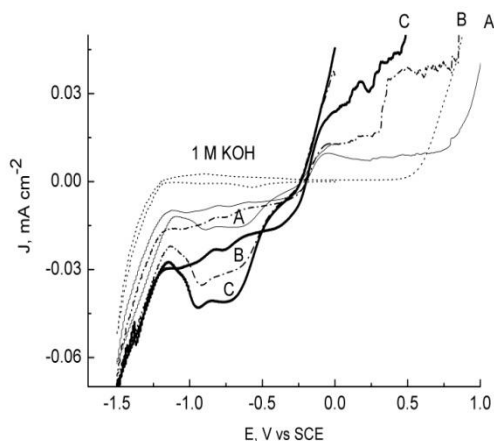
Fig.1a. Cyclic voltammograms of Pt RDE electrode, rpm = 0.
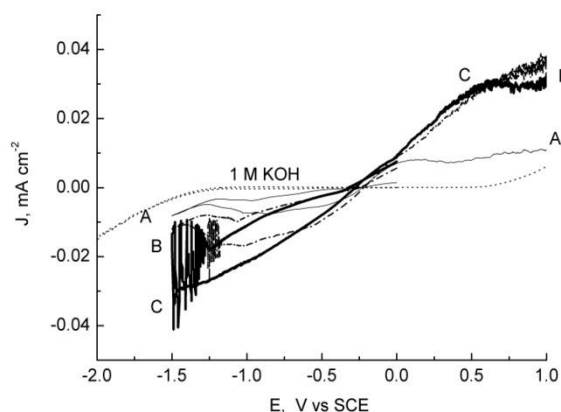Solutions: A,B and C, T = 298K, scan rate 0.1V s^{-1}

Fig.1b. Cyclic voltammograms of Pt RDE electrode, rpm = 1000.
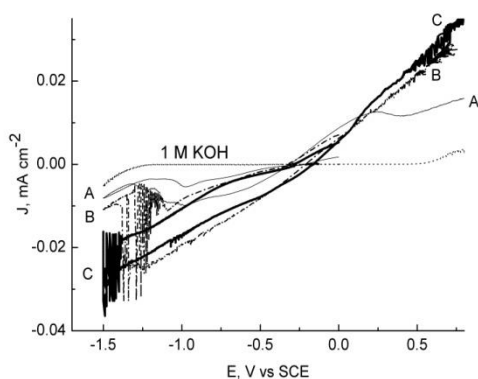Solutions: A,B and C, T = 298 K, scan rate 0.1V s^{-1}

Fig.1c. Cyclic voltammograms onto Pt
RDE electrode, rpm = 2000.
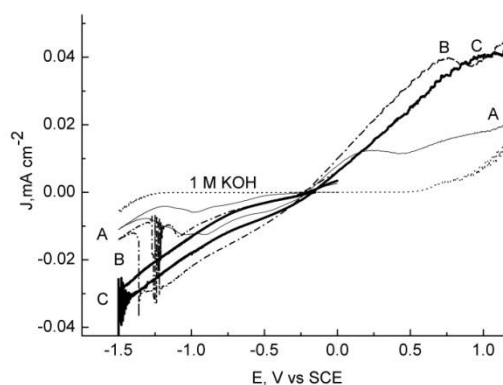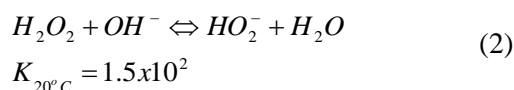Solutions: A, B and C, T = 298K, scan rate 0.1V s^{-1}

Fig.1d. Cyclic voltammograms onto Pt
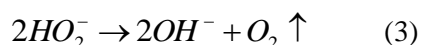RDE electrode, rpm = 3000.
Solutions: A, B and C, T = 298K, scan rate 0.1V s^{-1}

H_2O_2 is transformed almost completely into perhydroxyl ion (HO_2^-)

$$H_2O_2 + OH^- \Leftrightarrow HO_2^- + H_2O$$
$$K_{20^oC} = 1.5x10^2 \tag{2}$$

and subsequently within bulk solution and especially at catalytic surface:

$$2HO_2^- \to 2OH^- + O_2 \uparrow \tag{3}$$

The reaction of reduction of an HO_2^- ion starts at potentials about –0.2V and reaches its maximum rate at potentials –0.6V for all three investigated concentrations. The hydrogen evolution reaction (HER) starts at potentials after –1.2V, such as in 1M solution of KOH. In the case of scanning in the reverse direction an anode current is observed

immediately after reaching 0 V. This fact indicates that the oxidation reaction taking place at the anode is highly catalyzed by the platinum substrate [7]. It can be seen that in 1M solution of KOH without hydrogen peroxide, the oxidation reaction starts only after +0.6 V.

With a higher H_2O_2 concentration in the alkaline solution, higher limiting currents of the cathodic, as well as of the anodic reactions are reached (i.e., the rates of the reactions of both reduction and oxidation are increased).

The influence of forced convection on the electrode processes taking place on platinum RDE at rotation speed of the electrode – 1000, 2000 and 3000 rpm is shown in Fig.1b÷d. The start of the cathodic reaction (4) can be determined at potentials about –0.2 V. According to the main theoretical principle of the rotating disc electrode, its rotation creates conditions for occurrence of the electrochemical processes in conditions of

stationary diffusion [12]. The higher the rotation speed, the thinner is the boundary layer, where there is a uniform layer with constant reagent concentration, i.e., there are conditions of stationary diffusion. Criterially, if the limiting current density depends on the rotation speed, then diffusion is the limiting stage. Analysis of the CV curves indicates that at all three rotation speeds the limiting currents were: for electrolyte A ~0.008 mA cm^{-2}, for electrolyte B - 0.01 mA cm^{-2} and for electrolyte C – 0.02 mA cm^{-2}. Therefore, the rotation speed at the same concentration of the investigated solution does not affect the boundary current, i.e. the reaction speed. It is obvious that the limiting current density is determined solely by the hydrogen peroxide concentration. Therefore, the charge transfer is most probably the limiting stage and the reaction speed will be determined only by the reagent concentration [13].

An occurrence of current oscillations (with amplitude reaching ~ 0.10 mA cm^{-2}) could be observed using an RDE. This phenomenon is observed upon reduction of hydrogen peroxide on a platinum electrode, but in acidic medium [6, 14] and is accounted for by the formation/disintegration of a passive hydride layer on the platinum surface. Probably, the reason of oscillations in the alkaline medium is also the formation of a passive film of hydroxides generated at more negative potentials. The thorough clarification of this phenomenon is beyond the frame of the present study. However, it is significant enough for clarification of the possible reactions of hydrogen peroxide destruction in alkaline medium and could be the subject of another study.

The anode behavior of electrode processes indicates a clear dependence of the reaction speed (current density, respectively) only from the hydrogen peroxide concentration.

Fig.2 presents cyclic voltammetric curves obtained by the use of a platinum vertical electrode (platinum lamella) in the investigated solutions. Here, a significant difference is observed in the cathodic part of the curves compared to CV curves obtained on a horizontal platinum electrode (Fig.1a). In all three investigated electrolytes the cathodic reactions pass through a clearly marked maximum, unlike the flat observed at the horizontally positioned platinum lamella. The cause of such trend of the curve is that with a vertical electrode the natural convection, as a result of the Archimedian force, is not suppressed and the released bubbles „stir" the electrode surface, thus continuously providing a fresh reagent flow.

Analysis of the electrode reactions of hydrogen peroxide synthesized from CaO₂

It is a fact that cyclic voltammetric curves obtained on Pt and Au can be considered as a model for the electrode processes. For this reason these electrodes were chosen to determine the electrochemical activity of hydrogen peroxide (solution D) obtained by hydrolysis of $CaO_2 \times H_2O_2$ in the presence of KHCO₃.

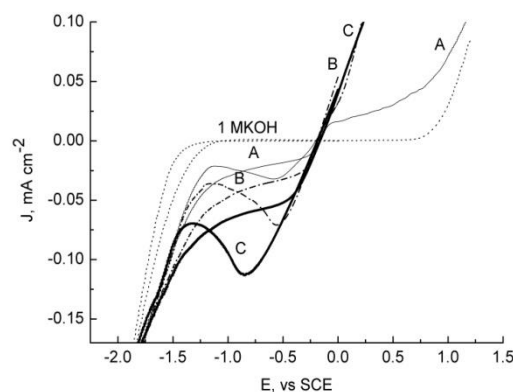**Fig.2.** Cyclic voltammograms onto vertical Pt electrode Solutions: A, B, C and D, T = 298K, scan rate 0.1V s^{-1}

Figure 2 presents a comparison between CV curves obtained on a platinum electrode in alkaline solution of stabilized H₂O₂ and the cyclic voltammetric curve obtained in synthesized medium of hydrogen peroxide electrolyte (solution D). It can be seen that the curve trend (respectively, the nature of electrode processes taking place) is identical to that obtained by investigation of stabilized H₂O₂ solutions. This fact is of great significance for the future development of the peroxide fuel cell, since it shows the feasibility of using *CaO₂* for producing hydrogen peroxide for fuel cells.

The cyclic voltammetric curves obtained in the investigated solutions (A, B, C and D) on a vertical gold electrode are presented in Figure 3. Gold demonstrates its catalytic activity in the manner defined by other authors as well [7, 14]. The cathodic reactions start almost immediately after initial scanning of the potential in negative direction (after 0V) and reach the maximum rate of reaction at −1.3V. Hydrogen evolution reaction starts after −2.0V.

The anodic reactions are also visibly catalyzed because they start as soon as a potential of 0 V is reached. The rates of both cathodic and anodic reactions in solutions depend on the concentration of hydrogen peroxide.
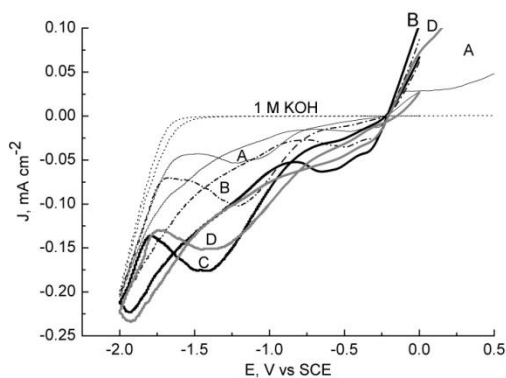
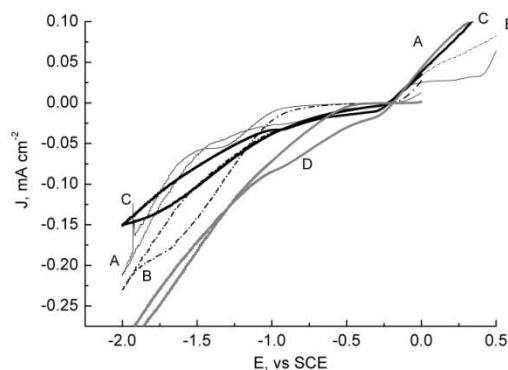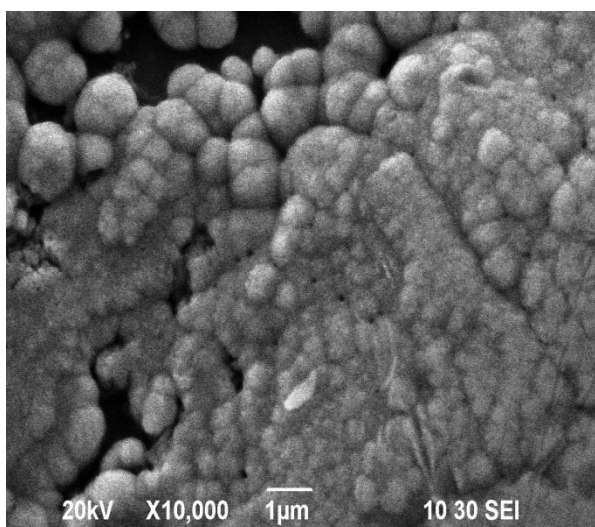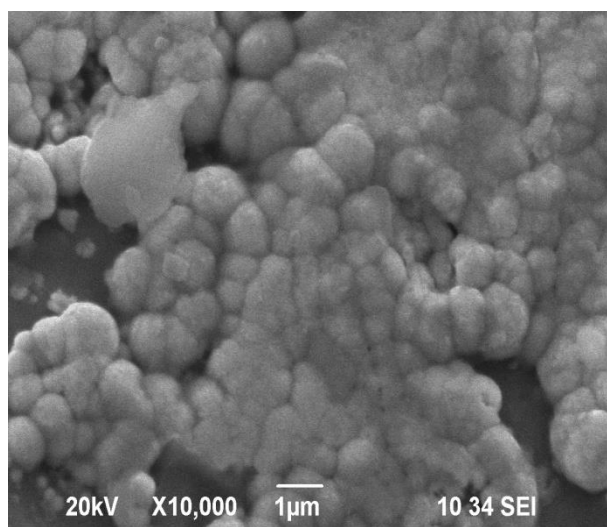**Fig.3.** Cyclic voltammograms onto vertical Au electrode. Solutions: A, B, C and D, T = 298K, scan rate 0.1V s^{-1}

Fig.4. Cyclic voltammograms obtained onto electrodeposited gold coating (thickness 2 μm) on substrate Ni foam.
Solutions: A, B, C and D, T = 298K, scan rate 0.1V s^{-1}

(a)

(b)

Fig.5. SEM images of electrodeposited coating Au onto Ni foam before (a) and after (b) electrochemical treatment in 0.42M H_2O_2 alkaline solution.

Fig.4 presents the CV curves obtained on an electrodeposited gold film. The results could be interpreted as similar to those obtained using a solid gold electrode.

The trend of a CV curve obtained in solution D (synthesized hydrogen peroxide) is analogous to the curve obtained at the same concentration in stabilized hydrogen peroxide (solution C). Therefore, the electrode reactions of synthesized hydrogen peroxide with scanning of the potential in cathode and anode direction are similar to those taking place in an alkaline solution of stabilized H$_2$O$_2$. This result once again corroborates the conclusions drawn here for the platinum electrode and shows the feasibility of using CaO$_2$ as a reagent in the production of H$_2$O$_2$ for HPFC.

Having in mind the high price of precious metals (platinum and gold), a further step was done in the present work – study of the catalytic activity of a gold electrodeposited film onto a lighter and less expensive material - nickel foam.

The morphology of the gold coating before and after electrochemical treatment in alkaline solution of hydrogen peroxide is presented in Figs. 5a and b. It is obvious that the gold coating deposited on nickel foam does not disintegrate. This fact, as well as the trend of the electrode processes allow to proceed to a further study – the use of nickel foam with electrodeposited films.

CONCLUSIONS

On the basis of the experiments made the following conclusions can be drawn:

The first cathodic reaction on a platinum electrode is a reduction of the peroxide ion (HO_2^-).

At more negative potentials current oscillations are observed. Based on the analogy to acidic medium, formation of a passive hydroxide film is supposed and only after that - recombination of the hydrogen atoms and evolution of hydrogen. The process of peroxide ion reduction does not occur under diffusion control.

It was found that on both solid gold and electrodeposited gold coating on nickel substrate, the reduction and oxidation reactions take place with high catalytic activity. The coat morphology does not change after electrochemical treatment in alkaline solution of hydrogen peroxide. The trends of the CVA curves (respectively, the chemistry of electrode processes) observed during working with an electrode with electrodeposited gold coating on nickel foam indicate the feasibility of using less expensive and scarce materials with electrodeposited films.

An important conclusion from this investigation is that the electrode processes taking place in hydrogen peroxide synthesized by hydrolysis of calcium peroxide in the presence of $KHCO_3$ are analogous to those in a stabilized alkaline solution of hydrogen peroxide. This result proves the thesis that synthesized hydrogen peroxide can be used directly as a reagent in hydrogen peroxide fuel cells.

REFERENCES

1. D.J. Brodrecht, D.N. Prater, J.J. Rusek, "Novel Fuel Cells Using Hydrogen Peroxide," - Swift Enterprises Ltd., West Lafayette, IN, Tech. Rep. 2001

2. G. H. Miley, N. Luo, J. Mather, R. Burton, Gl. Hawkins, L. Gu, E. Byrd, R. Gimlin, P. J. Shrestha, G. Benavides, J. Laystrom, D. Carroll, *J. Power Sources*, **165**, 509 (2007).

3. W. H. Philip, P. A. Kraft – NASA Technical Memorandum 103725, 1989

4. V. Stefanova, R. Miletiev, I. Simeonov, M. Georgiev, International Scientific Conference UNITECH'[11], Proceedings, Gabrovo, Bulgaria, 18-19 November, 2011, 438-443.

5. Hall E. Khudaish, A. Hart, *Electrochim. Acta*, **43**, 2015 (1998).

6. Xia Jing, Dianxue Cao, Yao Liu, Guiling Wang, Jinling Yin, Qing Wen, Yinyi Gao, *J. Electroanal. Chem.*, **658**, 46, (2011).

7. S. Yamazaki, Z. Siroma, H. Senoh, T. Ioroi, N. Fujiwara, K. Yasuda, *J. Power Sources*, **178** 20 (2008).

8. http://www.solvayinterox.com

9. E.R.Brown, R.F.Large, in A. Weissberger (Ed.) Cyclic Voltammetry, AC Polarograph and Related Technique in Electrochemistry, vol. I, (Part IIA), Wilye Interscience, New York, 1971

10. B.B. Damaskin, A. Petrij, Electrochimija, Moskva, Vysshaya shkola, (1986)

11. E.L. Littauer, K.C. Tsai, *Electrochim. Acta*, **24**, 681 (1979).

12. V.I. Gorohovskaya, V.M, Gorohovskij, Praktikum po ostsillographicheskoj poljarografii", Moskva, Vysshaya shkola (1973)

13. T.J. van Venrooij, M.T.M. Koper, *Electroch. Acta*, **40**, (1996) 1689-1696

14. G. Flätgen, S. Wasle, M. Lübke, Ch. Eickes, G. Radhakrishnan, K. Doblhofer, G. Ertl, *Electrochim. Acta*, **44,** 4499 (1999).

ИЗСЛЕДВАНЕ НА ЕЛЕКТРОДНИ РЕАКЦИИ НА ВОДОРОДЕН ПЕРОКСИД В АЛАКАЛНА СРЕДА ВЪРХУ Pt И Au ЕЛЕКТРОДИ ЧРЕЗ ЦИКЛИЧНА ВОЛТАМПЕРОМЕТРИЯ – ЧАСТ I

В. Стефанова[1], Ц. Доброволска[2], Р.Милетиев[3], М. Георгиев[1], И. Симеонов[3]

[1]*Химичнотехнологичен и металургичен университет, бул. Кл.Охридски 8, 1756 София, България*
[2] *Институт по физикохимия на БАН, ул. Акад. Г. Бончев, бл.11, 1113 София, България*
[3] *Технически университет, бул. Кл.Охридски 9, 1756 София, България*

(Резюме)

В настоящата статия, с помощта на циклична волтаперометрия (ЦВ), е изследвано влиянието на конвекция на електролита върху електродни реакции протичащи върху Pt и Au електрод в алкален разтвор на H_2O_2. Анализирано е също електрохимичното поведение на H_2O_2, получен чрез хидролиза на калциев пероксид CaO_2 в присъствие на калиев хидроген-карбонат ($KHCO_3$) с цел използването му като реагент (гориво и окислител) за водородни пероксидни горивни клетки (ВПГК).

Установено е, че първата катодна реакция протичаща върху Pt електрод е редукция на перхидроксилов йон (HO_2^-). Тя е последвана от образуване на хидрооксиден пасивен слой и последваща рекомбинация на водородните атоми до образуването на водород. Електродните процеси протичат в условията на стационарна дифузия и скоростта на реакцията се определя единствено от концентрацията на реагента.

Върху масивно злато, а също така върху златно покритие, електроотложено върху никелова пяна, реакциите на редукция, а също така и на окисление протичат с висока каталитична активност. Морфологията на златното покритие върху никелова пяна не се разрушава след електрохимичното третиране в алкален разтвор на H_2O_2. Ходът на ЦВ криви (съответно, на електродните реакции) на синтезиран и стабилизиран алкален разтвор на H_2O_2е аналогичен. Този резултат води до извода, че водороден пероксид получен чрез хидролиза на CaO_2 може да бъде използван като реагент (гориво или окислител) за ВПГК.

Investigation of electrode reactions in hydrogen peroxide alkaline medium onto Co, In and Ni by cyclic voltammetry – Part II

V. Stefanova[1], Ts. Dobrovolska[2], R. Miletiev[3], M. Georgiev[1], I. Simeonov[3]

[1]*University of Chemical Technology and Metallurgy 8 Kl. Ohridski , 1756 Sofia, Bulgaria*
[2]*) Institute of Physical chemistry Bulgarian Academy of Sciences G. Bonchev str. bld 11, 1113, Sofia, Bulgaria*
[3]*) Technical University 9 Kl. Ohridski, 1756 Sofia, Bulgaria*

The electrocatalytic activity of cobalt and indium (solid and electrodeposited), nickel and nickel foam towards the electrode reactions taking place in stabilized as well as synthesized (produced by calcium peroxide hydrolysis) hydrogen peroxide solutions was investigated. It was found that the cyclic voltammetry (CV) experiments carried out on electrodes of solid cobalt, indium and nickel indicated activity with respect to the anode reaction in alkaline hydrogen peroxide solution. The most probable reason for the observed behaviour is a formation of passive hydroxy-oxide layers on the surface of these metals. It was demonstrated that the nickel foam is a material suitable not only for anodes, but can also be used as substrate of various electrodeposited layers.

The cyclic voltammetry investigations, carried out on electrodeposited layers of Co and In indicate similar electrode activity compared to the results obtained with solid electrodes with respect to the anode reaction in alkaline hydrogen peroxide solution.

An important conclusion from performed experiments is that the data obtained by investigation of hydrogen peroxide medium synthesized through decomposition of CaO_2 are analogous to those obtained in stabilized hydrogen peroxide solution which renders this reagent suitable for use in fuel cells.

Keywords: Cyclic voltammetry, hydrogen peroxide, calcium peroxide, Co, In, Ni, electrode

INTRODUCTION

Increasing of the efficiency of fuel cell operation in an economic as well as in technological aspect is the main objective targeted by numerous research teams working in this area. Simplification of the fuel cell design, selection of the proper material for electrodes (which are at the same time catalysts of the respective cathodic and anodic reactions), and of electrolyte – these are the main parameters that directly influence the fuel cell efficiency [1, 2]. The team of Yamazaki et al. [3] established the feasibility of operation of a fuel cell without separation of the cathodic and anodic compartments, where an alkaline hydrogen peroxide medium can serve as a fuel as well as an electron acceptor during its operation. However, a suitable catalytic material shall be selected both for the cathodic, as well as the anodic reactions. A number of authors define some precious metals such as platinum, gold and silver as catalysts appropriate for the cathodic reaction, while nickel is found to be suitable for an anode [4]. A new material – nickel foam (polymer material with nickel coating), according to a number of authors, is also found to be a suitable material for operation of the anodes [4].

In our previous study, the electrode processes taking place on Pt and Au electrodes in alkaline hydrogen peroxide medium were examined [5]. The strong catalytic activity of the two metals for the cathodic and anodic reactions of H_2O_2 in 1M solution KOH was verified and it was found that hydrogen peroxide obtained through CaO_2 hydrolysis in the presence of $KHCO_3$ (non-stabilized) has the same electrochemical behavior as the stabilized H_2O_2.

The purpose of this investigation is to select materials suitable for catalysts of the electrode reactions taking place in stabilized, as well as in synthesized (obtained by hydrolysis of calcium peroxide) hydrogen peroxide among cobalt, indium (solid and electrodeposited), nickel and nickel foam.

EXPERIMENTAL

The following solutions were prepared for the experiments: basic electrolyte with concentration 1 M KOH, solution **A** – 0.1÷0.15 M H_2O_2 in 1M KOH; solution **B** – 0.2÷0.25 M H_2O_2 in 1M KOH;

---

* To whom all correspondence should be sent:
E-mail: vps@uctm.edu

solution **C** – 0.4÷0.45 M H_2O_2 in 1M KOH. The solutions **A, B** and C were prepared from 30 % solution of H_2O_2 and potassium hydroxide with *pro analysis* purity and distilled water. Solution D was prepared before each experiment by hydrolysis of CaO_2 in the following conditions: temperature 298 K, 50% excess $KHCO_3$, solid:liquid ratio = 1:10, contact time 5 min. The variations in H_2O_2 molar concentration in the investigated solutions were due to the low stability of the peroxide. Its concentration in the solution was determined before and after each experiment by a methodology proposed by the firm Solvay [6].

The composition of the electrolytes for deposition of cobalt and indium coatings was as follows: for deposition of cobalt - 0.3 M Co as $CoSO_4$ $7H_2O$ and 0.2 M diammonium hydrogen citrate ($C_6H_{14}N_2O_7$); for deposition of indium – 0.1M In as $InCl_3$ and 0.2 M $C_6H_{14}N_2O_7$. The deposition was carried out at current densities 3 A dm^{-2} for Co and 1 A dm^{-2} for In, with the same electric charge −1.2 Ah dm^{-3}. Chemical substances with purity *pro analysis* and bidistilled water were used for preparation of the electrolytes.

The electrode processes were investigated by the cyclic voltammetry. The experiments were carried out in a Gamry cell with capacity 200 cm^3 at room temperature without stirring of the electrolyte. The working electrode area was 1 to 2 cm^2. In the case of nickel foam that area was only geometrical, not actual, due to the highly developed surface. Nickel Foam (supplier Good Fellow) has a specificiations as follows: thickness 1.6mm, bulk density 0.45g.cm^{-3}, 20 pores/cm^2. The counter electrode (~2 см²) was made of platinum. A calomel reference electrode (Hg/Hg_2Cl_2) was used. Its potential, compared to a normal hydrogen electrode, was E_{SCE}=0.244V. The experiments were carried out with a computer-controlled GAMRY potentiostat-galvanostat Model G 300ZRA. The GAMRY FRAMEWORK PHE 200 program was used.

The scan rate was 0,1 V s^{-1}. In most cases scanning started from the potential of the reference calomel electrode and was continued until a sufficiently negative potential was reached, at which the reaction of hydrogen release is assumed to start. After that the scanning direction was reversed and scanning was carried out up to the selected potential in the anode zone.

The surface morphology of the coatings was studied by means of JEOL 6390 scanning electron microscope (SEM).

RESULTS AND DISCUSSION

The initial experiments were carried out with working electrodes made of solid metals – cobalt, indium and nickel. It was found that the electrode processes in all four solutions (A, B, C and D) run in the same manner, and that is why, in order to facilitate the presentation, only the curves obtained at the highest concentration of hydrogen peroxide (solution C) were presented in graphic form (Fig.1–3).
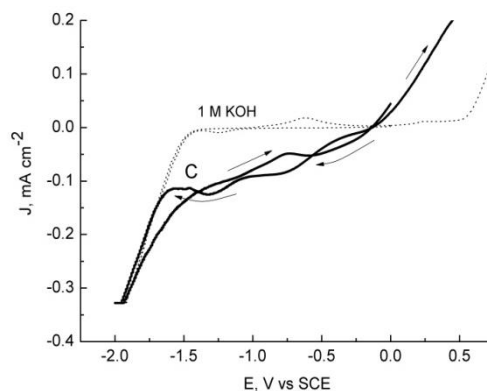

Fig. 1. Cyclic voltammograms of cobalt in 1 M KOH; solution C - 0.42 M H_2O_2 in 1 M KOH.

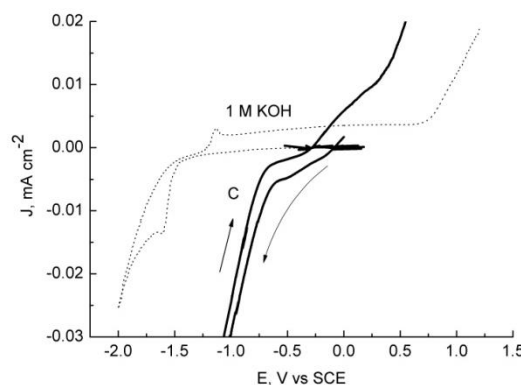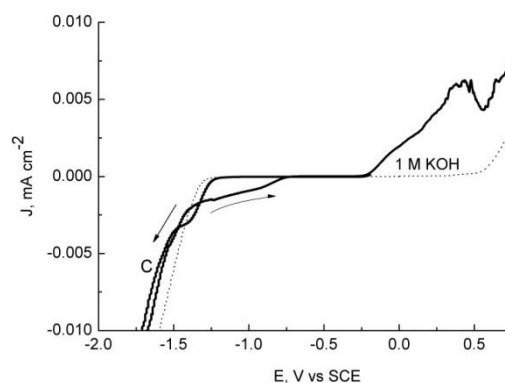**Fig. 2.** Cyclic voltammograms of indium in 1 M KOH; solution C - 0.42 M H_2O_2 in 1 M KOH.

**Fig. 3.** Cyclic voltammograms of nickel in 1 M KOH; solution C - 0.42 M H_2O_2 in 1 M KOH

Cyclic voltammograms obtained on a Co working electrode – in basic solution (1 M KOH) and in solution C are presented in Fig.1. Activity of

hydrogen peroxide can be observed in the cathodic zone, presented in two cathodic waves, at –0.8 V and after –1.2 V. Due to the high peroxide concentration, the first wave is most probably due to the reduction reaction of HO_2^- as follows:

$$HO_2^- + 2e^- + H_2O = 3OH^- \qquad (1)$$
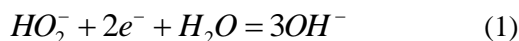
Upon transition to more negative potentials, a horizontal sector can be observed, most probably due to the growth of a passive oxy-hydroxide layer on the cobalt working electrode. According to [7], passivation of the cobalt surface is the result of alkalization of the cathode-contiguous layer and its covering with cobalt hydroxides. At the potentials of the "second wave" in the cathodic part of the cyclic curve some alkalization of the double layer takes place. This alkalization leads to the formation of hydroxide-oxyde layer.

The reaction of reduction of water and hydrogen evolution starts after potentials of –1.5 V, where it happens in aqueous solution 1 M KOH. The anode reaction taking place on the cobalt is marked. In the alkaline medium of hydrogen peroxide it is described by the equation [8]:

$$HO_2^- + OH^- \rightarrow O_2 + H_2O + 2e^- \qquad (2)$$
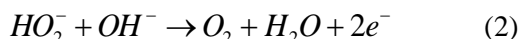
It starts immediately at the first positive potentials, beyond 0 V and evidences the fact that cobalt can be used as anode in the oxidation reaction of hydrogen peroxide. Here its activity coincides with that observed in gold and platinum [5].

A base cyclic voltammograms obtained onto indium in 1 M solution KOH (without hydrogen peroxide) is characterized by a cathode peak at potentials –1.5 V, which is related to the formation of a passive film of indium oxides and hydroxides (Fig.2). The formation of such passive film is confirmed by the investigations carried out in alkaline indium solution [7] and the high value of the stability constant of In(OH)$_3$ – 10^{-30} [9]. According to [10] formation of indium hydroxide starts at pH = 3.3 of the medium. In the working solution 1 M KOH the solution pH is more than 12, therefore the formation of a passive film is beyond doubt. In the reverse direction of the curve an anode peak is observed at potentials –1.1 V and corresponds to the dissolution of this passive film. Oxygen generation starts at potentials above 0.8 V.

In a hydrogen peroxide medium (curve C) - the beginning of the reduction reaction occurs at –0.4 V. At present it cannot be maintained whether this is a reduction reaction of the HO_2^- ion, or release

of hydrogen on a passivated indium layer. The anode reaction on indium working electrode shows activity similar to that of a cobalt electrode (compared to Figure 1).

Fig.3 presents cyclic voltammograms obtained in 1 M solution KOH and in alkaline solution of hydrogen peroxide on a solid nickel electrode. A minor peak observed in H$_2$O$_2$ solution in the range about -1.5 V evidences the possibility of formation of nickel oxide before the hydrogen release reaction. The anodic reaction runs at a high rate, which corresponds to the information presented in the literature [4].

On the basis of the results presented here above it can be concluded that cobalt, indium and nickel can be used successfully as anodes in alkaline hydrogen peroxide solutions. Most probably reason of such catalytic behavior of the oxidation reaction is that it takes place on the passive films formed on the three metals. The catalytic activity of the cathodic processes on cobalt and indium could be assumed, however, the type of the catalyzed reaction should investigated in more details, because the quantitative analysis of shown CVs shows that the magnitude of recorded currents with Co, In and Ni - electrodes are different.

Considering that the steps to higher efficiency of fuel cells operation include lighter structure and, to be sure, reduction of the electrode material prices, further research was carried out using nickel foam and cobalt and indium layers electrodeposited on it. Fig. 4 presents the cyclic voltammograms obtained in aqueous solution 1 M KOH and in alkaline hydrogen peroxide solution (solution C) onto nickel foam.
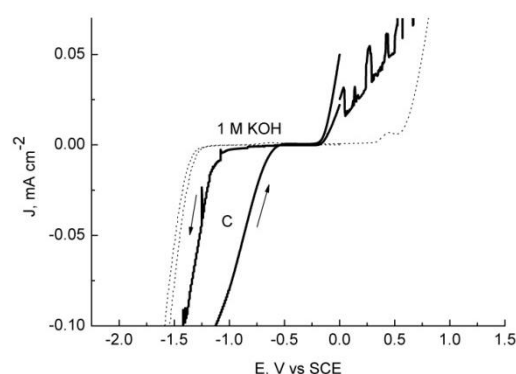

Fig. 4. Cyclic voltammograms of nickel foam in 1 M KOH and solution C - 0.42 M H$_2$O$_2$ in 1 M KOH

It can be said that the results are not different from those obtained with a solid nickel electrode – nickel foam demonstrates a high rate of the anodic reaction. The morphology of the nickel foam before and after the experiments is shown in Figure 5a and 5b.
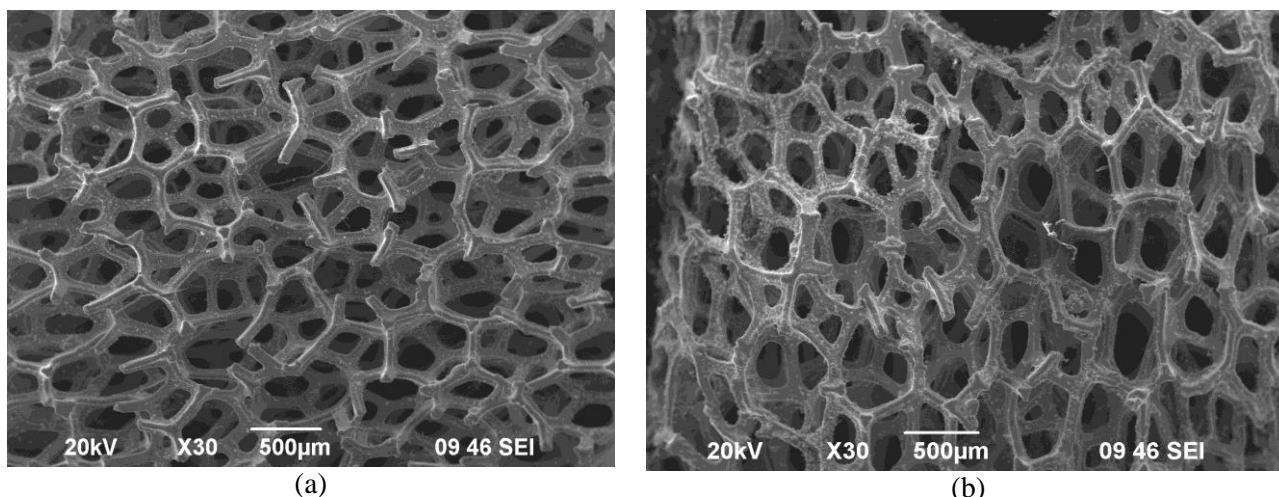
(a)

(b)

Fig. 5. SEM images of Ni foam before (a) and after (b) electrochemical treatment in 0.42 M H₂O₂ alkaline medium

Fig. 6. Cyclic voltammograms obtained onto electrodeposed Co coating (thickness 3 μm) on substrate Ni foam Solutions: A, B, C and D, T = 298K, scan rate 0.1V s⁻¹

It can be seen that in a chemically active medium, with the potential applied over quite a wide range – from -2.0 to +1.0 V does not have a destructive effect on this material.

Cyclic voltammograms obtained in hydrogen peroxide solutions of different concentrations on electrodeposited cobalt layer with thickness 3 μm on a nickel foam substrate are presented in Fig.6. The trend reported in experiments on a solid cobalt electrode is observed here as well - the cathodic reaction starts after –0.4 V, reaching the maximum reduction rate at –1.2 V and high rate of the anode reaction at positive potentials immediately after 0 V. No concentration dependency during the electrode reactions can be reported. The electrode reactions in solutions of stabilized hydrogen peroxide (curves A, B, C) and of non-stabilized H₂O₂ obtained by

(a)

(b)

Fig. 7. SEM images of electrodeposited cobalt coating on Ni foam before (a) and after (b) electrochemical treatment in 0.42 M H₂O₂ alkaline solution.
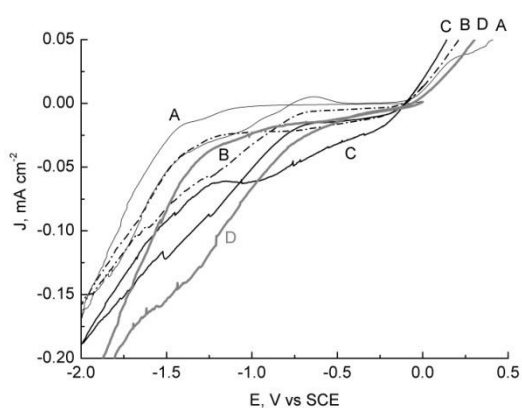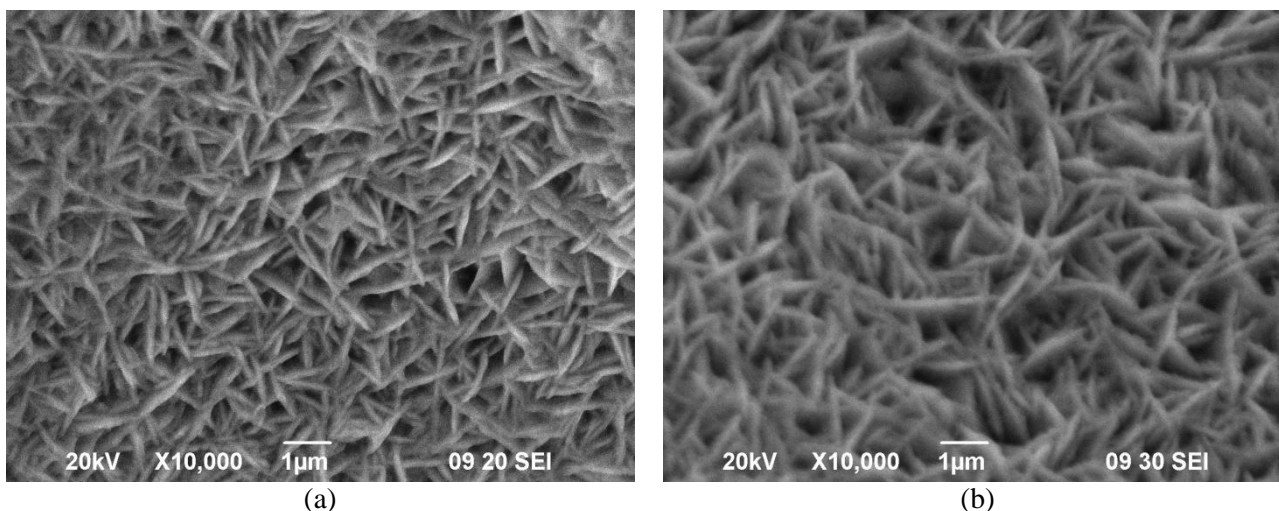
154

Fig. 8. Cyclic voltammograms obtained onto electrodeposed In coating (thickness 1 µm) on substrate Ni foam.
Solutions: A,, B, C and D, T = 298K, scan rate 0.1V s⁻¹

Analogous to that of cobalt, an investigation is carried out with solutions A, B, with and D. The obtained CV curves are presented in Figure 8. The analogy with the behavior of solid indium (compared to Figure 2) is obvious. Solution D (synthesized hydrogen peroxide) has a behavior similar to that of stabilized hydrogen peroxide. The morphologies of the indium coating before and after electrochemical investigations, presented in Figures 9a and b, prove the stability of the indium film. The pitting observed in the two photos can be accounted with the low thickness of the indium coating.

Even as a thin indium coating it can be stated that indium as a material is suitable for catalytic carrier of the anode reaction of hydrogen peroxide in alkaline solution.

(a)

(b)

Fig. 9. SEM images of electrodeposited In coating on Ni foam before (a) and after (b) electrochemical treatment in 0.42 M H₂O₂ alkaline solution.
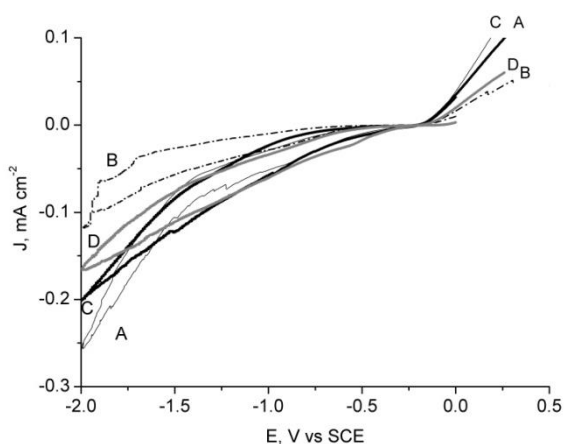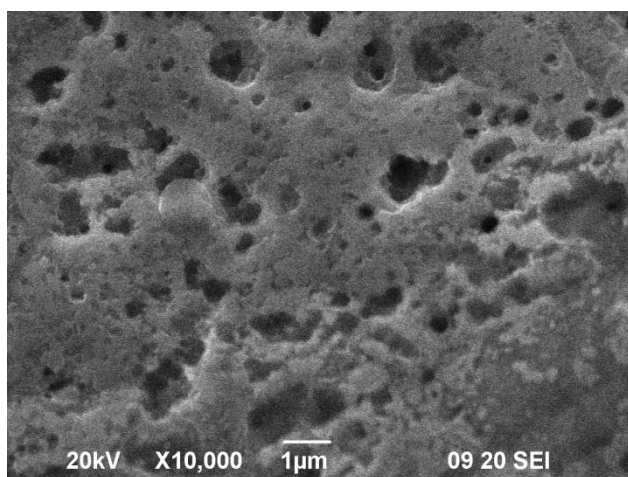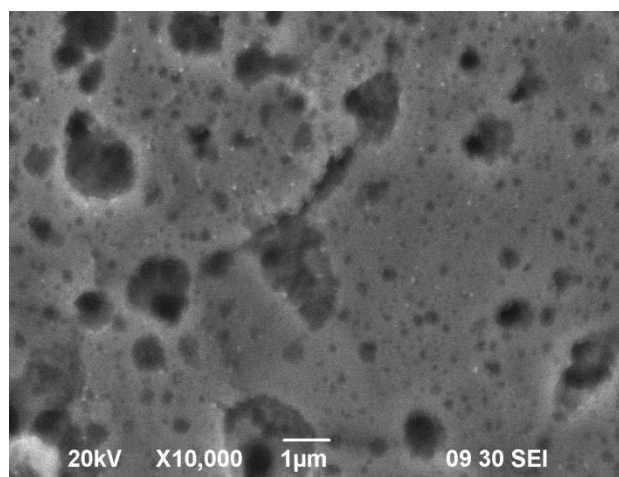
hydrolysis of calcium peroxide (curve D), have the similar behavior. Such conclusion was drawn also from another investigation carried out on working electrodes of gold and platinum [5].

The morphology of the cobalt coating before and after electrochemical treatment (investigated by cyclic voltammetry) is presented in Figure 7a and b. The typical crystallites of electrodeposited cobalt are unchanged after the investigations carried out, which confirm stability of the obtained coatings and further investigations of the nature of the electrode reactions on cobalt. Electrodeposition of indium is carried out with the same electric charge as cobalt. However, a layer of indium deposited on nickel foam is much thinner, ~1 µm. That is due to the fact that the electrolyte used for deposition of indium coatings has low cathodic current utilizability.

CONCLUSIONS

On the basis of the investigations carried out the following conclusions can be drawn:

The cyclic voltammetric investigations carried out on electrodes of solid cobalt, indium and nickel indicate activity with respect to the anode reaction in alkaline hydrogen peroxide medium. The most probable cause of such catalytic activity is the formation of passive hydroxy-oxide layers of the surface of these metals.

Nickel foam is a material suitable not only as anode in the anode reaction, but also as substrate for deposition of various electrodeposited layers.

The trends of CV curves obtained on cobalt and indium electrodeposited coating on nickel foam are similar to those obtained on solid Co and In electrodes. That indicates analogous activity with respect to the anode reaction in alkaline hydrogen

155

peroxide medium and therefore - the feasibility of making the fuel cell lighter through replacement of the solid electrodes by a lighter material – nickel foam with electrodeposited films of cobalt or indium.

An important conclusion from the present investigation is that the electrode processes taking place in hydrogen peroxide synthesized by hydrolysis of calcium peroxide in the presence of KHCO$_3$ are similar to those in a stabilized, alkaline hydrogen peroxide medium. This result corroborates the thesis that synthesized hydrogen peroxide can be used directly as reagent in hydrogen peroxide fuel cells.

REFERENCES

1. M.M. Mench, Fuel Cell Engines, John Wiley & Sons, Inc., 2008
2. S.M. Haile, *Acta Materialia*, **51**, 5981 (2003).
3. S. Yamazaki, Z. Siroma, H. Senoh, T. Ioroi, N. Fujiwara, K. Yasuda, *J. Power Sources*, **178**, 20 (2008).
4. F. Bidault, D.J.L. Brett, P.H. Middleton, N. Abson, N.P. Brandon, *Int. J. Hydrogen Energy*, **34**, 6799 (2009).
5. V. Stefanova, Tz. Dobrovolska, R. Miletiev, M. Georgiev, I. Simeonov, Bulg. Chem. Commun., **44**, 144 (2013).
6. http://www.solvayinterox.com
7. S. Nineva, Ts. Dobrovolska, I. Krastev, *J. Appl. Electrochem.*, **41**, 1397 (2011).
8. D. Cao, L. Sun, G. Wang, Y. Lv, M.Zhang, *J. Electrochem. Chem.* **621**, 31 (2008).
9. Справочник химика, т.3, Москва, Химия, 1965
10. I. Krastev, Ts. Dobrovolska, U. Lacnevac, S. Nineva, *J. Solid State Electrochem.*, 2012, DOI:10.1007/s10008-012-1766-8

ИЗСЛЕДВАНЕ НА ЕЛЕКТРОДНИ РЕАКЦИИ ВЪРХУ Co, In И Ni В АЛКАЛЕН РАЗТВОР НА ВОДОРОДЕН ПЕРОКСИД ЧРЕЗ ЦИКЛИЧНА ВОЛТАМПЕРОМЕТРИЯ – ЧАСТ II

В. Стефанова[1], Ц. Доброволска[2], Р.Милетиев[3], М. Георгиев[1], И. Симеонов[3]

[1]*Химичнотехнологичен и металургичен университет, бул. Кл.Охридски 8, 1756 София, България*
[2] *Институт по физикохимия на БАН, ул. Акад. Г. Бончев, бл.11, 1113 София, България*
[3] *Технически университет, бул. Кл.Охридски 9, 1756 София, България*

Постъпила на 3 юли, 2012 г.; коригирана на 6 ноември, 2012 г.

(Резюме)

Изследвана е електоро-каталитичната активност на кобалт и индий (масивен и електроотложен), никел и никелова пяна спрямо електродните реакции, протичащи в стабилизирани а също така и в синтезирани (получени чрез хидролиза на калциев пероксид) разтвори на водороден пероксид. Установено е, че циклични волтамперометрични експерименти проведени върху масивен кобалт, индий и никел показват активност по отношение на анодна реакция в алкален разтвор на водороден пероксид. Най-вероятна причина за наблюдаваното поведение е образуване на пасивни хидрокси-оксидни слоеве върху повърхността на тези метали. Доказано е, че никеловата пяна е материал, подходящ не само за анодите, но също може да бъде използван за подложка на различни електроотложени слоеве.

Циклични волтамперометрични изследвания, проведени върху електроотложени слоеве на Co и In, показват подобна електродна активност в сравнение с резултатите получени с масивни електроди по отношение на анодна реакция в алкален разтвор на водороден пероксид.

Важен извод от проведените експерименти е че резултатите, получени при изследване на водороден пероксид в синтезиран чрез разлагане на CaO$_2$ са аналогични на тези, получени в стабилизиран разтвор на водороден пероксид, което прави този реагент подходящ за използване в горивни клетки.

Investigation of the liquid tar product from the pyrolysis of yak-milk casein and its application in curing of epoxy resin

B. Purevsuren[1], Y. Davaajav[1], V.R. Genadiev[2], Il.V. Kotzev[2], I.K. Glavchev[2*]

[1]*Institute of Chemistry and Chemical Technology, Mongolian Academy of Sciences, Ulanbaatar-51, Mongolia*
[2]*University of Chemical Technology and Metallurgy, 1765 Sofia, 8, Kl. Ohridski Str., Bulgaria*

The liquid tar product, obtained by pyrolysis of yak-milk casein was investigated and was applied for curing of epoxy resin. Physico-chemical and thermal characteristics, IR and ^{1}H NMR spectra were recorded and compared with the data obtained with the most often used hardener diethylenetriamine. The absorbancies of the liquid tar product were determined by quantitative IR analysis. The curing of epoxy resin was performed at room temperature for 24 h and at 105ºC for 150 min. The optimal quantity of the liquid tar product for providing maximal degree of cure at 105ºC is 22.22%; at room temperature it is a 20% mixture with diethylenetriamine 50:50 g/g. From the physico-mechanical characteristics of the cured bars and coatings it was concluded that the investigated product is a good hardener of epoxy resins.

Key words: liquid tar product, pyrolysis, casein, epoxy resin, hardener

INTRODUCTION

At the Institute of Chemistry and Chemical Technology of the Mongolian Academy of Sciences different kinds of Mongolian raw material were studied. The results of the characterization of the products obtained by pyrolysis of animal bones were published in [1, 2]. The data from the thermal analysis of yak-milk casein were given in [3]. Its pyrolysis was described in [4]. The obtaining and characterization of biochar from pyrolysed yak-milk casein was published in [5]. The characterization of liquid tar product (LTP) from pyrolysed yak-milk casein was made in [6]. In this article the yields of biochar (28.3%) and LTP (37.5%) are given. The amounts of gas and water were 20.9% and 13.3%, respectively. The elemental composition of the LTP was: C 66.7%, H 8.3%, N 12.1% and O 12.9% (by difference). The sample was characterized by mass spectrometry, gas chromatography (GC)/MS and heated-probe MS, to give molecular weight distributions for comparison with molecular weight ranges indicated by analytical-scale size-exclusion chromatography (SEC). It appeared to consist mostly of moderate molecular weight fractions with elution times of 18–26 min. The components of these fractions were probably 3-dimensional. GC/MS analysis showed the presence of both aliphatic and aromatic nitrogen-containing components. Neither GC/MS nor heated-probe MS were able to detect more than about half of the tar components. The aim of our studies was to continue with the characterization of LTP and its application as a hardener of epoxy resins.

EXPERIMENTAL

The investigations were made with technical grade low-molecular bisphenol A based epoxy resin DER 331 of Dow Chemicals (USA) and laboratory made LTP by pyrolysis of yak-milk casein, prepared in the Mongolian Academy of Sciences. The curing agent used for comparison was technical grade diethylenetriamine (DETA), product of Alpha Chemical (India). Spectroscopy-grade carbon tetrachloride of Merck (Germany) was applied for preparation of LTP solutions for IR analysis. The amine numbers of LTP and DETA were determined with hydrochloric acid for analysis (Merck) by the method described in [7]. The ^{1}H NMR spectra of a solution of LTP in toluene – D8 (Merck) were recorded on a JEOL instrument (Japan). IR spectra were obtained from thin layers of LTP and from its 1% and 20% solutions in carbon tetrachloride on a Perkin Elmer apparatus (USA). The thermal analyses were made on an OD 102 MOM apparatus (Hungary). The curing of the mixtures of epoxy resin and hardeners (DETA or LTP) was made in polyethylene containers. The degree of curing was determined after grinding the cured samples, measuring their

---

* To whom all correspondence should be sent:
E-mail: ivgl@uctm.edu

weights at an accuracy of 0.0001 g before and after Neftochim (Bulgaria) for 4 h on a Soxhlet apparatus, subsequent 10 min extracting with acetone and heating at 105ºC to constant weight. The 4 h extraction was made with toluene because of the limited solubility of LTP in acetone; 10 min extraction with acetone was further performed to facilitate the drying of the samples. Physico-mechanical characteristics: density, Brinell hardness, impact resistance, adhesion on steel, wood and polystyrene (PS) surfaces, elasticity and pendulum hardness of the cured samples (bars or coatings) were determined by standard methods [9–14].

RESULTS AND DISCUSSION

It was shown in our previous investigation that yak-milk casein is a good hardener of epoxy resins [8]. However, it was difficult to prepare a mixture because of its poor solubility. The product from the pyrolysis of yak-milk casein is a liquid and its solubility in epoxy resins is very good. On the other hand, LTP has nitrogen containing groups capable to react with epoxy groups. It is well known that polyamines are applied as hardeners of epoxy resins at room temperature because of their high boiling pressure. It is of interest to compare the physico-chemical and thermal data of LTP with those of the most used polyamine DETA. The results are given in Tables 1 and 2.

Table 1. Characteristics of LTP and DETA.

Compound	pH	n_d^{20}	Amine number %	Specific density, g/cm^3
LTP	10.2	1.6735	4.47	1.02
DETA	8.7	1.4742	24.07	0.95

It is evident, that the amine number of LTP is 5.4 times lower than that of DETA. Therefore, larger quantities of LTP will be necessary for curing of epoxy resins. For comparison, the data of DETA, Merck, for synthesis, are: pH 12, refractive index 1.4826, specific density 0.949 – 0.952 g /cm³. The differences with the data of technical grade DETA can be explained with the content of impurities in it. The values of the thermal index of technical grade DETA confirm this assumption,

extracting with technical grade toluene, product of because the boiling point of DETA for synthesis is 206-209ºC. Probably, the high thermal stability of LTP is due not only to its molecular weight and the shape of its molecules, given in [6], but to the new products obtained at the higher temperatures. The values obtained by TG analysis show that LTP can be applied for curing of epoxy resins at high temperatures. The content of groups in LTP, available to cure epoxy resin is evident from their ^{1}H NMR and IR spectra. In the ^{1}H NMR spectra of the solution of LTP in toluene-D8 the following signals are registered: multiplate δ = 6.86 ppM for protons in aromatic rings and nitrogen containing groups; dublet δ = 0.9 ppM, singlet δ = 1.15 ppM and dublet δ = 2.15 ppM for protons in =CH- and =CH$_2$ groups. In the IR spectra there are peaks for groups described in [6]: -OH, aromatic rings, aliphatic groups. At 3220, 3200 and 1140 cm^{-1} there are peaks for –NH- , at 2980, 1460 and 815 cm^{-1} - for – CH$_2$ -. The absorbancies for –NH- and –CH$_2$– (internal standard) were determined and from their ratio the values of A* = $A_{NH}/A_{int.st}$ were calculated. On the base of the values of amine numbers of LTP in carbon tetrachloride solution (axis x) and the values of A* from their IR spectra (axis y), the most appropriate absorbancies for quantitative IR analysis were determined. The equations of the relationships A*/amine numbers were found for every absorbance and the coefficients *a* and *b* were determined. From the dispersion of the data the coefficients of correlation R were calculated. From these results the most appropriate absorbancies for quantitative IR analysis of LTP were determined: 3220 cm^{-1} for – NH- group and internal standard at 2980 cm^{-1} (minimal values of the coefficients: R = 0.01 and b = 0.75).

The determination of the optimal quantity of LTP for curing of epoxy resin was made using several experiments (series 1). The degree of cure was determined from the ratios of the weights of the samples cured at 105ºC 150 min (w$_1$) and the weights of the not cured part after extraction with toluene and acetone (w$_2$).

Table 2. TG data for LTP and DETA

Compound	E_{act} KJ/mol	n	I_{100}	I_{150}	I_{200}	I_{250}	I_{300}	I_{350}	I_{400}	I_{450}	I_{500}
LTP	9.51	0.53	6.44	12.63	18.82	31.9	43.56	48.64	52.01	72.58	89.97

Table 3. Determination of optimal quantity of LTP for curing epoxy resin DER 331

LTP, %	11.11	13.89	16.67	19.44	22.22	25	27.78	30.55
Degree of cure, %	93.35	95.85	97. 71	97.90	99.93	92.00	93.38	92.50

Table 4. Physico-mechanical characteristics of cured bars and 60 μm thick coatings

Series	Degree of cure, %	Density, g/cm^3	Brinell hardness, N/mm^2	Impact resistance, mm	Adhesion, knife test			Elasticity, mm	Pendulum hardness
					Steel	Wood	PS		
1	99.92	1.1481	34.43	230	2	2	2	20	0.88
2	92.92	1.0810	20.78	380	2	1	3	20	0.40
3	95.10	1.2112	29.06	150	2	1	2	20	0.73

It is evident that the influence of the quantity of LTP is not essential. The optimal quantity of LTP is 22.2% - two times larger than the optimal quantity of DETA for curing of this epoxy resin. If only nitrogen containing groups participate in the curing reaction, the optimal quantity should be about 50%. Probably other groups from LTP, eventually -OH participate in the curing reaction as well. It is known that this group is active at temperatures above 140ºC. Probably the –NH- groups lower both the temperature and the time of the curing reaction. The second series was made at 20ºC and 24 h curing with a LTP-DETA ratio from 80:20 g/g to 20:80 g/g to verify this hypothesis and to cure epoxy resin at room temperature. The obtained results confirmed that increasing of the quantity of DETA increases the degree of cure of the samples. With the optimal quantity of hardener 20% mixture of LTP: DETA = 50:50 g/g 93% degree of cure was achieved.

The physico-mechanical characteristics of the cured bars and coatings obtained with the optimal quantities of hardeners: 22.22% LTP, heating at 105ºC 150 min (series 1); 20% mixture of LTP:DETA = 50:50 g/g, at 20ºC 24 h (series 2) and 11% DETA at 20ºC 24 h (series 3) were determined (Table 4).

It is evident that the characteristics of the cured bars and coatings obtained with LTP are equal to or higher than those of samples, obtained with DETA. It may be, hence, concluded that LTP is a good hardener of epoxy resin.

REFERENCES

1 B. Purevsuren, B. Avid, T. Gerelmaa, Ya. Davaajav, T. J. Morgan, A. A. Herod, R. Kandiyoti, *Fue*l, **83**, 799, (2004).
2 B. Purevsuren, B. Avid, J. Narangerel, T. Gerelmaa, Ya. Davaajav, *J. Mat. Sci.*, **39**, 737, (2004).
3 B. Purevsuren, Ya. Davaajav, *J. Thermal Analysis and Calorimetry*, **65,** 147, (2001).
4 B. Purevsuren, Ya. Davaajav, *J. Thermal Analysis and Calorimetry*, **66,** 743, (2001)
5 B. Purevsuren, B. Avid, B. Tesche, Ya. Davaajav, *J. Material Science*, **38**, 2347, (2003).
6 B. Purevsuren, B. Avid, Ya. Davaajav, A. A. Herod, R. Kandiyoti, T. J. Morgan, *Eur. J. Mass Spectrom.,* **10**, 101, (2004).
7 BSS 758-79.
8 Mong. Pat. N 676, 07.04.92.
9 BSS 13694-76.
10 ISO 2039-1:2001.
11 EN ISO 6272.
12 EN ISO 2409
13 EN ISO 1519.
14 EN ISO 1522

ИЗСЛЕДВАНЕ НА ТЕЧНИЯТ КАТРАНЕН ПРОДУКТ ОТ ПИРОЛИЗ НА КАЗЕИН ОТ МЛЯКО НА ЯК И НЕГОВОТО ПРИЛОЖЕНИЕ ПРИ ВТВЪРДЯВАНЕ НА ЕПОКСИДНА СМОЛА

Б.Пуревсурен[1], И. Даваажав[1], В.Р.Генадиев[2], Ил.В.Коцев[2], И.К.Главчев[2]

[1] *Институт по химия и химична технология, Монголска академия на науките, Уланбатор – 51, Монголия.*
[2] *Университет по химична технология и металургия, 1765 София, Кл.Охридски № 8, България*

(Резюме)

Течният катранен продукт, получен при пиролиз на казеин от мляко на як беше изследван и бе използван при втвърдяване на епоксидна смола. Физико-химичните и топлинни характеристики, ИЧ и ¹Н ЯМР спектри бяха получени и сравнени със данните, получени от най-често използваният втвърдител диетилентриамин. Абсорбциите на течният катранен продукт бяха определени със количествен ИЧ-анализ. Втвърдяването на епоксидна смола беше правено при стайна температура за 24 ч. и при 105ºС за 150 мин. Оптималното количество на течният катранен продукт за достигане на максимална степен на омрежване при 105ºС е 22.22%; при стайна температура това е 20% смес със диетилентриамин 50:50 гр./гр. От физико-механичните характеристики на втвърдените пръти и покрития е установено, че изследваният продукт е добър втвърдител на епоксидни смоли.

Applicability comparison of different kinetic/diffusion models for 4-nitrophenol sorption on *Rhizopus oryzae* dead biomass

Z.L. Yaneva[1,2*], B.K. Koumanova[1], S.J. Allen[3]

[1]*Department of Chemical Engineering, University of Chemical Technology and Metallurgy, 8 Kliment Ohridski, 1756 Sofia, Bulgaria*

[2]*Chemistry Unit, Department of Pharmacology, Animal Physiology and Physiological Chemistry, Faculty of Veterinary Medicine, Trakia University, Students Campus, 6000 Stara Zagora, Bulgaria*

[3]*School of Chemistry and Chemical Engineering, Queen's University Belfast David Keir Building, Stranmillis Road Belfast BT9 5AG, Northern Ireland*

Nitrophenols represent one of the most challenging classes of pollutants requiring removal from wastewater streams due to their non-biodegradability and toxicity. The applicability of *Rhizopus oryzae* dead biomass as an alternative "eco-friendly" sorbent for 4-nitrophenol (4-NP) removal from aqueous phase was investigated in this study. The effect of initial sorbate concentration and adsorbent mass on the kinetics of adsorption were evaluated. The experimental kinetic results were analyzed by series of rate/mass transfer equations: pseudo-first, pseudo-second order model, Bangham's model, intra-particle diffusion model, and Elovich kinetic equation. Probably, 4-NP sorption on the dead biomass was mainly limited by chemisorption, but the role of intraparticle diffusion could not be neglected. The highest extend of 4-NP uptake determined in the recent study was 94 %.

Keywords: *Rhizopus oryzae* dead fungi, adsorption, 4-nitrophenol, kinetics

INTRODUCTION

Nitrophenols are the organic compounds that appear very frequently in the wastewater of the almost all heavy chemical industries. Mononitrophenols can be classified as compounds exhibiting moderate to high toxicity in the aquatic compartment [1]. 4-Nitrophenol (4-NP) could enter the environment during its production and use in high-temperature coal conversion, as an intermediate in the manufacture of parathion, methyl parathion and N-acetyl-p-amino-phenol. It is also found in suspended particulate matter in the atmosphere, originating mostly from secondary photochemical reactions in the air [2].

Among the processes used for the treatment of wastewaters rich in phenolic compounds, solid phase adsorption has been widely applied, and efficiency of various adsorbents have been reported in the literature [3, 4]. A number of scientific investigations proved the high adsorption activity of various biopolymers (unmodified/modified chitosan, lignine, etc) towards phenols, chlorophenols and dyes [5–7].

Rhizopus oryzae are saprophylic micro-organisms, which belong to the *Rhizopus fungi* group. Their cell walls consist mainly of chitin and chitosan. The mechanism of biosorption is quite complicated. Both living and dead biomasses exhibit biosorption capacity; performance of living biomass in binding metal ions depends not only on nutrient and environmental status, but also on cell age. The application of live biomass has some disadvantages: live cells systems are sensitive to the toxicity of the pollutants and to the working conditions (pH, temperature). Dead biomass is produced by physical (heating, autoclave treatment, and vacuum drying), chemical (treatment with acids, alkali and other organic and inorganic substances) and mechanical (mechanical grinding) methods [8, 9]. In addition it can be easily regenerated and reused. The role of different functional groups (i.e. amino, carboxyl, hydroxyl, phosphate) and cell wall components (chitin, chitosan, glucan, phosphomannan) of *Rhizopus oryzae* during rhodamine B adsorption was examined. Chemical group modification studies demonstrated that the carboxyl and amino groups were mainly responsible for the binding of rhodamine B on *Rhizopus oryzae* biomass. The adsorption capacity of the cell wall components with respect to rhodamine B followed the order: phosphomannan > chitosan > chitin ~ glucan [10].

The aim of this study was to investigate the applicability of *Rhizopus oryzae* as an alternative "eco-friendly" adsorbent for 4-nitrophenol removal from aqueous phase and to evaluate the adsorption mechanism. The applicability of five kinetic/mass transfer models: pseudo-first order, pseudo-second order, Elovich kinetic models, Bangham's equation and the intraparticle diffusion model, was examined on the basis of comparative estimation of the corresponding rate parameters, equilibrium capacity, and correlation coefficients.

EXPERIMENTAL

Adsorbate

4-Nitrophenol (4-NP) (Merck, 99 %), without further purification, was used as a sorbate in the investigations. Its physicochemical characteristics are presented in Table 1.

Table 1. Physicochemical properties of 4-NP [11]

Molar mass, kg kmol^{-1}	Density, g cm^{-3}	Solubility, g/100g H$_2$O	Molecular volume nm^3 mol^{-1}	pKa	Effective molecular diameter, nm	λ_{max}, nm
139.11	1.270*	1.7	0.191	7.08	0.813	228

* 20 ºC

Adsorbent

Rhizopus oryzae used in the recent study as a sorbent was supplied by the International Mycological Institute in Surrey, Great Britain, in the form of IMI strain 266680. The microorganisms were isolated from a soil in Sri Lanka. malt extract was inoculated by a standard sterile method. Three ceramic granules were added to each of the batch The spores dried at low temperature were reactivated and cultivated in malt extract (17 g dm^{-3} malt extract and 3 g dm^{-3} mycological peptone, dissolved in distilled water at pH 5.4±0.2) incubated at 32ºC for and 3 days in a platform shaker at 175 rpm. The reactors with malt extract to limit the microorganisms threadlike growth. The biomass obtained was precisely washed out consecutively with maternal lye and distilled water and then dried in an oven at 50ºC. The dried biomass was ground in a hammer mill and screened. The fraction used in the recent investigations was 0.15 – 0.50 mm.

Kinetic studies

The kinetic experiments were conducted in a standardized batch adsorber with a two-bladed impeller with a Heidolph RZR 2100 motor [12]. The kinetic experiments were carried out at initial 4-NP concentrations c_o 5, 10, 15, 20 mg dm^{-3}, masses of adsorbent w 1, 2 g, agitation rate n 200 rpm.

SPECORD UV-VIS, Carl Zeiss Jena, spectrophotometer was used for concentration determinations at the corresponding wavelength (λ 228 nm). The working temperature was 19±2 ºC and pH 6.1±0.2. The pH was measured using a LHP 403T TACUSSEL pH-meter. Blanks containing no adsorbate and replicates of each adsorption point were used for each series of experiments.

Table 2. Kinetic and mass transfer models

Model		
Pseudo-first order kinetic model [13]	$$\frac{dq_t}{dt} = k_1(q_e - q_t) \quad (1)$$	$$\log(q_e - q_t) = \log q_e - \frac{k_1}{2.303}t \quad (2)$$
Pseudo-second order kinetic model [14]	$$\frac{dq_t}{dt} = k_2(q_e - q_t)^2 \ (3)$$ $$\frac{1}{q_e - q_t} = \frac{1}{q_e} + k_2 t \ (4)$$	$$\frac{t}{q_t} = \frac{1}{k_2 q_e^2} + \frac{1}{q_e}t \quad (5)$$
Elovich kinetic model, [15, 16]	$$\frac{dq}{dt} = \alpha \exp(-\omega.q) \ (6)$$ $$q_t = \frac{1}{\omega}\ln(\alpha.\omega) + \frac{1}{\omega}\ln t \ (7)$$	$$q_t = A + B.\ln t \ (8)$$ $$A = \frac{1}{\omega}\ln(\alpha.\omega) \ (9)$$ $$B = \frac{1}{\omega} \ (10)$$
Bangham's equation [17]	$$\log\left[\log\left(\frac{c_o}{c_o - q_t.m}\right)\right] = \log\left(\frac{k_o.m}{2.303.V}\right) + \sigma.\log t \ (11)$$	
Intraparticle diffusion model [18]	$$q_t = k_i t^{0.5} \ (12)$$	

RESULTS AND DISCUSSION

Kinetics modeling

In order to investigate the mechanism of 4-NP sorption on *Rhizopus oryzae*, the applicability of the pseudo-first order, pseudo-second order, Elovich kinetic models, Bangham's equation and the intraparticle diffusion model were examined. The non-linear and linear forms of the models applied are resented in Table 2.

Effect of initial sorbate concentration

The experimental kinetic curves presenting the effect of initial nitrophenol concentration in the liquid phase (c_o) on the kinetics of its adsorption on *Rhizopus oryzae* are displayed in Fig. 1. Obviously, the system reached equilibrium approximately 50 min after the beginning of the sorption process. The highest extend of 4-NP removal attained was 94 %.

According to the experimental data, the equilibrium adsorption capacity (q_{exp}) increased directly proportionally (from 7.99 to 19.72 mg g^{-1}) with the increase of c_o. The values of the regression coefficients R_1^2 и R_2^2, calculated by the pseudo-first

and pseudo-second order kinetic models (Table 3) proved better applicability of the second-order model. The latter conclusion was unambiguously ascertained as by the nearly analogous modes of the experimental and model kinetic curves, juxtaposed on Figure 1 as q_t vs t, so by the nearly equal values of the experimental (q_{exp}) and the calculated by the second-order model (q_2) equilibrium sorption capacities (Table 3). The observed direct relationship between the values of the initial sorption rate (h) and c_o values could, probably, be due to the greater number of organic molecules that attack the active sites of the sorbent, as well as to the decreased mass transfer resistance they had to overcome.

The proven applicability of this model signified the role of chemisorption as probably one of the basic rate limiting mechanisms during 4-NP adsorption on the biomaterial studied.

The kinetic data were also analyzed using the Elovich equation. The corresponding model parameters (ω, α) determined along with the correlation coefficients (R_E^2) were given in Table 3.

Table 3. Values of the kinetic and diffusion parameters characterizing 4-NP sorption on *Rhizopus oryzae* - effect of initial sorbate concentration

| Pseudo-first order model	k_1, min^{-1}	q_{e1}, mg g^{-1}	q_{exp}, mg g^{-1}		R_1^2
5 mg dm^{-3}	0.0481	1.98	7.99		0.9320
10 mg dm^{-3}	0.0465	4.33	12.24		0.9314
15 mg dm^{-3}	0.0894	5.28	14.54		0.8790
20 mg dm^{-3}	0.1375	7.26	19.72		0.8865
Pseudo-second order model	k_2, g mg^{-1} min^{-1}	q_{e2}, mg g^{-1}	q_{exp}, mg g^{-1}	h, mg g^{-1} min^{-1}	R_2^2
5 mg dm^{-3}	0.0817	8.09	7.99	5.3504	0.9994
10 mg dm^{-3}	0.0336	12.39	12.24	5.1593	0.9979
15 mg dm^{-3}	0.0435	14.88	14.54	9.6432	0.9995
20 mg dm^{-3}	0.0418	19.92	19.72	16.5837	0.9992
Bangham's equation	k_0, dm^3 g^{-1}	σ			R_B^2
5 mg dm^{-3}	2.7500	0.2495			0.9725
10 mg dm^{-3}	1.6167	0.1875			0.9653
15 mg dm^{-3}	1.2409	0.1760			0.9145
20 mg dm^{-3}	1.4422	0.1423			0.8521
Elovich model	A	B	ω, g mg^{-1}	α, mg g^{-1} min^{-1}	R_E^2
5 mg dm^{-3}	5.3838	0.6319	1.5826	3167.8980	0.9544
10 mg dm^{-3}	7.2288	1.1364	0.8800	657.8480	0.9678
15 mg dm^{-3}	8.7751	1.4885	0.6718	540.8047	0.9162
20 mg dm^{-3}	13.3240	1.6302	0.6134	5778.8980	0.8630
Intraparticle diffusion model	k_{i1}, mg g^{-1} min$^{-0.5}$	k_{i2}, mg g^{-1} min$^{-0.5}$		R_{i1}^2	R_{i2}^2
5 mg dm^{-3}	0.4810	0.2055		0.9451	0.9421
10 mg dm^{-3}	1.8599	0.8619		0.8835	0.8333
15 mg dm^{-3}	1.2593	0.2056		0.9023	0.8103
20 mg dm^{-3}	2.8069	0.2647		0.9185	0.7598
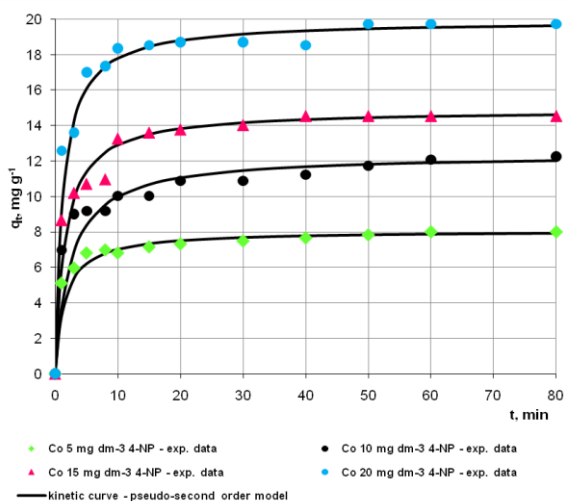
Fig. 1. Experimental and pseudo-second order model kinetic curves for 4-NP adsorption on *Rhizopus oryzae* - effect of initial sorbate concentration.

Elovich equation was used successfully to describe second-order kinetics assuming that the actual solid surfaces are energetically heterogeneous [19]. The analyses of the results outlined an inversely proportional relationship between c_o and the values of the parameter - ω, which is related to the extent of surface coverage and the activation energy for chemisorption. Consequently, the number of active sites available for adsorption was reduced due to the larger number of sorbate molecules at higher initial concentrations. Fig. 2 presented graphically the intraparticle diffusion model applied to the investigated system.
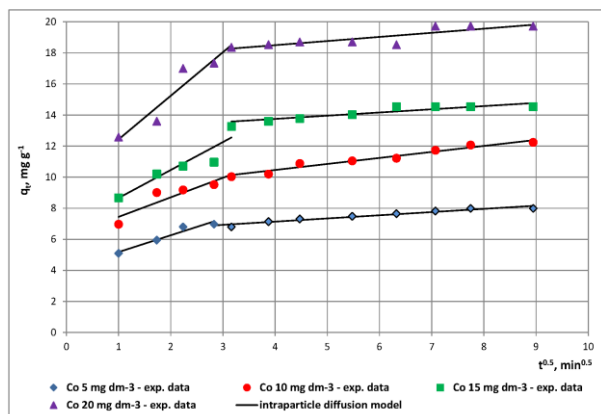

Fig. 2. Intraparticle diffusion model applied for the system 4-NP - *Rhizopus oryzae* - effect of initial sorbate concentration.

The plots consisted of only two linear sections, presuming the presence of macro- and transitional pores in the sorbent structure. The diffusion in them characterized with specific rate parameters, k_{i1} and k_{i2}, respectively (Table 3). The calculated values of k_{i1} were higher than that of k_{i2}. The reason could be as circumscription of the available vacant space for

diffusion in them, so of pore blockage. The values of the correlation regression coefficients characterizing the applicability of the intraparticle diffusion model (R_{i1}^2, R_{i2}^2) were lower than that of R_2^2, but commensurable with R_1^2. Actually, the three models stated above could describe the proposed sorption process to a definite extend, but they could not predict the high rate of adsorption during the first minutes of the process. Probably, the initial stages were controlled by external mass transfer or surface diffusion, followed by chemical reaction or a constant-rate stage, and diffusion causing gradual decrease of the process rate. The initial steep section of the plots associated with a sharp increase of the nitrophenol concentration was indicative of a rapid initial external mass transfer or chemical interactions between functional groups of the organic molecules with those of the biomaterial. After saturating the external solid particles surface, the molecules began to enter them in order to find new vacant active sites. The sorption of 4-NP molecules inside the pores of *Rhizopus oryzae*, however, increased the diffusion resistance and led to a decrease in the process rate.

The effect of initial sorbate concentration on the values of the second-order model parameters q_2, k_2 and h was examined by plotting the linear relationships between them and c_o:

$$q_2 = \frac{c_o}{A_q c_o + B_q} \tag{13}$$

$$k_2 = \frac{c_o}{A_k c_o + B_k} \tag{14}$$

$$h = \frac{c_o}{A_h c_o + B_h} \tag{15}$$

The values of the coefficients A_q, B_q, R_q^2, A_k, B_k, R_k^2, A_h, B_h and R_h^2 were calculated by linear regression analyses and presented in Table 4.

The substitution of q_2 and h values in eqn. (13) and (15) and then in eqn. (5), allowed working out the pseudo-second rate law rendering an account of the effect of initial nitrophenol concentration:

$$q_t = \frac{c_o t}{0.0086 c_o + 1.3006 + (0,0272 c_o + 0.5196)t} \tag{16}$$

Eqn. (16) is a generalized model for prediction of the adsorption capacity during 4-NP sorption on *Rhizopus oryzae* at various initial concentrations with time. The kinetic data for 4-NP adsorption on *Rhizopus oryzae* were analyzed by using the Bangham's equation to examine if pore diffusion

164

Table 4. Values of the empirical parameters for q_2, k_2 and h regarding c_o

A_q, g mg^{-1}	B_q, g dm^{-3}	R_q^2	A_k, mg g min^{-1}	B_k, mg^2 g dm^3 min^{-1}	R_k^2	A_h, g mg min^{-1}	B_h, g dm^3 min^{-1}	R_h^2
0.0272	0.5196	0.8877	25.98	−29.225	0.9291	0.0086	1.3006	0.0164

Table 5. Values of the kinetic and diffusion parameters characterizing 4-NP sorption on *Rh. oryzae* - effect of adsorbent mass.

Pseudo-first order model	k_1, min^{-1}	q_{e1}, mg g^{-1}	q_{exp}, mg g^{-1}		R_1^2
1 g	0.0465	4.33	12.24		0.9314
2 g	0.0573	0.94	7.23		0.8650
Pseudo-second order model	k_2, g mg^{-1} min^{-1}	q_{e2}, mg g^{-1}	q_{exp}, mg g^{-1}	h, mg g^{-1} min^{-1}	R_2^2
1 g	0.0336	12.39	12.24	5.1593	0.9979
2 g	0.8715	7.26	7.23	12.6743	0.9999
Bangham's equation	k_0, dm^3 g^{-1}	σ			R_B^2
1 g	1.6167	0.1875			0.9653
2 g	1.7456	0.1139			0.9526
Elovich model	A	B	ω, g mg^{-1}	α, mg g^{-1} min^{-1}	R_E^2
1 g	7.2288	1.1364	0.8800	657.8480	0.9678
2 g	5.9809	0.3177	3.1476	4.7630.10^7	0.9375
Intraparticle diffusion model	k_{i1}, mg g^{-1}min$^{-0.5}$	k_{i2}, mg g^{-1}min$^{-0.5}$		R_{i1}^2	R_{i2}^2
1 g	1.8599	0.8619		0.8835	0.8333
2 g	0.6883	0.1521		0.9999	0.9457

was the only controlling step in the adsorption process or not. The experimental data modeled by eqn. (8) did not yield a desired linear fit in the double logarithmic plot. This indicated that the adsorption kinetics was not limited only by pore-diffusion. The values of the Bangham's equation parameters k_o and σ along with the correlation coefficients (R_B) were presented in Table 3. The highest values of the three parameters estimated at c_o 5 mg dm^{-3}, seemed logical as the number of organic molecules competing for vacant active sites inside the sorbent pores was the lowest, consequently the obstacles, due to pore blockage, they had to overcome were reduced. According to the results, it could be concluded that both film and pore-diffusion played a significant role to different extend during the different stages of the sorption process.

Effect of adsorbent mass

The effect of adsorbent mass on the kinetics of 4-NP adsorption on *Rhizopus oryzae* was tested in the present investigations. The experimental kinetic curves (Fig. 3) displayed an outlined direct relationship between adsorbent quality and the extent of nitrophenol uptake from its model solutions. The latter statement was logical as the greater amount of adsorbent is related to larger number of vacant active sites for the organic molecules sorption. The sorption rate in the initial stages of the process was the highest. The system reached equilibrium, indicated by the horizontal section of the kinetic curves, approximately 40-50 min after the beginning of the process. The highest adsorption capacity attained was q_e 12.24 mg g^{-1}.

The experimental data were modeled by the pseudo-first order, pseudo-second order, Elovich kinetic models, Bangham's equation and the intraparticle diffusion model, to determine the prevailing mechanism/s during 4-NP sorption on the biomaterial and to examine the effect of adsorbent mass on the models kinetic and diffusion parameters (Table 5). The high values of the correlation coefficients ($R_2^2 > 0.9979$) and the approximately equal values of the calculated and experimentally obtained equilibrium adsorption capacities (q_2, q_e) (Table 5), calculated by the pseudo-second order model compared to the values of the parameters obtained by applying the first order equation (Table 5), proved the better applicability of the second order model. Thus, chemisorption could be accepted as one of the basic rate limiting mechanisms during 4-NP sorption on *Rhizopus oryzae*.

The above stated conclusion regarding the mechanism of the proposed sorption process was confirmed by the analyses of the applicability of Bangham's model, assuming pore diffusion as the major rate limiting mechanism, and Elovich kinetic equation based on the hypothesis of chemisorption. The values of Bangham's and Elovich equation parameters: k_o, σ, A, B, ω and α, along with the

165

regression coefficients (R_B^2 and R_e^2) were presented in Table 5. The values of R_B^2 and R_E^2 were commensurable but lower than R_2^2. Consequently, probably 4-NP sorption on the dead biomass was mainly limited by chemical interactions between the organic molecules and some functional groups of *Rhizopus oryzae*, but the role of intraparticle diffusion could not be neglected.
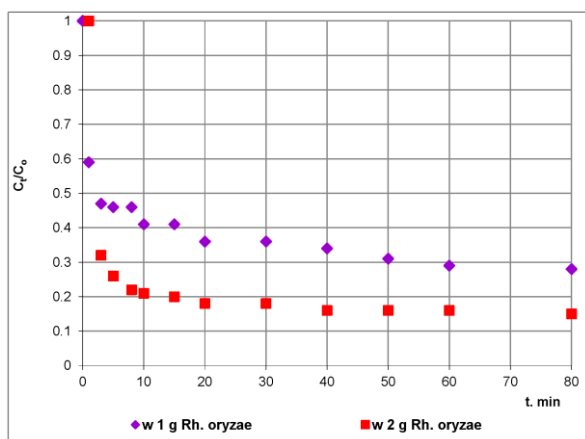

Fig. 3. Experimental kinetic curves of 4-NP adsorption on *Rhizopus oryzae* - effect of adsorbent mass.

The analyses of the results outlined a direct relationship between w and the values of the parameter ω, related to the extent of surface coverage and the activation energy for chemisorptions, as the larger adsorbent amount defined greater active sites available for adsorption.

As the values of R_{i1} are higher than those of R_1 and lower than R_2 (Table 5), an explicit conclusion whether chemisorption or intraparticle diffusion was the general rate controlling mechanism during 4-NP sorption on *Rhizopus oryzae* could not be withdrawn, i.e. either of the proposed processes could dominate during the different sorption stages.

The adsorbent loading increased when its mass was decreased, as unit sorbent mass got into contact with larger number of organic molecules. Moreover, the rate of intraparticle diffusion decreased at higher sorbent mass as indicated by the lower values of the rate coefficients (k_{i1}, k_{i2}), characterizing the experimental series with w 2 g *Rhizopus oryzae,* when compared to that with w 1 g sorbent (Table 5). Probably, the latter was due to the larger external surface area available for adsorption, followed by a sharp drop of 4-NP concentration in the liquid phase and respectively, reduction of the process driving force.

The conclusions of our scientific team, regarding the mechanism of the sorption process investigated were sustained by analyses of the adsorbate and adsorbent nature. As mentioned above, chitin and

chitosan are the basic components of *Rhizopus oryzae* cell walls. Chitosan characterized with well distinguished hydrophilic properties due to the presence of a polar amino group in its structure. As a result it expands in aqueous media and its active sites responsible for the formation of H-bonds become more easily accessible. According to Uzun and Guzel, 4-NP adsorption on chitosan was controlled by both physical and chemical adsorption [5, 6]. The pKa value for the 4-NP is 7.15, i.e. its aqueous solution characterized with low pH. The O-H bond could be easily destroyed, while the NO_2-group supports the resonance stability of the molecular structure through delocalization of the negative charge. The amino group of the chitosan is positively charged in the acidic 4-NP solution. Consequently, a chemical interaction between the negatively charged molecule and the positive charge of the biopolymer could take place.

The present investigations proved the high efficiency (94 %) of *Rhizopus oryzae* as an alternative adsorbent for 4-NP removal from aqueous phase and revealed the mechanism of the separation process at laboratory scale. Due to the harmful effects of these organic compounds and the urge for sustainable development for the natural water resources at global scale, however, the wastewaters containing them must be treated before being discharged to receiving natural water bodies. Consequently, the future perspectives of the applicability of the proposed "eco-friendly" adsorbent for industrial purposes include large-scale investigations of our scientific team with real wastewaters containing mononitrophenols and/or contaminated natural waters.

CONCLUSIONS

The mechanism of 4-NP adsorption on *Rhizopus oryzae* from aqueous medium on the basis of kinetic studies was investigated. As the theoretical kinetic curves predicted by the pseudo-second order model displayed an extremely high degree of correlation with the experimental data, the rate-limiting step might be chemical adsorption or chemisorption involving valency forces through exchange of electrons between the sorbate and the sorbent. The laboratory studies proved the high efficiency (94 % uptake extend) of *Rhizopus oryzae* dead biomass as an alternative adsorbent for removal of the toxic and recalcitrant organic contaminant 4-NP from aqueous phase, and outlined its future applicability in large-scale wastewater treatment technologies.

NOMENCLATURE

c_e equilibrium adsorbate concentration in the liquid phase, mg dm^{-3}

c_o initial adsorbate concentration in the liquid phase, mg dm^{-3}

d_p particle diameter, mm

h initial adsorption rate, mg g^{-1} min^{-1}

K_1 Bangham's model equilibrium constant for the first layer adsorption

K_2 Bangham's equilibrium constant for multilayer adsorption

k_i intraparticle diffusion rate constant, mg g^{-1}min$^{-0.5}$

k_o Bangham's equation parameters, dm g^{-1}

k_1 rate constant of pseudo-first order sorption, min^{-1}

k_2 rate constant of pseudo-second order sorption, g mg^{-1} min^{-1}

m adsorbent concentration, g dm^{-3}

n agitation rate, rpm

q_e the equilibrium sorbate concentration in the solid phase, mg g^{-1}

q_t the sorption capacity at equilibrium and at time t, mg g^{-1}

R the universal gas constant (8.314x10^{-3} kJ mol^{-1} K^{-1})

R^2 correlation coefficient

T temperature, K

t time, min

V solution volume, dm^3

w adsorbent mass, g

α the initial adsorption rate in Elovich equation, mg g^{-1} min^{-1}

λ maximum absorbance wavelength, nm

σ Bangham's equation parameter, ($\sigma < 1$)

ω parameter in Elovich model related to the extent of surface coverage and the activation energy for chemisorption, g mg^{-1}

REFERENCES

1. Agency for toxic substances, Nitrophenols, (1996).
2. W. Huang, Ch. Yao, S. Jin, Sh. Ying, X. Shen, Sorption of p-nitrophenol onto sediment in the presence of cetylpyridinium chloride and Pb(NO₃)₂: Influence of pH, *J. Hazard. Mater.*, **155**, 225, (2008).
3. K. Lin, J. Pan, Y. Chen, R. Cheng, X. Xu, Study on the adsorption of phenol from aqueous solution on hydroxyapatite nanopowders, *J. Hazard. Mater.*, **161**, 231, (2009).
4. P. Barkakati, A. Begum, M.L. Das, P.G. Rao, Adsorptive separation of Ginsenoside from aqueous solution by polymeric resins: Equilibrium, kinetic

and thermodynamic studies, *Chem. Eng. J.,* **161**, 34, (2010).
5. I. Uzun, F. Guzel, Kinetics and thermodynamics of the adsorption of some dyestuffs and p-nitrophenol by chitosan and MCM-chitosan from aqueous solution, *J. Colloid Interf. Sci.,* **274**, (2), 398 (2004).
6. I. Uzun, F. Guzel, Rate studies on the adsorption of some dyestuffs and p-nitrophenol by chitosan and monocarboxy-methylated(mcm)-chitosan from aqueous solution, *J. Hazard. Mater.,* **B 118**, 141, (2005).
7. S.J. Allen, B. Koumanova, Decolourization of water/wastewater using adsorption (Review), *J. Univ. Chem. Technol. Met. (Sofia),* **40,** (3), 175 (2005).
8. G. Yan, T. Viraraghavan, Effect of pretreatment on the bioadsorption of heavy metals on Mucor rouxii, *Water SA*, 26, 119 (2000).
9. B. Koumanova, Z. Yaneva, Low cost adsorbents for the removal of nitrophenols from wastewaters, Management of Intentional and Accidental Water Pollution. *NATO Security through Science Series*, Springer, 263, (2006).
10. S.K. Das, P. Ghosh, I. Ghosh, A.K. Guha, Adsorption of rhodamine B on *Rhizopus oryzae*: Role of functional groups and cell wall components. *Colloids and Surfaces B: Biointerfaces,* **65**, 30 (2008).
11. A.A.M. Daifullah, B.S. Girgis, Removal of some substituted phenols by activated carbon obtained from agricultural waste, *Wat. Res.*, **32**, (4), 1169 (1998).
12. B. Koumanova, P. Peeva-Antova, Adsorption of p-chlorophenol from aqueous solutions on bentonite and perlite, *J. Hazard. Mater.,* **90**, (3), 229 (2002).
13. S. Lagergren, Zur theorie der sogenannten adsorption gelöster stoffe, Kungliga Svenska Vetenskapsakademiens, *Handlingar,* 24, 1 (1898).
14. Y.S. Ho, G. McKay, Kinetic model for lead (II) sorption onto peat, *Adsorption Science & Technology*, 16, 243 (1998).
15. S.Z. Roginsky, Y. Zeldovich, *Acta Phys. Chem.* USSR, 1, 554 (1934).
16. S.H. Chien, W.R. Clayton, Application of Elovich equation to the kinetics of phosphate release and sorption on solids, *Soil Science Society of America Journal,* 44, 265 (1980).
17. C. Aharoni, S. Sideman, E. Hoffer, Adsorption of phosphate ions by colloid ioncoated alumina, *J. Chem. Technol. & Biotechnol.,* **29**, 404 (1979).
18. W.J. Weber, J.C. Morris, Kinetics of adsorption on carbon from solutions, *J. Sanitary Engineering Division,* **89**, 31 (1963).
19. E. Demirbas, M. Kobya, M.T. Sulak, Adsorption kinetics of a basic dye from aqueous solutions onto apricot stone activated carbon, *Biores. Technol.,* **99**, 5368 (2008

.

СРАВНЯВАНЕ НА ПРИЛОЖИМОСТТА НА РАЗЛИЧНИ КИНЕТИЧНИ/ДИФУЗИОННИ МОДЕЛИ ЗА СОРБЦИЯ НА 4-НИТРОФЕНОЛ ВЪРХУ МЪРТВА БИОМАСА *RHIZOPUS ORYZAE*

З.Л. Янева[1,2] *, Б.К. Куманова[1], С.Д. Алън[3]

[1]*Химикотехнологичен и металургичен университет, бул. Кл. Охридски 8, 1756 София*
[2]*Факултет по ветеринарна медицина, Тракийски университет, Студентски град, 6000 Стара Загора*
[3]*Катедра по химия и химично инженерство, Кралски университет, Белфаст, Северна Ирландия*

(Резюме)

Нитрофенолите представляват един от най-предизвикателните класове замърсители, изискващи отстраняване от водни потоци, поради тяхната трудна биоразградимост и токсичност. В тази публикация е изследвана приложимостта на мъртвата биомаса *Rhizopus oryzae* като алтернативен „еко-сорбент" за отстраняване на 4-нитрофенол (4-NP) от водна среда. Оценен е ефектът на началната концентрация на сорбата и масата на адсорбента върху кинетиката на адсорбция. Резултатите от изследване на кинетиката са анализирани чрез серия от скоростни/масопреносни уравнения: модели от псевдо-първи и псевдо-втори порядък, модел на Бангам, модел за вътрешна дифузия и кинетичното уравнение на Елович. Вероятно, сорбцията на 4-NP върху мъртвата биомаса се лимитира главно от хемисорбция, но не трябва да се пренебрегва ролята на вътрешната дифузия. Най-високата степен на отстраняване на 4-NP, постигната в това изследване, е 94 %.

On the contact angle of electrospun polyacrylonitrile nanofiber mat

B. Hadavi Moghadam [1], M. Hasanzadeh [1], A. K. Haghi [2,*]

[1] Department of Textile Engineering, Amirkabir University of Technology, Tehran, Iran
[2] Department of Textile Engineering, University of Guilan, Rasht, Iran

In this work, effects of four electrospinning parameters, including solution concentration (wt.%), applied voltage (kV), tip to collector distance (cm), and volume flow rate (ml/h), on contact angle (CA) of nanofiber mat are studied. To optimize and predict the CA of electrospun fiber mat, response surface methodology (RSM) and artificial neural network (ANN) are employed and a quantitative relationship between processing variables and CA of electrospun fibers is established. It is found that the solution concentration is the most important factor impacting the CA of electrospun fiber mat. The obtained results demonstrated that both the proposed models are highly effective in estimating CA of electrospun fiber mat. However, more accurate results are obtained by ANN model as compared to the RSM model. In ANN model the determination coefficient (R^2) and absolute percentage error between actual and predicted response are obtained as 0.965 and 1.97, respectively.

Keywords: Electrospinning, Contact angle, Response surface methodology, Artificial neural network

1. INTRODUCTION

The wettability of solid surfaces is a very important property of surface chemistry, which is controlled by both the chemical composition and the geometrical microstructure of a rough surface [1-3]. When a liquid droplet contacts a rough surface, it will spread or remain as droplet with the formation of angle between the liquid and solid phases. Contact angle (CA) measurements are widely used to characterize the wettability of rough surface [3–5]. There are various methods to make a rough surface, such as electrospinning, electrochemical deposition, evaporation, chemical vapor deposition (CVD), plasma, and so on.

Electrospinning as a simple and effective method for preparation of nanofibrous materials have attracted increasing attention during the last two decade [6]. Electrospinning process, unlike the conventional fiber spinning systems (melt spinning, wet spinning, etc.), uses electric field force instead of mechanical force to draw and stretch a polymer jet [7]. This process involves three main components including syringe filled with a polymer solution, a high voltage supplier to provide the required electric force for stretching the liquid jet, and a grounded collection plate to hold the nanofiber mat. The charged polymer solution forms a liquid jet that is drawn towards a grounded collection plate. During the jet movement to the collector, the solvent evaporates and dry fibers deposited as randomly oriented structure on the surface of a collector [8–13]. The electrospun nanofiber mat possesses high specific surface area, high porosity, and small pore size. Therefore, they have been suggested as excellent candidate for many applications including filtration [14], multifunctional membranes [15], biomedical agents [16], tissue engineering scaffolds [17–18], wound dressings [19], full cell [20] and protective clothing [21].

The morphology and the CA of the electrospun nanofibers can be affected by many electrospinning parameters including solution properties (the concentration, liquid viscosity, surface tension, and dielectric properties of the polymer solution), processing conditions (applied voltage, volume flow rate, tip to collector distance, and the strength of the applied electric field), and ambient conditions (temperature, atmospheric pressure and humidity) [9–12].

In this work, the influence of four electrospinning parameters, comprising solution concentration, applied voltage, tip to collector distance, and volume flow rate, on the CA of the electrospun PAN nanofiber mat was carried out using response surface methodology (RSM) and artificial neural network (ANN). First, a central composite design (CCD) was used to evaluate main and combined effects of above parameters. Then, these independent parameters were fed as inputs to

---

* To whom all correspondence should be sent:
E-mail: Haghi@Guilan.ac.ir

an ANN while the output of the network was the CA of electrospun fiber mat. Finally, the importance of each electrospinning parameters on the variation of CA of electrospun fiber mat was determined and comparison of predicted CA value using RSM and ANN are discussed.

2. EXPERIMENTAL

2.1. Materials

PAN powder was purchased from Polyacryle Co. (Iran). The weight average molecular weight (M_w) of PAN was approximately 100,000 g/mol. *N-N*, dimethylformamide (DMF) was obtained from Merck Co. (Germany) and was used as a solvent. These chemicals were used as received.

2.2. Electrospinning

The PAN powder was dissolved in DMF and gently stirred for 24 h at 50ºC. Therefore, homogenous PAN/DMF solution was prepared in different concentration ranged from 10 wt.% to 14 wt.%. Electrospinning was set up in a horizontal configuration as shown in Figure 1. The electrospinning apparatus consisted of 5 ml plastic syringe connected to a syringe pump and a rectangular grounded collector (aluminum sheet). A high voltage power supply (capable to produce 0–40 kV) was used to apply a proper potential to the metal needle. It should be noted that all electrospinnings were carried out at room temperature.
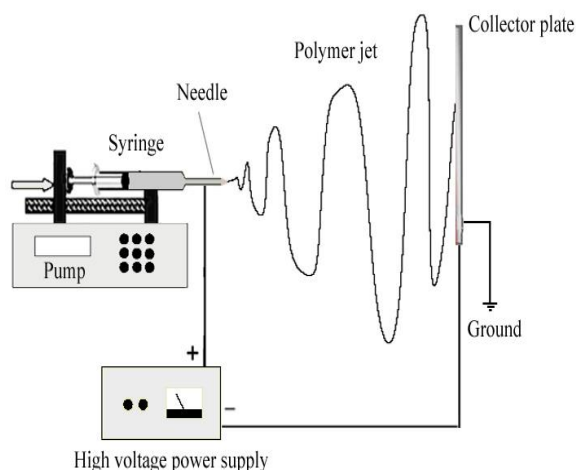

Fig. 1. Schematic of electrospinning set up.

2.3. Measurement and characterization

The morphology of the gold-sputtered electrospun fibers were observed by scanning electron microscope (SEM, Philips XL-30). The average fiber diameter and distribution was determined from selected SEM image by measuring at least 50 random fibers. The wettability of electrospun fiber mat was determined by CA measurement. The CA measurements were carried out using specially arranged microscope equipped with camera and PCTV vision software as shown in Figure 2. The droplet used was distilled water and was 1 µl in volume. The CA experiments were carried out at room temperature and were repeated five times. All contact angles measured within 20 s of placement of the water droplet on the electrospun fiber mat. A typical SEM image of electrospun fiber mat, its corresponding diameter distribution and CA image are shown in Figure 3.
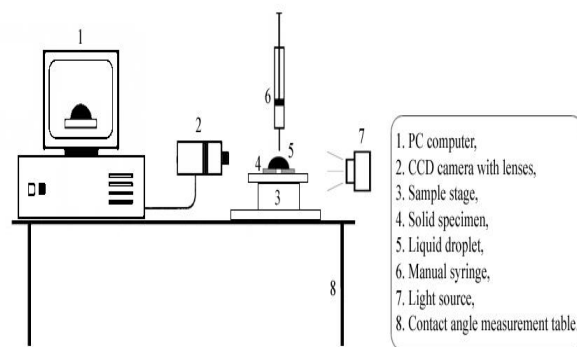

1. PC computer,
2. CCD camera with lenses,
3. Sample stage,
4. Solid specimen,
5. Liquid droplet,
6. Manual syringe,
7. Light source,
8. Contact angle measurement table.

Fig. 2. Schematic of CA measurement set up.

2.4. Experimental design
2.4.1. Response surface methodology

Response surface methodology (RSM) is a combination of mathematical and statistical techniques used to evaluate the relationship between a set of controllable experimental factors and observed results. This optimization process is used in situations where several input variables influence some output variables (responses) of the system [22–23].

In the present study, central composite design (CCD) was employed to establish relationships between four electrospinning parameters and the CA of electrospun fiber mat. The experiment was performed for at least three levels of each factor to fit a quadratic model. Based on preliminary experiments, polymer solution concentration (wt.%), applied voltage (kV), tip to collector
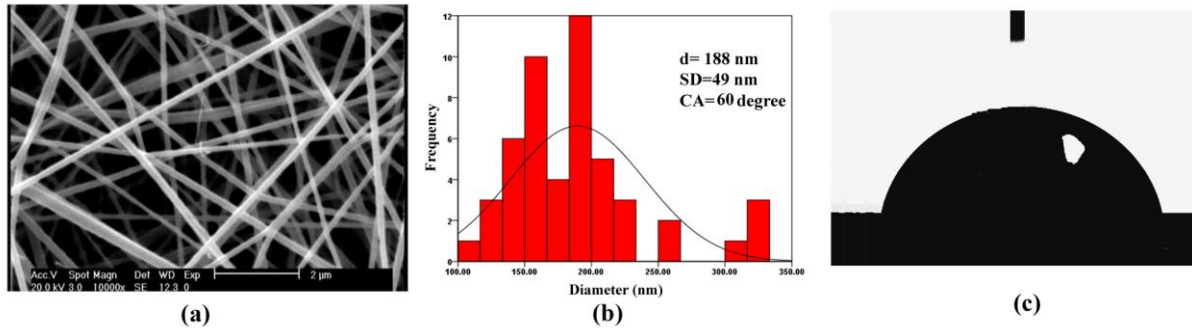
Fig. 3. A typical (a) SEM image, (b) fiber diameter distribution, and (c) CA of electrospun fiber mat.

distance (cm), and volume flow rate (ml/h) were determined as critical factors with significance effect on CA of electrospun fiber mat. These factors were four independent variables and chosen equally spaced, while the CA of electrospun fiber mat was dependent variable. The values of –1, 0, and 1 are coded variables corresponding to low, intermediate and high levels of each factor respectively. The experimental parameters and their levels for four independent variables are shown in Table 1. The regression analysis of the experimental data was carried out to obtain an empirical model between processing variables. The contour surface plots were obtained using Design-Expert® software.

Table 1. Design of experiment (factors and levels)

Factor	Variable	Unit	Factor level		
			-1	0	1
X_1	Solution concentration	(wt.%)	10	12	14
X_2	Applied voltage	(kV)	14	18	22
X_3	Tip to collector distance	(cm)	10	15	20
X_4	Volume flow rate	(ml/h)	2	2.5	3

The quadratic model, Equation (1) including the linear terms, was fitted to the data.

$$Y = \beta_0 + \sum_{i=1}^{4} \beta_i x_i + \sum_{i=1}^{4} \beta_{ii} x_i^2 + \sum_{i=1}^{3} \sum_{j=2}^{4} \beta_{ij} x_i x_j \quad (1)$$

where, Y is the predicted response, x_i and x_j are the independent variables, β_o is a constant, β_i is the linear coefficient, β_{ii} is the squared coefficient, and β_{ij} is the second-order interaction coefficients [22, 23].

The quality of the fitted polynomial model was expressed by the determination coefficient (R^2) and its statistical significance was performed with the Fisher's statistical test for analysis of variance (ANOVA).

2.4.2. Artificial neural network

Artificial neural network (ANN) is an information processing technique, which is inspired by biological nervous system, composed of simple unit (neurons) operating in parallel. A typical ANN consists of three or more layers, comprising an input layer, one or more hidden layers and an output layer. Every neuron has connections with every neuron in both the previous and the following layer. The connections between neurons consist of weights and biases. The weights between the neurons play an important role during the training process. Each neuron in hidden layer and output layer has a transfer function to produce an estimate as target. The interconnection weights are adjusted, based on a comparison of the network output (predicted data) and the actual output (target), to minimize the error between the network output and the target [6,24–25].
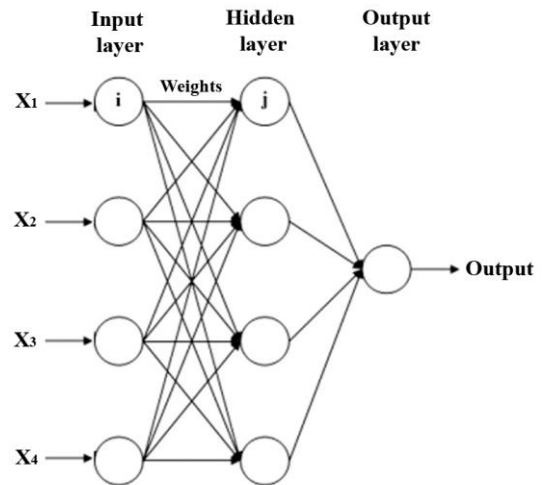

Fig. 4. The topology of artificial neural network used in this study.

In this study, feed forward ANN with one hidden layer composed of four neurons was selected. The ANN was trained using back-propagation algorithm. The same experimental data used for each RSM designs were also used as the input variables of the ANN. There are four neurons in the input layer corresponding to four electrospinning parameters and one neuron in the output layer corresponding to CA of electrospun

171

fiber mat. Figure 4 illustrates the topology of ANN used in this investigation.

3. RESULTS AND DISCUSSION

This section discusses in details the wettability behavior of electrospun fiber mat concluded from CA measurements. The results of the proposed RSM and ANN models are also presented followed by a comparison between those models.

3.1. The analysis of variance (ANOVA)

All 30 experimental runs of CCD were performed according to Table 2. A significance level of 5% was selected; that is, statistical conclusions may be assessed with 95% confidence. In this significance level, the factor has significant

effect on CA if the p-value is less than 0.05. On the other hand, when p-value is greater than 0.05, it is concluded the factor has no significant effect on CA.

The results of analysis of variance (ANOVA) for the CA of electrospun fibers are shown in Table 3. Equation (2) is the calculated regression equation.

$$CA = 25.80 - 9.89X_1 + 2.17X_2 + 4.33X_3 - 2.33X_4$$
$$- 1.63X_1X_2 - 1.63X_1X_3 + 1.63X_1X_4 - 0.88X_2X_3 - 0.63X_2X_4 + 0.37X_3X_4$$
$$+ 7.90X_1^2 + 6.40X_2^2 - 0.096X_3^2 + 2.90X_4^2 \tag{2}$$

From the p-values presented in Table 3, it can be concluded that the p-values of terms X_3^2, X_4^2, X_2X_3, X_2X_4 and X_3X_4 is greater than the

Table 2. The actual design of experiments and response

| No. | Electrospinning parameters | | | | Response |
	X_1 Concentration	X_2 Voltage	X_3 Distance	X_4 Flow rate	CA (°)
1	10	14	10	2	44±6
2	10	22	10	2	54±7
3	10	14	20	2	61±6
4	10	22	20	2	65±4
5	10	14	10	3	38±5
6	10	22	10	3	49±4
7	10	14	20	3	51±5
8	10	22	20	3	56±5
9	10	18	15	2.5	48±3
10	12	14	15	2.5	30±3
11	12	22	15	2.5	35±5
12	12	18	10	2.5	22±3
13	12	18	20	2.5	30±4
14	12	18	15	2	33±4
15	12	18	15	3	25±3
16	12	18	15	2.5	26±4
17	12	18	15	2.5	29±3
18	12	18	15	2.5	28±5
19	12	18	15	2.5	25±4
20	12	18	15	2.5	24±3
21	12	18	15	2.5	21±3
22	14	14	10	2	31±4
23	14	22	10	2	35±5
24	14	14	20	2	33±6
25	14	22	20	2	37±4
26	14	14	10	3	19±3
27	14	22	10	3	28±3
28	14	14	20	3	39±5
29	14	22	20	3	36±4
30	14	18	15	2.5	20±3

Table 3. Analysis of variance for the CA of electrospun fiber mat

Source	SS	DF	MS	F-value	Probe > F	Remarks
Model	4175.07	14	298.22	32.70	<0.0001	Significant
X_1-Concentration	1760.22	1	1760.22	193.01	<0.0001	Significant
X_2-Voltage	84.50	1	84.50	9.27	0.0082	Significant
X_3-Distance	338.00	1	338.00	37.06	<0.0001	Significant
X_4-Flow rate	98.00	1	98.00	10.75	0.0051	Significant
X_1X_2	42.25	1	42.25	4.63	0.0481	Significant
X_1X_3	42.25	1	42.25	4.63	0.0481	Significant
X_1X_4	42.25	1	42.25	4.63	0.0481	Significant
X_2X_3	12.25	1	12.25	1.34	0.2646	
X_2X_4	6.25	1	6.25	0.69	0.4207	Significant
X_3X_4	2.25	1	2.25	0.25	0.6266	
X_1^2	161.84	1	161.84	17.75	0.0008	Significant
X_2^2	106.24	1	106.24	11.65	0.0039	Significant
X_3^2	0.024	1	0.024	0.0026	0.9597	
X_4^2	21.84	1	21.84	2.40	0.1426	
Residual	136.80	15	9.12			
Lack of Fit	95.30	10	9.53	1.15	0.4668	

Table 4. Weights and bias obtained in training ANN

Hidden layer	Weights	IW_{11} 1.0610	IW_{12} 1.1064	IW_{13} 21.4500	IW_{14} 3.0700
		IW_{21} -0.3346	IW_{22} 2.0508	IW_{23} 0.2210	IW_{24} -0.2224
		IW_{31} -0.6369	IW_{32} -1.1086	IW_{33} -41.5559	IW_{34} 0.0030
		IW_{41} -0.5038	IW_{42} -0.0354	IW_{43} 0.0521	IW_{44} 0.9560
	Bias	b_{11} -2.5521	b_{21} -2.0885	b_{31} -0.0949	b_{41} 1.5478
Output layer	Weights	LW_{11} 0.5658 LW_{21} 0.2580 LW_{31} -0.2759 LW_{41} -0.6657			
	Bias	b 0.7104			

significance level of 0.05, therefore they have no significant effect on the CA of electrospun fiber mat. Since the above terms had no significant effect on CA of electrospun fiber mat, these terms were removed. The fitted equations in coded unit are given in Equation (3).

$$CA = 26.07 - 9.89X_1 + 2.17X_2 + 4.33X_3 - 2.33X_4$$
$$- 1.63X_1X_2 - 1.63X_1X_3 + 1.63X_1X_4$$
$$+ 9.08X_1^2 + 7.58X_2^2$$

(3)

Now, all the p-values are less than the significance level of 0.05. Analysis of variance showed that the RSM model was significant (p<0.0001), which indicated that the model has a good agreement with experimental data. The determination coefficient (R^2) obtained from regression equation was 0.958.

3.2. Artificial neural network

In this study, the best prediction, based on minimum error, was obtained by ANN with one hidden layer. The suitable number of neurons in the hidden layer was determined by changing the number of neurons. The good prediction and minimum error value were obtained with four neurons in the hidden layer. The weights and bias of ANN for CA of
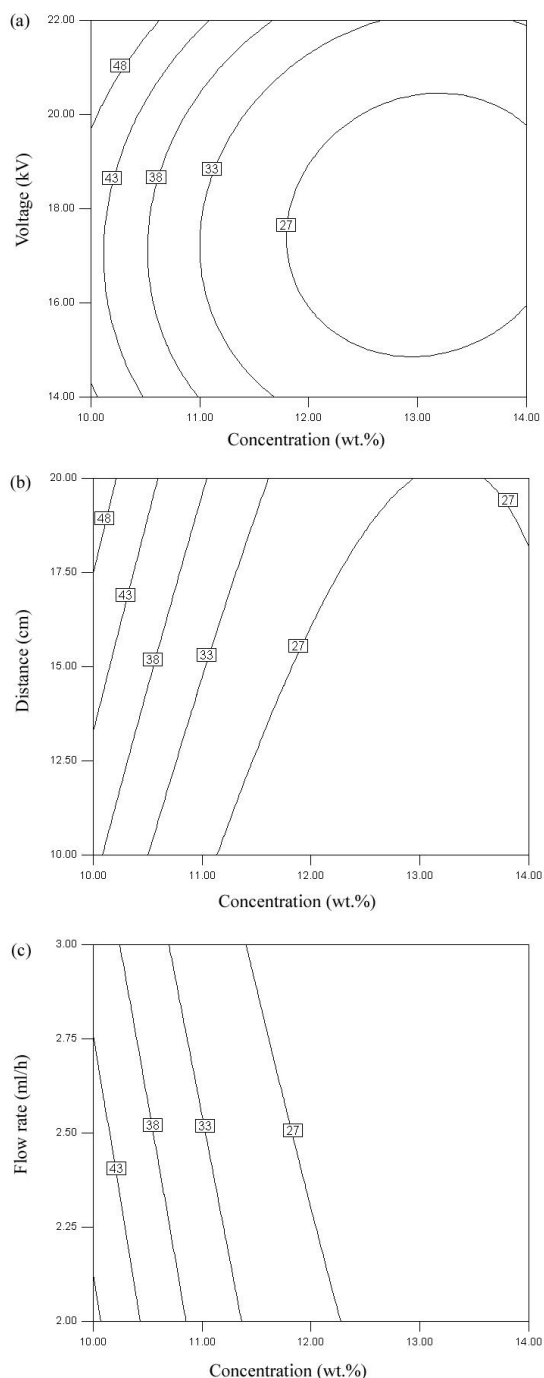
Fig. 5. Contour plots for contact angle of electrospun fiber mat showing the effect of: (a) solution concentration and applied voltage, (b) solution concentration and spinning distance, (c) solution concentration and volume flow rate.

electrospun fiber mat are given in Table 4. The R^2 and mean absolute percentage error were 0.965 and 5.94% respectively, which indicates that the model was shows good fitting with experimental data.

3.3. Effects of significant parameters on response

The morphology and structure of electrospun fiber mat, such as the nanoscale fibers and

interfibrillar distance, increases the surface roughness as well as the fraction of contact area of droplet with the air trapped between fibers. It is proved that the CA decrease with increasing the fiber diameter [26], therefore the thinner fibers, due to their high surface roughness, have higher CA than the thicker fibers. Hence, we used this fact for comparing CA of electrospun fiber mat. The interaction contour plot for CA of electrospun PAN fiber mat are shown in Figure 5.

As mentioned in the literature, a minimum solution concentration is required to obtain uniform fibers from electrospinning. Below this concentration, polymer chain entanglements are insufficient and a mixture of beads and fibers is obtained. On the other hand, the higher solution concentration would have more polymer chain entanglements and less chain mobility. This causes the hard jet extension and disruption during electrospinning process and producing thicker fibers [27]. Figure 5 (a) show the effect of solution concentration and applied voltage at middle level of distance (15 cm) and flow rate (2.5 ml/h) on CA of electrospun fiber mat. It is obvious that at any given voltage, the CA of electrospun fiber mat decrease with increasing the solution concentration.

Figure 5 (b) shows the response contour plot of interaction between solution concentration and spinning distance at fixed voltage (18 kV) and flow rate (2.5 ml/h). Increasing the spinning distance causes the CA of electrospun fiber mat to increase. Because of the longer spinning distance could give more time for the solvent to evaporate, increasing the spinning distance will decrease the nanofiber diameter and increase the CA of electrospun fiber mat [28,29]. As demonstrated in Figure 5 (b), low solution concentration cause the increase in CA of electrospun fiber mat at large spinning distance.

The response contour plot in Figure 5 (c) represented the CA of electrospun fiber mat at different solution concentration and volume flow rate. Ideally, the volume flow rate must be compatible with the amount of solution removed from the tip of the needle. At low volume flow rates, solvent would have sufficient time to evaporate and thinner fibers were produced, but at high volume flow rate, excess amount of solution fed to the tip of needle and thicker fibers were resulted [28-30]. Therefore the CA of electrospun fiber mat will be decreased.

As shown by Equation (4), the relative importance (RI) of the various input variables on the output variable can be determined using ANN weight matrix [31].

174

$$RI_j = \frac{\sum_{m=1}^{N_h}((|IW_{jm}|/\sum_{k=1}^{N_i}|IW_{km}|)\times|LW_{mn}|)}{\sum_{k=1}^{N_i}\left\{\sum_{m=1}^{N_h}((|IW_{km}|/\sum_{k=1}^{N_i}|IW_{km}|)\times|LW_{mn}|)\right\}}\times100 \quad (4)$$

where RI_j is the relative importance of the jth input variable on the output variable, N_i and N_h are the number of input variables and neurons in hidden layer, respectively ($N_i =4$, $N_h =4$ in this study), IW and LW are the connection weights, and subscript "n" refer to output response (n=1) [31]. The relative importance of electrospinning parameters on the value of CA calculated by Equation (4) and is shown in Figure 6. It can be seen seen that, all of
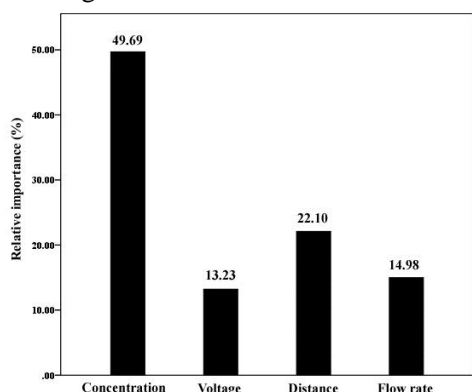

Fig. 6. Relative importance of electrospinning parameters on the CA of electrospun fiber mat.

the input variables have considerable effects on the CA of electrospun fiber mat. Nevertheless, the solution concentration with relative importance of 49.69% is found to be most important factor affecting the CA of electrospun nanofibers. These results are in close agreement with those obtained with RSM.

3.4. Optimizing the CA of electrospun fiber mat

The optimal values of the electrospinning parameters were established from the quadratic form of the RSM. Independent variables (solution

concentration, applied voltage, spinning distance, and volume flow rate) were set in range and dependent variable (CA) was fixed at minimum. The optimal conditions in the tested range for minimum CA of electrospun fiber mat are shown in Table 5. This optimum condition was a predicted value, thus to confirm the predictive ability of the RSM model for response, a further electrospinning and CA measurement was carried out according to the optimized conditions and the agreement between predicted and measured responses was verified. Figure 7 shows the SEM, average fiber diameter distribution and corresponding CA image of electrospun fiber mat prepared at optimized conditions.

3.5. Comparison between RSM and ANN model

Table 6 gives the experimental and predicted values for the CA of electrospun fiber mat obtained from RSM as well as ANN model. It is demonstrated that both models performed well and a good determination coefficient was obtained for both RSM and ANN. However, the ANN model shows higher determination coefficient ($R^2=0.965$) than the RSM model ($R^2=0.958$). Moreover, the absolute percentage error in the ANN prediction of CA was found to be around 5.94%, while for the RSM model, it was around 7.83%. Therefore, it can be suggested that the ANN model shows more accurately result than the RSM model. The plot of actual and predicted CA of electrospun fiber mat for RSM and ANN is shown in Figure 8.

4. CONCLUSIONS

The morphology and properties of electrospun nanofibers depends on many processing parameters. In this work, the effects of four electrospinning parameters namely; solution

Table 5. Optimum values of the process parameters for minimum CA of electrospun fiber mat

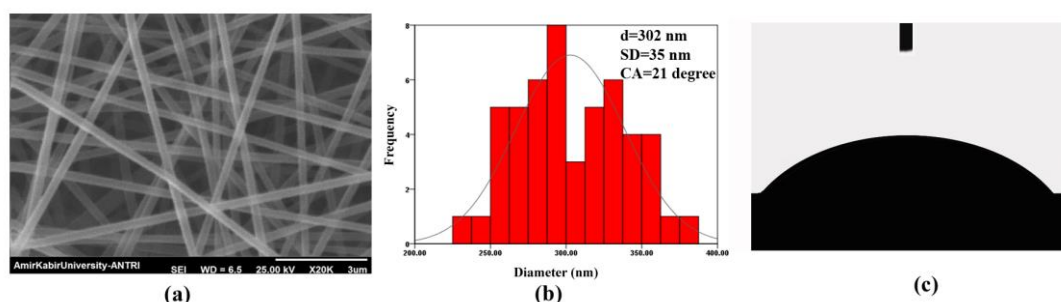| Solution concentration (wt.%)	Applied voltage (kV)	Spinning distance (cm)	Volume flow rate (ml/h)	Predicted CA (°)	Observed CA (°)
13.2	16.5	10.6	2.5	20	21

Fig. 7. (a) SEM image, (b) fiber diameter distribution, and (c) CA of electrospun fiber mat prepared at optimized conditions.

Table 6. Experimental and predicted values by RSM and ANN models

| No.	Experimental	Predicted		Absolute error (%)	
		RSM	ANN	RSM	ANN
1	44	47	48	6.41	9.97
2	54	54	54	0.78	0.46
3	61	59	61	3.70	0.42
4	65	66	61	2.06	6.06
5	38	39	38	2.37	0.54
6	49	47	49	5.10	0.68
7	51	51	51	0.35	0.45
8	56	58	56	4.32	0.17
9	48	45	60	6.17	24.37
10	30	31	27	4.93	9.35
11	35	36	31	2.34	11.15
12	22	22	21	1.18	4.15
13	30	30	32	1.33	6.04
14	33	28	33	13.94	0.60
15	25	24	25	5.04	0.87
16	26	26	26	0.27	1.33
17	29	26	26	10.10	9.16
18	28	26	26	6.89	5.91
19	25	26	26	4.28	5.38
20	24	26	26	8.63	9.77
21	21	26	26	24.14	25.45
22	31	30	31	2.26	0.57
23	35	31	35	10.34	0.66
24	33	36	32	8.18	2.18
25	37	37	37	0.59	0.34
26	19	29	21	52.11	10.23
27	28	30	30	7.07	8.20
28	39	34	31	12.05	21.30
29	36	35	36	1.72	0.04
30	20	25	20	26.30	2.27
R^2		0.958	0.965		
Mean absolute error (%)				7.83	5.94
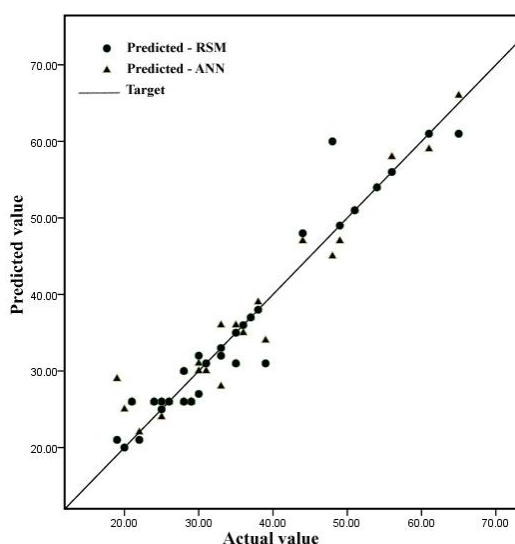
Fig. 8. Comparison between the actual and predicted contact angle of electrospun nanofiber for RSM and ANN model

concentration (wt.%), applied voltage (kV), tip to collector distance (cm), and volume flow rate (ml/h) on CA of PAN nanofiber mat were investigated using two different quantitative models, comprising RSM and ANN. The RSM model confirmed that solution concentration was the most significant parameter in the CA of electrospun fiber mat. Comparison of predicted CA using RSM and ANN were also studied. The obtained results indicated that both RSM and ANN model shows a very good relationship between the experimental and predicted CA values. The ANN model shows higher determination coefficient (R^2=0.965) than the RSM model. Moreover, the absolute percentage error of prediction for the ANN model was much lower than that for RSM model, indicating that ANN model had higher modeling performance than RSM model. The minimum CA of electrospun fiber mat estimated by RSM equation obtained at conditions of 13.2 wt.% solution concentration, 16.5 kV of the applied voltage, 10.6 cm of tip to collector distance, and 2.5 ml/h of volume flow rate.

REFERENCES

1. M. Miwa, A. Nakajima, A. Fujishima, K. Hashimoto, T. Watanabe, *Langmuir,* **16**, 5754 (2000).
2. D. Öner, T. J. McCarthy, *Langmuir,* 16, 7777 (2000).
3. M. E. Abdelsalam, P. N. Bartlett, T. Kelf, J. Baumberg, *Langmuir,* **21**, 1753 (2005).
4. A. Nakajima, K. Hashimoto, T. Watanabe, K. Takai, G. Yamauchi, A. Fujishima, *Langmuir,* **16**, 7044 (2000).
5. W. Zhong, S. Liu, X. Chen, Y. Wang, W. Yang, *Macromolecules,* **39**, 3224 (2006).
6. A. Shams Nateri, M. Hasanzadeh, *J. Comput. Theor. Nanosci.,* **6**, 1542 (2009).
7. A. Kilic, F. Oruc, A. Demir, *Text. Res. J.,* **78**, 532 (2008).
8. D. H. Reneker, I. Chun, *Nanotechnology* **7**, 216 (1996).
9. Y. M. Shin, M. M. Hohman, M. P. Brenner, G. C. Rutledge, *Polymer,* **42**, 9955 (2001).
10. D. H. Reneker, A. L. Yarin, H. Fong, S. Koombhongse, *J. Appl. Phys.,* **87**, 4531 (2000).
11. S. Zhang, W. S. Shim, J. Kim, *Mater. Design,* **30**, 3659 (2009).
12. O. S. Yördem, M. Papila, Y. Z. Menceloğlu, *Mater. Design,* **29**, 34 (2008).
13. I. S. Chronakis, *J. Mater. Process. Tech.,* **167**, 283 (2005).
14. F. Dotti, A. Varesano, A. Montarsolo, A. Aluigi, C. Tonin, G. Mazzuchetti, *J. Ind. Text.,* **37**, 151 (2007).
15. Y. Lu, H. Jiang, K. Tu, L. Wang, *Acta Biomater.,* **5**, 1562 (2009).
16. H. Lu, W. Chen, Y. Xing, D. Ying, B. Jiang, *J. Bioact. Compat. Pol.,* **24**,158 (2009).
17. D. R. Nisbet, J. S. Forsythe, W. Shen, D. I. Finkelstein, M. K. Horne, *J. Biomater. Appl.,* **24**, 7 (2009).
18. Z. Ma, M. Kotaki, R. Inai, S. Ramakrishna, *Tissue Eng.,* **11**, 101 (2005).
19. K. H. Hong, *Polym. Eng. Sci*., **47**, 43 (2007).
20. W. Zhang, P. N. Pintauro, *ChemSusChem.*, **4**, 1753 (2011).
21. S. Lee, S. K. Obendorf, *Text. Res. J.,* **77**, 696 (2007).
22. R.H. Myers, D.C. Montgomery, C.M. Anderson-cook, *Response surface methodology: process and product optimization using designed experiments,* 3rd ed., John Wiley and Sons, USA (2009).
23. S. Y. Gu, J. Ren, G. J. Vancso, *Eur. Polym. J.,* **41**, 2559 (2005).
24. V.R.G. Dev, J.R. Venugopal, M. Senthilkumar, D. Gupta, S. Ramakrishna, *J. Appl. Polym. Sci.,* **113**, 3397 (2009).
25. A.L. Galushkin, *Neural networks Theory*, Springer, Moscow Institute of Physics & Technology (2007).
26. M. Ma, Y. Mao, M. Gupta, K. K. Gleason, C. Rutledge, *Macromolecules,* **38**, 9742 (2005).
27. A. K. Haghi, M. Akbari, *Phys. Status. Solidi. A.,* **204**, 1830 (2007).
28. M. Ziabari, V. Mottaghitalab, A. K. Haghi, in *Nanofibers: Fabrication, Performance, and Applications,* W. N. Chang, Nova Science Publishers, USA (2009).
29. S. Ramakrishna, K. Fujihara, W. E. Teo, T. C. Lim, Z. Ma, *An Introduction to Electrospinning and Nanofibers*, World Scientific Publishing, Singapore (2005).
30. S. Zhang, W. S. Shim, J. Kim, *Mater. Design,* **30**, 3659 (2009).
31. M.B. Kasiri, H. Aleboyeh, A. Aleboyeh, *Environ. Sci. Technol.,* **42**, 7970 (2008).

ОТНОСНО КОНТАКТИЯ ЪГЪЛ С ПОДЛОЖКАТА НА ЕЛЕКТРОПРЕДЕНИ ВЛАКНА ОТ ПОЛИАКРИЛОНИТРИЛ

Б. Хадави Могадам, М. Хасанзаде, А. К. Хаги

¹ Департамент по текстилно инженерство, Технологичен университет Амиркабир, Техеран, Иран
² Департамент по текстилно инженерство, Университет в Гилан, Ращ, Иран

(Резюме)

Изследван е ефектът на четири параметъра на електропредето: концентрация на разтвора, приложено напрежение, разстояние между дюзата и приемника и обемния дебит върху контактния ъгъл (CA) с подложката на нановлакна от полиакрилонитрил. Приложени са методология на повърхността на отклика (RSM) и изкуствена невронна мрежа (ANN) за оптимизирането и предсказването на контактия ъгъл с подложката на електропредени влакна от полиакрилонитрил. Намерени са количествени зависимости между контактния ъгъл и работните параметри. Намерено е, че концентрацията на разтвора най-важния фактор за контактния ъгъл с подложката. Получените резултати показват, че и двата модела са много ефективни при оценяване на контактния ъгъл. По-точни са резултатите, получени с изкуствена невронна мрежа. При този модел коефициентът на корелация (R^2) и процентната грешка между действителния и предсказания отговор са съответно 0,965 и 1,97.

On the production optimization of polyacrylonitrile electrospun nanofiber

M. Hasanzadeh [1,2], B. Hadavi Moghadam [1], M. H. Moghadam Abatari [3], A. K. Haghi [4, *]

[1] *Department of Textile Engineering, Amirkabir University of Technology, Tehran, Iran*
[2] *Department of Chemical Engineering, Imam Hossein Comprehensive University, Tehran, Iran*
[3] *Department of Mathematics, Faculty of Mathematical Sciences, University of Guilan, Rasht, Iran*
[4] *Department of Textile Engineering, University of Guilan, Rasht, Iran*

Response surface methodology (RSM) based on central composite design (CCD) was employed to model and optimize the electrospinning parameters such as solution concentration (wt.%), applied voltage (kV), tip to collector distance (cm), and volume flow rate (ml/h), that have important effects on average fiber diameter (AFD) and contact angle (CA) of nanofiber mat. It is observed that polymer solution played an important role to the AFD and CA of nanofibers. Analysis of variance (ANOVA) showed a high determination coefficient (R^2) value of 0.9640 and 0.9683 for AFD and CA respectively, which indicated that the both models have a good agreement with experimental data. According to model optimization of the process, the minimum CA of electrospun fiber mat is given by following conditions: 13.2 wt.% solution concentration, 16.5 kV of the applied voltage, 10.6 cm of tip to collector distance, and 2.5 ml/h of volume flow rate.

1. INTRODUCTION

Recently, it was demonstrated that electrospinning can produce superfine fiber ranging from micrometer to nanometer using an electric field force. In the electrospinning process, a strong electric field is applied between polymer solution contained in a syringe with a capillary tip and grounded collector. When the electric field overcomes the surface tension force, the charged polymer solution forms a liquid jet and travels towards collection plate. As the jet travels through the air, the solvent evaporates and dry fibers deposits on the surface of a collector [1-4].

The electrospun nanofibers have high specific surface area, high porosity, and small pore size. Therefore, they have been suggested as excellent candidate for many applications including filtration, multifunctional membranes, tissue engineering, protective clothing, reinforced composites, and hydrogen storage [5,6].

Studies have shown that the morphology and the properties of the electrospun nanofibers depend on many parameters including polymer solution properties (the concentration, liquid viscosity, surface tension, and dielectric properties of the polymer solution), processing parameters (applied voltage, volume flow rate, tip to collector distance, and the strength of the applied electric field), and

ambient conditions (temperature, atmospheric pressure and humidity) [5-8].

Response surface methodology (RSM) is a combination of mathematical and statistical techniques used to evaluate the relationship between a set of controllable experimental factors and observed results. This optimization process is used in situations where several input variables influence some output variables of the system. The main goal of RSM is to optimize the response, which is influenced by several independent variables, with minimum number of experiments [9,10]. Therefore, the application of RSM in electrospinning process will be helpful in effort to find and optimize the electrospun nanofibers properties.

In this paper, a study has been conducted to investigate the relationship between four electrospinning parameters (solution concentration, applied voltage, tip to collector distance, and volume flow rate) and electrospun PAN nanofiber mat properties such as average fiber diameter (AFD) and contact angle (CA). and combined effects of above parameters. Then, these independent parameters were fed as inputs to an ANN while the output of the network was the CA of electrospun fiber mat. Finally, the importance of each electrospinning parameters on the variation of CA of electrospun fiber mat was determined and comparison of predicted CA value using RSM and ANN are discussed.

---

* To whom all correspondence should be sent:
E-mail: Haghi@Guilan.ac.ir

2. EXPERIMENTAL

2.1. Materials

Polyacrylonirile (PAN, M_w=100,000) was purchased from Polyacryle Co. (Iran) and *N-N*, dimethylformamide (DMF) was obtained from Merck Co. (Germany).

The polymer solutions with different concentration ranged from 10 wt.% to 14 wt.% were prepared by dissolving PAN powder in DMF and was stirred for 24 h at 50°C. These polymer solutions were used for electrospinning.

2.2. Electrospinning

A schematic of the electrospinning apparatus is shown in Figure 1. A polymer solution was loaded in a 5 mL syringe connected to a syringe pump. The tip of the syringe was connected to a high voltage power supply (capable to produce 0-40 kV). Under high voltage, a fluid jet was ejected from the tip of the needle and accelerated toward the grounded collector (aluminum foil). All electrospinnings were carried out at room temperature.
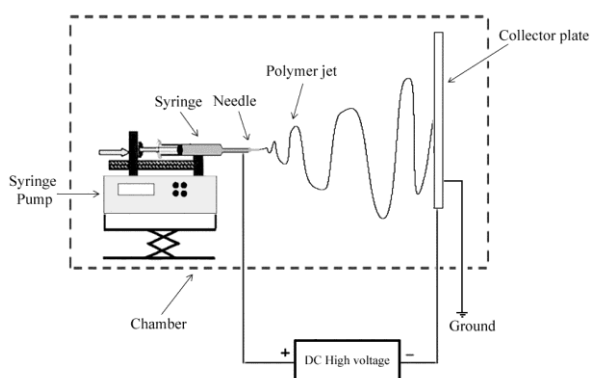

Fig. 1. Schematic of electrospinning set up.

2.3. Measurement and characterization

The electrospun nanofibers were sputter-coated with gold and their morphology was examined with a scanning electron microscope (SEM, Philips XL-30). Average diameter of electrospun nanofibers was determined from selected SEM image by measuring at least 50 random fibers using Image J software.

The wettability of electrospun fiber mat was determined by water contact angle measurement. Contact angles were measured by specially arranged microscope equipped with camera and PCTV vision software as shown in Figure 2. The

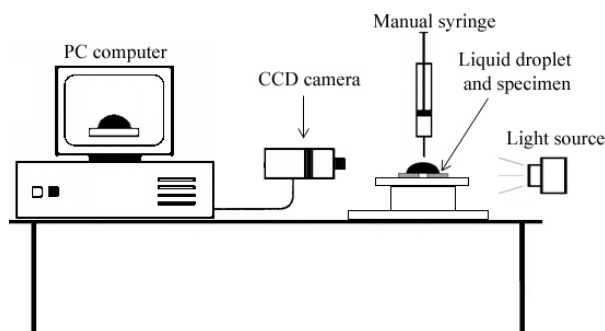volume of the distilled water for each measurement was kept at 1 μl.

Fig. 2. Schematic of contact angle measurement set up.

2.4. Experimental design by RSM

In this study, the effect of four electrospinning parameters on two responses, comprising the AFD and the CA of electrospun fiber mat, was evaluated using central composite design (CCD). The experiment was performed for at least three levels of each factor to fit a quadratic model. Polymer solution concentration (X_1), applied voltage (X_2), tip to collector distance (X_3), and volume flow rate (X_4) were chosen as independent variables and the AFD and the CA of electrospun fiber mat as dependent variables (responses). The experimental parameters and their levels are given in Table 1.

Table 1. Design of experiment (factors and levels).

Factor	Variable	Unit	Factor level		
			-1	0	1
X_1	Solution concentration	(wt.%)	10	12	14
X_2	Applied voltage	(kV)	14	18	22
X_3	Tip to collector distance	(cm)	10	15	20
X_4	Volume flow rate	(ml/h)	2	2.5	3

A quadratic model, which also includes the linear model, is given below:

$$Y = \beta_0 + \sum_{i=1}^{4}\beta_i x_i + \sum_{i=1}^{4}\beta_{ii} x_i^2 + \sum_{i=1}^{3}\sum_{j=2}^{4}\beta_{ij} x_i x_j \quad (1)$$

where, Y is the predicted response, x_i and x_j are the independent variables, β_0 is a constant, β_i is the linear coefficients, β_{ii} is the squared coefficients and β_{ij} is the second-order interaction coefficients [9,10].

The statistical analysis of experimental data was performed using Design-Expert software (Version 8.0.3, Stat-Ease, Minneapolis, MN, 2010) including analysis of variance (ANOVA). A design of 30 experiments for independent variables and responses for AFD and CA are listed in Table 2.

Table 2. The actual design of experiments and responses for AFD and CA.

No.	Electrospinning parameters				Responses	
	X_1	X_2	X_3	X_4	AFD (nm)	CA (°)
	Concentration	Voltage	Distance	Flow rate		
1	10	14	10	2	206±33	44±6
2	10	22	10	2	187±50	54±7
3	10	14	20	2	162±25	61±6
4	10	22	20	2	164±51	65±4
5	10	14	10	3	225±41	38±5
6	10	22	10	3	196±53	49±4
7	10	14	20	3	181±43	51±5
8	10	22	20	3	170±50	56±5
9	10	18	15	2.5	188±49	48±3
10	12	14	15	2.5	210±31	30±3
11	12	22	15	2.5	184±47	35±5
12	12	18	10	2.5	214±38	22±3
13	12	18	20	2.5	205±31	30±4
14	12	18	15	2	195±47	33±4
15	12	18	15	3	221±23	25±3
16	12	18	15	2.5	199±50	26±4
17	12	18	15	2.5	205±31	29±3
18	12	18	15	2.5	225±38	28±5
19	12	18	15	2.5	221±23	25±4
20	12	18	15	2.5	215±35	24±3
21	12	18	15	2.5	218±30	21±3
22	14	14	10	2	255±38	31±4
23	14	22	10	2	213±37	35±5
24	14	14	20	2	240±33	33±6
25	14	22	20	2	200±30	37±4
26	14	14	10	3	303±36	19±3
27	14	22	10	3	256±40	28±3
28	14	14	20	3	283±48	39±5
29	14	22	20	3	220±41	36±4
30	14	18	15	2.5	270±43	20±3

.

3. RESULTS AND DISCUSSION

3.1. Morphological analysis of nanofibers

PAN solution in DMF were electrospun under different conditions, including various PAN solution concentrations, applied voltages, volume flow rates and tip to collector distances, to study the effect of electrospinning parameters on the morphology and properties of electrospun nanofibers.

Figure 3 shows the SEM images and fiber diameter distributions of electrospun fibers in different solution concentration as one of the most effective parameters to control the fiber morphology. As observed in Figure 3, the AFD increased with increasing solution concentration. It was suggested that the higher solution concentration would have more polymer chain entanglements and less chain mobility. This causes the hard jet extension and disruption during electrospinning process and producing thicker fibers.
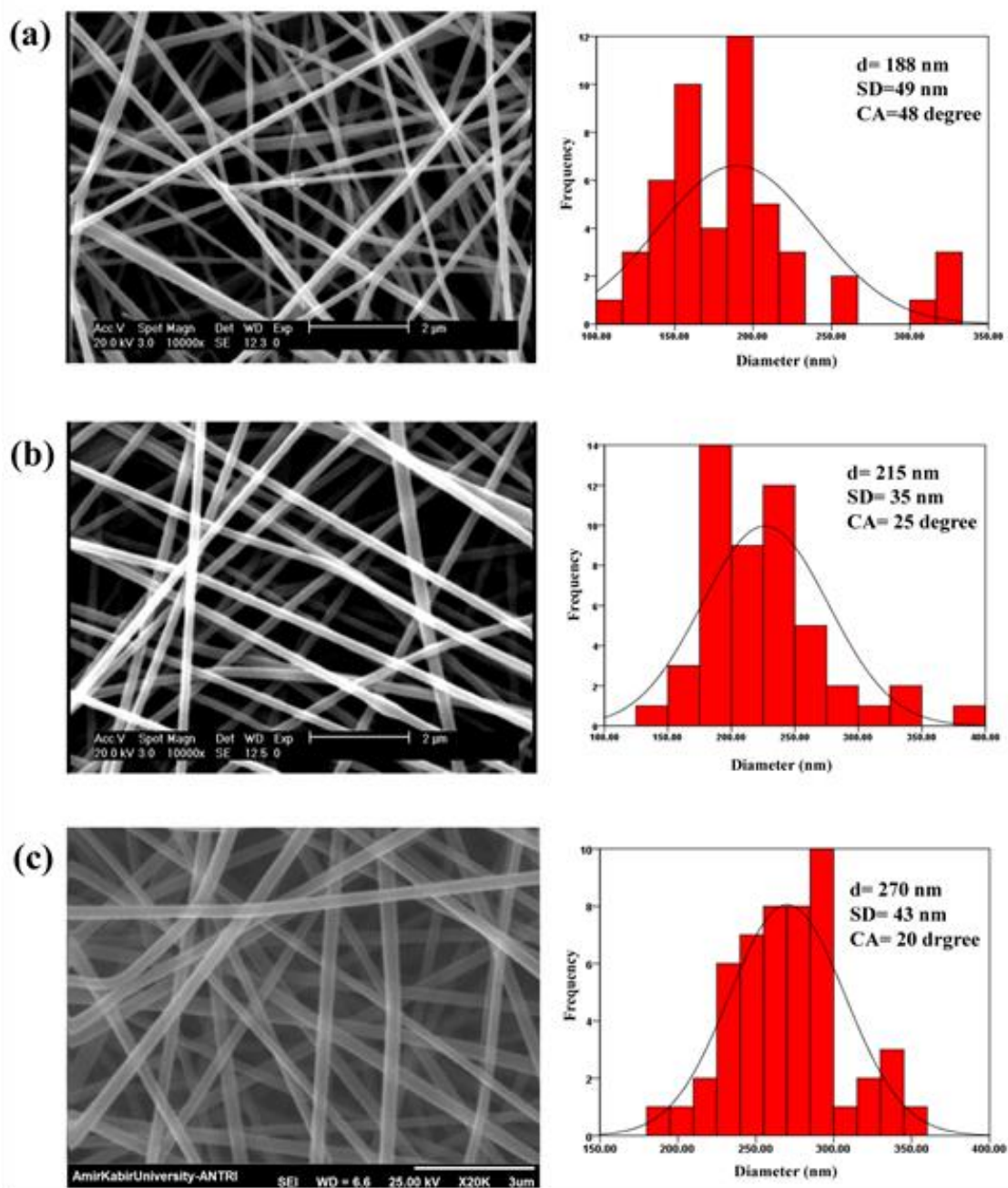
Fig. 3. The SEM images and fiber diameter distributions of electrospun fibers in solution concentration of (a) 10 wt.%, (b) 12 wt.% and (c) 14 wt.%.

The SEM image and corresponding fiber diameter distribution of electrospun nanofiber in different applied voltage are shown in Figure 4. It is obvious that increasing the applied voltage cause an increase followed by a decrease in electrospun fiber diameter. As demonstrated by previous researchers [7,8], increasing the applied voltage may decrease, increase or may not change the fiber diameter. In one hand, increasing the applied voltage will increase the electric field strength and higher electrostatic repulsive force on the jet, favoring the thinner fiber formation. On the other hand, more surface charge will introduce on the jet and the solution will be removed more quickly from the tip of needle. As a result, the AFD will be increased [8,11].
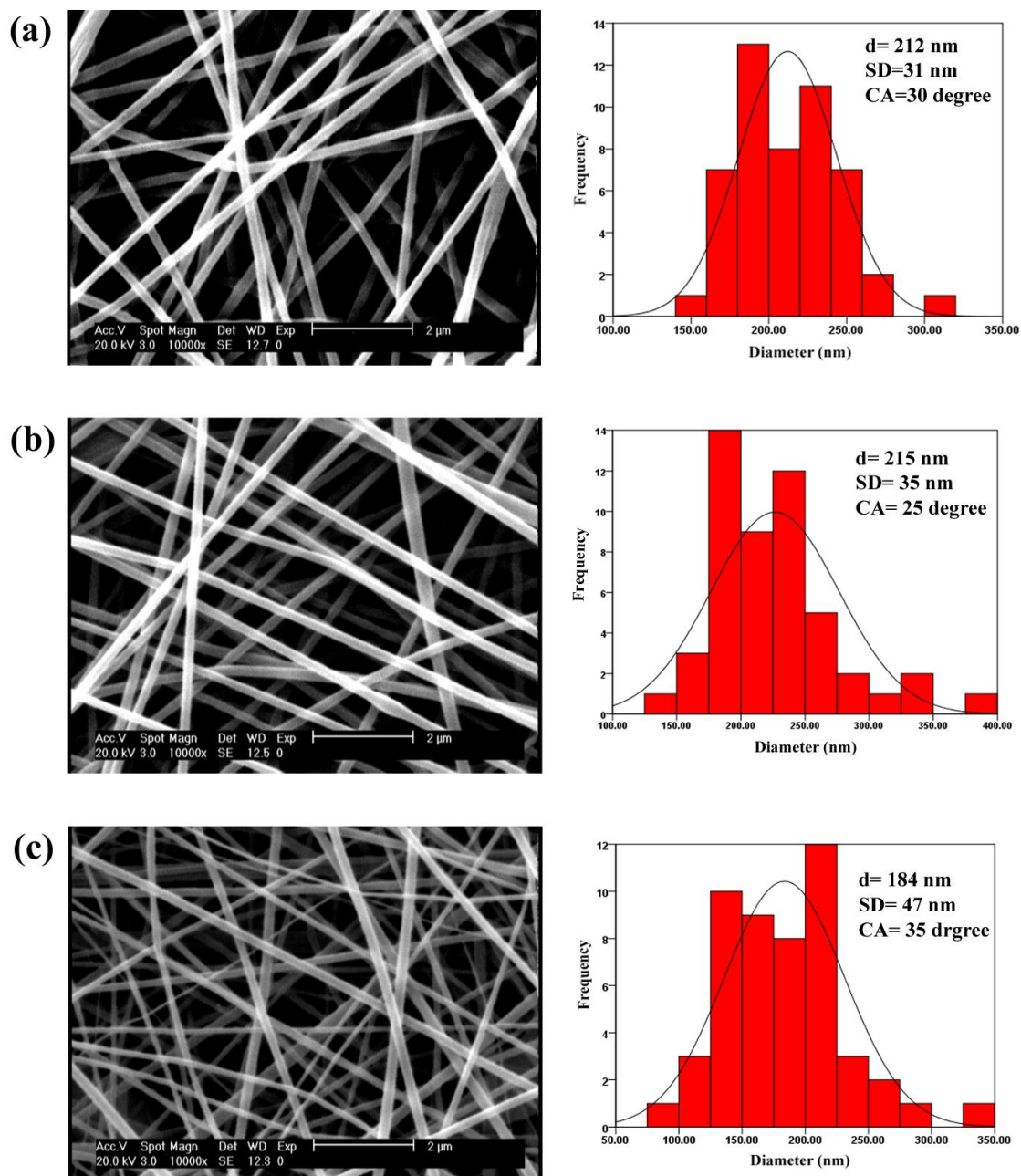
Fig. 4. The SEM images and fiber diameter distributions of electrospun fibers in applied voltage of (a) 14 kV, (b) 18 kV and (c) 22 kV.

Figure 5 represents the SEM image and fiber diameter distribution of electrospun nanofiber in different spinning distance. It can be seen that the AFD decreased with increasing tip to collector distance. Because of the longer spinning distance could give more time for the solvent to evaporate, increasing the spinning distance will decrease fiber diameter [3,8].
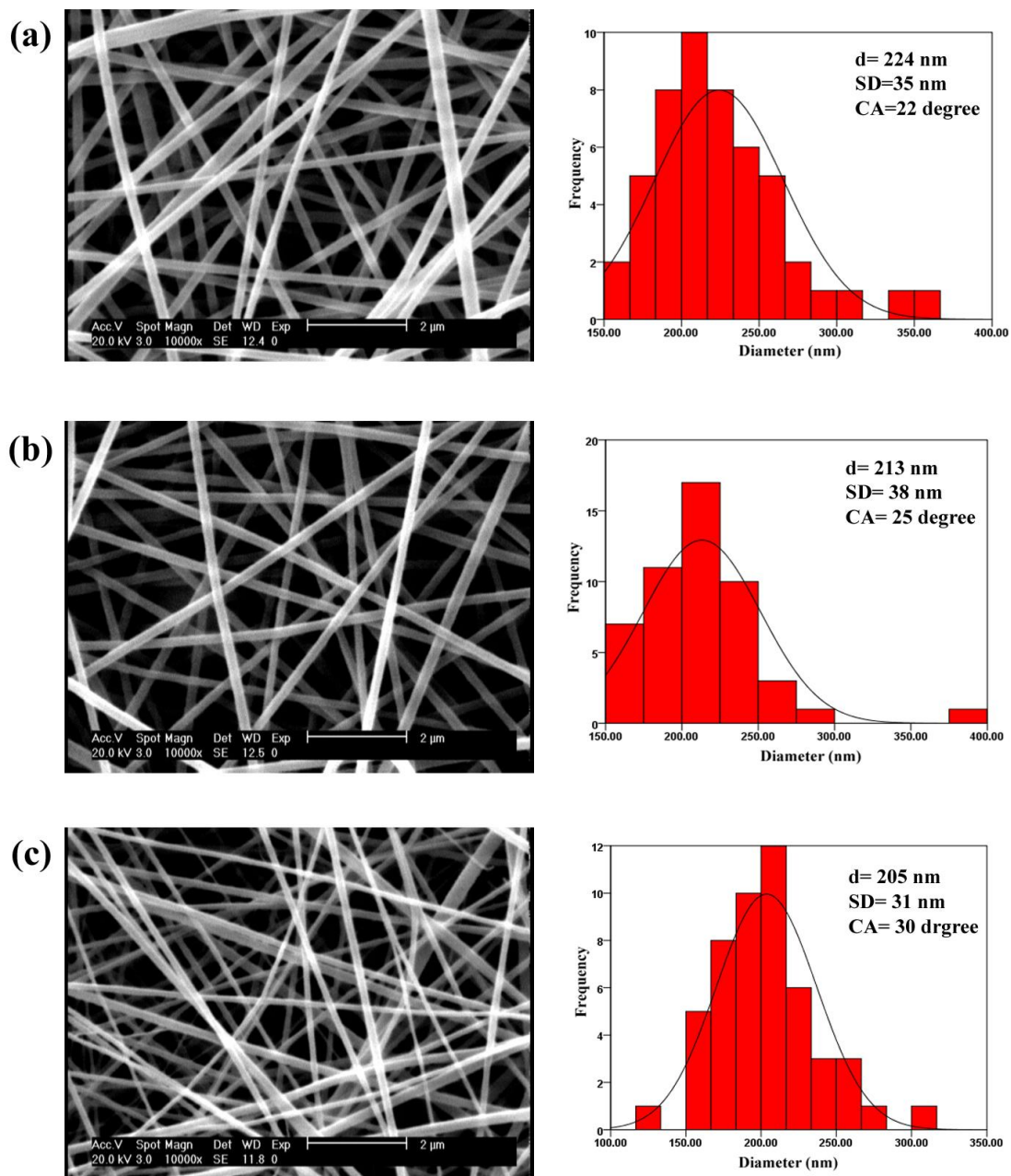

Fig. 5. The SEM images and fiber diameter distributions of electrospun fibers in tip to collector distance of (a) 10 cm, (b) 15 cm and (c) 20 cm.

183

The SEM image and fiber diameter distribution of electrospun nanofiber in different volume flow rate are illustrated in Figure 6. It is clear that increasing the volume flow rate cause an increase in average fiber diameter. Ideally, the volume flow rate must be compatible with the amount of solution removed from the tip of the needle. At low volume flow rates, solvent would have sufficient time to evaporate and thinner fibers were produced, but at high volume flow rate, excess amount of solution fed to the tip of needle and thicker fibers result [3,12].
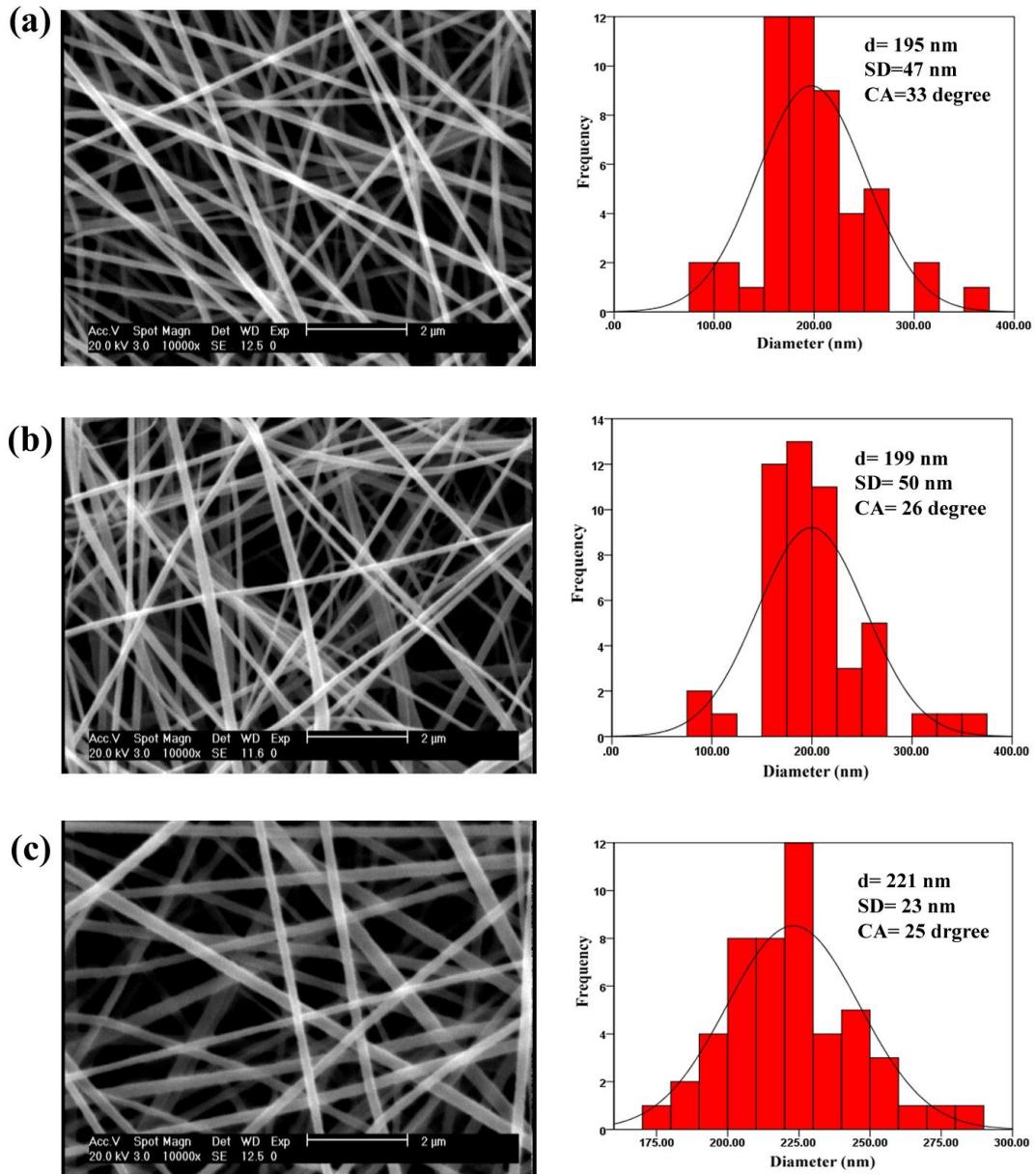
Fig. 6. The SEM images and fiber diameter distributions of electrospun fibers in volume flow rate of (a) 2 ml/h, (b) 2.5 ml/h and (c) 3 ml/h.

3.2. The analysis of variance (ANOVA)

The analysis of variance for AFD and CA of electrospun fibers has been summarized in Table 3 and Table 4 respectively, which indicated that the predictability of the models is at 95% confidence interval. Using 5% significance level, the factor is considered significant if the p-value is less than 0.05.

From the p-values presented in Table 3 and Table 4, it is obvious that p-values of terms X_3^2, $X_4^2, X_2X_3, X_1X_3, X_2X_4$ and X_3X_4 in the model of AFD and X_3^2, X_4^2, X_2X_3, X_2X_4 and X_3X_4 in the model of CA were not significant (p>0.05).

The approximating function for AFD and CA of electrospun fiber obtained from Equation 2 and 3 respectively.

$$AFD = 211.89 + 31.71X_1 - 15.28X_2 - 12.78X_3 + 12.94X_4 - 8.44X_1X_2 + 6.31X_1X_4 + 18.15X_1^2 - 13.85X_2^2 \quad (2)$$

$$CA = 26.07 - 9.89 X_1 - 2.17 X_2 + 4.33 X_3 \\ 2.33X_4 - 1.63X_1X_2 - 1.63X_1X_3 + 1.63X_1X_4 + 9.08X_1^2 + 7.58X_2^2 \quad (3)$$

Analysis of variance for AFD and CA showed that the models were significant (p<0.0001), which indicated that the both models have a good agreement with experimental data. The value of determination coefficient (R^2) for AFD and CA was evaluated as 0.9640 and 0.9683 respectively.

The predicted versus actual response plots of AFD and CA are shown in Figures 7 and 8 respectively. It can be observed that experimental values are in good agreement with the predicted values.

Table 3. Analysis of variance for average fiber diameter (AFD).

Source	SS	DF	MS	F-value	Probe > F	Remarks
Model	31004.72	14	2214.62	28.67	<0.0001	Significant
X_1-Concentration	17484.50	1	17484.50	226.34	<0.0001	Significant
X_2-Voltage	4201.39	1	4201.39	54.39	<0.0001	Significant
X_3-Distance	2938.89	1	2938.89	38.04	<0.0001	Significant
X_4-Flow rate	3016.06	1	3016.06	39.04	<0.0001	Significant
X_1X_2	1139.06	1	1139.06	14.75	0.0016	Significant
X_1X_3	175.56	1	175.56	2.27	0.1524	
X_1X_4	637.56	1	637.56	8.25	0.0116	Significant
X_2X_3	39.06	1	39.06	0.51	0.4879	
X_2X_4	162.56	1	162.56	2.10	0.1675	
X_3X_4	60.06	1	60.06	0.78	0.3918	
X_1^2	945.71	1	945.71	12.24	0.0032	Significant
X_2^2	430.80	1	430.80	5.58	0.0322	Significant
X_3^2	0.40	1	0.40	0.0052	0.9433	
X_4^2	9.30	1	9.30	0.12	0.7334	
Residual	1158.75	15	77.25			
Lack of Fit	711.41	10	71.14	0.80	0.6468	

Table 4. Analysis of variance for contact angle (CA) of electrospun fiber mat.

Source	SS	DF	MS	F-value	Probe > F	Remarks
Model	4175.07	14	298.22	32.70	<0.0001	Significant
X_1-Concentration	1760.22	1	1760.22	193.01	<0.0001	Significant
X_2-Voltage	84.50	1	84.50	9.27	0.0082	Significant
X_3-Distance	338.00	1	338.00	37.06	<0.0001	Significant
X_4-Flow rate	98.00	1	98.00	10.75	0.0051	Significant
X_1X_2	42.25	1	42.25	4.63	0.0481	Significant
X_1X_3	42.25	1	42.25	4.63	0.0481	Significant
X_1X_4	42.25	1	42.25	4.63	0.0481	Significant
X_2X_3	12.25	1	12.25	1.34	0.2646	
X_2X_4	6.25	1	6.25	0.69	0.4207	
X_3X_4	2.25	1	2.25	0.25	0.6266	
X_1^2	161.84	1	161.84	17.75	0.0008	Significant
X_2^2	106.24	1	106.24	11.65	0.0039	Significant
X_3^2	0.024	1	0.024	0.0026	0.9597	
X_4^2	21.84	1	21.84	2.40	0.1426	
Residual	136.80	15	9.12			
Lack of Fit	95.30	10	9.53	1.15	0.4668	
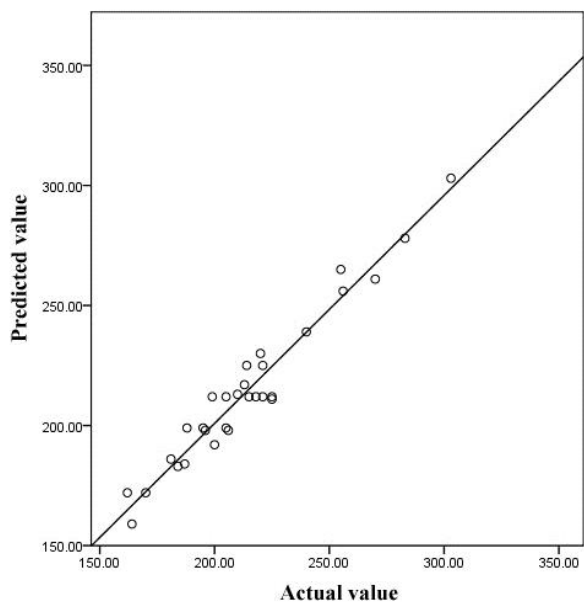
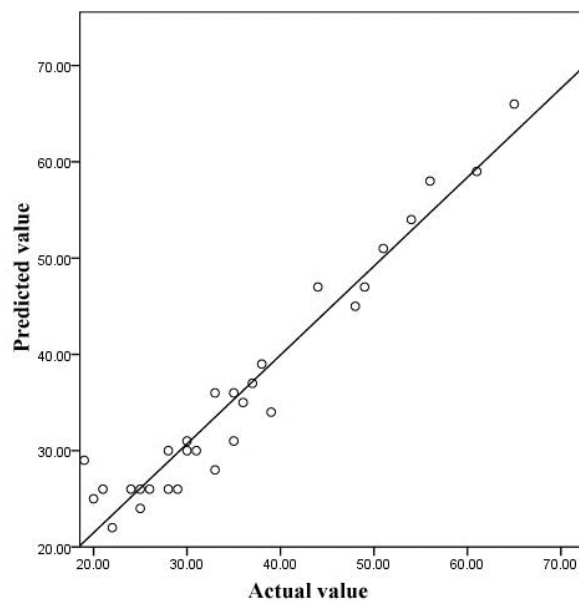**Fig. 7.** The predicted versus actual plot for AFD of electrospun fiber mat.

Fig. 8. The predicted versus actual plot for CA of electrospun fiber mat.

3.3. Effects of significant parameters on AFD

The response surface and contour plots in Figure 9 (a) indicated that there was a considerable interaction between solution concentration and applied voltage at middle level of spinning distance (15 cm) and flow rate (2.5 ml/h). It can be seen an increase in AFD with increase in solution concentration at any given voltage that is in agreement with previous observations [11,12]. Generally, a minimum solution concentration is required to obtain uniform fibers from electrospinning. Below this concentration, polymer chain entanglements are insufficient and a mixture of beads and fibers is obtained. On the other hand, the higher solution concentration would have more polymer chain entanglements and less chain mobility. This causes the hard jet extension and

disruption during electrospinning process and producing thicker fibers [7].

Figure 9 (b) shows the response surface and contour plots of interaction between solution concentration and flow rate at fixed voltage (18 kV) and spinning distance (15 cm). It can be seen that at fixed applied voltage and spinning distance, an increase in solution concentration and volume flow rate results in fiber with higher diameter. As mentioned in the literature, the volume flow rate must be compatible with the amount of solution removed from the tip of the needle. At low volume flow rates, solvent would have sufficient time to evaporate and thinner fibers were produced, but at high volume flow rate, excess amount of solution fed to the tip of needle and thicker fibers were resulted [3,8].
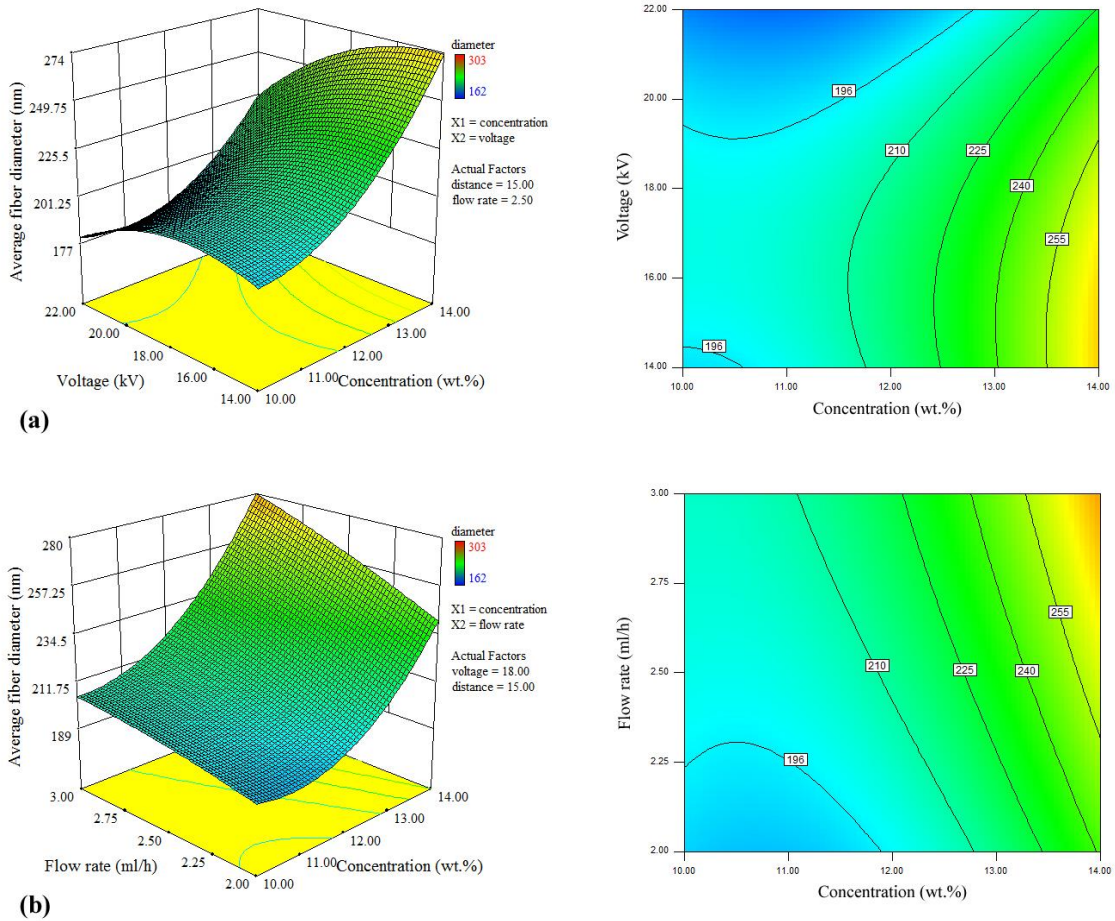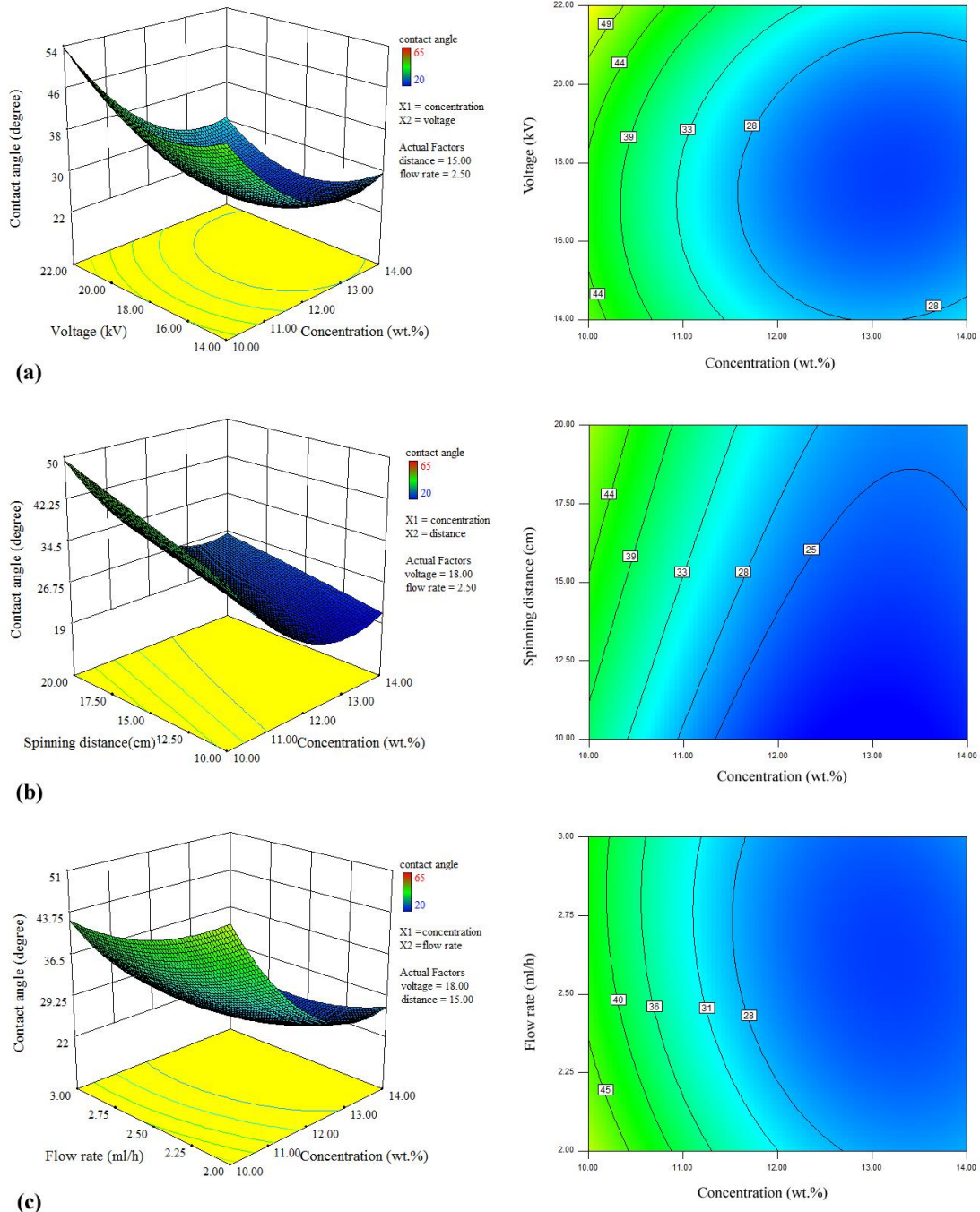

(a)

(b)

Fig. 9. Response surface and contour plots of AFD showing the effect of: (a) solution concentration and applied voltage, (b) solution concentration and volume flow rate.

3.4. Effects of significant parameters on CA

The response surface and contour plots in Figure 10 (a) represented the CA of electrospun fiber mat at different solution concentration and applied voltage. It is obvious that at fixed spinning distance

and volume flow rate, an increase in applied voltage and decrease in solution concentration result the higher CA. The tip to collector distance was found to be another important processing parameter as it influences the solvent evaporating rate and deposition time as well as electrostatic

field strength. The impact of spinning distance on CA of electrospun fiber mat is illustrated in Figure 10 (b). Increasing the spinning distance causes the CA of electrospun fiber mat to increase. As demonstrated in Figure 10 (b), low solution concentration cause an increase in CA of electrospun fiber mat at large spinning distance.

The response plots in Figure 10 (c) shows the interaction between solution concentration and volume flow rate at fixed applied voltage and spinning distance. It is obvious that at any given flow rate, CA of electrospun fiber mat will increase as solution concentration decreases.

(a)

(b)

(c)

Fig. 10. Response surface and contour plots of CA showing the effect of: (a) solution concentration and applied voltage, (b) solution concentration and spinning distance, (c) solution concentration and volume flow rate.

3.5. Determination of optimal conditions

It is well known that the value of CA for hydrophilic surfaces is less than 90º. Fabrication of these surfaces has attracted considerable interest for both fundamental research and practical studies. So, the goal of the present study is to minimize the CA of electrospun nanofibers. The optimal conditions of the electrospinning parameters were established from the quadratic form of the RSM. Independent variables namely, solution concentration, applied voltage, spinning distance, and volume flow rate were set in range and dependent variable (CA) was fixed at minimum. The optimal conditions in the tested range for minimum CA of electrospun fiber mat are shown in Table 5.

Table 5. Optimum values of the process parameters for minimum CA of electrospun fiber mat.

Parameter	Optimum value
Solution concentration (wt.%)	13.2
Applied voltage (kV)	16.5
Spinning distance (cm)	10.6

This optimum condition was a predicted value, thus to confirm the predictive ability of the RSM model for response, a further electrospinning was carried out according to the optimized conditions and the agreement between predicted and measured responses was verified. The measured CA of electrospun nanofiber mat (21º) was very close to the predicted value estimated to 20º. Figure 11 shows the SEM image and AFD distribution of electrospun fiber mat prepared at optimized conditions.

4. CONCLUSIONS

In this study, the effects of electrospinning parameters, comprising solution concentration (wt.%), applied voltage (kV), tip to collector distance (cm), and volume flow rate (ml/h) on average diameter and CA of electrospun PAN nanofibers were investigated by statistical approach. Response surface methodology (RSM) was successfully employed to model and optimize the electrospun nanofibers diameter and CA. The response surface and contour plots of the predicted AFD and CA indicated that the nanofiber diameter and its CA are very sensitive to solution concentration changes. It was concluded that the polymer solution concentration was the most significant factor impacting the AFD and CA of electrospun fiber mat. The R^2 value was 0.9640 and 0.9683 for AFD and CA respectively, which indicates a good fit of the models with experimental data. The optimum value of the solution concentration, applied voltage, spinning distance, and flow rate were found to be 13.2 wt.%, 16.5 kV, 10.6 cm and 2.5 ml/h, respectively, for minimum CA of electrospun fiber mat.
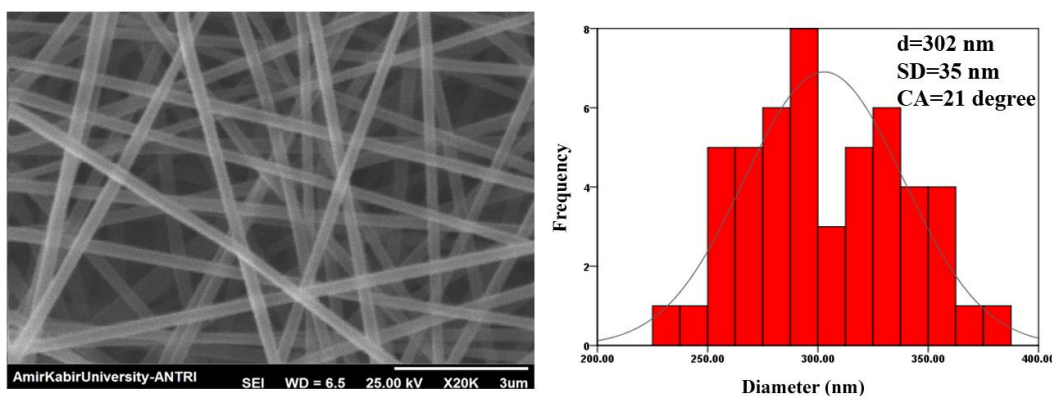

Fig. 11. SEM image and fiber diameter distribution of electrospun fiber mat prepared at optimized conditions.

REFERENCES

1. A. Shams Nateri and M. Hasanzadeh, *J. Comput. Theor. Nanosci.,* **6**, 1542 (2009).
2. A. Kilic, F. Oruc and A. Demir, *Text. Res. J.,* **78**, 532 (2008).
3. S. Ramakrishna, K. Fujihara, W. E. Teo, T. C. Lim, and Z. Ma, Editors, *An Introduction to Electrospinning and Nanofibers*, National University of Singapore, World Scientific Publishing, Singapore (2005).
4. P. J. Brown, K.Stevens, Editors, *Nanofibers and Nanotechnology in Textiles*, Woodhead Publishing, Cambridge, UK (2007).
5. Y. M. Shin, M. M. Hohman, M. P. Brenner and G. C. Rutledge, *Polymer,* **42**, 9955 (2001).
6. O. S. Yördem, M. Papila and Y. Z. Menceloğlu, *Mater. Design,* **29**, 34 (2008).
7. A. K. Haghi, and M. Akbari, *Phys. Status. Solidi. A.,* **204**, 1830 (2007).
8. M. Ziabari, V. Mottaghitalab, and A. K. Haghi, in *Nanofibers: Fabrication, Performance, and Applications*, Edited by W. N. Chang, Nova Science Publishers, USA (2009), pp. 153-182.
9. R. H. Myers, D. C. Montgomery, and C. M. Anderson-cook, Editors, *Response surface methodology: process and product optimization using designed experiments*, 3rd ed., John Wiley and Sons, USA (2009).
10. S. Y. Gu, J. Ren, G. J. Vancso, *Eur. Polym. J.,* **41**, 2559 (2005).
11. C. Zhang, X. Yuan, L. Wu, Y. Han, J. Sheng, *Eur. Polym. J.,* **41**, 423 (2005).
12. S. Zhang, W. S. Shim, J. Kim, *Mater. Design,* **30**, 3659 (2009).

ОТНОСНО ОПТИМИЗАЦИЯТА НА ПРОИЗВОДСТВОТО НА ЕЛЕКТРОПРЕДЕНИ НАНОВЛАКНА ОТ ПОЛИАКРИЛАМИД

М. Хасанзаде[1,2], Б. Хадави Могадам[1], М.Х. Могадам Абатари[3], А.К. Хаги[4]

[1] *Департамент по текстилно инженерство, Технологичен университет Амиркабир, Техеран, Иран*
[2] *Департамент по инженерна химия, Университет „Имам Хосейн", Техеран,Иран*
[3] *Департамент по математика, Факултет по математични науки, Университет в Гилан, Ращ, Иран*
[4] *Департамент по текстилно инженерство, Университет в Гилан, Ращ, Иран*

(Резюме)

Приложена е методология на повърхнината на отклика (RSM), основана на централно композиционен планиран експеримент за моделирането и оптимизацията на параметрите на електропредене – концентрация на разтворите (тегл. %), приложеното напрежение (kV), разстоянието от дюзата до приемника (см) и обемния дебит (ml/h), имащи важно значение за средния диаметър на влакната (AFD) и контактния ъгъл на с подложката (CA). Отбелязано е, че полимерните разтвори имат важна роля за AFD и за CA при нановлакната. Анализът на дисперсията показва висок коефициент на корелация от 0.9640 и съоъветно 0.9683 за AFD и CA, което показва че двата модела се съгласуват добре с опитните данни. Според моделирането на процеса минимален контактен ъгъл с подложката за електропредените влакна се наблюдава при следните условия: концентрация на разтвора - 13.2 тегл.%, приложено напрежение - 16.5 kV; разстояние от дюзата то приемника - , 10.6 cm и обемен дебит на потока - 2.5 ml/h.

Propene yield enhancement from metathesis of ethene and 2-butene on mixed HBeta-alumina supported molybdenum-based catalysts using aluminum nitrate as alumina precursor

B. Netiworaruksa[1], S. Phatanasri[1]*, P. Praserthdam[1], W. Phongsawat[1], K. Suriye[2]

[1] *Center of Excellence on Catalysis and Catalytic Reaction Engineering, Department of Chemical Engineering, Faculty of Engineering, Chulalongkorn University, Bangkok 10330, Thailand*
[2] *SCG Chemicals Co.,Ltd. 1Siam-cement Rd, Bang sue, Bangkok 10800, Thailand*

The mixed HBeta-alumina supported molybdenum-based catalysts with 4 wt% Mo loading were prepared by incipient wetness impregnation method. Aluminum nitrate and aluminum oxide were used as alumina precursors in mixing with HBeta zeolite followed by calcination at 550ºC. The catalyst using aluminum nitrate as alumina precursor, Mo/AN+Hß(550), markedly outperformed its counterpart using aluminum oxide as precursor, Mo/AO+Hß(550), in both 2–butene conversion and propene selectivity from metathesis of ethene and 2–butene. The relatively higher metal-support interaction, as well as the derivation of surface tetrahedral molybdenum oxide species were discernible on Mo/AN+Hß(550), as observed from H_2-TPR and UV-vis spectra, respectively. In addition, the higher acidity obtained on Mo/AN+Hß(550), presumably due to the better protection of HBeta zeolite structure achieved by the optimum compatibility between Al using aluminum nitrate as alumina precursor and HBeta, was believed to play a significant role for the enhancement of propene yield by metathesis of ethene and 2–butene.

Keywords: Aluminum nitrate; Molybdenum-based catalyst; Metathesis; Propene

INTRODUCTION

Metathesis reaction of ethene and 2-butene is an alternative way to produce propene, the demand of which is rapidly increasing on the worldwide market. In this way the C4 alkenes from the refineries and steam crackers can be upgraded [1–4]. The catalysts used for such reaction are mostly based on rhenium, molybdenum and tungsten [5]. Though rhenium-based catalysts supported on alumina or silica-alumina are the most interesting ones due to their high activity even at room temperature, the costs of rhenium compounds are high and catalysts with low rhenium loadings have only negligible activities [6]. Supported molybdenum oxide catalysts have received much attention, as they are widely used in petrochemical processes including metathesis of alkenes [6]. Liu *et al.* [6] have found that the supported Mo/HBeta catalysts show some activities for the olefin metathesis; however, the catalytic performance remarkably increases after addition of Al_2O_3. Moreover, they have reported that a molybdenum-based catalyst impregnated on HBeta-Al_2O_3(Mo/Hß–Al_2O_3) with an optimum Mo loading

of 4 wt% was the best catalyst for the metathesis of ethene and 2-butene to propene among the catalysts evaluated, namely, Mo/MgO, Mo/Al_2O_3, Mo/MCM-22, Mo/ZSM-35, Mo/silicate and 6Mo/SAPO-11 [5, 7]. The relatively poor metathesis activity of Mo/HBeta without Al_2O_3 was ascribed to the possible dealumination of framework Al in HBeta upon the high loading of Mo [8]. Though alumina addition into the composite support has been proposed to protect the framework of HBeta from being destroyed upon Mo loadings to a large extent due to the preferential migration of Mo species on the alumina surface [9, 10], the synergistic effect of alumina precursor on the metathesis activity has not yet been observed.

Therefore, this work aims at investigating the enhancement of propene production by metathesis of ethene and 2-butene on mixed HBeta-alumina supported molybdenum-based catalyst by adopting aluminum nitrate as a precursor for alumina. All catalysts were prepared by incipient wetness impregnation of 4 wt % of molybdenum on a mixed HBeta-alumina support. The catalyst characterization was conducted by employing techniques of BET surface area assessment, X-Ray diffraction, NH_3-TPD, UV-vis spectra and H_2-TPR.

---

* To whom all correspondence should be sent:
E-mail: s_phatanasri@yahoo.com

EXPERIMENTAL

2.1 Preparation of catalysts

HBeta zeolite (Si/Al = 27) manufactured by Tosoh Corporation physically mixed with either aluminum nitrate nonahydrate ($AlN_3O_3.9H_2O$, Fluka) or aluminum oxide (Fluka) was used as a support with HBeta/Al-precursor ratio of 70:30. The mixed support samples were calcined in air at predetermined temperatures ranging from 350–950 ºC for 2 h before impregnation with an aqueous solution of ammonium molybdate tetrahydrate ($(NH_4)_6Mo_6O_{24}\cdot 4H_2O$) to obtain 4 wt% of molybdenum. The catalysts were designated as Mo/AN+Hß(y) and Mo/AO+Hß(y) for the samples prepared from the support of HBeta mixed with aluminum nitrate and aluminum oxide, respectively. After impregnation, all catalysts were calcined in air at 680ºC for 2 h.

2.2 Catalyst characterization

X-ray diffraction patterns of all catalysts were collected on an X-ray diffractometer (Siemens D5000) using Ni filters Cu Kα radiation from 20º to 80º.

Brunauer-Emmett-Teller (BET) surface areas, as well as the pore volumes of the catalysts were obtained on a surface area analyzer (Micromeritics ASAP 2010).

The catalyst reducibility was assessed by temperature programmed reduction with hydrogen (H_2–TPR). A portion of 0.2 g of the catalyst sample was placed in a quartz tube and pretreated in Ar flow (50 ml/min) at 200ºC for 2 h. Then the carrier gas was replaced with 10% H_2 at the same flow rate and was balanced with Ar in the temperature range of 40 to 800ºC. The peak area assessment was made by a Micromeritics Chemisorb 2750 automated system supplied with Chemi Soft TPx software.

The catalyst acidity was determined by the technique of ammonia temperature programmed desorption (NH_3-TPD). A portion of 0.2 g of the catalyst sample was placed in a quartz tube and was pretreated in helium flow (50 ml/min) at 200ºC for 2 h. Then, the catalyst sample was adsorbed till saturation with 15% NH_3 balanced with He. The physisorbed ammonia was desorbed in a helium gas flow for about 1 h. The sample was subsequently heated from 40 to 800ºC at a heating rate of 10ºC/min. The peak area assessment was made by a Micromeritics Chemisorb 2750 automated system supplied with Chemi Soft TPx software.

UV-vis spectra were recorded on a Lambda 650 UV-vis spectrometer equipped with a diffuse reflectance attachment at room temperature in the range of 200–900 nm.

2.3 Catalytic performance for metathesis reaction

A portion of 2.0 g of catalyst was placed in a fixed bed reactor with inner diameter (ID) of 7.5 mm to which a type K thermocouple was mounted. The catalyst was pretreated at 550ºC with a heating rate of 10ºC/min in a nitrogen flow for 1 h and was cooled down to reaction temperature of 120ºC (pressure=0.1MPa). The feed consisting of 4% C_2H_4, 2% rrans–2–C_4H_8 balanced with N_2 (equivalent to C_2H_4/trans–2–C_4H_8 ratio of 2:1) was used. The sample analysis was performed on a Shimadzu GC 2014 gas chromatograph equipped with a column of packed 10% silicone SE-30 (3.02 m with 0.53 mm ID) and a flame ionization detector using nitrogen as the carrier gas (5 ml/min).

RESULTS

The physical properties of the molybdenum-based catalysts impregnated on mixed HBeta and aluminum oxide calcined at 550ºC, Mo/AO+Hß(550), and mixed HBeta and aluminum nitrate calcined at the same temperature, Mo/AN+Hß(550), are shown in Table 1.

No significant difference in pore volume was observed for both samples, while the BET surface areas and pore sizes of both samples were in the range of 412–423 m^2/g and 6.38–8.64 nm, respectively. The relative crystallinity of Mo/AN+Hß(550) was slightly higher than that of Mo/AO+Hß(550). The conversions of 2-butene and propene selectivities for the metathesis reaction of ethene and 2-butene on Mo/AN+Hß(550) and Mo/AO+Hß(550) are shown in Figs. 1 and 2, respectively. It is clearly seen that Mo/AN+Hß(550) using aluminum nitrate as a precursor markedly outperformed its counterpart using aluminum oxide as a precursor,

Table 1. Physical properties of catalysts prepared with different Al-precursors.

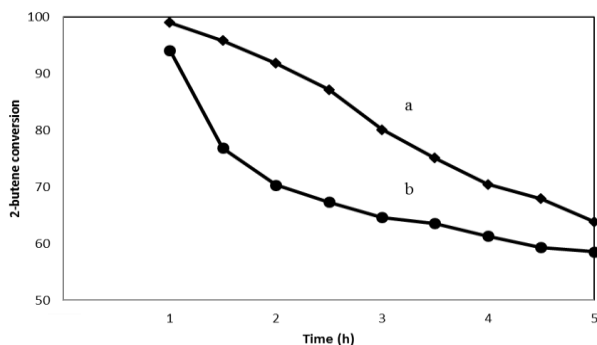| Sample	4%Mo/AlO(550)-Hβ	4%Mo/AlN(550)-Hβ
BET surface area (m^2/g)	423	412
Pore volume (cm^3/g)	0.40	0.38
Pore size (nm)	6.38	8.64
Relative crystallinity (%)	51	55

Fig.1. Metathesis conversion on mixed support molybdenum-based catalysts using different Al-precursors. (a) = Mo/AN(550)-HB and (b) = Mo/AO(550)-HB.
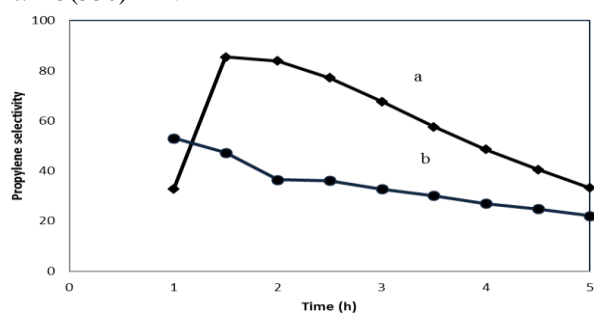

Fig.2. Metathesis selectivity on mixed support molybdenum-based catalysts using different Al-precursors. (a) = Mo/AN(550)-HB and (b) = Mo/AO(550)-HB

Fig.3. H_2-TPR profiles for mixed support molybdenum-based catalysts using different Al-precursors.

Fig.4. UV-vis spectra of mixed support molybdenum-based catalysts using different Al-precursors. (a)= Mo/AN(550)-HB, (b)= Mo/AO(550)-HB.

Mo/AO+Hß(550), in both 2-butene conversion and propene selectivity throughout the observed 5 h on stream. This reflects the different interaction characteristics between Al and HBeta obtained using different Al precursors and hence the different metal-support interaction characteristics obtained on both catalyst samples. The H_2–TPR profiles of both catalyst samples are shown in Fig. 3. The Mo/AO+Hß(550) catalyst displayed an H_2–TPR peak at about 400ºC while a relatively broader peak at higher temperature (around 500 to 600°C) was observed for the Mo/AN+Hß(550) catalyst.

The stronger metal-support interaction obtained on the catalyst sample using aluminum nitrate as Al precursor might be responsible, among the other things, for the better catalyst performance on metathesis reaction. Fig. 4 shows the UV-vis spectra of both catalyst samples. The relatively strong peak around 230 nm corresponding to the surface tetrahedral Mo oxide species [1] was clearly observed on the catalyst sample using aluminum nitrate as Al precursor. This should be responsible for the improved metathesis activity of Mo/AN+Hß (550) favored by the existence of surface tetrahedral active sites. As shown in Fig. 5, the
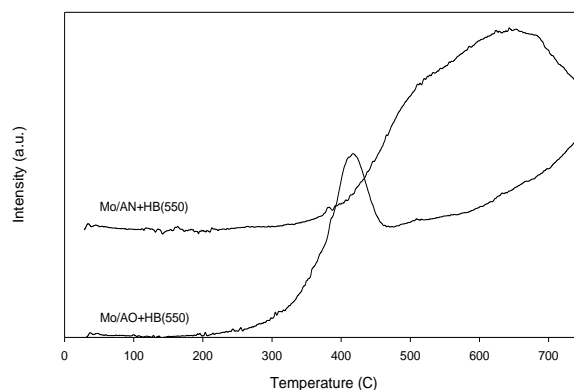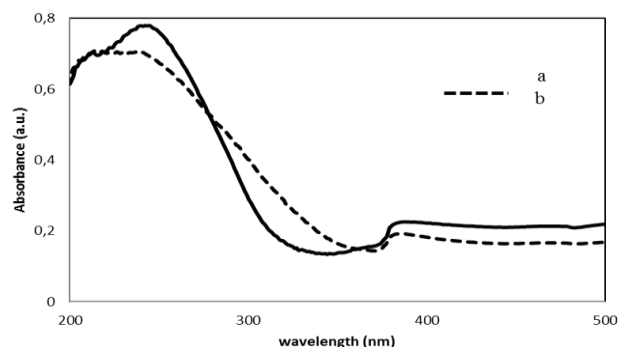
NH$_3$–TPD profiles of both catalyst samples reveal that Mo/AN+Hß(550) displays higher acidity than its counterpart, Mo/AO+Hß(550). The Brønsted acid-derived surface hydroxyl group was believed to react with molybdenum oxide crystallites, from which the metathesis active site of surface tetrahedral molybdenum oxide species could be obtained. Phongsawat *et al.* [11] have studied the metathesis of ethylene and 2-pentene for propylene production on SiO_2–Al_2O_3 supported rhenium catalysts. They have found that the weak acidity equivalent to the NH$_3$–TPD profile at around 300ºC or lower was not strong enough for isomerization reaction and metathesis activity to be maintained. Therefore, the acid strength in this case was supposed to be moderate enough to promote metathesis activity essentially without significant contribution to isomerization. This should be one of the factors that promote the enhancement of propene production by metathesis reaction.

Catalyst heat treatment may somewhat influence the thermal stability of the support structure which may affect the catalytic performance. Therefore, the calcination temperatures of mixed HBeta and alumina, using aluminum nitrate as a precursor,
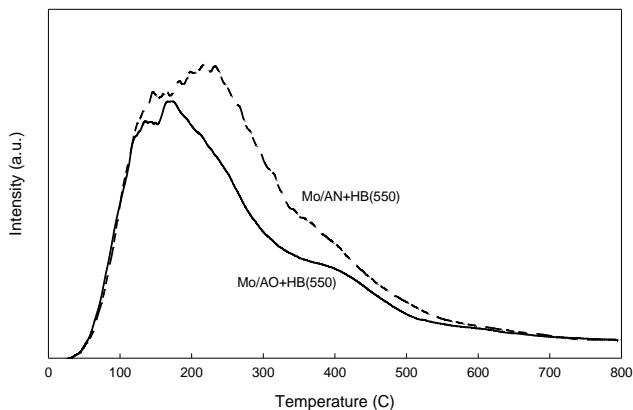
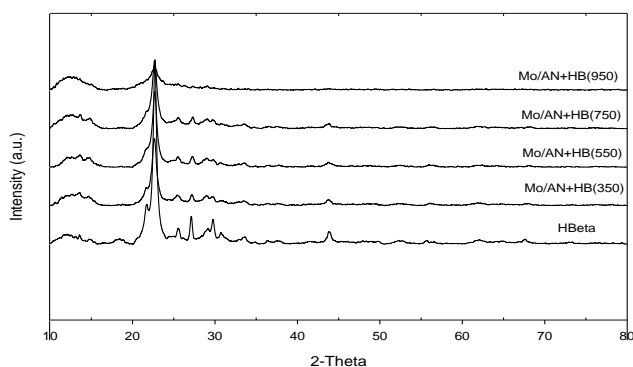**Fig.5**. NH$_3$-TPD profiles for mixed support molybdenum-based catalysts using different Al-precursors.

Fig.6. X-ray diffraction pattern of mixed support molybdenum-based catalysts using different Al-precursors calcined at different temperatures.

were varied from 350 to 950ºC. The XRD patterns of the catalysts calcined at different temperatures are shown in Fig. 6. The characteristic peaks of HBeta zeolite were observed for all catalysts due to the amorphous characteristics of alumina. It was found that the crystallinity of the catalysts markedly decreased at calcination temperatures higher than 750ºC. The structural collapse of HBeta zeolite may occur at high calcination temperature especially for the catalyst calcined at 950ºC designated as Mo/AN+Hß(950). The conversion of 2-butene and propene selectivity by metathesis reaction on those catalysts calcined at different temperatures are demonstrated in Figs. 7 and 8, respectively. The catalyst performance on both 2-butene conversion and propene selectivity deteriorated with the higher calcination temperatures during the 5 h on stream. The adverse effect of high calcination temperature was evidently most pronounced on the catalyst calcined at 950ºC with almost no propene formed on Mo/AN+Hß(950) even at the early period of reaction. This may be attributed to the structural collapse of HBeta zeolite at such high temperature
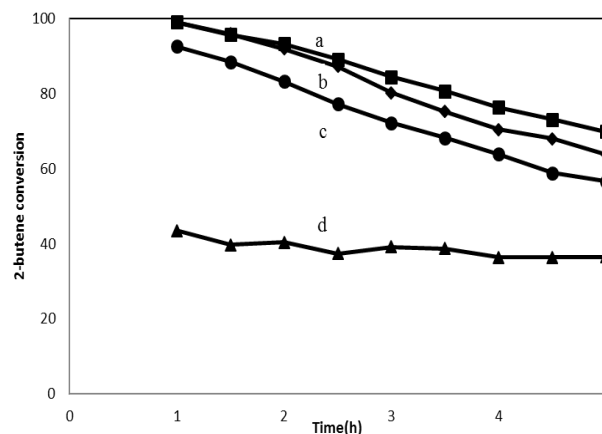

Fig.7. Metathesis conversion on mixed support molybdenum-based catalysts using different Al-precursors calcined at different temperatures. (a) = Mo/AN(350)-HB, (b) = Mo/AN(550)-HB, (c) = Mo/AN(750)-HB, and (d) = Mo/AN(950)-HB.

Fig.8. Metathesis selectivity on mixed support molybdenum-based catalysts using different Al-precursors calcined at different temperatures. (a) = Mo/AN(350)-HB, (b) = Mo/AN(550)-HB, (c) = Mo/AN(750)-HB, and (d) = Mo/AN(950)-HB.
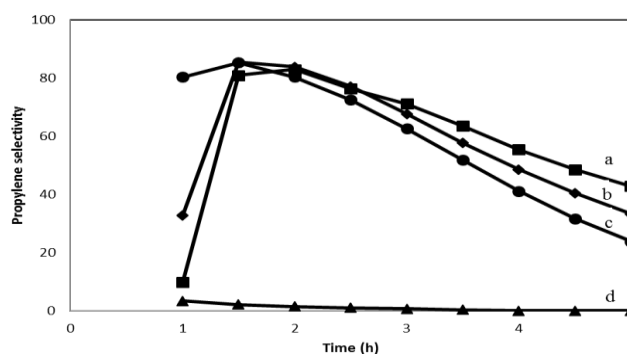
as evidenced by the considerably low crystallinity on its XRD pattern.

DISCUSSIONS

The significantly low metathesis activity of Mo/AN+Hß calcined at 950ºC due to structural collapse of HBeta is analogous to the adverse effect of dealumination derived at high Mo loading contents in Mo/HBeta without alumina addition, as found by Liu *et al*. [6]. According to Liu *et al*. [10], the HBeta particles were surrounded by irregular alumina floccules as observed from high-resolution SEM images. The preferential distribution of Mo species in alumina rather than in HBeta, as observed from the quantitative EDS analysis using aluminum nitrate as precursor of alumina, may contribute to the better formation of Al floccules with HBeta which favors the preferential migration of Mo in the alumina surface. As a consequence, better protection of the HBeta structure by alumina using aluminum nitrate as a precursor and hence

higher acidity contributing to the good metathesis activity of propene formation from ethene and 2-butene might be achieved. Though the precise role of aluminum nitrate as alumina precursor on the enhancement of propene production is subject to further investigation, we are strongly convinced that the optimum compatibility between Al and HBeta is the key factor to obtain an active catalyst for metathesis reaction with the acquisition of optimum metal-support interaction and Brønsted acidity. Our further work to modify the mixing of Al and HBeta by adopting sol-gel preparation is under investigation and the preliminary results seem to support our expectation.

CONCLUSIONS

The mixed HBeta-alumina supported molybdenum catalyst calcined at 550ºC using aluminum nitrate as a precursor, Mo/AN+Hß(550), markedly outperformed its counterpart using aluminum oxide as a precursor, Mo/AO+Hß(550), in both 2-butene conversion and propene selectivity throughout the observed 5 h on stream of metathesis reaction between ethene and 2-butene. The relatively stronger metal-support interaction on Mo/AN+Hß(550), as observed from H_2-TPR, as well as the derivation of surface tetrahedral molybdenum oxide species, as observed from UV-vis spectra should be, among other factors, responsible for the relatively good metathesis activity of the catalyst. The higher acidity acquired on Mo/AN+Hß(550), probably due to the better protection of HBeta zeolite structure achieved by the optimum compatibility between Al using aluminum nitrate as precursor and HBeta, was believed to play a significant role for the enhancement of propene production by metathesis reaction of ethene and 2-butene.

REFERENCES

1. X. Li, W. Zhang, S. Liu, H. Huang, X. Han, L. Xu, X. Bao, J. Phys. Chem. C. **113** (2009) 8228-8233.
2. J.C. Mol, J. MOL. CATAL. A-CHEM. 213 (2004) 39-45.
3. C. Pariya, K.N. Jayaprakash, A. Sarkar, COORDIN. CHEM. REV. 168 (1998) 1-48.
4. R.M. Venner, S.I. Kantorowicz, Petroleum Technology Quarterly. 6 (2001) 141-142,144.
5. i.Y.I. J.C. Mol, B. Zumreoglu-Karan, A.J Amass (Eds.), Kluwer Academic Publishers (1990) 247.
6. S. Liu, S. Huang, W. Xin, J. Bai, S. Xie, L. Xu, Catal. Today. 93-95 (2004) 471-476.
7. S.L.L. S.J. Huang, W.J. Xin, J. Bai, S.J. Xie, L.Y. Xu, Q.X. Wang, Chin. , Petrochem. Technol. 32 (2003) 191.
8. X. Li, W. Zhang, S. Liu, X. Han, L. Xu, X. Bao, J. MOL. CATAL. A-CHEM. 250 (2006) 94-99.
9. X. Li, W. Zhang, S. Liu, L. Xu, X. Han, X. Bao, J. Catal.. 250 (2007) 55-66.
10. X. Zhu, X. Li, S. Xie, S. Liu, G. Xu, W. Xin, S. Huang, L. Xu, Catalysis Surveys from Asia. 13 (2009) 1-8.
11. W.Phongsawat, B.Netiworaruksa, K.Suriye, P.Praserthdam, J.Panpranot, Catal. Lett. 142 (2012) 1141-1149.

УСКОРЯВАНЕ НА ПРЕВРЪЩАНЕТО НА ПРОПЕН ЧРЕЗ ПРЕГРУПИРАНЕ НА ЕТИЛЕН И 2-БУТЕН ВЪРХУ СМЕСЕН КАТАЛИЗАТОР НА ОСНОВАТА НА МОЛИБДЕН, НАНЕСЕН ВЪРХУ Нß-АЛУМИНИЕВ ТРИОКСИД, ПОЛУЧЕН ОТ АЛУМИНИЕВ НИТРАТ

Б. Нетиворарукса[1], С. Фатанасри[1], П. Прасертдам[1], В. Фонгсават[1], К. Сурийе[2]

[1] *Център за върхови постижения по катализ и каталитично инженерство, Катедра по инженерна химия, Факултет по инженерство, Университет Чулаланкорн, Банкок 10330, Тайланд*
[2] *SCG Химикали Ко.,LOOД ул. Сиам-cement 1, Банг сю, Банкок 10800, Тайланд*

(Резюме)

Катализаторът, съдържащ 4% тегл. молибден се приготвя по метода на началното импрегниране с влага. Като прекурсори за получаването на подложката от алуминиев оксид се използват алуминиев нитрат и алуминиев триосид. Те се смесват с Нß зеолит, след което сместа се калцинира при 550°C. Катализаторът Mo/AN+Нß(550), получен с алуминиев нитрат като прекурсор забележимо превъзхожда другия (Mo/AO+Нß(550)), при превръщането на 2-бутен и по отношение на селективността спрямо пропен при прегрупирането на етилена и 2-бутена. Относително силните взаимодействия метал-подложка, както и получаването на повърхностни тетраедрични форми на молибденовия оксид са забележими при Mo/AN+Нß(550) и са установени с помощта на H_2-TPR and UV-видими спектри. Освен това се приема, че високата киселинност, получена при Mo/AN+Нß(550) има значителна роля за ускоряването на прегрупирането на етилена и 2-бутена до пропен. Вероятно това се дължи на по-добрата защита на Нß-зеолитната структура от алуминия, постигната при използването на алуминиев нитрат като прекурсор.

Electricity generation during sauerkraut fermentation process

Y. V. Hubenova[1], M. Y. Mitov[2]

[1]*Plovdiv University, Faculty of Biology, Department of Biochemistry and Microbiology, 24 Tsar Asen str., 4000 Plovdiv, Bulgaria,*
[2]*South-West University, Faculty of Mathematics and Natural Sciences, Department of Chemistry, 66 Ivan Mihajlov str., 2700 Blagoevgrad, Bulgaria*

The possibility of using sauerkraut juice as an anolyte in a microbial fuel cell (MFC) was previously proved by us. In this study, fifty day-long MFC experiments covering the total term of the sauerkraut fermentation process were performed. A change in the electrochemical behavior of sauerkraut juice, associated with the successive loading of different dominating microbial species in the mixed microflora, as well as accumulation of various intermediate and end metabolites, was observed by means of cyclic voltammetry. The highest MFC power density of 1.87 W/m^3 was achieved by using a fresh sauerkraut juice as an anolyte at the early stage of fermentation, when hetero-fermentative species are developed into the medium. However, the maximum power density of a MFC permanently loaded with external resistance was obtained after a month operation, corresponding to the lower development of hetero-fermentative lactic acid bacteria and their substitution with homo-fermentative bacteria. Stable long-term current density of 1.05±0.10 A/m^3 was generated at the later fermentation stages.

Keywords: microbial fuel cell, sauerkraut fermentation, electricity generation

INTRODUCTION

The great idea of the microbial fuel cell (MFC) concept is connected with electricity generation based on the naturally occurring metabolic processes of microorganisms. Thus, the MFC technology is expected to have an impact on both electricity production from renewable sources and biodegradable waste purification [1–4].

Food industry is one of the biggest sources of waste biomass. Different methods for its minimization or re-utilization, depending on the specific origin and technology, are in use [5, 6].

Recently, MFC technology has been proposed as an alternative of some of these technologies [7, 8], however, a lot of research has to be done for its practical implementation.

The sauerkraut production, based on lactic acid fermentation of cabbage, is wide-spread in many countries. In our recent study, the possibility to use sauerkraut juice as an anolyte in MFC was proved [9].

The aim of the present work was to verify the possibility for continuous electricity generation by MFC based on sauerkraut fermentation. For this purpose, long-term experiments covering the total period of the sauerkraut fermentation process were performed.

EXPERIMENTAL

Cabbage fermentation was undertaken in a 5 l fermentor, placed into a thermostat-incubator at 16 °C. 4% NaCl soultion was used as a brine.

The electrochemical behavior of the produced sauerkraut juice in the progress of the fermentation process was examined by means of cyclic voltammetry (CV). A sample of the juice was taken from the fermentor and placed into a three-electrode electrochemical cell. Platinum ORP electrode was used as a working electrode, platinum mesh as a counter electrode and Ag/AgCl as a reference. The potential was swept with a scan rate of 25 mV/s. The CV measurements were performed on a 35-2 PJT potentiostat-galvanostat (Radiometer-Tacussel, France) with IMT-101 electrochemical interface and VoltaMaster2 software.

Sauerkraut juice (100 ml) along with cut pieces of cabbage leaves as a carbohydrate source were introduced in the anodic compartments of two identical double-chamber MFCs. Buffered solution (pH 7) of 0.1 M $K_3[Fe(CN)_6]$ was placed in the cathodic chambers and served as a catholyte. The anodic and cathodic compartments were connected with a salt bridge. Rectangular shaped pieces of carbon felt (SPC–7011, 30 g/m^2, Weißgerber GmbH & Co. KG) with geometric area of 21 cm^2 were used as both anodes and cathodes. The

---

* To whom all correspondence should be sent:
E-mail: *jolinahubenova@yahoo.com*

inoculated MFCs were kept in a thermostat-incubator at 16 °C along the whole experiment duration. One of them (MFC 1) was kept at open circuit and once per day polarization measurements by stepwise change of the external resistance from 10 kΩ to 0 Ω were carried out. The second microbial fuel cell (MFC 2) was permanently polarized by switching a load resistance (1 kΩ) in the external circuit and its terminal voltage was monitored by a digital multimeter (Lamar RE67). From the obtained data, the generated current was estimated by using Ohm's law. Periodically, polarization measurements by varying the external resistance were accomplished.

As a control experiment, cabbage juice was periodically taken from the fermentor, introduced into a third MFC and after stabilization of the open curcuit voltage (OCV), polarization measurements at variable resistances were performed.

RESULTS AND DISCUSSION

The CV-measurements performed with the sauerkraut juice reveal that a broad anodic peak with varying intensity and potential appears in the voltamograms. At the first days of the fermentation process the peak intensity grew and its potential shifted from –380 to –270 mV (*vs.* Ag/AgCl) – Fig.1a. Till the 10th day the CV-pattern remained unchanged, but with the progress of the fermentation process the anodic peak shifted to more positive potentials and its height was reduced – Fig.1b.

The recorded variable electrochemical behaviour could be associated with the successive loading of different dominating microbial species in the mixed microflora, as well as with oxidation of various intermediate and end metabolites produced during fermentation. The sauerkraut production is based on lactic acid fermentation. The starter for sauerkraut is the normal mixed biota of cabbage, in which the main species are *Leuconostoc mesenteroides* and *Lactobacillus plantarum*. The addition of 2.25–2.50 % salt restricts the activities of gram-negative bacteria, while the lactic acid rods and cocci are favored. The activities of the cocci usually cease when the acid content increases to 0.7–1.0 %. The final stages of sauerkraut production are effected by *L. plantarum* and *L. brevis. P. cerevisiae* and *E. faecalis* may also contribute to product development. The final total acidity is generally 1.6–1.8 %, with lactic acid at 1.0–1.3 % and pH in the range of 3.1 to 3.7 [10]. The depletion of the main substrates at the end of the process is the most probable reason for the

observed decrease of the anodic peak intensity in the CVs.

The MFC experiments using sauerkraut juice as an anolyte confirmed the possibility for electricity generation along the sauerkraut fermentation process – Fig.2. The obtained data show that the system is rapidly adaptive and starts to produce electricity immediately after innoculation of the MFC.
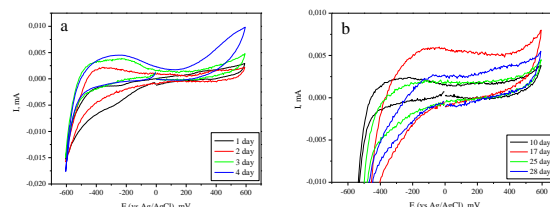

Fig. 1. Cyclic voltammograms obtained with sauerkraut juice at different stages of fermentation.

When not loaded with an external resistance (MFC 1), the OCV initially increased from 470 to 750 mV and held at close values for two weeks (Fig.2a). After this period it sharply dropped back to 500 mV and then gradually grew up to a stationary value of 580±15 mV. Analogous tendencies in the change of the maximum power density, estimated from the obtained polarization curves, were observed. The highest value of 745 mW/m³ was achieved at the 4th day after MFC innoculation. After two weeks the generated power drastically dropped to 220 mW/m³, but afterwords it gradually increased to 300±25 mW/m³. At the end of the experiment both OCV and maximum power values fell down.

Complex variation of OCV and maximum power density was also observed when a load resistance was permanently switched on in the external current circuit (MFC 2, Fig.2b). The obtained lower values could be assigned to the fact that the system was enduringly under "stress" caused by the continuous electricity production. This is especially valid for the initial period, when a significant decrease of the maximum power was observed. During the next stage, however, the variation of both OCV and maximum power values is similar to that achieved with MFC 1.
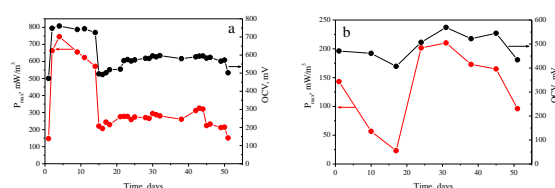

Fig. 2. Variation of OCV and maximum power density obtained with: a) MFC 1; b) MFC 2.

Interesting features were obtained in the control MFC experiment. The highest maximum power density of 1.87 W/m³ was achieved with the sauerkraut juice taken at the 10th day of the fermentation process. This value exceeds 2.5 times that obtained with MFC 1 (Fig.3), which indicates some differences in the culture development, when it is performed in a bioreactor with a MFC. Most probably, these differences are connected with cell inhibition effects in the case of MFC, which has a volume much smaller than that of the fermentor. The tendency to drastic lowering of the maximum power at the second half of fermentation in comparison to the values recorded at the first half was also observed in the control experiment.

The ability for continuous electricity generation was demonstrated by the experiment performed with MFC 2. During the whole experiment duration the MFC was loaded with a constant external resistance ($R_{ext.}$=1 kΩ), except when polarization measurements by stepwise change of the load resistance were carried out. The variation of the generated current densities with time is shown in Fig. 4.
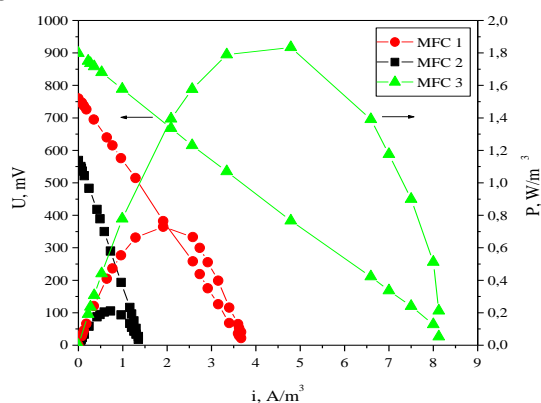

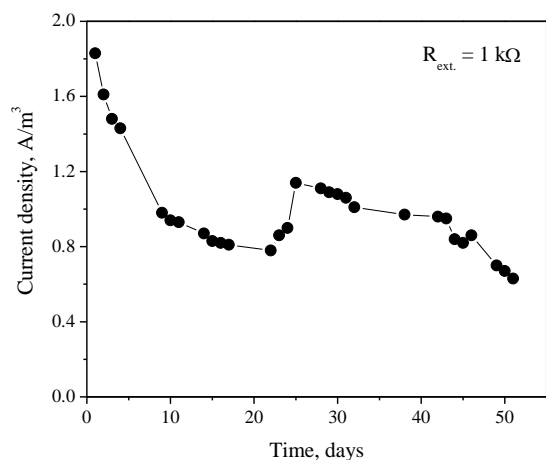**Fig. 3.** Optimal polarization and power curves obtained during three MFC experiments.

Fig. 4. Variation of generated current with time.

The measured terminal voltage reached a stable value few minutes after the circuit was closed through the external resistance. The highest current value was registered at the first day of the experiment. A steep decrease of the current was observed till the 9th day, after which the current continued to diminish with a slower rate. After three weeks, however, it began to restore and stabilized at 1.05±0.10 A/m³ for eighteen days. A subsequent current fall down to the end of experiment was observed.

Comparing the results obtained by all MFC experiments, some charateristic features could be pointed out. Generally, the whole process could be divided into several distinct stages.

In the case when the system was not permanently disturbed (MFC 1), the OCV and maximum power values initially increased, reaching maxima at the fourth day of cultivation. This initial period of adaptation may be assigned to the first phase of fermentation, where anaerobic bacteria such as *Klebsiella* and *Enterobacter* lead the fermentation, and begin producing an acidic environment that favours later bacteria [11]. During the next period corresponding to the second fermentation phase, in which the acid levels become too high for many bacteria, and *Leuconostoc mesenteroides* and other *Leuconostoc spp.* take dominance, the MFC outputs slightly decreased but remained relatively high. The end of this stage was traced out by a sharp fall down of the electric parameters (OCV and power density) two weeks after the beginning of the experiment. Lower but relatively stable output values in comparison with those obtained during the second stage were observed along the third one. These results are not suprising having in mind that in the third fermentation phase various *Lactobacillus* species including *L. brevis* and *L. plantarum* ferment any remaining sugars, further lowering the pH [11, 12].

Three stages in the process progress could be also distinguished from the current-time plot (Fig.4), obtained with the continuously loaded MFC 2. In this case, however, a steep drop of the electrical parameters was observed during the first stage in contrary to the increase in OCV and maximum power attained with MFC 1. This result could be explained taking into account that the system under permanent load had no acclimation period and the microorganisms tried to recover the energy required for their own growth and development in a competition with the continuous electricity flux. This also explains the retardation of the first and the second stages, as well as the much

lower OCV and power values obtained by polarization curve analysis in comparison with those achieved with MFC 1 and in the control experiment.

In all cases, a drop of MFC outputs was observed at the end of experiments. We suppose that this is most probably due to exhaustion of the carbohydrate source and the gradual dying away of the culture.

CONCLUSIONS

Electricity generation was achieved by using sauerkraut juice as an anolyte in double-chamber MFCs. The energy recovery process could be performed continuously but the obtained outputs depend on the specific features of the fermentation phases.

Based on the obtained results in this study, further investigations aiming at the development of biosensors for monitoring of processes during sauerkraut production are feasible.

REFERENCES

1 A.E. Franks, K.P. Nevin, *Energies,* **3**, 899 (2010).
2 Z. Du, H. Li, T. Gu, *Biotechnol. Adv.,* **25**, 464 (2007).
3 F. Davis, H. Sèamus, *Biosensors&Bioelectronics,* **22**, 1224 (2007).
4 R. Bullen, T. Arnot, J. Lakeman, F. Walsh, *Biosensors&Bioelectronics,* **21**: 2015 (2006).
5 G.T. Kroyer, *Lebensmittel-Wissenschaft Technol.,* **28**, 547 (1995).
6 Y.D. Hang, *J. Food Sci.,* **69**, CRH104 (2004).
7 B. Cercado-Quezada, M.-L. Marie-Line Delia, A. Bergel, *Bioresource Technol.,* **101**, 2748 (2010).
8 S.E. Oh, B.E. Logan, *Water Res.,* **39**, 4673 (2005).
9 Y. Hubenova, A. Slavchev, M. Mitov, In: Proceedings of the 2nd Microbial Fuel Cell Conference "Waste to Energy", Gwangju, Korea, 2009, p. 280.
10 H.D. Belitz, W. Grosch, P. Schieberle, *Food Chem..* Springer-Verlag Berlin Heidelberg, 2009.
11 E.R. Farnworth, Handbook of Fermented Functional Foods. CRC, 2003.
12 M. Battcock, S. Azam-Ali, Fermented Fruits and Vegetables - A Global Perspective. FAO Agricultural Services Bulletin, 1998.

ГЕНЕРИРАНЕ НА ЕЛЕКТРИЧЕСТВО ПО ВРЕМЕ НА ФЕРМЕНТАЦИЯ НА ЗЕЛЕ

Й. В. Хубенова[1], М. Й. Митов[2]

[1]Пловдивски университет „Паисий Хилендарски", Катедра по биохимия и микробиология, ул. „Цар Асен" 24, 4000 Пловдив, България,
[2]Югозападен университет „Неофит Рилски", Катедра по химия, ул. „Иван Михайлов" 66, 2700 Благоевград, България

(Резюме)

Възможността за използване на зелев сок като анолит в микробиологичен горивен елемент (МГЕ) бе доказана от нас в предишно изследване. В настоящата работа са представени резултатите от 50-дневни експерименти, обхващащи целия период на процеса на ферментация на зеле. Чрез циклична волтамперометрия бе проследено изменението на електрохимичното поведение на зелев сок, свързано с последователното редуване на различни доминиращи микробиални видове в смесената микрофлора, както и натрупването на междинни и крайни метаболити. Най-висока плътност на мощността от 1.87 W/m^3 бе постигната при използване като анолит в МГЕ на зелев сок в начална фаза на ферментацията, когато в средата доминират хетеро-ферментативни микробиални видове. Максималната плътност на мощността на МГЕ с постоянно свързано товарно съпротивление, обаче, бе получена след един месец работа, когато е налице забавено развитие на хетеро-ферментативните млечно-кисели бактерии и тяхната замяна с хомо-ферментативни бактерии. Относително постоянна плътност на тока от 1.05±0.10 A/m^3 бе генерирана за период от 2 седмици през по-късните етапи на ферментацията.

Ab initio study of ion replacement in Spinach plastocyanin protein

M. Reza Housaindokht[1,2], M. Sargolzaei[1,2*], M. Reza Bozorgmehr [3]

[1] *Biophysical Chemistry Laboratory, Department of Chemistry, Faculty of Science Ferdowsi University of Mashhad, Mashhad, Iran*
[2] *Biotechnology Research Center of Ferdowsi University of Mashhad, Mashhad, Iran*
[3] *Department of Chemistry, Faculty of Science, Mashhad Branch, Islamic Azad University, Mashhad, Iran*

Ion replacement in protein active site is attracting considerable interest due to its application in some spectroscopic methods like perturbed angular correlation. Theoretical consideration of ion replacement in plastocyanin was done using the two layer ONIOM method. The copper (I) and copper (II) ions in the plastocyanin active site were replaced by silver (I) and cadmium (II), respectively. Optimization of the four proteins was done with LANL2DZ and SDD basis sets. Molecular orbital, natural bond orbital and atom in molecule analysis were used to determine the electronic structures of the four active sites. The total energy of copper (I) plastocyanin is lower than that of silver (I) plastocyanin. Copper (II) plastocyanin showed a lower energy than cadimum(II) plastocyanin. HOMO and LUMO orbital energies of the copper (I) and cadmium (II) active sites are lower than those of the silver (I) and copper (II) active sites, respectively. The four active sites displayed different charge distribution. Atom in molecule theory demonstrated different values for electronic density and bond ellipticity for the four active sites.

Key words: Electronic structure**;** Protein active site; *ab initio*; DFT; AIM; NBO

1. INTRODUCTION

Large molecular systems such as catalysts, nanotubes and bimolecular systems are not simple enough to be investigated by quantum methods alone. Therefore, the ONIOM method has been developed to overcome this problem. ONIOM method has been used to study the mechanism of enzyme catalyzed reactions, electronic structure of protein active site and ion replacement in protein structure [1–8].

Plastocyanin (PC), also known as blue copper (BC) protein, is a small soluble copper protein with a barrel-like structure. Multiconfigurational approach has been used for consideration of the electronic structure and charge transfer of model complex systems of plastocyanin. Excellent agreement has been found between the experimental and the calculated spectra [9]. Smbhu *et al.* used a theoretical method for poplar plastocyanin to calculate the standard reduction potentials *in vitro*. They showed that calculated potentials are in excellent agreement with the experimental one [10]. Density functional theory (DFT) calculation of the active site of plastocyanin was performed for model complexes. These model complexes were constructed by exchanging His,

Cys and Met residues by imidazol, methyl-thiolate and dimethyl-sulfide, respectively [11]. Perturbed angular correlation spectroscopy (PAC), which is based on gamma ray emission from radioactive nuclei, has been used to study the binding of plastocyanin to reduced photosystem 1 of spinach by substituting copper (I) and copper (II) by silver (I) and cadmium (II), respectively [12,13]. A question that needs to be answered is whether the electronic structure of silver(I) and cadmium(II) active sites is similar to that of copper(I) and copper(II) active sites or not. The present work is an attempt to show the main difference between the electronic structures of the active sites of copper(I) and silver(I) protein and also between copper(II) and cadmium(II) protein using ONIOM approach, molecular orbital (MO), natural bond orbital (NBO) and atom in molecule(AIM) theory analysis.

2. COMPUTATIONAL DETAILS

The experimental X-ray structure of plastocyanin was retrieved from the Brookhaven Protein Databank (PDB ID: 1ylb and 1plc). PDB code of reduced and oxidized form of plastocyanin is 1ylb and 1plc, respectively. The two layer ONIOM hybrid method was used for calculations. The active site of plastocyanin consisting of 38 atoms including metal ion and side chain of His37, His87, Cys84 and Met92 was used as QM region.

* To whom all correspondence should be sent:
E-mail: : mohsen.sargolzaei@gmail.com

Beckes three-parameter hybrid exchange functional and the Lee-Yang-Parr correlation functional DFT hybrid B3LYP method [14,15] by employing the effective core potentials of Hay and Wadt with double-e valence (LanL2DZ) basis set [16] and the Stuttgart Dresden Dunning pseudopotentials (SDD) basis set [17,18] were used for the QM region. For the remaining part of the protein structure UFF force field was used. All calculations were performed using the GAUSSIAN 03 package [19]. NOC software, downloaded from *http://noch.sourceforge.net/*, was used for representation of protein structure. The active site complex of the proteins was extracted from the optimized protein structure and was used for further analysis. NBO analysis was used for evaluating atomic charge and second-order interaction energies [20]. The topological properties of electron density were analyzed for the four active site complexes using the AIM2000 program [21 Correspondence 24].

3. RESULTS AND DISCUSSION

3.1 Spinach plastocyanin protein

Fig. 1 shows the PDB structure of the spinach plastocyanin. As clearly seen, there is one active site in this protein. The active site is consisting of one copper ion, two histidines, one cysteine and one methionin residue. For the present study, we used the copper ion and the side chain of the mentioned residues as high layer and the other parts of the protein as low layer.
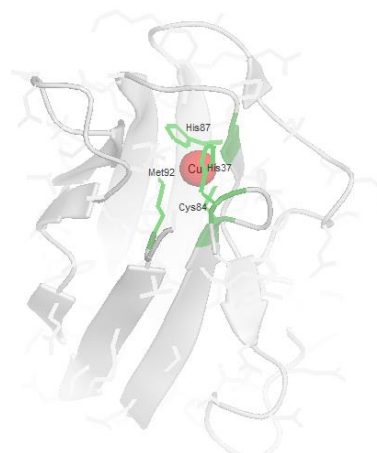

Fig. 1. Spinach plastocyanin protein structure along with active sites

3.2 Energy analysis

Table 1 shows the high and low layer energy of ONIOM calculation for all basis sets. The main difference among the four active site energies is seen in the energy of the model system with high level of the calculation. Copper (I) active site shows the lowest energy among other active sites. The order of decrease in total energy is as follows:

Copper (I) < copper (II) < silver (I) < cadmium (II) active site

Data in Table 1 show that energy values are not sensitive to the selection of basis set.

3.3 Structure parameters analysis

Table 2 illustrates the bond distance of the metal ion of the protein active site from His to the sulfur atom of the Cys and Met ligand. Bond distances were derived from two PDB entries that were

Table 1. Energy analysis of the four plastocyanin active sites

	Cu^+-PC		Ag^+-PC		Cu^{2+}-PC		Cd^{2+}-PC	
Basis set	SDD	LANL2DZ	SDD	LANL2DZ	SDD	LANL2DZ	SDD	LANL2DZ
E_{low}(model)	0.3	0.3	0.26	0.26	0.34	0.35	0.31	0.31
E_{high}(model)	−1683.6	−906.3	−1633.2	−855.8	−1683.2	−905.9	−1654	−757.9
E_{low}(real)	2.32	2.27	2.26	2.43	2.29	2.3	2.24	2.25
E_{total}	−1681.6	−904.3	−1631.2	−853.9	−1681.3	−903.9	−1652	−755.9

Table 2. Bond distances of the four active sites along with experimental data

X^*-PC	Cu^+-PC		Ag^+-PC			Cu^{2+}-PC		Cd^{2+}-PC		
Basis set	*SDD*	*LANL2DZ*	*SDD*	*LANL2DZ*	*Exp*	*SDD*	*LANL2DZ*	*SDD*	*LANL2DZ*	*Exp*
His87										
X-N	1.99	2.02	2.23	2.26	2.09	1.97	1.99	2.21	2.26	2.06
His37										
X-N	1.99	2.02	2.23	2.25	2.07	1.97	1.96	2.22	2.25	1.91
Met92										
X-S	3.09	3.11	3.28	3.52	3.10	2.60	2.59	2.71	2.77	2.82
Cys84										
X-S	2.21	2.28	2.44	2.57	2.12	2.42	2.27	2.72	2.74	2.07

*X stands for metal ion

Table 3. Bond angles of the four active sites along with experimental data

X*-PC	Cu⁺-PC		Ag⁺-PC			Cu²⁺-PC		Cd²⁺-PC		
		LANL2D		*LANL2D*			*LANL*		*LANL2D*	
Basis set	*SDD*	*Z*	SDD	*Z*	Exp	*SDD*	*2DZ*	*SDD*	*Z*	Exp
His87										
X-N-C20	125.32	125.38	125.31	124.62	126.46	124.89	122.12	121.07	124.41	125.99
X-N-C17	126.78	127.01	126.76	127.46	127.89	127.71	129.86	131.45	128.38	123.93
His37										
X-N-C5	123.14	122.26	121.28	122.47	125.98	121.71	124.10	118.90	115.54	128.97
X-N-C2	129.12	130.10	130.70	130.22	128.63	129.86	127.46	133.58	137.27	123.10
Met92										
X-S-C30	98.57	97.98	107.41	89.27	117.26	116.61	111.66	107.47	110.44	96.48
X-S-C28	129.67	130.65	138.29	138.95	122.51	135.80	130.51	127.81	123.03	126.86
Cys84										
X-S-C	109.90	109.38	111.03	109.78	113.63	105.12	108.65	99.88	104.85	110.42

*X stands for metal ion

mentioned above. Except the distance between sulfur and copper (I) ion, LAnl2dz basis set can reproduce experimental bond distance lengths more accurately than SDD basis set in the copper (I) active site. ONIOM calculation with SDD basis set can predict all bond lengths more accurately than Lanl2dz one. Besides bond distances between sulfur and metal ion in the Met ligand, ONIOM calculation with the Lanl2dz basis set shows the accurate bond lengths for other distances of the copper (II) active site. For cadmium (II) active site Lanl2dz basis set shows strong prediction with respect to SDD basis set for metal-sulfur distance in Met92 ligand, but weak prediction is seen for other bond distances.

Table 3 shows selected bond angles of the four active sites. For copper (I) active site, Lanl2dz basis set can reproduce X-N- $C\delta$ and X-N- $C\gamma$ bond angles of the His 87 and also X-N- Cβ of the His 37 more accurately than SDD basis set. For silver (I) active site, Lanl2dz basis set gives better prediction than SDD basis set for X-N- $C\gamma$ bond angle of the His87 and X-N- $C\delta$, X-N- Cβ of the His 37. Except X-N- Cγ bond angle of the His 87, LanL2dz shows better prediction than SDD basis set. Finally, except X-N- $C\delta$, X-N- Cβ and X-S- $C\varepsilon$ bond angle, the prediction of bond angles by Lanl2dz is worse than by SDD basis set.

3.4 MO analysis

Fig. 2 shows the highest occupied molecular orbital (HOMO) and the lowest unoccupied molecular orbital (LUMO) of the four active sites. The HOMO and LUMO energies varied as follows:

$E_{Homo-Cd(II)} < E_{Homo-Cu(II)} < E_{Homo-Cu(I)} < E_{Homo-Ag(I)}$

$E_{Lumo-Cd(II)} < E_{Lumo-Cu(II)} < E_{Lumo-Cu(I)} < E_{Lumo-Ag(I)}$

Based on these results, one can conclude that Ag^{1+} active site in plastocyanin can donate an electron to a partner more feasibly than Cu^{1+} active site. Also, comparision of LUMO orbitals energies shows that

Cd^{2+} active site can receive an electron more comfortably than Cu^{2+} active site.
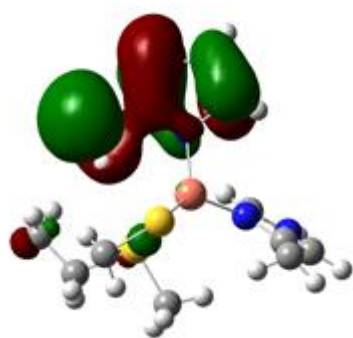
3.5 NBO analysis

Table 4 shows the natural charge of atoms in the four active sites. As clearly seen, insertion of silver ion into the active site increases some atom charges such as $C\varepsilon$ of the His37; Cβ and $C\delta$ of the His87 and reduces some atom charges such as $N\delta$ of the His37; $C\gamma$ of the His87; Cβ of the Met92 and $S\gamma$ of the Cys84. Insertion of cadmium (II) into the copper (II) active site caused decreasing of charge density on Cβ of the His37 and Cβ of the His87.
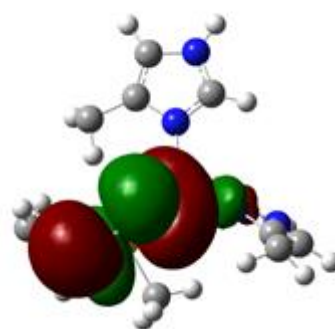
Table 5 shows the stabilization energy of the donor-acceptor interaction of the four active sites. For all active sites, the strongest interaction is between Nε lone pair and $\sigma^*_{N\delta- C\varepsilon}$ bond.

Table 4: Atomic charges of plastocyanin active sites

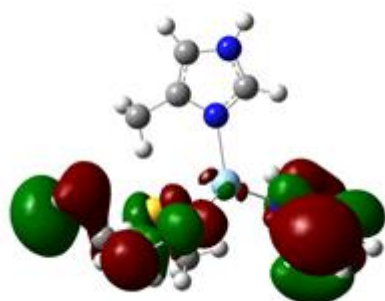|	Cu⁺ *active site*	Ag⁺ *active site*	Cu²⁺*active site*	Cd²⁺*active site*
	Charge			
His37				
Cβ	0.557	0.559	–0.009	0.033
Cγ	–0.171	–0.254	0.099	0.063
Cδ	0.261	0.061	0.075	0.069
Nδ	–0.178	0.026	–0.545	–0.443
Cε	0.094	–0.093	0.26	0.21
Nε	–0.156	–0.161	–0.234	–0.267
His87				
Cβ	0.564	–0.528	–0.009	0.056
Cγ	–0.18	0.319	0.085	0.058
Cδ	0.269	–0.267	0.085	0.077
Nδ	–0.159	–0.402	–0.541	–0.441
Cε	0.074	0.312	0.268	0.227
Nε	–0.159	–0.125	–0.235	–0.265
Met92				
Cβ	–0.128	0.58	0.121	0.076
Cγ	–0.027	–0.123	–0.086	–0.092
Sδ	0.032	0.075	0.048	0.003
Cε	–0.087	–0.086	–0.152	–0.142
Cys84				
Cβ	–0.547	–0.075	0.09	0.156
Sγ	–0.082	0.0104	–0.217	–0.079
Metal				
Cu⁺	0.557	-	-	-
Ag⁺	-	0.387	-	-
Cu²⁺	-	-	1.404	-
Cd²⁺	-	-	-	1.329

203

HOMO-Cu(I)
E= -0.33419 hartree

LUMO-Cu (I)
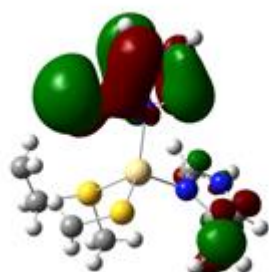E= -0.28245 hartree
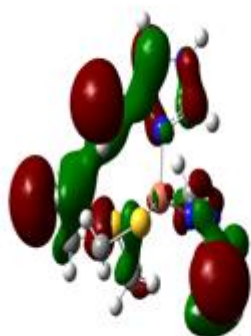
HOMO-Cu (II)
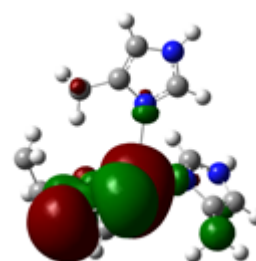E= -0.42924 hartree
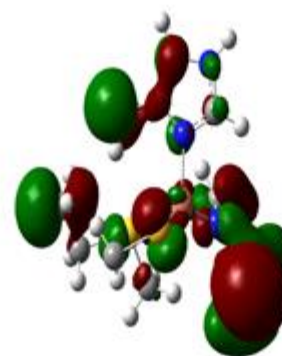
LUMO-Cu (II)
E= -0.41315 hartree

HOMO-Ag (I)
E= -0.28778 hartree

LUMO-Ag (I)
E= -0.27423 hartree

HOMO-Cd (II)
E= -0.47696 hartree

LUMO-Cd (II)
E= -0.41156 hartree

Fig. 2.HOMO and LUMO orbitals of plastocyanin active sites

Table 5: Stabilization energies of donor-acceptor interaction

	Cu$^+$ *active site*	Ag$^+$ *active site*	Cu^{2+} *active site*	Cd^{2+} *active site*
	Charge transfer E(2), E(j)-E(i),F(i,j)			
BD(Cu- Cβ)(Met92)→ BD*(Cγ-β)(Met92)	30.24–0.41–0.143	–	–	–
LP(Nϵ)(His37) →BD*(Cγ – Cδ)(His37)	34.43–0.59–0.188	–	–	–
LP(Nϵ)(His37) →BD*(Nδ– Cϵ)(His37)	49.10–0.47–0.193	–	–	–
LP(Nϵ)(His87) →BD*(Cγ – Cδ)(His87)	34.88–0.59–0.189	–	–	–
LP(Nϵ)(His87) →BD*(Nδ– Cϵ)(His87)	47.67–0.46–0.188	–	–	–
LP(Nδ)(His37) →BD*(Sg-Cu)(Cys)	–	–	48.45–0.83–0.184	–
LP(Nϵ)(His37) →BD*(Cγ – Cδ)(His37)	–	–	50.62–0.55–0.158	–
LP(Nϵ)(His37) →BD*(Nδ– Cϵ)(His37)	–	–	147.00–0.41–0.219	–
BD*(Cβ –Cu)(Met92) →LP*(Cu38)	–	–	213.86–0.02–0.109	–
BD*(Cβ-Cu)(Met92) →Ry*(Cu38)	–	–	43.29–0.13–0.126	–
LP(Nδ)(His37) →LP*(Ag)	–	28.51–0.72–0.190	–	–
LP(Nϵ)(His37)→BD*(Nδ– Cϵ)(His37)	–	75.04–0.47–0.239	–	–
LP(Nδ)(His37) →LP*(Ag)	–	29.53–0.78–0.200	–	–
LP(Nϵ)(His87)→ BD*(Nδ– Cϵ)(His87)	–	–	–	35.79–0.48–0.168
BD (Cβ -Sγ)(His87)→ LP*(Cd)	–	–	–	18.82–0.33–0.108

3.6 AIM analysis

Table 6 shows the results of AIM analysis for all active site complexes. In the case of copper (I) active site, the data show that high electron density exists for the Cu-N bond of the His37 and His87 ligands. Because of $\nabla^2\rho<0$, no charge depletion is registered for all bonds. Bond ellipticity(ϵ), which can be used to detect conjugation and hyperconjugation, is large only for Cu-S bond of Met92 and Cys84 ligands. For Ag (I) active site, the same trend as for copper (I) active site is seen. The charge density behavior of copper (II) active site is similar to that of copper (I) and silver (I) active sites, but high bond ellipticity is found only for Cu-S of the Cys84 ligand. For the cadmium active site, the behavior of charge density is similar to that for other active sites, but bond ellipticity of Cd-S of Met92 ligand shows a high value.

Table 6: Atom in molecule properties of metal-ligand bonds

X*	X–N(His87)	X–N(His37)	X–S(Met92)	X-S(Cys84)
Cu$^+$				
ρ	0.077	0.077	0.015	0.062
$\nabla^2\rho$	–0.122	–0.117	–0.007	–0.060
ϵ	0.050	0.064	0.101	0.110
Ag$^+$				
ρ	0.065	0.065	0.009	0.047
$\nabla^2\rho$	–0.074	–0.073	–0.005	–0.039
ϵ	0.059	0.069	0.093	0.092
Cu^{2+}				
ρ	0.080	0.086	0.019	0.064
$\nabla^2\rho$	–0.124	–0.136	–0.010	–0.057
ϵ	0.064	0.075	0.077	0.101
Cd^{2+}				
ρ	0.061	0.062	0.032	0.028
$\nabla^2\rho$	–0.061	–0.063	–0.023	–0.021
ϵ	0.070	0.074	0.081	0.079

*X stands for metal ion

4. CONCLUSION

The ion replacement in plastocyanin was studied by the ONIOM calculation method. The results revealed the main difference between the four proteins. Total protein energy of copper (I) and copper (II) was found to be lower than that of silver (I) and cadmium (II) proteins, respectively. Also, HOMO and LUMO orbital energies of copper (I) and cadimum (II) active sites are lower than those of silver (I) and copper (II) active sites. Natural charges of atoms in the four active sites illustrated that substitution of ion in plastocyanin can cause different charge distribution in the plastocyanin active site. Also, atom in molecule theory showed different electronic density and bond ellipticity for bonds of the central metal ion with atoms of surrounding ligands. Although the substitution of silver (I) with copper (I) in PAC spectroscopy can help to derive useful information about binding of plastocyanin to photosytem I, ONIOM results show that the electronic structures of the substituted active sites are different.

REFERENCES

1 R. F. M. F. O. I. Erdogan, International Journal of Quantum Chemistry (SCI) **111**, 174 (2011).
2 K. A. O'Brien, Salter, E. A. & Wierzbicki, International Journal of Quantum Chemistry (SCI) **107**, 2197 (2007).
3 M. P. G. Gleeson, D., Journal of Chemical Information and Modeling **49**, 670 (2009).
4 T. M. Kerdcharoen, K., Chemical Physics Letters **355**, 257 (2002).
5 D. M. L. York, T.-S.; Lundberg, M.; Morokuma; Keiji, In Multi-scale Quantum Models for Biocatalysis, Springer Netherlands **7**, 21 (2009).

6   T. A. Kar, B.; Duan, X.; Pachter, R., Chemical Physics Letters **392**, 176 (2004).

7   S. T. Namuangruk, D.; Limtrakul, J., Journal of Molecular Catalysis A: Chemical **256**, 113 (2006).

8   A. V. F. Steven M. A. Donald, Feliu Maseras, Canadian Journal of Chemistry **87**, 1273 (2009).

9   B. O. Roos, ChemInform Abstract **30**, 19 (1999).

10   S. N. S. Datta, J.; Pandey, A., Journal of Physical Chemistry B **108**, 8007 (2004).

11   P. J. Matěj, V., Molecular Physics **106**, 2733 (2008).

12   E. S. Danielsen, H. V.; Bauer, R.; Hemmingsen, L.; Bjerrum, M. J.; Hansson, Biochemistry **38**, 11531 (1999).

13   K. H. Sas, A.; Hemmingsen, L.; Danielsen, E.; Gendal, L., Journal of Biological Inorganic Chemistry **11**, 409 (2006).

14   A. D. Becke, Journal of Chemical Physics **98**, 1372 (1993).

15   A. D. Becke, Journal of Chemical Physics **98**, 5648 (1993).

16   P. J. W. Hay, W. R. Wadt, Journal of Chemical Physics **82**, 270 (1985).

17   D. H. e. Andrae, U.; Dolg, M.; Stoll, H.; Preuß, H.,, Theoretical Chemistry Accounts: Theory, Computation, and Modeling (Theoretica Chimica Acta) **77**, 123 (1990).

18   D. H. e. Andrae, U.; Dolg, M.; Stoll, H.; Preuß, H., Theoretical Chemistry Accounts: Theory, Computation, and Modeling (Theoretica Chimica Acta) **78**, 247 (1991).

19   M. J. Frisch, G. W. T., H. B. Schlegel, G. E. Scuseria, M. A. Robb, J. R. Cheeseman, J. A. Montgomery, T. Vreven, K. N. Kudin, J. C. Burant, J. M. Millam, S. S. Iyengar, J. Tomasi, V. Barone, B. Mennucci, M. Cossi, G. Scalmani, N. Rega, G. A. Petersson, H. Nakatsuji, M. Hada, M. Ehara, K. Toyota, R. Fukuda, J. Hasegawa, M. Ishida, T. Nakajima, Y. Honda, O. Kitao, H. Nakai, M. Klene, X. Li, J. E. Knox, H. P. Hratchian, J. B. Cross, V. Bakken, C. Adamo, J. Jaramillo, R. Gomperts, R. E. Stratmann, O. Yazyev, A. J. Austin, R. Cammi, C. Pomelli, J. W. Ochterski, P. Y. Ayala, K. Morokuma, G. A. Voth, P. Salvador, J. J. Dannenberg, V. G. Zakrzewski, S. Dapprich, A. D. Daniels, M. C. Strain, O. Farkas, D. K. Malick, A. D. Rabuck, K. Raghavachari, J. B. Foresman, J. V. Ortiz, Q. Cui, A. G. Baboul, S. Clifford, J. Cioslowski, B. B. Stefanov, G. Liu, A. Liashenko, P. Piskorz, I. Komaromi, R. L. Martin, D. J. Fox, T. Keith, M. A. Al-Laham, C. Y. Peng, A. Nanayakkara, M. Challacombe, P. M. W. Gill, B. Johnson, W. Chen, M. W. Wong, C. Gonzalez, J. A. Pople, Gaussian 03, Revision B.03; Gaussian. Inc.Wallingford, CT, U.S: 2004.

20   A. E. C. Reed, L. A.; Weinhold, F., Chem. Rev. **88** 899 (1988).

21   R. F. W. Bader, Atoms in Molecules: A. Quantum Theory; Oxford University. Press: Oxford, UK, (1990).

22   R. Bader, Atoms in Molecules: A Quantum Theory. Oxford University Press: USA, (1994.).

23   R. F. W. Bader, Chemical Reviews **91** 893 (1991).

24   R. F. W. Bader Accounts of Chemical Research **18**, 9 (1985).

АВ INITIO-ИЗСЛЕДВАНЕ НА ЗАМЕСТВАНЕТО НА ЙОНИ В ПРОТЕИНА ПЛАСТОЦИАНИН В СПАНАКА

М. Реза Хусаиндокт[2], М. Сарголзаеи[1,2*], М. Реза Бозоргмер[3]

[1] *Лаборатория по биофизикохимия, Катедра по химия, Научен факултет, Университет Фердоуси в Машхад, Машхад, Иран*

[2] *Изследователски център по биотехнология при Университет Фердоуси в Машхад, Машхад, Иран*

[3] *Катедра по химия,Department of Chemistry, Научен факултет, Клон Машхад,Mashhad Branch, Ислямски университет Азад, Машхад, Иран*

(Резюме)

Замяната на йони в активните центрове на протеини предизвиква значителен интерес поради нейното приложение при някои спектроскопски методи, например при PACS (Perturbed Angular Correlation Spectroscopy). Теоретичното разглеждане на замяната на йони в пластоцианина е извършено с помощта двуслойния ONIOM-метод. Медните йони (едно и двувалентни) в активния център на пластоцианина се заместват съответно със сребърни (I) и кадмий (II). Извършена е оптимизация на четирите протеина с LANL2DZ и SDD базисни мрежи. Молекулните орбитали, естествените орбитали на връзките и атомите са използвани за определяне на електронните структури на четирите активни центрове. Общата енергия на пластоцианина с мед (I) е по-ниска от тази на пластоцианин със сребро (I). Пластоцианинът с мед (II) показва по-ниска енергия от този с кадмий (II). НОМО и LUMO-орбиталните енергии на активните центрове с мед (I) и кадмий (II) са по-ниски от тези при сребро (I) и мед (II). Четирите активни центрове показват различно разпределение на заряда. Установени са различни стойности на електронната плътност и елиптичността на връзките за четирите активни центрове.

Evaluation of the potential application of $La_{2-x}Sr_xCuO_{4-\delta}$ and $Nd_{2-x}Sr_xNiO_{4-\delta}$ as alternative cathode materials for solid oxide fuel cells

S. Kozhukharov, M. Machkova, V. Kozhukharov, S.P. Simeonov*

Laboratory of Advanced Materials Research, University of Chemical Technology and Metallurgy, Sofia, Bulgaria

Comparative analysis between two cathode materials for the preparation of solid oxide fuel cells was performed. Series of layered perovskites $La_{2-x}Sr_xCuO_{4-\delta}$ were synthesized by the nitrate citrate method with different levels of Sr - substitution. Cathode materials area specific resistance (ASR) at different temperatures and fuel cells resistances at different temperatures are the indicative criteria the present work is focused on, in order to evaluate and compare the operating characteristics of both cathodes. For the determination of these parameters electrochemical impedance spectroscopy (EIS) over "cathode/interlayer/electrolyte/interlayer/cathode" structured symmetrical cells for the ASR determination was applied. Afterwards voltammograms over "anode/electrolyte/interlayer/cathode" structured anode supported SOFC (AS–SOFC) for the determination of cells resistance were acquired. Voltamogramms were recorded for different times of SOFCs exposure under real operation conditions, thus evaluating cells capacity to operate for a long period of time. AFM topography observations were performed in order to indirectly explain the differences in the behavior of the samples tested. The potential application of both cathode materials as alternative SOFC was evaluated and conclusions were drawn.

Keywords: SOFC, cathodes, $La_{2-x}Sr_xCuO_{4-\delta}$, $Nd_{2-x}Sr_xNiO_{4-\delta}$, perovskites

INTRODUCTION

During the recent decades the demand for new energetic sources has sharply increased. In this context, the solid oxide fuel cells (SOFCs) have been found to be an attractive alternative of the already utilized energetic systems. Furthermore, SOFCs could be used for co-generation of electricity and valuable products for the chemical industry as well [1 – 4]. Nevertheless, the application of SOFCs as industrial integrated products recommends standardization in order to guarantee their reliable and harmless usage for prolonged periods of time.

Each layer of the multilayered ceramic element performs its own function. The most widely spread materials for SOFC application are described in several review papers [5, 6]. Generally the SOFC is composed by cathode (air electrode), anode (fuel electrode), electrolyte, functional layers in between, interconnectors and sealings.

The requirements, related to the SOFC household and industrial exploitation, predetermine the large scientific R&D activities intended for new ceramic materials and technologies for their synthesis. Thus, studies are carried out on the synthesis and characterization of cathode materials as: $La_{0,5}Sr_{0,5}CoO_3$, $LaCoO_3$, $LaNi_{0,6}Fe_{0,4}O_3$ [7, 8], $Ce_{0,9}$ $Sm_{0,1}O_{1,95}$, $La_{0,5}Sr_{0,5}Co_{0,2}Fe_{0,8}O_3$ [9, 10], $LaMnO_3$, $La_{1-x}Sr_xCoO_{3-\delta}$, $La_{1-x}Sr_xCo_{1-y}Fe_yO_{3-\delta}$ [11, 12] and others [13]. Typical electrolyte in the SOFC technology is yttria stabilized zirconia (YSZ) owing to its ionic conductivity and electrical insulating properties at temperatures 700–1000ºC. Disadvantage of this material is its relatively high chemical activity towards some elements that are often present in the cathode composition. This can be overcome by including gadolinium doped ceria (CGO) as barrier interlayers between the cathode and the electrolyte. In most cases the anode material is Ni-cermet as a porous fuel electrode.

It was established from previous works, that there is a permanently increasing interest in the development of new materials for SOFC applications [14]. Nowadays, the evolution of the SOFC technology leads to new challenges. One of the main problems to deal with appears to be the lowering of the operation temperature. New generation of fuel cells - intermediate temperature SOFSs (ITSOFCs) achieves performance at temperatures in the range of 700–850ºC, which allows the use of significantly less expensive construction materials in comparison to the older generation SOFCs with an operation temperature range of 1000ºC. Overcoming of the problem is

* To whom all correspondence should be sent:
E-mail: stefan_sim83@yahoo.com

related to structural and functional changes in the entire fuel cell device.

It was described [15] that at low operation temperatures, the polarization losses and the importance of catalysis of the electrode reactions sharply increase. At the cathode, mixed potentials can arise when traces of combustible substances determine the electrode potential in competition with oxygen. In the present work temperatures below 700ºC will not be applied during tests due to the operation characteristics of the YSZ electrolyte. It is known that its ionic conductivity cannot be activated below 700ºC.

The aim of the present research work is to compare the variations of two cells resistances as a function of the operating temperature as one of the indicative criteria for the fuel cells performance. The variation of the resistance as a function of the test duration was also indicated. Symmetrical cells with cathode-electrolyte-cathode structure were used to determine the cathode resistance by electrochemical impedance spectroscopy (EIS) where the area specific resistance (ASR) was determined for both cathode materials. Later on two different anode supported fuel cells (AS-SOFC) with anode-electrolyte-interlayer-cathode structure were prepared and tested with the two different cathode materials. The variation of the fuel cells resistance as a function of the current density was determined. AFM observations were carried out in order to explain the differences between the fuel cells with the different cathodes.

EXPERIMENTAL

Cell assembling

Two kinds of test objects were used in the present work:

(i) Symmetric cells **-** They were composed by two cathode layers screen printed on both sides of the electrolyte layer. CGO containing paste was screen printed, dried and sintered as a barrier layer between the cathode and the YSZ, thus preventing the formation of insulating layers from the cathode components and the electrolyte. It was synthesized *via* classical ceramic method. Preliminarily prepared pastes containing La₂₋ₓSrₓCuO₄₋δ and Nd₂₋ₓSrₓNiO₄₋δ, were afterwards screen printed on both sides of the sintered solid electrolyte.

(ii) Anode supported SOFC - For AS-SOFC preparation, anode supported half cells were used. They were supplied from SOFCPOWER S.r.l. [16], composed by YSZ- solid electrolyte and a Ni cermet anode. Functional CGO interlayer was

deposited *via* screen printing, followed by screen printing deposition of La₂₋ₓSrₓCuO₄, and Nd₂₋ₓSrₓNiO₄₋δ cathode materials.

After each cycle of deposition every layer was sintered in an individual thermal cycle. The primer CGO layer was treated in the following cycle: an increase with a step of 1ºC/min up to 400ºC, followed by a 3ºC/min step up to 1250ºC. The final cooling rate was 5ºC/min. The cathode layer was treated at 900ºC for 2h and a cooling rate at 5ºC/min was applied. Thus, the obtained bi-layer film had a total thickness of 30 μm.

Characterization procedures

The following methods were applied for characterization of the cells obtained.

(i)- Determination of the area specific resistance (ASR) of both cathode materials on symmetrical cells. It was determined by high temperature AC impedance spectroscopy on Autolab PGStat-30, produced by EcoChemie, The Netherlands. The measurements were performed at open circuit voltage (OCV) in the frequency range of 1 MHz to 0,1 Hz in the temperature interval between 500 and 700ºC. The EIS analysis yielded results on the determination of the polarization resistance of the cathode materials. The polarization resistance obtained on a Nyquist plot of the EIS curves was used in the calculation of the ASR.

(ii)- V - J characteristics of the anode supported fuel cell. It was performed in a high temperature furnace with controlled gas flows, product of ECN – The Netherlands. Acquisition of the voltammograms: it was performed in a galvanostatic regime at 50mA/cm² for 180 sec. The voltammograms were done at the maximum threshold: 0,420A/cm² and at the minimum threshold: 500mV. The voltammetric measurements were executed at 900, 850, 800, 750 and 700ºC, respectively. The test procedure was started after initial achieving of the operation temperature in nitrogen atmosphere for reduction of NiO into Niº and stabilizing the Ni:YSZ cermet anode layer and stable charging of the cell up to 0.3 A/cm² and retention of this temperature for 2 h.

RESULTS AND DISCUSSION

Determination of the Area Specific Resistance.

It was determined on symmetric cells, prepared as was described above. After the polarization resistance was obtained from the EIS measurements, the ASR was calculated according to equation 1, where S is the area of the tested

electrode. The division into two gives the value for one of the cathode layers.

$$ASR = \frac{R_p \times S}{2} \qquad (1)$$

It was established that the samples of the symmetric cells with the respective cathodes show almost identical values of the ASR for the five temperatures in the range from 500 to 700°C, as is shown in Figure 1(a , b) below.
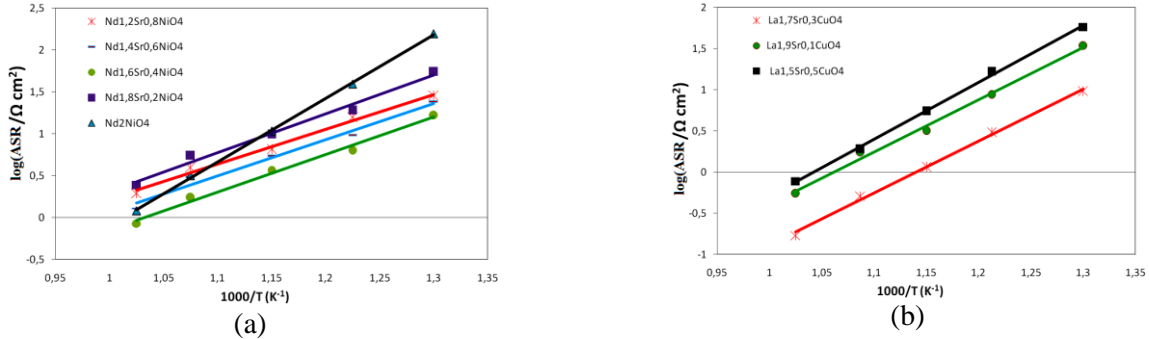

(a)   (b)

Fig. 1. Values of the area specific resistance of a) $Nd_{2-x}Sr_xNiO_4$ and b) $La_{2-x}Sr_xCuO_4$ for different temperatures, expressed in 1000/T (K^{-1})
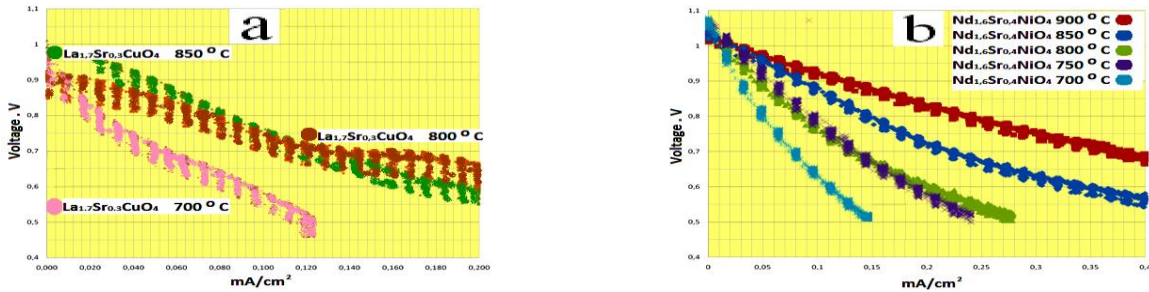
Fig. 2. SOFC Voltammograms acquired for $La_{1,7}Sr_{0,3}CuO_{4-δ}$ at 700, 800, 850^{0}C   (b) $Nd_{1,6}Sr_{0,4}NiO_{4-δ}$, at 700, 750, 800, 850, 900^{0}C.

The similarity of the diagrams evinces that both electrodes possess identical area specific resistances, and even almost the same trends of dependence of ASR *vs.* temperature. In addition, the analysis shows a low cathode resistance that allows us to consider both materials as suitable for cathode materials application. As shown in the literature, the resistance of IT SOFC cathode should be in the order of 1 Ωcm^2 at 700ºC [16, 17].

The performed analysis showed different ASR values obtained for the different levels of Sr-substitution. The lowest resistance values were detected for $La_{1,7}Sr_{0,3}CuO_4$, as well as for $Nd_{1,6}Sr_{0,4}NiO_{4-δ}$ - tested samples. The latter two cathode materials were used in the subsequent experiments of the complete AS-SOFCs tests; simplifying these materials with indexes LSC and NSN, respectively.

3.2. V–J characteristics

There is a clear deviation between the theoretical and the real correlation values of the electric potential and the current density [18]. This difference is determined by losses caused by various sources, as for example: 1 – losses from

activation of the electrodes; 2 – losses from Ohmic polarization, (i.e: polarization resistance R_p), and 3 – losses from the gas transport, caused by the diffusion between the feeding combustible gas and the gaseous products. Here it should be mentioned that the presence of the combustion products decreases the concentration of the feeding gas and consequently – its partial pressure. It is clear that the rate of all these losses depends on the composition of the SOFC components and on their properties, (i.e. density, thickness, porosity, etc.). That was the reason we performed a comparative analysis on the electrochemical behavior of cells, either with $La_{1,7}Sr_{0,3}CuO_4$, or with $Nd_{1,6}Sr_{0,4}NiO_{4-δ}$ at different operation temperatures**.** The results obtained are presented in Figure 2 (a,b) for both LSC and NSN samples.

Figure 2 shows the considerable difference in the behaviour of the respective cells. The correlation of the results of Figure 1 and Figure 2 leads to a surprising fact: although the characteristics shown in Figure 1 are almost identical, the voltammograms in Figure 2 reveal remarkable differences for the complete ITSOFC with the respective cathodes. The open circuit

209

voltages for the LSC sample, position (a) are in the range of 850 mV and do not reach 1000 mV, whereas they are between 1000 and 1100 mV in position (b) for the NSN sample. Additionally, at 700°C the cell with the former cathodic material achieves the 500 mV threshold at 0,120mA/cm^2, while that with the latter one reaches it at 0,150mA/cm^2. Higher differences between LSC and NSN cathode cells even arise at elevated temperatures. Thus, at 800 and 850°C the cells achieve the 500 mV threshold at about 0,240 mA/cm^2, whereas the cells with Ni-based cathodes reach it at 0,275 mA/cm^2 at 800°C, and at more than 0,400 mA/cm^2 at 850°C, respectively. At 900°C no voltammogram for the lanthanum cathode cells could be detected, because the material suffered partial fusion at this temperature.

Furthermore, the shapes of the curves reveal supplemental differences. Possible explanation about the phenomenon in the latter case could be the decomposition of the water molecules, rendering additional H$_2$ supply. In this way, at higher current densities, the additional decomposition of the water, (coming either from the fuel humidity, or as a product of the H$_2 \rightarrow$ H$_2$O$_{(g)}$), could deliver additional quantities of hydrogen, thus increasing the efficiency of the entire ITSOFC.

The curves for 800 and 850°C of position (a) reveal almost indistinguishable double inflections, indicating the presence of different processes in the respective ranges of the voltammograms. They could originate from structural changes in the respective cathode materials, as is explained in the next paragraph.

The polarization resistance R$_p$ could be calculated by equation 2, taking in account that the polarization resistance expresses the relation between the changes of current density (ΔJ) and the voltage (ΔV) in a given range.

$$R_p = \frac{\Delta V}{\Delta J}, \ \Omega/\text{cm}^2. \qquad (2)$$

Both cells showed their lowest R$_p$ values at 700°C. Their values were estimated to be 3.666 kΩ/cm^2 for LSC and 3.333 kΩ/cm^2 for NSN, respectively. In other words, at 700°C the cell with the NSN electrode slightly exceeds that with the LSC one. Nevertheless, at 850°C the R$_p$ value for nickelate was estimated to be 0.75kΩ/cm^2, whereas for LSC it reaches 1.5 kΩ/cm^2. This fact is an additional evidence for the better behavior of Nd$_{1,6}$Sr$_{0,4}$NiO$_{4-\delta}$, compared to La$_{1,7}$Sr$_{0,3}$CuO$_{4-\delta}$, at higher temperatures. The contradiction between the identical ASR behavior in Figure 1, and the remarkable differences in Figure 2 is a direct evidence for either the incompatibility of LSC with the rest of the components of the fuel cells, or the presence of cell "destructive" processes at temperatures above 750°C. This contradiction reveals that the cells possess rather distinguishable electrical characteristics, although they are identical for both cathode materials.

3.3. Durability tests

The duration of the time elapsed until the breakdown of whatever industrial product at operation conditions, (i.e. temperature, pressure, etc.), is considered as durability. The breakdown of the respective product appears at the moment of the sharp dissipation of its parameters from their nominal or initial values. Thus, in the present case significant difference between the respective cells arises regarding their durability. Figure 3 shows voltammograms recorded for different times of SOFCs exposure to real operation conditions.
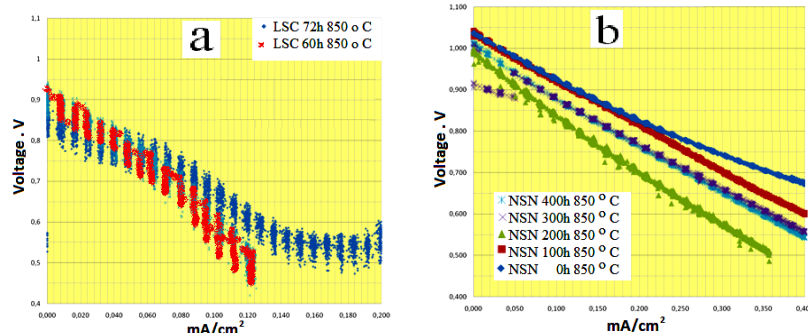
Fig. 3. Voltammograms acquired during the durability tests. (a)- La$_{1,7}$Sr$_{0,3}$CuO$_{4-\delta}$. (b)- Nd$_{1,6}$Sr$_{0,4}$NiO$_{4-\delta}$

Apparently, the durability tests prove the statement that the NSN cathode sample displays excellent durability, incomparable to that of LSC cathode cells. Indeed, the voltammograms maintain the shape of straight lines even after 400 hours for the NSN sample, whereas the LSC sample exhibits curves with clear inflexions even after 60 h. This

means that the durability of NSN cathode exceeds that of LSC by about 6 or 7 times.

Furthermore, the Nd$_{1,6}$Sr$_{0,4}$NiO$_{4-\delta}$ reveals a surprising improvement of their voltammograms after 200 hours. The polarization resistances (R$_P$) for the respective curves could be calculated by the equation 1. Thus, the R$_P$ calculations have evinced the presence of a posterior improvement after 200 hours of exposure. Immediately after the stable charging of the cell, (see experimental part), the NSN-cell sample had R$_P$ equal to 1.000 kΩ/cm^2, compared to 1.430 kΩ/cm^2 after 200 hours and 1.143 kΩ/cm^2 after 400 hours, respectively. The values obtained are an additional evidence of the subsequent improvement of the electric characteristics of the NSN cells. Because the structural transformations for such ceramic materials are generally inconvertible, it looks more likely that the subsequent improvement of the NSN cells after 200 h is a consequence of other

phenomena. Indeed, a hypothetic explanation can be assumed that after deterioration (or inactivation) of a part of the cathode, enhancement of another part takes place. The reason for this enhancement could be the additional portion of H$_2$ originating from the thermal decomposition of water. In this way, H$_2$ undergoes oxidation on the intact zone of the cathode, compensating the obstructed area.

The remarkable difference between the durability of LSC and NSN was observed *via* structural measurements, as well. They are shortly discussed in the next section.

3.4. Surface topology characterization

The inflections in positions (a) of Figures 2 and 3, commented above in the present text could generally be a consequence of structural deterioration of the La$_{1,7}$Sr$_{0,3}$CuO$_4$. This suggestion was confirmed by the AFM observations done and 3D surface topology shown in Figure 4.

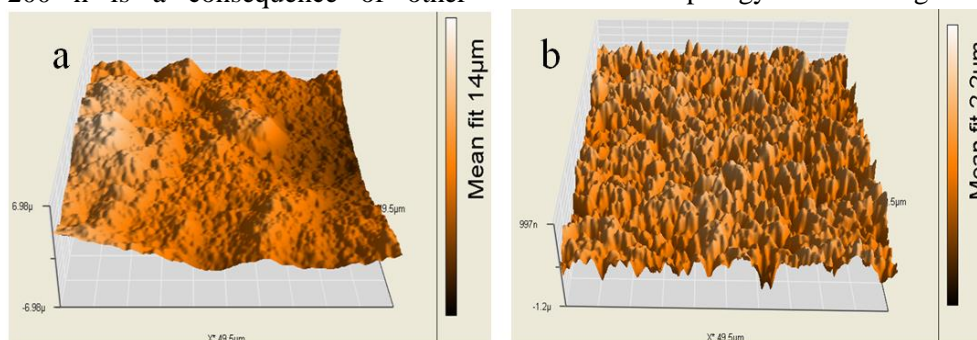**Fig. 4.** AFM 3 D images of cathodes of cells after durability tests. (a)- La$_{1.7}$Sr$_{0.3}$CuO$_{4,}$ after 72 hours. (b)- Nd$_{2-x}$Sr$_x$NiO$_{4-\delta}$, after 400 hours

Figure 4 obviously confirms that the surface of the NSN cathode material is much rougher and its structural conformation is preserved even after 400 hours. This roughness could be an indirect evidence for better porosity and higher specific area. On the contrary, on the image of the LSC cathode (Figure 4-a) different morphology is observed. The reason for this lower porosity is that the cathode material has suffered partial fusion in the high temperature operation conditions. Afterwards, the fused liquid material has filled the pores. Subsequently, the presence of liquid (fused) phase in the electrode obviously leads to posterior agglomeration processes in the structure of the LSC electrode. That is the reason for the uniform distribution of the pores in the latter case (see Fig.4 position b), compared to the irregular distribution of the roughness in the former case (see Fig.4 position a). In other words, the 6 to 7 times lower durability of the former material is caused by partial diffusion of the material. Consequently, the lower durability of LSC originates from its lower thermal resistance.

4. CONCLUSIONS.

After the analysis of the results obtained, the following conclusions could be drawn:

1) Both tested LSC and NSN cathode samples reveal similar trends of evolution of the ASR with the temperature. However, the operation characteristics for all cell samples are rather distinguishable. The remarkable differences between the respective LSC and NSN fuel cells are a direct evidence either for the incompatibility of LSC with the rest cells components or for the incapability of this cathode to operate in the temperature range chosen for the present work. This contradiction reveals that the SOFC possesses rather distinguishable electrical characteristics, although the ASR values of both cathodic materials are identical.

2) After the acquisition of the operation characteristics for the entire cells, it was proved that

LSC samples suffer structural deterioration at temperatures higher than 700ºC. The respective voltammograms are curved, due to presence of inflexions for the SOFC containing $La_{1,7}Sr_{0,3}CuO_{4-\delta}$ cathode. The voltammograms of the NSN cell are straight lines, showing the thermal stability of the NSN cathode material. Furthermore, at 850°C the polarization resistance of LSC (1.5 kΩ/cm^2) is twice higher than that of NSN (0.75 kΩ/cm^2), despite their equal values at 700ºC. This is a clear indication that both cathodes are more suitable for work in the intermediate rather than in the high temperature range.

3) Besides the confirmation of the results from the previous measurements, the durability tests performed show that NSN is 6-7 times more durable than the LSC cathode.

4) The AFM surface topology study undoubtedly shows that the LSC material undergoes partial fusion accompanied by agglomeration processes.

A general conclusion can be made based on the analysis performed. The NSN cathode is a promising material to be included in the given configuration of anode supported zirconia based ITSOFC. As for the LSC material, its potential should be tested in combination with different electrolytes that can achieve ionic conductivity at less aggressive temperatures that should not lead to phase transformation in the cathode structure.

REFERENCES:

1. N. Hart, N. Brandon, M. Day, Shemilt, *J. Mater. Sci.* **36,** 1077 (2001).
2. J. Kilner, *Bol. Soc. Esp. Ceram. Vidrio* **37,** 247 (1997).
3. S. Singhal, *Solid State Ionics,* **135,** (2000).
4. V. Kozhukharov, M. Machkova, M. Ivanova, N. Brashkova, Proc. VIIth. Int. Symposium, Solid Oxide Fuel Cells, (SOFC-VII), EPOCHAL Tsukuba Intern. Congress Centre, Tsukuba (Japan), June 2001; H. Yokokawa, S. C. Singhal (Eds.), The Electrochem. Soc. Inc., Pennington NJ (USA) 2001; pp. 244 – 254
5. V. Kozhukharov, N. Brashkova, M. Ivanova, J. Carda, M. Machkova, *Bol. Soc. Esp. Ceram. Vidrio* **41,** 471 (2002).
6. V. Kozhukharov, M. Machkova, N. Brashkova, G. Tzaneva, Proc. 13-th. Conference on Glass and Ceramics 29 Sept.- 1-Oct. 1999, Varna Bulgaria Vol. **II** Ceramics. B. Samuneva, S. Bachvarov, I. Gutzov, Y. Dimitriev (Eds.); Publ. House "Science Invest" (1999), p. 19
7. R. Chiba, F. Yoshimura, Y. Sakurai, Y. Tabata, M. Arakawa, *Solid State Ionics* **175**, 23 (2004).
8. M. Jorgensen, S. Primdahl, M. Mogensen, *Electrochim. Acta* **44,** 4195 (1999).
9. J. Zhang, Y. Ji, H. Gao, T. He, J. Liu, *J. of Alloys Compounds* **395,** 322 (2005).
10. Y. Liu, S. Hashimoto, K. Nishino, K. Takei, M. Mori, *J. Power Sources* **164,** 56 (2007).
11. J. Fergus, R. Huy, X. Li, D. Wilkinson, J. Zhang (Eds.), Solid Oxide Fuel Cells: Materials Properties and Performance, CRC press (2009) p. 131
12. M.B. Lopez, Ph.D. Thesis, Universidad Autonoma de Barcelona, (Spain), 2007.
13. D. Todorovsky, R. Todorovska, N. Petrova, M. Uzunova-Bujnova, M. Milanova, S. Anastasova, E. Kashchieva, S. Groudeva-Zotova, *J. Univ. Chem. Tech. Met,* (Sofia) **41,** 93 (2006).
14. S. Simeonov, M. Machkova, V. Kozhukharov, J-G. Grenier, *Annual Proceed. University of Rousse,* (Bulgaria) **49,** (9.1), 8 (2010)available at: http://conf.ru.acad.bg/bg/docs/cp10/9.1/9.1-1.pdf
15. "High temperature Solid Oxide Fuel Cells: Fundamentals, Design and Applications". S. Singhal, K. Kendall (Eds.), Elsevier, Oxford, (UK), 2003, p. 44.
16. SOFCPOWER S.r.l., available at: http://www.sofcpower.com/index.php?page=home&hl=en_GB,
17. L-P. Sun, Q. Li, H. Zhao, L-H. Huo, J-C. Grenier, *J. Power Sources* **183,** 43 (2008).
18. Q. Li, H. Zhao, L. Huo, L. Sun, X. Cheng, J-C. Grenier, *Electrochem. Commun.* **9,** 1508 (2007).
19. M. Gong, X. Liu, J. Trembly, C. Johnson, *J. Power Sources,* **168**, 289 (2007).

ИЗСЛЕДВАНЕ И ОЦЕНКА НА ПОТЕНЦИАЛНОТО ПРИЛОЖЕНИЕ КАТО АЛТЕРНАТИВНИ КАТОДНИ МАТЕРИАЛИ ЗА ТВЪРДООКИСНИ ГОРИВНИ КЛЕТКИ НА La$_{2-x}$Sr$_x$CuO$_{4-δ}$ И Nd$_{2-x}$Sr$_x$NiO$_{4-δ}$,

С. Кожухаров, М. Мачкова, В. Кожухаров, С. П. Симеонов

Химикотехнологичен и металургичен университет, 1756 София

(Резюме)

Проведен беше сравнителен анализ между двата катодни материала за прилагането им в твърдоокисни горивни клетки. Серия от т. нар. слоеви перовскити тип La$_{2-x}$Sr$_x$CuO$_{4-δ}$ бяха синтезирани по нитрат-цитратен метод с различно степен на заместване със Sr. Специфичното повърхностно съпротивление (ASR) при различни температури,както и съпротивленията на самите горивни клетки при различни температури са показателния критерии върху които се фокусира настоящата работа с цел да се сравнят операционните характеристики на двата катода. За определянето на тези параметри бе проведен анализ със импедансна спектроскопия (EIS) върху симетрично структурирани клетки "катод/междинен функционален слой/електролит/междинен функционален слой/катод" за определянето на ASR. След което бяха получени волтамограми от анодно базирани горивни клетки "анод/електролит/междинен функционален слой/катод" за определянето на съпротивлението на така окомплектованите горивни клетки. Бяха снети волтамограми при различно време на подлагане под реални операционни условия, за оценка на капацитета на работа за дълги периоди от време. Атомно силова микроскопия AFM беше приложена за наблюдения на топографията и косвеното обяснение на разликите в поведението на тестваните образци. Потенциалното прилагане и на двата катодни материала като алтернативи на съществуващите беше оценено със съотвтните изводи и заключения.

Optimal energy saving and management in antibiotics production

D. Dobrudzhaliev[2], D. Nikolova[1], B. Ivanov[1]*, A. Aidan[3]

[1]*Institute of Chemical Engineering-BAS, Acad. G. Bonchev Str., Bl. 103, Sofia 1113-Bulgaria**

[2] *Prof. Dr. Assen Zlatarov University Bourgas Prof. Yakimov Str. 1, 8000 Bourgas-Bulgaria*

[3]*American University of Sharjah, PO Box 26666, Sharjah United Arab Emirates*

Energy efficiency is a very important indicator in the stability assessment of industrial processes. The optimal utilization of energy is a vital task today, as it determines the state of environment, technology and product price. The present work describes a method for the reduction of energy consumption by heat integration, in a system of bioreactors for the production of antibiotics. A scheme for heat integration of two heat reservoirs is suggested, ensuring performance at different time intervals. A mathematical model of the processes taking place in the two reactors is developed. On the base of the model, a strategy for optimal control of energy resources using heat integration of two heat reservoirs is proposed. The optimization task is formulated in terms of the Mixed Integral Non-Linear Programming (MINLP). The proposed method is applied to a real industrial process for antibiotics production.

INTRODUCTION

There is a contemporary problem with efficient energy consumption. The energy sources are constantly decreasing and have a negative effect on the environment, thereby forcing the search for alternative resources.

In industrial systems, the optimal utilization of the energy resources is one of the main problems [1]. All up-to-date scientific achievements and engineering practices are involved in solving these problems as early as the design phase. In existing production lines, it is necessary to make the most of the energy using suitable engineering solutions.

In most of the chemical and biochemical productions, a number of heating and cooling processes are usually involved according to the technological scheme [2, 3]. They most often result in major energy losses. The production of antibiotics is one of such processes [4]. In this case, one could effectively decrease, as well as control, the energy consumption, using the approach of heat integration of the production processes.

AIM

The aim of the present work is to suggest a practical method for energy saving by heat integration of a system of bioreactors in the production of antibiotics, using heat reservoirs and their control methods. Thus, the costs of energy resources could be decreased.

PROBLEM DESCRIPTION

A bioreactor system for the production of antibiotics was studied. The process involves preparation of a nutrient, followed by its sterilization and cooling to working temperature for the fermentation process. The nutrient preparation and its sterilization involve the use of water vapor as an energy carrier. The fermentation is performed after cooling the sterilized nutrient to working temperature of 30°C. Technical and cooled water is used for this process. The idea for reduction of energy consumption is to integrate these two processes. If a certain reactor is in a regime of cooling, then the energy released could be stored in a heat reservoir to be used for the preparation of nutrients in another reactor. This would save energy in the second reactor, and also reduce the amount of technical water required for these processes. The idea can be implemented by designing a proper scheme. Furthermore, the major factors providing maximum utilization of the internal energy in both reactors should be determined.

Figs. 1 (a) and (b) show such a scheme for running the processes. The determination of the controlling factors is reduced to the parameters of the time intervals. The process conditions should provide a minimum value of the energy used by the external systems.

* To whom all correspondence should be sent:
E-mail: bivanov@bas.bg

PRODUCTION OF ANTIBIOTICS

One of the most common methods used for the production of antibiotics is the preparation of the substrate by fermentation. It is carried out in bioreactors, and the sequence of processes and their conditions are listed below:

Stage 1:Nutrient preparation

*1.*This process is carried out by mixing micelles and nutrient in a subsidiary reactor.

Stage 2:Fermentation components

1. Mixing of component V_1 from Tank *A* with V_{21} with water at 20ºC (*CW*20) by stirring for 1 hour until nutrition medium *NMA* is obtained.
2. Mixing of component V_1 from Tank *B* with V_{22} *CW*20 by stirring for certain time until nutrition medium *NMB* is obtained.

Stage 3:Fermentation process

1. Transfer of *NMA* to reactor F_C and heat from 20ºC to 55ºC.
2. Heating *NMA* from 55° to 100°C using steam.
3. Sterilization of *NMA* with 100°C steam for about 0.5 h.
4. Transfer of *NMB* to F_C and mixing it with *NMA* to obtain *AB_IAB*.
5. Addition of V_{35} *CW*20.
6. Heat the mixture V_C with vapor to T = 55ºC to obtain medium *NMAB*.
7. Heat the mixture *NMAB* with water vapor from 55ºC to 120ºC.
8. Sterilization of *NMAB* with water vapour at temperature of 120ºC.
9. Cooling *NMAB* from 120ºC to 45ºC using *CW*20.
10. Cooling of *NMAB* from 45ºC to 30ºC using 5ºC cooled water (*CW*5).
11. Addition of *IMX* to *NMAB* up to volume V_{max} to obtain *FM*.
12. Cooling the medium *FM* to T_{fer} using *CW*5 and carry out fermentation for 120 h – 150 h until the product *FB* is obtained.

Stage 4: Dilution

1. Transfer *FB* to an intermediate reservoir.
2. Addition of V_d with water *CW*20 for deactivation to obtain the product *DFB*.

Stage 5: Filtration

1. Filtering the *DFB* to obtain concentrated material *DSC*.

Stage 6: Sterilization of the empty fermenter

1. Washing the empty fermenter with *CW*20.
2. Sterilization of the washed fermenter with water vapor with temperature of 130ºC.
3. Sterilization of the washed fermenter with water vapor with temperature of 130ºC.

PROCESS ORGANIZATION

According to the technology (Stages 1-6), there are a number of processes requiring the use of external energy (*STEAM*, *CW*20, *CW*5) for heating and cooling. The problem with their dependence on external energy sources can be solved by creating conditions for heat integration. In Fig.1, the "H" reactor will be regarded as the fermenter, where the processes 3.1–3.7 have ended. By the end of 3.7, the mixture in the fermenter would have a temperature of T_{str} = 120ºC. Processes 3.8 and 3.9 are carried out at T_{str} = 30ºC.

HEAT INTEGRATION USING HEAT OF THE RESERVOIR

According to the technological regulations, some of the processes require the use of external energy (*STEAM*, *CW*20, *CW*5) for heating and cooling. The reduction of external energy used can be achieved by using a certain scheme of heat integration. The process of "Cooling" the reactor after sterilization does not coincide with the processes of preparation of the nutrient for sterilization in another reactor. For this reason, it is not possible to use the scheme of heat integration suggested in the publication by Boyadjiev *et al.* [4]. Therefore, heat reservoirs must be used to store the energy from the hot reactor, until it is utilized for the preparation of the nutrient in a subsequent reactor. It may also be used in the process of dilution after fermentation. A hot reactor is the fermenter F_H where the processes of feeding the raw materials and sterilization. (3.1-3.7). It should be cooled down to temperature of 30ºC to carry out fermentation. A cold reactor (fermenter) F_C, where the preparation of the nutrient and its sterilization is carried out.
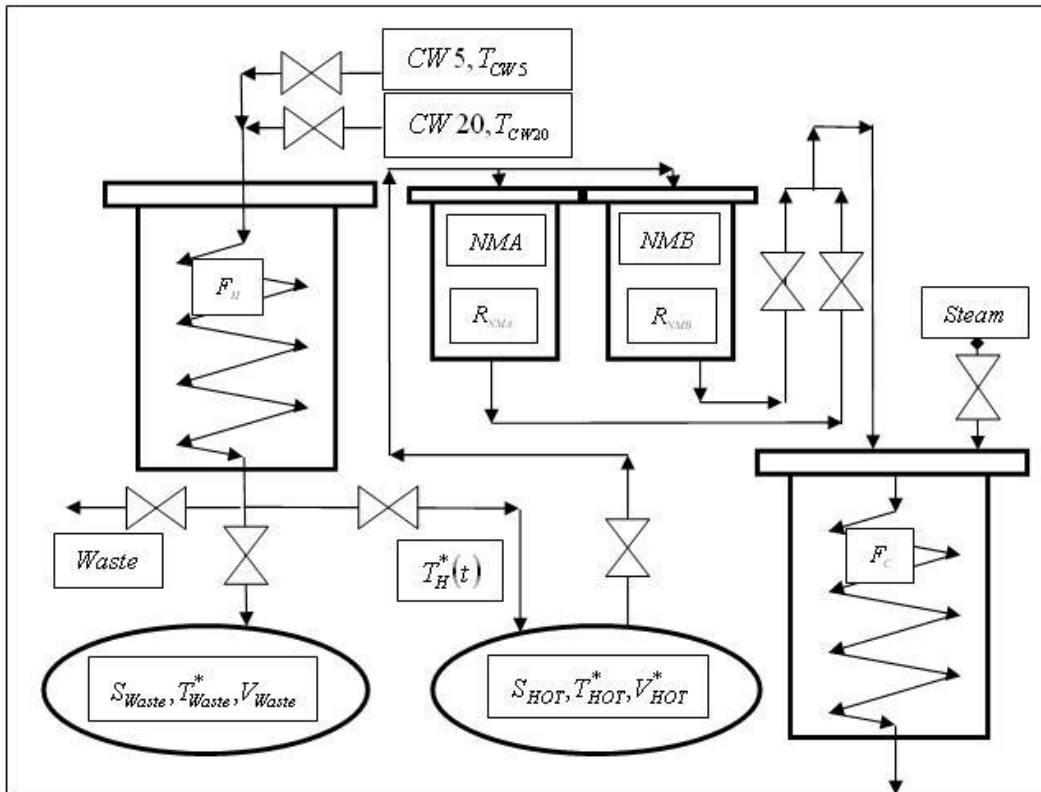
Fig 1a. Heat integration with heat reservoirs.
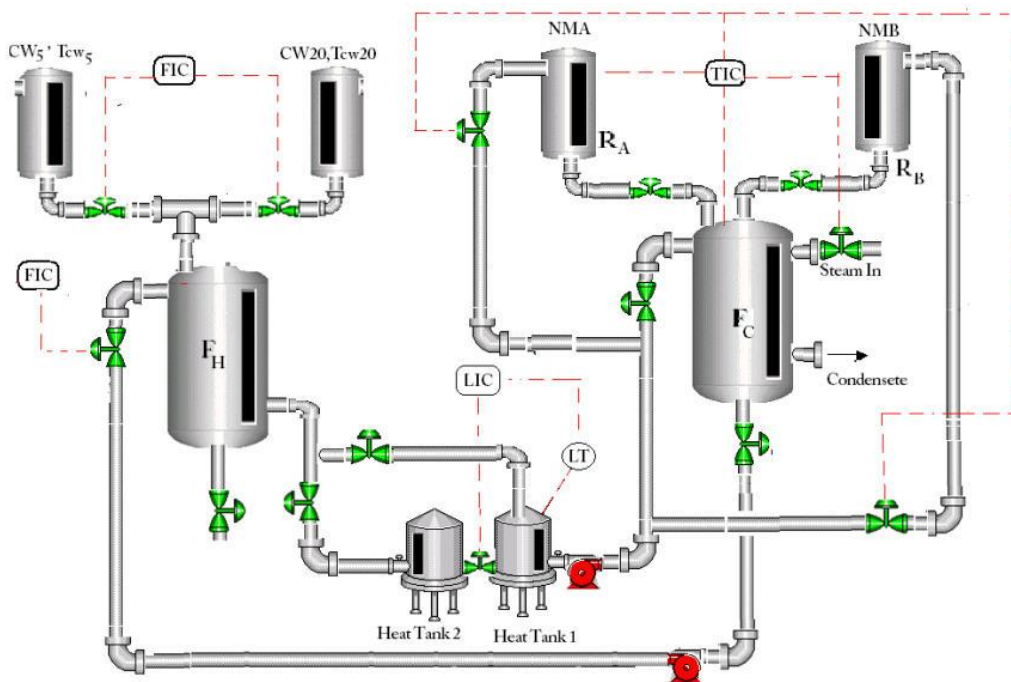
Fig 1b. Piping and instrumentation diagram for heat integration and heat reservoirs.

According to the scheme suggested, the hot reactor F_H is cooled with water $CW20$ using its serpentine. Thus, the water flowing out of the serpentine is stored in heat tank 1. It will

subsequently be used when the processes of nutrient preparation are carried out in another fermentation reactor F_C (processes 3.1-3.5). The volume of this heat tank should be as large as to

contain the amount of water necessary to maintain the processes. The second heat tank is designed to store the water required to carry out process 4.2, and its volume should be as large as the amount of water needed for the process. The design presented in Fig.1 can provide for the processes involved in the technological regulation. The task of process control is to determine the controlling variables ensuring minimum costs (water, vapor) the scheme.

MATHEMATICAL MODEL

It is assumed that for each of the four stages cooling will be carried out by certain dependence of the change of cooling water flow with time. This assumption provides a possibility to use models of the processes with ordinary differential equations. These equations describing the processes of heat- and mass transfer are:

1. An equation describing the change of the temperature of the mixture in reactor F_H when a flow of $CW20$ or $CW5$ of certain flow rate F_{Wi} - is described by an equation for each time interval:

$$\frac{dT_{Fi}}{dt} = \frac{(\Phi_{Wi}-1)}{\Phi_{Wi}} \frac{(F_{Wi}Cp_{Wi})}{V_F Cp_F}(T_i^{in}-T_{Fi}), \forall i \in (1 \div 4) \quad (1)$$

where:

- $T_i^{in} = x_i T_{W20} + (1-x_i)T_{W5}$, $x_i = \{0 \vee 1\}$,

- $\Phi_{Wi} = \left|\frac{T_{Fi}-T_i^{in}}{T_{Fi}-T_i^*}\right| = \exp\left(\frac{UA}{F_{Wi}Cp_{Wi}}\right)$, A is

the heat exchange surface of the serpentine in $[m^2]$,

- U is the total coefficient of heat transfer, in $[kWm^{-2}K^{-1}]$,

- Cp_F, Cp_{W20}, Cp_{W5} in $[kJm^{-3}K^{-1}]$,

- $Cp_{Wi} = x_i Cp_{W20} + (1-x_i)Cp_{W5}$, Cp_{W20} and Cp_{w5} are the specific heat capacities of $CW20$ and $CW5$.

- The flow rate of the cooling water through the serpentine is F_{wi} [m³/s].

2. The temperature at the serpentine outlet is determined for each time interval by the equation:

$$T_i^* = \frac{(\Phi_{Wi}-1)}{\Phi_{Wi}}T_{Fi} + \frac{1}{\Phi_{Wi}}T_i^{in}, \quad \forall i \in (1 \div 4) \quad (2)$$

The solution of equation (1) was to be found under initial condition $T_{Fr}(0)$, where $T_{Fr}(0) = T_{str}(0)$, at $i=1$ and $T_{Fr}(0) = T_{Fri}(0)(t_{i-1})$ at $i>1$. It should be taken into account that the temperature of the water flowing out of the serpentine T_i^* must be lower than that of the material contained in the fermenter T_{Fri} i.e. $T_{Fi} \geq T_i^*$.

3. The volumes of the tanks $S1$, $S2$, SW and their temperatures for each time interval are described by:

$$\left.\begin{array}{l}\frac{dV_{S1}^i}{dt} = y_i^{S1}F_{Wi} \\ Cp_{Wi}V_{S1}^i\frac{dT_{S1}^i}{dt} = y_i^{S1}F_{Wi}Cp_{Wi}(T_i^*-T_{S1}^i)\end{array}\right\}, \forall i \in (1 \div 4) \quad (3)$$

At initial conditions $V_{S1}^i(0)=V_{S1}^{(i-1)}(t_{(i-1)})$, $T_{S1}^i(0)=T_{S1}^{(i-1)}(t_{(i-1)})$ and at $i=1$ for the first time interval – 1 $V_{S1}^i(0)=0$, $T_{S1}^i(0)=T_i^{in}$.

$$\left.\begin{array}{l}\frac{dV_{S2}^i}{dt} = y_i^{S2}F_{Wi} \\ Cp_{Wi}V_{S2}^i\frac{dT_{S2}^i}{dt} = y_i^{S2}F_{Wi}Cp_{Wi}(T_i^*-T_{S2}^i)\end{array}\right\}, \forall i \in (1 \div 4) \quad (4)$$

At initial conditions $V_{S2}^i(0)=V_{S2}^{(i-1)}(t_{(i-1)})$, $T_{S2}^i(0)=T_{S2}^{(i-1)}(t_{(i-1)})$ and at $i=1$ for the first time interval – $V_{S1}^i(0)=0$, $T_{S2}^i(0)=T_i^{in}$.

$$\left.\begin{array}{l}\frac{dV_{SW}^i}{dt} = y_i^{SW}F_{Wi} \\ Cp_{Wi}V_{SW}^i\frac{dT_{SW}^i}{dt} = y_i^{SW}F_{Wi}Cp_{Wi}(T_i^*-T_{SW}^i)\end{array}\right\}, \forall i \in (1 \div 4) \quad (5)$$

At initial conditions $V_{SW}^i(0)=V_{SW}^{(i-1)}(t_{(i-1)})$, $T_{SW}^i(0)=T_{SW}^{(i-1)}(t_{(i-1)})$ and at $i=1$ for the first time interval $-V_{SW}^i(0)=0$, $T_{SW}^i(0)=T_i^{in}$, $y_i^{S1} = \{0 \vee 1\}$, $y_i^{S2} = \{0 \vee 1\}$, $y_i^{SW} = \{0 \vee 1\}$ depending on the that whether the corresponding heat tank is filled during the given time interval or not.

4. Cooling flow values $F_{Wi}(t)$ with time. In general the flow through the cooling serpentine can be presented by the expression:

$$F_{Wi}(t) = \left.\begin{array}{l}sign(F_{MAX}-F_i(t))+ \\ (1-sign(F_{MAX}-F_i(t)))F_{MAX}\end{array}\right\}, \forall i \in (1 \div 4), \quad (6)$$

at

$$F(t)_i = A_i + (B_i - A_i)\exp(-C_i t), \quad \forall i \in (1 \div 4), \quad (7)$$

Where $sign(.)=1$ when $(F_{MAX}-F_i(t)) \geq 0$ and $sign(.)=0$ at $(F_{MAX}-F_i(t))<0$. The values of the coefficients A_i, B_i, C_i should be determined.

Another possible method for controlling the cooling water flow is at a constant flow rate within the intervals. This method is comparatively easy for implementation, but the effectiveness of each method should be compared. In this method the values of the coefficients are $A_i = 0$, $B_i \geq 0$ and $C_i = 0$ for each $i \in (1 \div 4)$.

By the end of the fourth interval, when the procedure ends, the parameters of the heat tanks are $V_{S1}^*, V_{S2}^*, V_{SW}^*$ and $T_{S1}^*, T_{S2}^*, T_{SW}^*$.

AIMS OF HEAT INTEGRATION

The aim of heat integration is to minimize the quantities of resources used (vapor and cooling water) to accomplish the processes in both reactors. This can be achieved by providing maximum possible heat recovery from the cooled reactor. The heat stored in the tank $S1$ is further used for the preparation of the fermentation medium in another reactor, while the amount contained in $S2$ is used in stage 4.2. The energy used during the cooling with water $CW5$ should also be taken into account.

The objective function of heat integration is expressed by:

$$Cost_{INT} = MIN\left\{Cost_{Steam}^* + Cost_{W5}^* + Cost_{Water}^*\right\}, \quad (8)$$

where:

- $Cost_{Steam}^*$ is the cost of vapor,

- $Cost_{W5}^*$ is the cost of energy from $CW5$ by cooling,

- $Cost_{Water}^*$ is the cost of the water used to carry out the processes in the cases when heat reservoirs are used.

These components can be found using the following expressions:

$$\left. \begin{array}{l} Cost_{Steam}^* = C_{Steam} Cp_W V_{S1}^* \left(T_{St}^* - T_{S1}^*\right) + \\ \qquad C_{Steam} Cp_W \left(V_F - V_{S1}^*\right)\left(T_{St}^* - T_{W20}\right), \\ Cost_{W5}^* = C_{W5} Cp_F V_F \left(T_{F3} - T_{F4}\right), \\ Cost_{Water}^* = C_{W20} \left(\begin{array}{l} \left(V_{Water} - V_{S1}^*\right) + \\ \left(V_{4.2.} - V_{S2}^*\right) + V_{SW}^* \end{array} \right) \end{array} \right\}, (9)$$

where,

$$V_{Water} = V_{2.1.} + V_{2.2.} + V_{3.5.},$$

C_{W5} is the cost of unit energy from $CW5$ in lv/kJ,

C_{Steam} is the cost of unit energy for water vapor lv/kJ, while C_{Water}- the cost of the water used $lv./m^3$.

CONTROLLING VARIABLES

The essence of the process control is to determine the controlling variables which would ensure that the minimum amount of resources is used in order to carry out the processes in the two reactors. These variables are:

$$\{A_i, B_i, C_i, t_i\}, \quad \forall i \in \overline{1,4} \qquad (10)$$

as continuous variables defining the cooling water flow rate with time and the duration of each time interval, as well as

$$\left. \begin{array}{l} x_i = \{0 \vee 1\}, \quad y_i^{S1} = \{0 \vee 1\}, \\ y_i^{S2} = \{0 \vee 1\}, \quad y_i^{SW} = \{0 \vee 1\} \end{array} \right\}, \quad \forall i \in \overline{1,4} \quad (11)$$

as Boolean variables determining the sequence by which the cooling agents $CW5$ or $CW20$ are used.

IV. Constraints. The constraints are related to the requirements of the technology towards the duration of the processes and the technical limitations of the cooling devices (serpentine).

$$\left. \begin{array}{l} \sum_{i=1}^{i=4} t_i \leq t_f \\ V_{S1}^* \leq V_{2.1} + V_{2.2} + V_{3.5} \\ V_{S2}^* \leq V_{Waste} \\ \sum \left(y_i^{S1} + y_i^{S2} + y_i^{SW}\right) \leq 1 \\ \left(y_i^{S1} + y_i^{S2} + y_i^{SW}\right) = x_i, \forall i \in \overline{1,4} \\ Cost_{INT} < Cost_{NO\_INT} \\ T_{F4} \leq T_{fer} \end{array} \right\}, (12)$$

where $Cost_{NO\_INT}$ are the costs of energy and water, when the processes are carried out without heat integration.

CONTROL WITH HEAT INTEGRATION

For the control, the variables (10) and (11) should be determined. These variables should give a minimum of the goal function (8) under the limitations posed by (12).

The task formulated is that of MINLP, and it can also be solved using well known methods and programming systems such as GAMS *Brooke A. D. et al. (1998)* [5] or *MATLAB* [6].

MOTIVATING EXAMPLE

The suggested method of heat integration was implemented in a production line for antibiotics. The technological process consists of 6 main stages which have the following parameters (Antibiotics production of Actavista Co., Razgrad branch):

__Stage 1__: Preparation of the nutrient

1. This process is carried out by mixing micelles and the nutrient in a subsidiary reactor having a volume of $5m^3$.

<u>**Stage 2**</u>: *Preparation of the components of the fermentation medium*

1. Mixing $2m^3$ of component *A* with $V_{2.1.} = 10m^3$, with water at 20^oC ($CW20$), and stirring for 1 hour to obtain nutrient *NMA*.

2. Mixing $2m^3$ of component *B* with $V_{2.2.} = 10m^3$, with $CW20$, and stirring for 1 hour to obtain nutrient *NMB*.

<u>**Stage 3**</u>: *Process of fermentation*

1. Transfer of *NMA* to reactor F_C and heating it from 20^oC to 55^oC.

2. Heating *NMA* from 55^oC to 100^oC using water vapor.

3. Sterilization of *NMA* with water vapor at 100^oC for about 30 minutes.

4. Transfer *NMB* to F_C, and mixing it with *NMA* to obtain *AB IAB*.

5. Addition of $V_{3.5.} = 17m^3 to 18m^3$ and $CW20$.

6. Heating the 42 m^3 mixture to $T = 55^oC$ with vapor to obtain the mixture *NMAB*.

7. Heating the mixture *NMAB* from 55^oC to 120^oC with water vapor for 1.5-2 hours.

8. Sterilization of *NMAB* with water vapor at 120^oC for 30 minutes.

9. Cooling *NMAB* from 120^oC to 45^oC using $CW20$.

10. Cooling *NMAB* from 45^oC to 30^oC with 5^oC cooled water ($CW5$) for 30 minutes.

11. Addition of *IMX* to *NMAB* for $t = 0.75h$ to volume of $47m^3$ to obtain *FM*.

12. Cooling the *FM* medium to $t = 30^oC$ using $CW5$ and carry out fermentation for $120h - 150h$ to obtain the product *FB*.

<u>**Stage 4**</u>: *Dilution*

1. Transfer *FB* to an intermediate reservoir for 1 hour.

2. Addition of $23m^3$ $CW20$ for deactivation to obtain the product *DFB*.

<u>**Stage 5**</u>: *Filtration*

1. Filtration of *DFB* for $12h$ to obtain the concentrated material *DSC*.

Stage 6: *Sterilization of the empty fermenter*

1. Washing the empty fermenter with $CW20$.
2. Sterilization of the washed fermenter with water vapor at 130^oC for $2h$.

The process parameters are as follows:

$Cp_F = Cp_{W20} = Cp_{W5} = 4200 kJm^{-3}K^{-1}$, $T_{W5} = 5^oC$,

$T_{W20} = 20.00^oC$, $U = 1.20 kWm^{-2}K^{-1}$,

$A = 56.55m^2$, $T_F(0) = T_{st}^* = T_{F0} = 120^oC$,

$t_f = 6000s$, $V_{3.5.} = 18m^3$, $F_{MAX} = 0.04m^3/s$,

$V_{Waste} = 23m^3$, $V_{2.1.} = V_{2.2.} = 10m^3$,

$C_{W20} = 2.184lv/m^3$, $T_{fer} = 30^oC$,

$C_{Steam} = (CG_{steam}/4.184)10^{-6} lv/kJ$,

$CG_{Steamt} = 277.00 lv/GCal$,

$C_{W5} = (CG_{W5}/4.184)10^{-6} lv/kJ$,

$CG_{W5} = 681.00 lv/GCal$.

The scheme of the heat integration of the processes was implemented, and the optimal controlling parameters were determined. MATLAB R2006a was used for the calculations and the optimization procedure was performed with the FMINCON module.

Table 1 shows the optimal values of the controlling parameters obtained from the solution of the optimization procedure according to the module used.

Table 1. Continuous controlling variables

i	t_{in} [sec.]	A_i	B_i	C_i	x_i	y_i^{S1}	y_i^{S2}	y_i^{SW}	T_{St1} ^oC	$T_{Fi}(t_i)$ ^oC
1	2005.8	0.0	0.0189	0.0	1	1	0	0	64.75	79.50
2	601.9	0.0	0.0382	0.0	1	0	1	0	64.75	69.26
3	1469.8	0.0	0.0400	0.0	1	0	0	1	64.75	50.94
4	1922.5	0.0	0.0400	0.0	0	0	0	0	64.75	30.00

Table 2 Discrete controlling variables

i	t_{in} [sec.]	A_i	B_i	C_i	x_i	y_i^{S1}	y_i^{S2}	y_i^{SW}	T_{St1} ^oC	$T_{Fi}(t_i)$ ^oC
1	1784.8	0.0152	0.0219	1.0686e-4	1	1	0	0	62.2	81.8
2	575.7	0.0383	0.0400	1.0000e-4	1	0	1	0	62.2	71.5
3	1902.3	0.0400	0.0204	0.0100	1	0	0	1	62.2	48.3
4	1737.2	0.0400	0.0399	0.0100	0	0	0	0	62.2	30.0

Table 3. Costs of energy resources

Resource	Costs for system without heat integration $lw.$	Costs for system with heat integration and continuous controlling variables $lw.$	Costs for system with heat integration and discrete controlling variables $lw.$	Saving %
$Cost_{STEAM}$	1168.40	720.84	695.23	38.30(40.49)
$Cost_{W20}$	377.15	161.24	128.41	57.24(66.00)
$Cost_{W5}$	389.89	527.95	601.48	-35.40(-54)
$Cost_{SUM}$	**1935.44**	**1410.03**	**1425.12**	**27.14(26.36)**

The controlling variables for the case when the cooling flows have flow rates constant in time but different in time intervals, i.e. the case of quasi-optimal control, are presented in Table 2.

Fig.2 shows the change of the temperatures in the reactor and at the serpentine outlet during the time intervals for the case when heat integration was used with continuous controlling variables. Fig.3 is for the case with discrete variables.
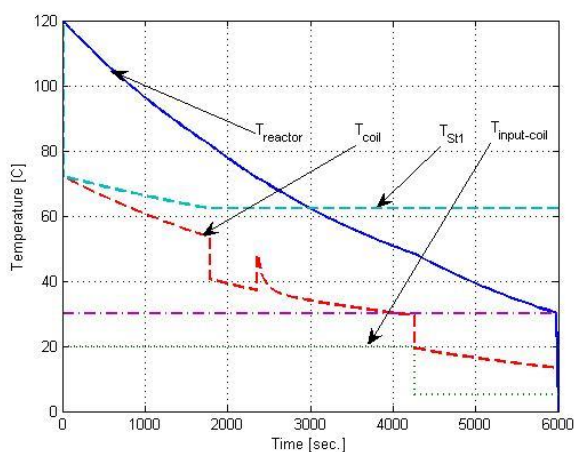

Fig. 2. Change of the temperatures in the reactor for the case of the system with heat integration and continuous controlling variables.

The costs of the resources used for heating and cooling in the system with two heat tanks under optimal control, as well as that for a system without heat integration, are presented in Table 3.

It can be seen that heat integration and optimal control of the process gives substantial reduction of water CW20 used for cooling by 57% and increase of cooling water CW5 by 35%. Simultaneously, the water vapor necessary for the processes decreases by about 38%. The use of heat tanks obviates the necessity to co-ordinate the processes in all reactors, and results in a total saving of energy sources (cooling water and water vapor) of about 27%. It should also be noted that the heat integration system decreased the consumption of water vapor and cooling water CW20.
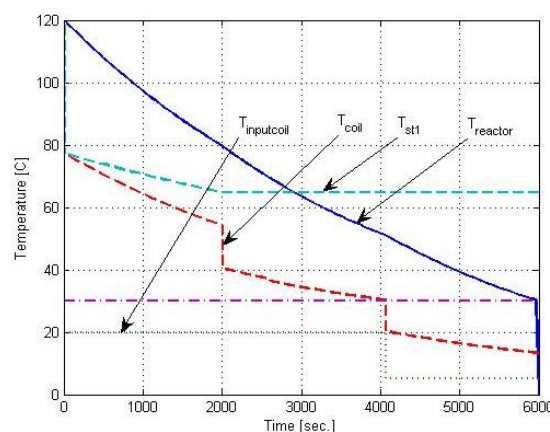
Fig.3. Change of the temperatures in the reactor for the case of the system with heat integration and discrete controlling variables.
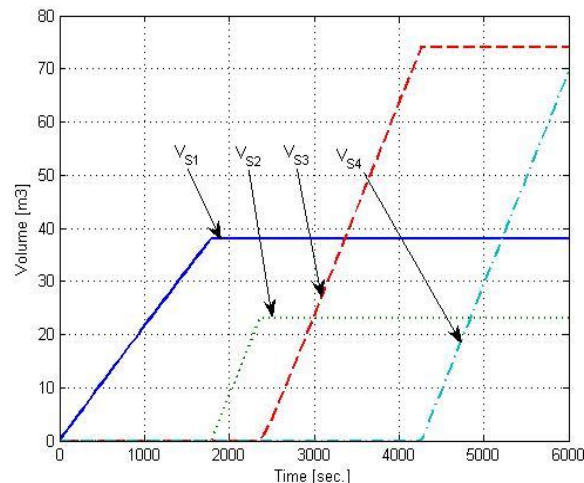
Fig.4. Change of heat tank volumes with time under continuous controlling variables .

The optimal control system requires a special device designed to follow the optimal law for controlling the cooling water flow rates (Fig.4) in the individual intervals. A much simpler law for controlling the cooling water flow rates (Fig.5) can be used by quasi-optimal control, and the economical results obtained would be similar. Furthermore, the quasi-optimal control does not require special controlling devices, thereby making its implementation much easier.

Fig.5. Change of heat tank volumes with time under discrete controlling variables.

Fig. 6. Change of cooling agents flow rates under continuous controlling variables.
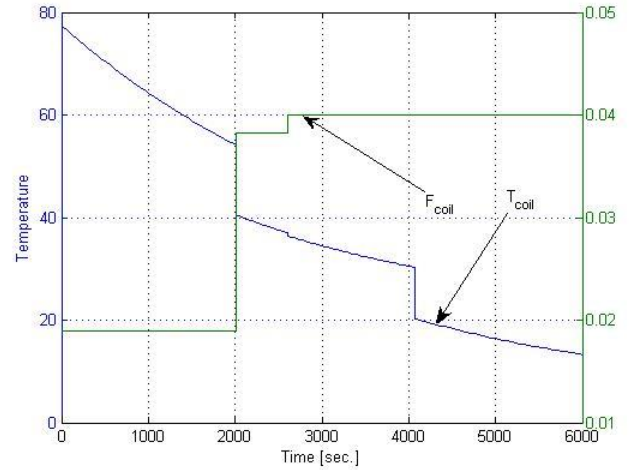
Fig. 7. Change of cooling agents flow rates under discrete controlling variables.

CONCLUSION

On the basis of the obtained results, the following can be concluded:

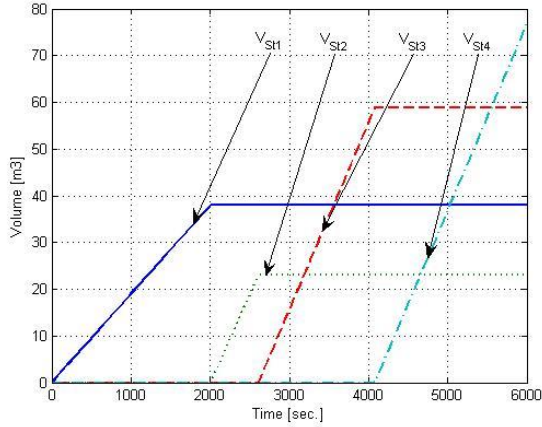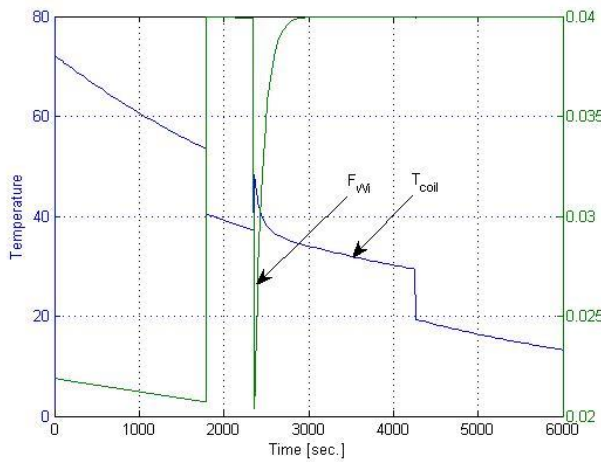A new structure for heat integration with two heat storage tanks and an appropriate mathematical model are developed. An optimal process control strategy is proposed. The optimization task is formulated in terms of the Mixed Integral Non-Linear Programming (MINLP) with minimization of the cost of used resources.

The proposed method is successfully applied to the industrial process of antibiotics production.

NOTATIONS

F_H	Hot reactor
F_C	Cold reactor
$S1$	Heat tank 1
$S2$	Heat tank 2
SW	Heat tank $SW\,2$
NMA	Mixture of water with component A
NMB	Mixture of water with component B
AB_IAB	Mixture of NMA and NMB
$NMAB$	Nutrient medium
IMX	Mixture of water and nutrients in the reactor auxiliary
FM	Fermentation medium - mixture of IMX and $NMAB$
DFB	The deactivated product after termination of fermentation
$CW5$	Water with $5^o C$
$CW\,20$	Water with $20^o C$
T_{Fi}	Temperature of the hot fermenter during t - time interval $\left[\,^o C\right]$
$T_{W\,20}$	Temperature of the water $CW\,20\ \left[\,^o C\right]$
T_{W5}	Temperature of the water $CW5\ \left[\,^o C\right]$

221

T_{S1}^i	Temperature in the heat tank $S1$ during i- time interval $\left[{}^oC \right]$
T_{S2}^i	The temperature in the heat tank $S2$ during i-h time interval $\left[{}^oC \right]$
T_{SW}^i	The temperature in the heat tank SW during i- time interval, $\left[{}^oC \right]$
T_i^{in}	Water temperature at the entrance of the coil $\left[{}^oC \right]$
T_i^*	Water temperature at the output of the coil $\left[{}^oC \right]$
V_F	Volume of the hot fermenter $\left[m^3 \right]$
V_{S1}^i	Volume of water in the heat tank $S1$ during i- time interval $\left[m^3 \right]$
V_{S2}^i	Volume of water in the heat tank $S2$ during i- time interval $\left[m^3 \right]$
V_{SW}^i	Volume of water in the heat tank SW during i- time interval $\left[m^3 \right]$
V_{S1}^*	Volume of water in the heat tank $S1$ in the end of the i- time interval $\left[m^3 \right]$
V_{S2}^*	Volume of water in the heat tank $S2$ in the end of the i- time interval $\left[m^3 \right]$
V_{SW}^*	Volume of water in the heat tank SW in the end of the i time interval $\left[m^3 \right]$
V_{Water}	Total volume of water used for the whole process $\left[m^3 \right]$
$V_{2.1.}$	Volume of NMA during stage 2.1 $\left[m^3 \right]$
$V_{2.2.}$	Volume of NMB during stage 2.1 $\left[m^3 \right]$
$V_{3.5.}$	Volume of water added in stage 3.5 $\left[m^3 \right]$
Cp_F	Specific heat capacities of hot fermenter $\left[kJm^{-3}K^{-1} \right]$
Cp_{W20}	Specific heat capacities of water $CW20$ $\left[kJm^{-3}K^{-1} \right]$
Cp_{W5}	Specific heat capacities of water $CW5$ $\left[kJm^{-3}K^{-1} \right]$
Cp_{Wi}	Specific heat capacities of used water $\left[kJm^{-3}K^{-1} \right]$
y_i^{S1}	Binary variable $y_i^{S1} = \{0 \vee 1\}$
y_i^{S2}	Binary variable $y_i^{S2} = \{0 \vee 1\}$
y_i^{SW}	Binary variable $y_i^{SW} = \{0 \vee 1\}$
x_i	Binary variable $x_i = \{0 \vee 1\}$
F_{Wi}	Flow rate of the cooling water through the coil $\left[m^3/s \right]$.
A	Heat transfer surface of the coil $\left[m^2 \right]$
U	Overall heat transfer coefficient $\left[kWm^{-2}K^{-1} \right]$,
$\left.\begin{array}{l} A_i \\ B_i \\ C_i \end{array}\right\}$	Values of the coefficients should be determined
$Cost_{Steam}^*$	Value of steam used for process $[lv]$
$Cost_{W5}^*$	Value of the energy use of cooling water $CW5$ $[lv]$
$Cost_{Water}^*$	Value the water used to carry out the processes in the cases when heat reservoirs are used $[lv]$
C_{Steam}	Price per unit of energy used for process steam $[lv/kJ]$
C_{W5}	Price per unit of energy used for cooling water $CW5$ process $[lv/kJ]$
C_{Water}	Price per unit volume of cooling water $CW20$ used for process $[lv./m^3]$
$Cost_{NO\_INT}$	Cost of energy and water required to the process in the case in absence of heat integration $[lv]$
CG_{Steamt}	Price per unit of energy used for process steam $[lv/GCal]$

CG_{W5}	Price per unit of energy used for process cooling water $CW5$ $[lv/GCal]$
C_{W5}	Price per unit of energy used for process cooling water $CW5$ $[lv/kJ]$
t_i	Duration of the i-time interval $[s]$
t_f	Time to complete the cooling process $[s]$
lv	Bulgarian Leva

REFERENCES

1 Vaselenak J. A., Grossmann I. E., Westerberg A. W., Heat integration in batch processing, *Ind. Eng. Chem. Process Des. Dev.*, Vol. 25, No. 2, pp. 357-366, 1986.

2 Ivanov B., Peneva K., Vaklieva-Bancheva N., Synthesis of Cost Optimal Heat Integrated Batch Systems, *Hung. J. Ind. Chem.*, Vol. 21, pp. 7-14, 1993.

3 Ivanov B., Vaklieva-Bancheva N., Peneva K., Synthesis of Batch Systems with Heat Storage Tanks. Design and Retrofit Problems, *Bulg. Chem. Com.*, Vol. 26, No 1, pp. 122-133, 1993. Boyadjiev Ch., Ivanov B., Vaklieva-Bancheva N., Pandelides C., Shah N., Optimal energy integration in batch antibiotics manufacture, *Comp. Chem. Eng.*, Vol. 20, S31-S36, 1996.

4 Brooke A., Kendrick D., Meeraus A., Raman R., GAMS: A User's Guide, GAMS Development Corporation, Washington, 1998.

5 User's Guide: Optimization Toolbox For Use with MATLAB_, Version 5, 2006, USA, The MathWorks, Inc. http://www.mathworks.com.

ОПТИМАЛНО УПРАВЛЕНИЕ ПОТРЕБЛЕНИЕТО НА ЕНЕРГИЯТА ПРИ ПРОИЗВОДСТВОТО НА АНТИБИОТИЦИ

Др. Добруджалиев[2], Д. Николова[1], Б. Иванов[1], А. Айдан[3]

[1]Институт по инженерна химия – БАН, ул. „Акад. Г. Бончев", бл. 103, 1113 София, България
[2]Университет „Проф. д-р Асен Златаров", Ул. „Проф. Якимов" №1, 8000 Бургас, България
[3]Американски университет на Шариах, ПК 26666, Шариах, Обединени арабски емирства

(Резюме)

Енергийната ефективност е много важен показател при оценката на стабилността на промишлените процеси. Оптималното използване на енергията е основна задача и днес, тъй като тя определя състоянието на околната среда, технологиите и цената на продукта. В настоящата работа се описва метод за намаляване потреблението на енергия в резултат на топлина интеграция в система биореактори за производство на антибиотици. Предложена е схема за топлинната интеграция с два топлинни резервоара. Разработен е математичен модел на процесите, които протичат в двата реактора. Използвайки този модел е предложен метод за управление на енергийните ресурси, чрез топлинна интеграция с два топлинни резервоара. Задачата за управление е формулирана като задача на смесеното нелинейно програмиране. Методът е тестван на примера на производството на антибиотици.

Crystal structures of two polysubstituted derivatives of cyclohexanone

I. Manolov[*1], C. Maichle-Mössmer[2]

[1)]*Department of Pharmaceutical Chemistry, Faculty of Pharmacy, Medical   University, 2, Dunav St, BG-1000 Sofia, Bulgaria*
[2)]*Institute of Inorganic Chemistry, Auf der Morgenstelle 18, D-72076 Tübingen,   Germany*

The structure of 2,4-diacetyl-5-hydroxy-5-methyl-3-(4-nitrophenyl)-cyclohexanone (I) was determined by X-ray crystallography. The symmetry operation (-x + 2, - y + 1, -z) generates the whole molecule. The compound crystallizes in an orthorhombic system and was characterized thus: P_{bca}, a = 8.6405(10), b=18.682(2), c=20.187(4), α= β=γ=90 º, Z =.8, V = 3258.7 (8) $Å^3$. The crystal structure was solved by direct methods and refined by full-matrix least-squares on F^2 to final values of R1 = 0.0687 and wR2 = 0.1225. The structure of 2,4-Diacetyl-3-(4-fluorophenyl)-5-hydroxy-5-methylcyclohexanone (II) was determine by X-ray crystallography. The symmetry operation (-x + 2, - y + 1, -z) generates the whole molecule. The compound crystallizes in a monoclinic system and was characterized thus: $P2_1$/c, a=5.7045 (5), b=18.120 (3), c=16.1678 (11), α= γ= 90 º, β= 96.192 (6) º, Z = 4, V = 1661.5 (3) $Å^3$. The crystal structure was solved by direct methods and refined by full-matrix least-squares on F^2 to final values of R1 = 0.0699 and wR2 = 0. 0.2100.

Key words: 2,4-Diacetyl-5-hydroxy-5-methyl-3-(4-nitrophenyl)-cyclohexanone, 2,4-Diacetyl-3-(4-fluorophenyl)-5-hydroxy-5-methylcyclohexanone, 1,3-dicarbonyl compounds, crystal structure, aldol condensation reaction

INTRODUCTION

The investigations on the interaction between 1,3-dicarbonyl compounds (2,4-pentanedione or ethylacetoacetate) and aldehydes or ketones began at the end of the 19th century and are continuing till present [1-4]. The results are diverse. It has been accepted that different condensation products are synthesized at different molar ratios of the reactants, by varying temperature or type of catalyst.

In this research the interaction between some aromatic aldehydes and 2,4-pentanedione at a molar ratio of 1:1, 1:2 or 1:4 in the presence of piperidine as a catalyst and glacial acetic acid was studied. The interaction was performed at room temperature for 2 h (Fig. 1).

EXPERIMENTAL

The crystal structure of the compounds was determined using the single crystal X-ray diffraction method. Data collection was carried out at –60 ºC using graphite-monochromated Mo$K_α$ radiation ($λ$ = 1.5418 Å) on an ENRAF NONIUS four circle diffractometer. The unit cell was determined and refined using the CAD4-EXPRESS program. A semiempirical absorption correction was performed using the PLATON/ABS PSI program [5]. The structure was solved with direct methods by SHELXS97 [6] and refined with SHELXL97 [7] by least-squares methods based on F^2. All non-hydrogen atoms were fully refined and all hydrogen atom positions were taken from the electron density map and refined isotropically. The plots of the molecular structure were made using the DIAMOND program (CRYSTAL IMPACT GbR, Bonn, Germany).

Complete data collection parameters and details of the structure solution and refinement are given in Table 1. These data can be obtained free of charge from The Cambridge Crystallographic Data Centre *via* www.ccdc.cam.ac.uk/data_request/cif

RESULTS AND DISCUSSION

The structure of the synthesized compounds was proven by IR, ^{1}H-NMR and mass-spectral analyses. Single crystals suitable for X-ray structure analysis could be obtained by crystallization from an ethanol solution, which afforded colorless crystals. The crystal and structure-refinement data are summarized in Tables 1 – 7.
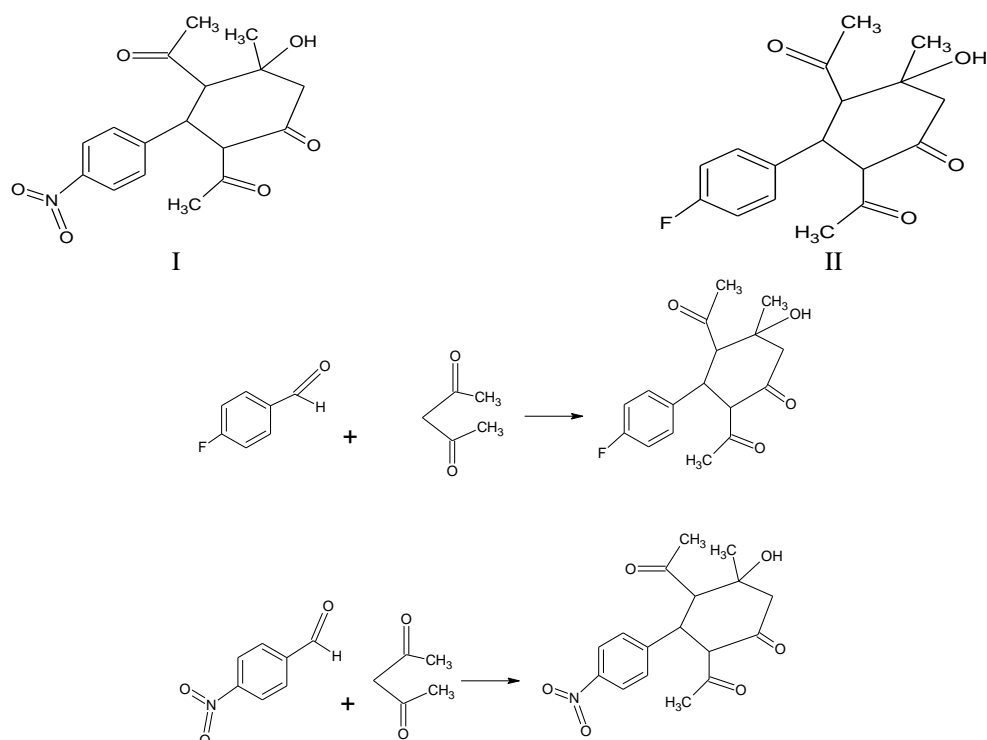
Fig.1. Chemical formula of the title compounds

Table 1. Crystal and experimental data for 2,4-Diacetyl-5-hydroxy-5-methyl-3-(4-nitrophenyl)-cyclohexanone (I) and 2,4-Diacetyl-3-(4-fluorophenyl)-5-hydroxy-5-methylcyclohexanone (II).

|	I	II
Chemical formula	$C_{17}H_{19}NO_6$	$C_{17}H_{19}FO_4$
Formula weight	333.33	306.32
Temperature	213 (2) K	223 (2) K
Crystal system:	Orthorhombic	Monoclinic
Space group:	Pbca	P 2$_1$/n
	a = 8.6405(10)Å	a=5.7045(5)Å
	b = 18.682 (2)Å	b=18.120 (3)Å
	c = 20.187 (4)Å	c=20.1
	α= β=γ=90 º	β=96.192 (6) º
		α=γ=90 º
Volume	3258.7 (8) Å^3	1661.5 (3) Å^3
Z	8	4
Density (calculated)	1.359 Mg/m^3	1.225 Mg/m^3
Radiation :	MoKα (λ= 0.71073 Å)	MoKα (λ= 1.5418 Å)
F(000)	1408	648
Crystal size	0.30 x 0.15 x 0.15 mm	.50 x 0.15 x 0.15 mm
No. of reflections collected	2205	3998
No. of independent reflections	1673	2827
θ range for data collection [°]	5.83 to 20.81	5.50 to 64.96
Data / restraints / parameters	1673 / 0 / 273	2827 / 0 / 276
Goodness-of-fit on F^2	1.078	1.067
R indices [I>2σ (I)]	R1 = 0.0687, wR2 = 0.1225	R1 = 0.0699,wR2 = 0.2100
R indices (all data)	R1 = 0.2550, wR2 = 0.1590	R1 = 0.0792,wR2 = 0.2210
Refinement:	Full matrix	Full matrix
	(Δ/ σ)$_{max}$ = 0.001	
	(Δ/ρ)$_{max}$ = 0.38 eÅ^{-3}	
	(Δ/ρ)$_{min}$ = - 0.21 eÅ^{-3}	
Measurement:	Enraf-Nonius CAD4	Enraf-Nonius CAD4
Program system:	Enraf-Nonius SDP	Enraf-Nonius SDP
Structure determination:	MULTAN	MULTAN
CCDC deposition number:	706401	706402
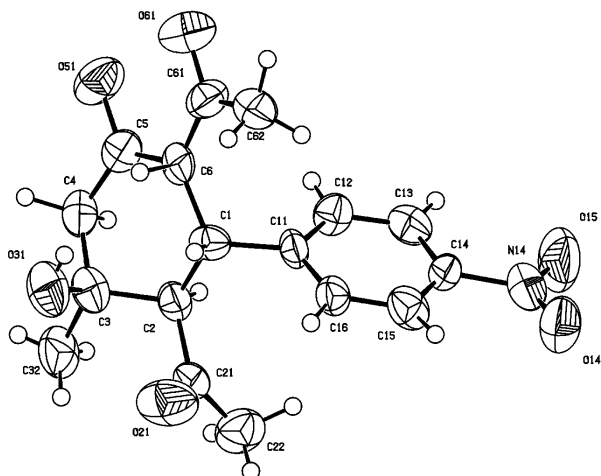
Fig. 2. ORTEP structurte of 2,4-diacetyl-5-hydroxy-5-methyl-3-(4-nitrophenyl)-cyclohexanone (I), showing 50% probability ellipsoids.
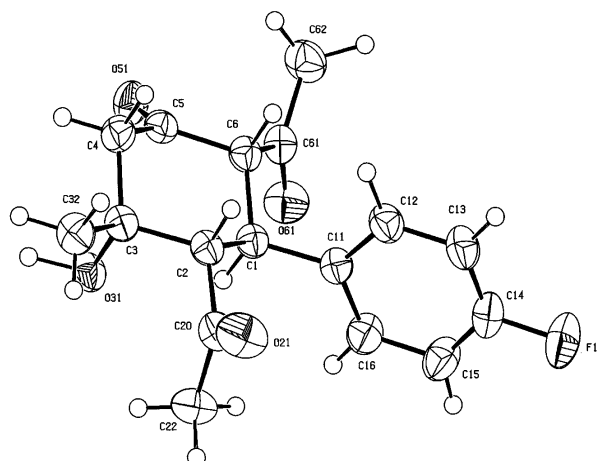

Fig. 3. ORTEP structure of 2,4-diacetyl-3-(4-fluorophenyl)-5-hydroxy-5-methylcyclohexanone (II), showing 50% probability ellipsoids.

The interaction of 4-bromobenzaldehyde, 4-hydroxybenzaldehyde and 4-methoxybenzaldehyde with 2,4-pentandione results in the formation of the respective 3-(4-substituted-benzylidene)pentane-2,4-dione [8].We established that the condensation process between aromatic aldehydes (containing a nitro group or a fluorine atom at para-position of the aromatic nucleus compared to aldehyde group) and 1,4-pentandione produced polysubstituted derivative of cyclohexanone (fig.: 2 and 3). These two substituents reveal –I-effect and strong -M-effect. X-ray crystal analysis proved a carbocyclic product, a result of the interaction between one mole aldehyde and two moles 2,4-pentandione, namely 2E-4-diacetyl-5-hydroxy-5-methyl-3-(4'-nitro-phenyl)-cyclohexanone or 2E-4-diacetyl-5-hydroxy-5-methyl-3-(4'-fluorophenyl)-cyclohexanone

Table 2. Atomic coordinates (x 10^4) and equivalent isotropic displacement parameters (A^2x10^3) for 2,4-diacetyl-5-hydroxy-5-methyl-3-(4-nitrophenyl)-cyclohexanone (I).

Atom	x	y	z	U (eq)
C 1	2663 (10)	1890 (5)	3991 (4)	47 (2)
C 2	3546 (10)	2560 (4)	3769 (5)	47 (2)
C 3	2533 (12)	3219 (5)	3687 (4)	57 (2)
C 4	1370 (15)	3065 (6)	3149 (5)	62 (3)
C 5	580 (12)	2362 (5)	3231 (4)	54 (2)
C 6	1106 (10)	1837 (5)	3653 (4)	47 (2)
C 11	3689 (9)	1251 (4)	3912 (4)	43 (2)
C 12	3860 (12)	927 (5)	3308 (4)	51 (3)
C 13	4914 (12)	378 (5)	3198 (5)	56 (3)
C 14	5784 (9)	176 (4)	3732 (6)	52 (2)
C 15	5664 (12)	488 (5)	4338 (5)	59 (3)
C 16	4609 (11)	1021 (5)	4425 (4)	48 (2)
C 21	4871 (12)	2699 (4)	4242 (5)	52 (2)
C 22	6485 (14)	2644 (7)	3973 (7)	75 (3)
C 32	3483 (17)	3863 (6)	3518 (7)	77 (4)
C 61	123 (12)	1223 (5)	3760 (5)	59 (2)
C 62	421 (10)	709 (4)	4314 (4)	70 (3)
O 14	7672 (8)	- 617 (3)	4112 (4)	93 (2)
O 15	7166 (9)	- 637 (3)	3075 (4)	112 (3)
O 21	4639 (7)	2839 (3)	4825 (3)	94 (2)
O 31	1678 (7)	3386 (3)	4293 (3)	79 (2)
O 51	- 722 (8)	2282 (3)	2893 (3)	80 (2)
O 61	- 1099 (7)	1135 (3)	3427 (3)	84 (2)
N 14	6962 (11)	- 393 (4)	3626 (5)	77 (3)

Table 3. Atomic coordinates (x 10^4) and equivalent isotropic displacement parameters (A^2 x 10^3) for 2,4-diacetyl-3-(4-fluorophenyl)-5-hydroxy-5-methylcyclohexanone (II)

Atom	x	y	z	U (eq)
C 1	455 (4)	7077 (1)	11011 (2)	33 (1)
C 2	2355 (4)	7048 (1)	10391 (2)	33 (1)
C 3	2335 (4)	6307 (1)	9931 (2)	35 (1)
C 4	2871 (5)	5686 (2)	10577 (2)	38 (1)
C 5	1031 (4)	5701 (1)	11171 (2)	35 (1)
C6	816 (4)	6427 (1)	11629 (2)	34 (1)
C 11	498 (5)	7812 (1)	11459 (2)	34 (1)
C 12	2456 (5)	8043 (2)	11982 (2)	42 (1)
C 13	2494 (6)	8726 (2)	12373 (2)	47 (1)
C 14	550 (5)	9167 (2)	12231 (2)	46 (1)
C 15	- 1407 (6)	8966 (2)	11727 (2)	50 (1)
C 16	- 1433 (5)	8281 (2)	11339 (2)	44 (1)
C 20	2182 (5)	7707 (2)	9803 (2)	40 (1)
C 22	- 66 (6)	7860 (2)	9261 (2)	54 (1)
C 32	4110 (5)	6290 (2)	9288 (2)	45 (1)
C 61	- 1143 (5)	6363 (1)	12196 (2)	38 (1)
C 62	- 541 (7)	5979 (2)	13006 (2)	52 (1)
O 21	3891 (4)	8097 (1)	9779 (2)	63 (1)
O31	- 3 (3)	6195 (1)	9531 (1)	39 (1)
O51	- 264 (4)	5184 (1)	11272 (1)	45 (1)
O 61	- 3095 (4)	6606 (1)	11985 (1)	51 (1)
F 1	582 (4)	9845 (1)	12605 (1)	66 (1)

Table 4. Selected bond lengths (Å) for 2,4-diacetyl-5-hydroxy-5-methyl-3-(4-nitrophenyl)-cyclohexanone (I)

Bond	Length	Bond	Length
C 1 – C 11	1.496 (10)	C 5 – C 6	1.377 (10)
C 1 – C 6	1.512 (10)	C 6 – C 61	1.444 (11)
C 1 – C 2	1.532 (10)	C 14 – N 14	1.487 (11)
C 2 – C 21	1.513 (10)	C 21 – O 21	1.223 (9)
C 2 – C 3	1.521 (10)	C 21 – C 22	1.500 (12)
C 3 – O 31	1.462 (8)	C 61 – O 61	1.261 (9)
C 3 – C 32	1.495 (12)	C 61 – C 62	1.496 (10)
C 3 – C 4	1.506 (11)	O 14 – N 14	1.231 (8)
C 4 – C 5	1.490 (12)	O 15 – N 14	1.214 (8)
C 5 – O 51	1.323 (9)		

Table 5. Selected bond angles (°) for 2,4-diacetyl-5-hydroxy-5-methyl-3-(4-nitrophenyl)-cyclohexanone (I)

Bond	Angle	Bond	Angle
C 11 – C 1 – C 6	115.2 (7)	C 5 – C 6 – C 61	117.7 (9)
C 11 – C 1 – C 2	109.0 (7)	C 5 – C 6 – C 1	121.8 (9)
C 6 – C 1 – C 2	111.4 (8)	C 61 – C 6 – C 1	120.5 (9)
C 21 – C 2 – C 3	111.4 (7)	C 16 – C 11 – C 1	120.7 (8)
C 21 – C 2 – C 1	109.4 (7)	C 12 – C 11 – C 1	120.8 (8)
C 3 – C 2 – C 1	114.0 (8)	C 15 – C 14 – N 14	119.3 (10)
O 31 – C 3 – C 32	107.3 (8)	C 13 – C 14 – N 14	117.4 (10)
O 31 – C 3 – C 4	107.9 (8)	O 21 – C 21 – C 22	121.0 (9)
C 32 – C 3 – C 4	110.8 (9)	O 21 – C 21 – C 2	121.3 (9)
O 31 – C 3 – C 2	111.8 (7)	C 22 – C 21 – C 2	117.6 (9)
C 32 – C 3 – C 2	111.1 (10)	O 61 – C 61 – C 6	121.0 (9)
C 4 – C 3 – C 2	107.9 (8)	O 61 – C 61 – C 62	117.3 (9)
C 5 – C 4 – C 3	113.3 (9)	C 6 – C 61 – C 62	121.4 (9)
O 51 – C 5 – C 6	121.3 (9)	O 15 – N 14 – O 14	122.0 (9)
O 51 – C 5 – C 4	115.6 (9)	O 15 – N 14 – C 14	120.0 (10)
C 6 – C 5 – C 4	123.0 (10)	O 14 – N 14 – C 14	118.0 (9)

Table 6. Selected bond lengths (Å) for 2,4-diacetyl-3-(4-fluorophenyl)-5-hydroxy-5-methylcyclohexanone (II)

Bond	Length	Bond	Length
C 1 – C 11	1.515 (3)	C 5 – O 51	1.214 (3)
C 1 – C 6	1.543 (3)	C 5 – C 6	1.520 (3)
C 1 – C 2	1.555 (3)	C 6 – C 61	1.525 (4)
C 2 – C 20	1.522 (4)	C 14 – F 1	1.367 (3)
C 2 – C 3	1.535 (3)	C 20 – O 21	1.208 (4)
C 3 – O 31	1.432 (3)	C 20 – C 22	1.499 (4)
C 3 – C 32	1.528 (4)	C 61 – O 61	1.211 (3)
C 3 – C 4	1.544 (4)	C 61 – C 62	1.490 (4)
C 4 – C 5	1.498 (4)		

Table 7. Selected bond angles (°) for 2,4-diacetyl-5-hydroxy-5-methyl-3-(4-fluorophenyl)-cyclohexanone (II)

Bond	Angle	Bond	Angle
C 11 – C 1 – C 6	111.61 (19)	C 4 – C 5 – C 6	115.2 (2)
C 11 – C 1 – C 2	111.2 (2)	C 5 – C 6 – C 61	109.2 (2)
C 6 – C 1 – C 2	109.7 (2)	C 5 – C 6 – C 1	111.0 (2)
C 20 – C 2 – C 3	112.8 (2)	C 61 – C 6 – C 1	113.1 (2)
C 20 – C 2 – C 1	111.9 (2)	C 16 – C 11 – C 1	120.0 (2)
C 3 – C 2 – C 1	111.9 (2)	C 12 – C 11 – C 1	121.7 (2)
O 31 – C 3 – C 32	110.1 (2)	C 15 – C 14 – F 1	118.5 (3)
O 31 – C 3 – C 2	107.49 (19)	C 13 – C 14 – F 1	118.7 (3)
C 32 – C 3 – C 2	112.1 (2)	O 21 – C 20 – C 22	121.1 (3)
O 31 – C 3 – C 4	108.0 (2)	O 21 – C 20 – C 2	118.7 (3)
C 32 – C 3 – C 4	110.4 (2)	C 22 – C 20 – C 2	120.2 (2)
C 2 – C 3 – C 4	108.7 (2)	O 61 – C 61 – C 62	122.3 (3)
C 5 – C 4 – C 3	108.6 (2)	O 61 – C 61 – C 6	121.0 (2)
O 51 – C 5 – C 4	123.4 (2)	C 62 – C 61 – C 6	116.7 (2)
O 51 – C 5 – C 6	121.4 (2)		

Florencio at al.[9] established that during the reaction between nickel acetylacetonate dihydrate and p-nitrobenzyl chloride with dimethyl sulfoxide as a solvent only the monoalkylation product was obtained instead of the expected mixture of dialkylation and monoalkylation products. In this reaction a compound with empirical formula $C_{17}H_{19}NO_6$ was obtained, which was analyzed by X-ray diffraction methods in order to obtain conformational data. The product was 2E-4-diacetyl-5Z-methyl-3-(p-nitrophenyl)-cyclohex-1-en-1,5E-diol. The unit cell dimensions reported by Florencio were: a= 20.176(2), b=8.623(3), c=18.746(9) Å [9]. Our data do not correspond to their data: a = 8.6405 (10), b=18.682(2) and c=20.187(4)Å. analogous results were obtained using 4-fluorobenzaldehyde. The bond lengths were longer than the respective ones of the compound containing a nitro group. It seems that the electronegativity and the mesomeric effect of the nitro group is due to the difference in the bond length.The two cyclohexan rings were in a distorted half-chair conformation. The acetyl group was attached to C2 in a trans-equatorial position and the hydroxyl group attached to C3 was situated in an axial position for both compounds. Ponomarev et al.[10] described the synthesis of a cyclic product with the same molecular formula based only on the data of a spectral analysis as well as data of elemental analysis for carbon, hydrogen and fluorine. However, the results of the elemental analysis do not correspond to the formula suggested by them. The synthesized by us substance corresponds to the suggested formula. The results are based on the spectral, elemental and X-ray crystal structure analysis.

REFERENCES

1. R. E. Lutz, T. A. Martin, J. F. Codington, et al. *J. Org. Chem.*, **14,** 982 (1949).
2. E. J. Valente, G. Ruggiero, C. W. Miller, J. D. Zubkovski, D. Eggleston. *Mater. Synth. Charact.* 1997 [Proc. Am. Soc. Symp. 1994, 19-60] [Chem. Abstr. 1998, 128, 243631x].
3. K. B. Rall, V. V. Peraklin. *Dokladi Nauk SSSR*, **100**, 715, (1955).
4. S. G. Schulman, L. S. Rosenberg. *The J.Phys.Chem.*, **83**, 447 (1979).
5. A. L. Spek, PLATON: General Crystallographic Tool; Utrecht University, The Netherlands, 1998.
6. G. M. Sheldrick, *Acta Cryst.*, **A46,** 467 (1990).
7. G. M. Sheldrick. SHELXL97. Program for crystal structure refinement, University of Gottingen, Germany 1997.
8. I. Manolov, C. Maichle-Moessmer, *Asian Chem. Lett.*, **14**, 55 (2010).
9. F. Florencio, P. Smith-Verdier, and S. Garcia-Blanco. *Cryst. Struct. Comm.,* **6**, 561 (1977).
10. O. A. Ponomarev, N. S. Pivnenko, and V. F. Lavrushin. *Ukr. Khim. J.,* **46,** 972 (1980).

КРИСТАЛНИ СТРУКТУРИ НА ДВЕ ПОЛИСУБСТИТУИРАНИ ПРОИЗВОДНИ НА ЦИКЛОХЕКСАНОНА

Ил. Манолов[*1], Ц. Майхле-Мьосмер[2]

[1)] *Департамент по фармацевтична химия, Фармацевтичен факултет, Медицински университет, 1000 София*
[2)] *Институт по неорганична химия, 72076 Тюбинген, Германия*

(Резюме)

Структурата на 2,4-диацетил-5-метил-5-хидрокси-3-(4-нитрофенил)циклохексанон (I) е определена чрез монокристален рентгеноструктурен анализ. Съединението кристализира в орторомбична кристална система и пространствена група P_{cn}, с параметри на елементарната клетка a=8.6405(10), b=18.682(2), c=20.187(4), $\alpha = \beta = \gamma = 90$ º, Z =.8, V = 3258.7 (8) $Å^3$. Кристалната структура е доказана с директни методи и точно определена с помощта на метода на най-малките квадрати за F^2 до стойност R1 = 0.0687. Структурата на 2,4-диацетил-3-(4-флуорофенил)-5-хидрокси-5-метилциклохексанон (II) е определена чрез монокристален рентгеноструктурен анализ. Съединението кристализира в моноклинна кристална система и пространствена група $P2_1/c$, с параметри на елементарната клетка , a=5.7045 (5), b=18.120 (3), c=16.1678 (11), $\alpha = \gamma = 90$ º, $\beta = 96.192$ (6) º, Z = 4, V = 1661.5 (3) $Å^3$. Кристалната структура е доказана с директни методи и точно определена с помощта на метода на най-малките квадрати за F^2 до стойност R1 = 0.0699.

Determination of As, Zn, Pt, B, Hg, Cd, Tl and U in environmental materials by high resolution radial viewing 40.68 MHz inductively coupled plasma optical emission spectrometry (ICP - OES)

N. Velitchkova[1], O. Veleva[1], S. Velichkov[2], P. Markov[2], N. Daskalova[2*]

[1] *Geological Institute, Bulgarian Academy of Sciences, Acad. G. Bontchev Street, bl. 24, 1113 Sofia, Bulgaria*

[2] *Institute of General and Inorganic Chemistry, Bulgarian Academy of Sciences, Acad. G. Bontchev Street, bl. 11, 1113, Sofia, Bulgaria*

The possibilities and limitations of high resolution radial viewing 40.68 MHz inductively coupled plasma optical emission spectrometry (ICP - OES) were shown in the determination of As, Zn, Pt, B, Hg, Cd, Tl and U in environmental materials. Improvement of the detection limits was achieved by optimization of the operating conditions. The lowest detection limits were obtained under robust conditions (excitation temperature ≈ 7200 K in pure solvent and in presence of Al, Ca, Fe, Mg and Ti as a complex environmental matrix). The detection limits in the determination of As, Zn, B, Hg, Cd, Tl and U satisfy the requirements for maximum permissible concentrations in soils and drinking waters. In the determination of Pt in road dust an improvement of the detection limit was achieved by the development of a new column method with *2-mercaptobenzimidazole* immobilized on activated carbon for separation of the matrix elements Al, Ca, Fe, Mg and Ti and pre-concentration of platinum.

Keywords: ICP - OES, Environmental materials, Spectral interferences, Line selection, Detection limits

INTRODUCTION

Matrix effects in ICP - OES include non-spectral and spectral interferences [1, 2]. A large number of research groups have investigated the non-spectral matrix effects by optimization of excitation in order to suppress or eliminate this type of interferences [3 – 6]. Summarizing the investigation of non-spectral matrix effects in the presence of different matrices, the conclusion can be drawn that the robust plasma conditions are more appropriate when compared to the non-robust plasma conditions, but elimination of non-spectral matrix effects cannot be achieved [7, 8]. Our investigations show that non – spectral matrix effects can be totally removed by precise matching of the acid and matrix contents in both reference and sample solutions [9 – 11]. In the present paper the non-spectral matrix effects were totally removed by precise matching of the acid and matrix contents in both reference and sample solutions and are not subject of the present investigation.

Spectral interferences may drastically deteriorate the analytical characteristics of ICP–OES [1, 2]. Analysis of a variety of complex environmental matrices ensures that all possible types will encounter soon or later. The most difficult samples from this point of view are the soils and the sediments. Such materials normally contain high concentrations of Al, Ca and Mg, which cause significant background enhancement in many regions of the spectrum; they also contain high concentrations of Fe and to a lesser extent Ti, which can give rise to serious line overlap interferences in the determination of trace elements [12].

In our previous papers the possibilities of ICP – OES and Q-concept as a basic methodology for improvement of the true detection limits by using different excitation conditions in ICP were shown:

(i) in the determination of traces of rare earth elements in line-rich rare earth matrices at T_{exc} ≈ 6000 K [13];

(ii) in the determination of a large number of dopants with different characteristics (charge and ionic radius) (Na, Rb, Al, Fe, Cr, Ga, Nb, Ni, Mn, Yb, Tm, Er, Ho, Tb, Nd, Ge, Zr and Ce) in single crystals of potassium titanylphosphate ($KTiOPO_4$). The lowest detection limits were obtained at different excitation temperatures for analytes with different spectral characteristics:

T_{exc} ≈ 6200 K for Na, Rb, Al, Ga, Tm, Er, Ho, Tb, Nd and Ce;

* To whom all correspondence should be sent:
E-mail: das15482@svr.igic.bas.bg

$T_{exc} \approx 7200$ K for Fe, Cr, Nb, Ni, Ge and Zr [14].

The general purpose of the present paper was to investigate the possibilities of a radial 40.68 MHz ICP and spectrometer with high resolution (spectral bandwidth = 5 pm) in the determination of As, Zn, Pt, B, Hg, Cd, Tl and U in the presence of a complex matrix containing Al, Ca, Fe, Mg and Ti in environmental materials. The optimization procedure of the experimental conditions in the determination of traces of elements in complex matrices will be presented. Quantification of spectral interferences is made by Q-values for line interference Q_{IJ} (λ_a) and Q-values for wing background interference $Q_{WJ}(\Delta\lambda_a)$, for each of the interferents [15].

2. EXPERIMENTAL

2.1. Instrumentation

The experiments were performed with a radial viewing ICP - OES system Horiba Jobin Yvon ULTIMA 2 (Longjumeau, France) equipment, whose characteristics are specified in Table 1. The operating conditions were modified by varying the incident power and the sheathing gas flow rate, whereas the carrier gas flow rate was kept constant (0.4 l min^{-1}) (Table 2). This is the optimal value of the carrier gas flow rate in accordance with the recommendations for the Meinhard nebulizer in the user manual to the JY ULTIMA 2 equipment. The prominent lines with wavelengths below 200 nm were measured by a nitrogen-purged spectrometer in accordance with the recommendation of the manufacturer. The quantitative information about the type of the spectral interferences was derived from wavelength scans around the candidate

(prominent) analysis lines in the presence of Al, Ca, Mg, Fe and Ti as interferents. The quantitative data for the spectral interferences were obtained in the presence of 2 mg ml^{-1} Al, Ca, Mg, Fe, and Ti as interferents, separately. Q-values for line interferences Q_I (λ_a) and Q-values for wing background interference $Q_w(\Delta\lambda_a)$ were obtained around the selected prominent lines of As, Zn, Pt, B, Hg, Cd, Tl and U. The total background signal in the presence of a complex environmental matrix is [15]:

$$X_{BL} = X_B + X_{WJ}(\Delta\lambda_a) + X_{IJ}(\lambda_a) \quad \text{where:}$$

– X_B is the solvent blank (due to source and solvent);

– $X_{WJ}(\Delta\lambda_a)$ - the wing background level with respect to the solvent blank for the interferents (J = Al, Ca, Mg, Fe or Ti);

– $X_{IJ}(\lambda_a)$ - the net interfering signals with respect to the wing background level $X_{WJ}(\Delta\lambda_a)$ of the interferents (J = Al, Ca, Mg, Fe or Ti).

The following signals were measured: X_A, X_B, $X_{WJ}(\Delta\lambda_a)$ and $X_{IJ}(\lambda_a)$. The measured signals were then reduced to sensitivities:

- the sensitivity of the analysis line S_A (defined as the net line signal X_A per unit analyte concentration C_A;

- the interferent sensitivities $S_{WJ}(\Delta\lambda_a)$ and $S_{IJ}(\lambda_a)$, defined as interferent signals $X_{WJ}(\Delta\lambda_a)$ and $X_{IJ}(\lambda_a)$, respectively, per unit interferent concentration C_{IJ}.

Finally, the sensitivities were used for the calculation of the Q-values for wing background interference $Q_{WJ}(\Delta\lambda_a) = S_{WJ}(\Delta\lambda_a) / S_A$ and the Q-values for line interference $Q_{IJ}(\lambda_a) = S_{IJ}(\Delta\lambda_a) / S_A$.

Table 1. Specification of HORIBA Jobin - Yvon ULTIMA 2 (France) ICP system

Monochromator	HORIBA Jobin - Yvon ULTIMA 2
Mounting	Czerny - Turner, focal length 1 m
Grating	Holographic, 2400 grooves mm^{-1}
Wavelength range	First and second order
Entrance slit	0.015 / 0.02 mm
Exit slit	0.02 / 0.08 mm
Practical spectral bandwidth	5 pm in the 2^{-nd} order from 160 nm to 320 nm and 10 pm in the 1^{-st} order from 320 to 800 nm
Detectors	High Dynamic Detectors based on PMT's
Rf generator	Solid state RF 40.68 MHz
Frequency	40.68 MHz
Power output	0. 5 - 1. 55 kW
Nebulizer	Meinhard, concentric glass
Spray chamber	JY Glass cyclonic spray chamber
Plasma torch	Fully demountable
Pump	Peristaltic, two channels, twelve-roller

Table 2. Operating conditions with the 40.68 MHz ICP HORIBA JY ULTIMA 2 (France)

Variable parameters	$T_{exc} \approx 6200$ K, Mg II 280.270 nm / Mg I 285.213 nm line intensity ratio = 4.0	$T_{exc} \approx 7200$ K, Mg II 280.270 nm / Mg I 285.213 nm line intensity ratio = 11.4
Incident power, (kW)	1.00	1.00
Outer argon flow rate, (l min^{-1})	13	13
Nebulizer, Meinhard, type TR 50 C1, pressure, bar	3.2	3.2
Carrier gas flow rate, (l min^{-1})	0.4	0.4
Sheath gas flow rate, (l min^{-1})	1.0	0.2
Sum = Carrier gas +Sheath gas flow rate, (l min^{-1})	1.4	0.6
Liquid uptake rate, (ml min^{-1})	1.0	1.0
Observation height, (mm)	10	10

The true detection limits ($C_{L, \text{true}}$) were calculated by Eq. 1 [13]:

$$C_{L, \text{true}} = 2/5 \ \Sigma_J \ Q_{IJ} (\lambda_a) \times C_{IJ} + C_{L, \text{conv}} \quad (1)$$

where:

$$C_{L, \text{conv}} = 2\sqrt{2} \times 0.01 \times \text{RSDBL} \times [\text{BEC} + \Sigma_J \ Q_{IJ}(\lambda_a) \times C_{IJ} + \Sigma_J \ Q_{WIJ}(\Delta\lambda_a) \times C_{IJ}] \quad (2)$$

Therefore, the ($C_{L, \text{true}}$) is obtained by Eq. 3:

$$C_{L, \text{true}} = 2/5 \ \Sigma_J \ Q_{IJ} (\lambda_a) \times C_{IJ} + 2\sqrt{2} \times 0.01 \times \text{RSDB} \times [\text{BEC} + \Sigma_J \ Q_{IJ}(\lambda_a) \times C_{IJ} + \Sigma_J Q_{WIJ}(\Delta\lambda_a) \times C_{IJ}] \quad (3)$$

The detection limit of the analytes in pure solvent (or dilute acid) is defined by Eq. 4 [13]:

$$C_L = 2\sqrt{2} \times 0.01 \times \text{RSDB} \times \text{BEC} \quad (4)$$

This equation (4) is written in terms of the background equivalent concentration in pure solvent (BEC) and relative standard deviation of the background (RSDB=1%) [15].

2.2. Reagents and test solutions

Reagents of highest purity grade were used: 30 % HCl, 65 % HNO$_3$, 47 % HBr (Suprapur, Merck), bi-distilled water from a quartz apparatus, activated carbon GAS 1240 (Norit N.V. Netherlands) with specific surface area of 1240 m^{2}g^{-1} and buffer solutions (Merck): pH = 1 (0.1 M HCl). Plastic or PTFE ware was used throughout.

Stock solutions of the analytes (1 mg ml^{-1}) were prepared from Merck single element standard solutions. Stock solutions of the matrix components Al, Ca, Mg, Fe and Ti (10 mg ml^{-1}) were prepared by dissolving the corresponding chlorides with a purity of 99.9999% in hydrochloric acid. The possible presence of impurities causes an uncertainty when matrix concentration of 2 mg ml^{-1} is used. Q-values were measured by using the following test solutions: 10 μg ml^{-1} for each analyte and 2 mg ml^{-1} for each interferent, separately.

2.3. Certified reference materials

1. International Atomic Energy Agency IAEA / Soil 7;
2. Certified reference material BCR-723 - road dust;
3. National Water Research Institute certified standard, TMDA-51.2, certified standard for trace elements in diluted Lake Ontario water.

3. RESULTS AND DISCUSSION

3.1. Optimization of the operating conditions

3.1.1. Pure solvent. The results presented in Table 3 lists the sensitivities of the analysis line S_A – values for the atomic and the ionic prominent lines with different excitation potentials (E_q) for elements with various ionization potentials (V_i) at $T_{exc} \approx 6200$ K where the Mg II 280.270 nm / Mg I 285.213 nm line intensity ratio is equal to 4 and at $T_{exc} \approx 7200$ K (Mg II / Mg I = 11.4), as well as the detection limits in pure solvent derived by the above mentioned operating conditions (Table 2). The ionization and excitation potentials were taken from [16]. The detection limits in pure solvent were calculated by using Eq.4. The change in T_{exc} was achieved by varying the sheath gas flow rate (Table 2) and was measured by the Boltzmann plot method with titanium lines [17]. The main outcome from the investigations was:

Table 3. Values of S_A for the atomic and ionic prominent lines for $T_{exc} \approx 6200$ K (1) and $T_{exc} \approx 7200$ K (2)

Atomic prominent lines, λ, nm	Ionization potential, V [16]	$T_{exc} \approx 6200$ K (1) $S_{A\,(1)} \times 10^6$	$T_{exc} \approx 7200$ K (2) $S_{A\,(2)} \times 10^6$	$S_{A(2)}/S_{A(1)}$ ratio	$C_{L(1)}$, ng ml^{-1}	$C_{L(2)}$, ng ml^{-1}
As I 193.695	9.81	330	1000	3.0	8.4	3.0
Zn I 213.856	9.39	342	990	2.9	13.0	4.5
Pt I 265.945	9.00	326	880	2.7	37.8	14.0
B I 249.773	8.30	480	960	2.0	10.2	5.1
Ionic prominent lines, λ, nm	Sum = ionization + excitation potentials	$T_{exc} \approx 6200$ K (1) $S_{A\,(1)} \times 10^6$	$T_{exc} \approx 7200$ K (2) $S_{A\,(2)} \times 10^6$	$S_{A(2)}/S_{A(1)}$ ratio	$C_{L(1)}$, ng ml^{-1}	$C_{L(2)}$, ng ml^{-1}
Hg II 194.277	16.83	375	1200	3.2	6.5	2
Cd II 214.338	14.77	520	1670	3.2	6.0	1.7
Tl II 190.852	12.60	420	1260	3.0	11.2	7.0
U II 385.958	9.44	450	1260	2.8	4.0	1.4

Table 4. Identification of matrix lines which influence the platinum prominent lines

Analytes, Wavelengths, λ, nm	Interferents, wavelength of interfering line, λ, nm	$\Delta\lambda_{ka}^*$, nm	$Q_{WJ}(\Delta\lambda_a)$	$Q_{IJ}(\lambda_a)$
Pt II 203.646 BEC = 0.23 µg ml^{-1} C_L = 7.0 ng ml^{-1}	Al II 203.993 [19]	+0.347	7.2×10^{-4}	0
	Ca	-	0	0
	Fe 203.643 [20]	-0.003	9.6×10^{-5}	8.5×10^{-3}
	Mg	-	0	0
	Ti 203.681	+0.035	2.4×10^{-5}	6.6×10^{-5}
Pt II 214.423 BEC = 0.26 µg ml^{-1} C_L = 8.0 ng ml^{-1}	Al I 214.539 [19]	+0.116	1.9×10^{-4}	2.3×10^{-4}
	Ca	-	0	0
	Fe 214.445 [19, 20]	+0.022	1.9×10^{-5}	3.7×10^{-5}
	Mg	-	0	0
	Ti 214.361 [19, 20]	-0.062	1.9×10^{-5}	0
Pt I 217.467 BEC = 0.43 µg ml^{-1} C_L = 12.0 ng ml^{-1}	Al I 217.403 [19, 20]	-0.064	7.1×10^{-4}	2.0×10^{-3}
	Ca	-	0	0
	Fe I 217.486 [19, 20]	+0.019	5.1×10^{-5}	5.7×10^{-5}
	Mg	-	0	0
	Ti	-	0	0
Pt I 193.670 BEC=0.44 µg ml^{-1} C_L = 13.0 ng ml^{-1}	Al 193.564	+ 0.106	2.4×10^{-3}	6.0×10^{-3}
	Ca	-	0	0
	Fe 193.657 [19, 20]	- 0.015	3.1×10^{-5}	2.1×10^{-5}
	Mg	-	0	0
	Ti 193.657	- 0.013	2.7×10^{-5}	3.0×10^{-6}
Pt I 265.945 BEC= 0.48 µg ml^{-1} C_L = 14.0 ng ml^{-1}	Al I 266.039 [19, 20]	+ 0.094	1.7×10^{-5}	0
	Ca	-	0	0
	Fe 265.924 [19, 20]	- 0.021	7.1×10^{-6}	7.0×10^{-6}
	Mg	-	0	0
	Ti	-	0	0

* $\Delta\lambda_{ka}$ is the wavelength distances between the analyte and interfering lines

(i) The sensitivities of all atomic and ionic prominent lines are higher at $T_{exc} \approx 7200$ K in comparison with the corresponding values at $T_{exc} \approx 6200$ K (column 3 versus column 4). The enhancement factors decrease with decreasing ionization potentials of the analytes for atomic prominent lines or with decreasing of the sum = ionization potential + excitation potentials of elements for ionic prominent lines (column 5). The atomic lines of elements with low to medium ionization potentials ($V_i \le 8$ eV) were denoted as "soft" lines. All other atomic and ionic lines were denoted as "hard" lines [1, 18].

Table 5. Values of S_{IFe} (λ_a) and S_{WFe} ($\Delta\lambda_a$) for the prominent lines of Zn, Pt, B, Hg, Cd, Tl and U for $T_{exc} \approx 6200$ K (1) and $T_{exc} \approx 7200$ K (2). Interferent: 2 mg ml^{-1} Fe

Prominent lines, λ, nm	$T_{exc} \approx 6200$ K (1)		$T_{exc} \approx 7200$ K (2)		$S_{IFe\,(2)}(\lambda_a)$ / $S_{IFe\,(1)}(\lambda_a)$ ratio	$S_{WFe\,(2)}(\Delta\lambda_a)$ / $S_{WFe\,(1)}(\Delta\lambda_a)$ ratio
	$S_{IFe\,(1)}(\lambda_a)$ × 10^6	$S_{WFe\,(1)}(\Delta\lambda_a)$ × 10^6	$S_{IFe\,(2)}(\lambda_a)$ × 10^6	$S_{WFe\,(2)}(\Delta\lambda_a)$ × 10^6		
Zn I 213.856	0.003	-	0.0099	-	3.3	-
Pt I 265.945	0.003	0.003	0.006	0.006	2.0	2.0
B I 249.773	0.025	0.003	0.048	0.0058	1.9	1.9
Hg II 194.277	0.004	0.005	0.012	0.0168	3.0	3.4
Cd II 214.338	0.011	0.004	0.0334	0.0104	3.2	2.8
Tl II 190.852	0.290	0.280	0.870	0.850	3.0	3.0
U II 385.958	0.270	0.220	0.780	0.650	2.9	3.0

Table 6. Values of Q_{IFe} (λ_a) and Q_{WFel} ($\Delta\lambda_a$) for the prominent lines of Zn, Pt, B, Hg, Cd, Tl and U for $T_{exc} \approx 6200$ K (1) and $T_{exc} \approx 7200$ K (2). Interferent: 2 mg ml^{-1} Fe

Prominent lines, λ, nm	$T_{exc} = 6200$ K (1)		$T_{exc} = 7200$ K (2)		$Q_{IFe\,(2)}(\lambda_a)$ / $Q_{IFe\,(1)}(\lambda_a)$ ratio	$Q_{WFe\,(2)}(\Delta\lambda_a)$ / $Q_{WFe\,(1)}(\Delta\lambda_a)$ ratio
	$Q_{IFe\,(1)}(\lambda_a)$	$Q_{WFe\,(1)}(\Delta\lambda_a)$	$Q_{IFe\,(2)}(\lambda_a)$	$Q_{WFe\,(2)}(\Delta\lambda_a)$		
Zn I 213.856	9.0×10^{-6}	0	1.0×10^{-5}	0	1.10	-
Pt I 265.945	9.2×10^{-6}	9.2×10^{-6}	6.8×10^{-6}	6.8×10^{-6}	0.74	0.74
B I 249.773	5.2×10^{-5}	6.25×10^{-6}	5.0×10^{-5}	6.0×10^{-6}	0.96	0.96
Hg II 194.277	1.1×10^{-5}	1.3×10^{-5}	1.0×10^{-5}	1.4×10^{-5}	0.91	1.10
Cd II 214.338	2.1×10^{-5}	7.7×10^{-6}	2.0×10^{-5}	6.2×10^{-6}	0.95	0.81
Tl II 190.852	6.9×10^{-4}	6.7×10^{-4}	6.9×10^{-4}	6.8×10^{-4}	1.00	1.00
U II 385.958	6.0×10^{-4}	4.9×10^{-4}	6.2×10^{-4}	5.2×10^{-4}	1.00	1.10

Table 7. Values of S_{IAl} (λ_a) and S_{WAl} ($\Delta\lambda_a$) for the prominent lines of As, Pt and Tl for $T_{exc} \approx 6200$ K (1) and $T_{exc} \approx 7200$ K (2). Interferent: 2 mg ml^{-1} Al

Prominent lines, λ, nm	$T_{exc} \approx 6200$ K (1)		$T_{exc} \approx 7200$ K (2)		$S_{IAl\,(2)}(\lambda_a)$ / $S_{IAl\,(1)}(\lambda_a)$ ratio	$S_{WAl\,(2)}(\Delta\lambda_a)$ / $S_{WAl\,(1)}(\Delta\lambda_a)$ ratio
	$S_{IAl\,(1)}(\lambda_a)$ × 10^6	$S_{WAl\,(1)}(\Delta\lambda_a)$ × 10^6	$S_{IAl\,(2)}(\lambda_a)$ × 10^6	$S_{WAl\,(2)}(\Delta\lambda_a)$ × 10^6		
As I 193.695	1.5	0.9	3.7	1.8	2.5	2.0
Pt I 193.670	4.2	1.2	5.8	2.3	1.4	1.9
Tl II 190.852	0.3	0.24	1.0	0.71	3.3	3.0

Table 8. Values of Q_{IAl} (λ_a) and Q_{WAl} ($\Delta\lambda_a$) for the prominent lines of As, Pt and Tl for $T_{exc} \approx 6200$ K (1) and $T_{exc} \approx 7200$ K (2). Interferent: 2 mg ml^{-1} Al

Prominent lines, λ, nm	$T_{exc} \approx 6200$ K (1)		$T_{exc} \approx 7200$ K (2)		$Q_{IAl\,(2)}(\lambda_a)$ / $Q_{IAl\,(1)}(\lambda_a)$ ratio	$Q_{WAl\,(2)}(\Delta\lambda_a)$ / $Q_{WAl\,(1)}(\Delta\lambda_a)$ ratio
	$Q_{IAl\,(1)}(\lambda_a)$	$Q_{WAl\,(1)}(\Delta\lambda_a)$	$Q_{IAl\,(2)}(\lambda_a)$	$Q_{WAl\,(2)}(\Delta\lambda_a)$		
As I 193.695	4.6×10^{-3}	2.7×10^{-3}	3.7×10^{-3}	1.8×10^{-3}	0.80	0.70
Pt I 193.670	1.1×10^{-2}	3.1×10^{-3}	5.8×10^{-3}	2.3×10^{-3}	0.53	0.74
Tl II 190.852	7.1×10^{-4}	5.6×10^{-4}	7.9×10^{-4}	5.6×10^{-4}	1.10	1.00

It follows therefore that all prominent lines shown in Table 3 are "hard" lines and by adjusting the operating conditions it is possible to obtain the optimum temperatures for the emission of distinct lines of analytes.

(ii) The detection limits in pure solvent decrease at $T_{exc} \approx 7200$ K in comparison with the detection limits at $T_{exc} \approx 6200$ K (column 6 versus column 7).

3.1.2 Complex environmental matrix. The optimization of experimental conditions in the determination of traces of elements in complex matrices requires a procedure consisting of the following three steps:

3.1.2.1. Identification of all matrix lines which influence the prominent lines of the analytes. The identification requires a detailed study of the spectrum of the interferents. The interfering lines were identified by measuring their position with respect to that of the relevant analysis lines in a separate scan of the analyte in the presence of 2 mg ml^{-1} Al, Ca, Fe, Mg and Ti as interferents separately. Table 4 shows, as an example, the identification of the spectrum of Al, Ca, Fe, Mg and Ti as interferents around five prominent lines of platinum by using 40.68 MHz ICP and spectrometer with high resolution (practical spectral bandwidth = 5 pm). The following special features should be noted:

(i) Known from the existing spectral tables [19 – 21] is the line of Al II 203.993. This matrix line is far away from the most prominent line of platinum Pt II 203.646 ($\Delta\lambda_{ka} = + 0.347$ nm), but even though it influences the line and wing background interference level;

(ii) The wide lines Al I 214.539 nm [53] and Al I 217.403 nm [19, 20] determine Q_{IAl} (λa) > 0 around the prominent lines of Pt II 214.423 nm and Pt I 217.467 nm, respectively;

(iii) The Al 193. 564 nm is not listed in the existing spectral tables [19 – 21]. At a practical spectral bandwidth = 5 pm this line was registered as a wide complex line (Al 193.588 nm, Al 193.573 nm, Al 193. 570 nm, Al 193. 564 nm, Al 193.554 nm and Al 193.547 nm), which influenced the background intensity in the investigated spectral window up to 193.757 nm;

(iv) The following four matrix lines: Ti 203. 681 nm (in the spectral window of Pt II 203.646 nm) and Al 193.564 nm, Fe 193.655 nm, Ti 193.657 nm (in the spectral window of Pt I 193.670 nm) were register. These lines are not noted in the existing spectral tables [19 – 21], but they determine the line

interference and wing background interference levels around Pt II 203.646 and Pt I 193.670 nm.

In addition, Pt I 265.945nm (the fifth prominent line, in accordance with the detection limits in pure solvent) was chosen as analysis line. This prominent line is relatively free of line interference (only $Q_{IFe} = 7.0 \times 10^{-6}$). However, this involves a trade-off between spectral interferences and sensitivity, if the most intense lines suffer from interference.

It may be than concluded that the type and the magnitude of the spectral interferences are specific for a given matrix and cannot be predicted in general terms. The data presented in Table 4 shows that there are unknown matrix lines, very wide known matrix lines, in some cases out of the spectral window of the corresponding prominent lines, but just these matrix lines determine the line and wing background level. Therefore, only detailed experimental study can reveal the situation for each matrix type.

3.1.2.2. Quantification of type of spectral interferences under different experimental conditions. The spectral interferences in the presence of 2 mg ml^{-1} Al, Ca, Fe, Mg or Ti separately around the selected prominent lines of elements with different ionization potentials at $T_{exc} \approx 6200$ K and 7200 K were studied by 40.68 MHz ICP and spectrometer with high resolution. The change in T_{exc} was affected by varying the sheath gas flow rate (Table 2) and was measured by the Boltzmann plot method with titanium lines [17]. The investigations show that the line interference level using a spectrometer with high resolution is determined by aluminium, iron and titanium.

The magnitudes of the sensitivities of interfering signals are presented in Tables 5 and 6. S_{IJ} (λ_a) and S_{WJ} ($\Delta\lambda_a$) values (Table 5) and the magnitudes of Q_{IJ} (λ_a) and Q_{WJ} ($\Delta\lambda_a$) values (Table 6) in the presence of 2 mg ml^{-1} iron as interferent for the prominent lines of Zn, Pt, B, Hg, Cd, Tl and U. Tables 7 and 8 list the magnitudes of sensitivities of interfering signals (Table 7) and the magnitudes of Q-values (Table 8) in the presence of 2 mg ml^{-1} aluminium as interferents for the prominent lines of As, Pt and Tl. The prominent lines, which are influenced by line interferences in the presence of iron (Tables 5, 6) or aluminium (Tables 7, 8) are included in Tables 5 – 8. Here we would like to illustrate the cases of variation of Q-values as a function of T_{exc}. The following comes to a conclusion:

Table 9. Line selection in the determination of As, Zn, Pt, B, Hg, Cd, Tl and U in environmental materials. Interferents: Al, Ca, Fe, Mg and Ti

Analytes, wavelengths, λ, nm	Interferents	$Q_{WJ}(\Delta\lambda_a)$	$Q_{IJ}(\lambda_a)$
As I 193.695 BEC = 0.1 µg ml^{-1} C_L = 3.0 ng ml^{-1}	Al	1.8×10^{-3}	3.7×10^{-3}
	Ca	0	0
	Fe	5.9×10^{-5}	0
	Mg	0	0
	Ti	2.6×10^{-5}	0
As I 189.042 **BEC = 0.15 µg ml^{-1}** **C_L = 4.3 ng ml^{-1}**	**Al**	$\mathbf{4.4 \times 10^{-4}}$	**0**
	Ca	**0**	**0**
	Fe	**0**	**0**
	Mg	**0**	**0**
	Ti	**0**	**0**
Zn I 213.856 BEC = 0.05 µg ml^{-1} C_L = 1.4 ng ml^{-1}	Al	8.0×10^{-6}	0
	Ca	2.0×10^{-6}	0
	Fe	0	1.0×10^{-5}
	Mg	0	0
	Ti	2.0×10^{-6}	4.0×10^{-6}
Zn II 202.548 **BEC = 0.06 µg ml^{-1}** **C_L = 1.7 ng ml^{-1}**	**Al**	$\mathbf{2.0 \times 10^{-5}}$	**0**
	Ca	$\mathbf{1.0 \times 10^{-6}}$	**0**
	Fe	$\mathbf{1.0 \times 10^{-5}}$	**0**
	Mg	$\mathbf{4.0 \times 10^{-6}}$	**0**
	Ti	$\mathbf{2.0 \times 10^{-5}}$	**0**
Pt II 203.646 BEC = 0.23 µg ml^{-1} C_L = 7.0 ng ml^{-1}	Al	7.2×10^{-4}	0
	Ca	0	0
	Fe	9.6×10^{-5}	8.5×10^{-3}
	Mg	0	0
	Ti	2.4×10^{-5}	6.6×10^{-5}
Pt II 214.423 BEC = 0.26 µg ml^{-1} C_L = 8.0 ng ml^{-1}	Al	1.9×10^{-4}	2.3×10^{-4}
	Ca	0	0
	Fe	1.9×10^{-5}	3.7×10^{-5}
	Mg	0	0
	Ti	1.9×10^{-5}	0
Pt I 217.467 BEC = 0.43 µg ml^{-1} C_L = 12.0 ng ml^{-1}	Al	7.1×10^{-4}	2.0×10^{-3}
	Ca	0	0
	Fe	5.1×10^{-5}	5.7×10^{-5}
	Mg	0	0
	Ti	0	0
Pt I 193.670 BEC = 0.46 µg ml^{-1} C_L = 13.0 ng ml^{-1}	Al	2.4×10^{-3}	6.0×10^{-3}
	Ca	0	0
	Fe	3.1×10^{-5}	2.1×10^{-5}
	Mg	0	0
	Ti	2.7×10^{-5}	3.0×10^{-6}
Pt I 265.945 **BEC = 0.50 µg ml^{-1}** **C_L = 14.0 ng ml^{-1}**	**Al**	$\mathbf{1.7 \times 10^{-5}}$	**0**
	Ca	**0**	**0**
	Fe	$\mathbf{7.1 \times 10^{-6}}$	$\mathbf{7.0 \times 10^{-6}}$
	Mg	**0**	**0**
	Ti	**0**	**0**
B I 249.773 BEC = 0.18 µg ml^{-1} C_L = 5.1 ng ml^{-1}	Al	0	0
	Ca	0	0
	Fe	6.0×10^{-6}	5.0×10^{-5}
	Mg	1.0×10^{-5}	0
	Ti	1.2×10^{-5}	0

Table 9 (continued)

Analytes, wavelengths, λ, nm	Interferents	$Q_{WJ}(\Delta\lambda_a)$	$Q_{IJ}(\lambda_a)$
B I 249.678 BEC = 0.20 µg ml^{-1} C$_L$ = 5.6 ng ml^{-1}	Al	0	0
	Ca	0	0
	Fe	6.0×10^{-6}	5.0×10^{-5}
	Mg	4.0×10^{-6}	0
	Ti	1.2×10^{-5}	0
B I 208. 959 BEC = 0.23 µg ml^{-1} C$_L$ = 6.5 ng ml^{-1}	**Al**	$\mathbf{6.0 \times 10^{-5}}$	**0**
	Ca	**0**	**0**
	Fe	**0**	**0**
	Mg	**0**	**0**
	Ti	**0**	**0**
Hg II 194.277 BEC = 0.07 µg ml^{-1} C$_L$ = 2.0 ng ml^{-1}	Al	4.7×10^{-4}	0
	Ca	0	1.0×10^{-5}
	Fe	1.4×10^{-5}	
	Mg	3.4×10^{-6}	0
	Ti	1.0×10^{-5}	1.9×10^{-5}
Hg I 253.652 BEC = 0.07 µg ml^{-1} C$_L$ = 2.0 ng ml^{-1}	**Al**	**0**	**0**
	Ca	$\mathbf{7.7 \times 10^{-6}}$	**0**
	Fe	$\mathbf{2.0 \times 10^{-4}}$	**0**
	Mg	$\mathbf{5.1 \times 10^{-5}}$	**0**
	Ti	$\mathbf{8.7 \times 10^{-5}}$	**0**
Cd II 226. 502 BEC = 0.05 µg ml^{-1} C$_L$ = 1.4 ng ml^{-1}	Al	0	0
	Ca	1.3×10^{-6}	0
	Fe	2.0×10^{-5}	8.0×10^{-5}
	Mg	0	0
	Ti	8.0×10^{-5}	0
Cd II 214.438 BEC = 0.06 µg ml^{-1} C$_L$ = 1.7 ng ml^{-1}	**Al**	**0**	**0**
	Ca	$\mathbf{1.3 \times 10^{-6}}$	**0**
	Fe	$\mathbf{6.2 \times 10^{-6}}$	$\mathbf{2.0 \times 10^{-5}}$
	Mg	**0**	**0**
	Ti	$\mathbf{8.0 \times 10^{-5}}$	**0**
Tl II 190.852 BEC = 0.14 µg ml^{-1} C$_L$ = 4.0 ng ml^{-1}	Al	3.6×10^{-4}	4.3×10^{-4}
	Ca	0	0
	Fe	2.0×10^{-5}	5.3×10^{-4}
	Mg	0	0
	Ti	2.6×10^{-4}	8.8×10^{-4}
Tl II 190.876 BEC = 0.24 µg ml^{-1} C$_L$ = 7.0 ng ml^{-1}	Al	5.6×10^{-4}	8.4×10^{-4}
	Ca	0	0
	Fe	4.0×10^{-4}	6.9×10^{-4}
	Mg	0	0
	Ti	4.0×10^{-4}	1.5×10^{-3}
Tl I 276.787 BEC = 0.54 µg ml^{-1} C$_L$ = 15.0 ng ml^{-1}	**Al**	$\mathbf{1.0 \times 10^{-5}}$	**0**
	Ca	$\mathbf{1.0 \times 10^{-5}}$	**0**
	Fe	$\mathbf{1.4 \times 10^{-4}}$	**0**
	Mg	$\mathbf{2.5 \times 10^{-4}}$	**0**
	Ti	$\mathbf{4.5 \times 10^{-5}}$	**0**
U II 385.958 BEC = 0.05 µg ml^{-1} C$_L$ = 1.4 ng ml^{-1}	Al	0	0
	Ca	5.0×10^{-5}	0
	Fe	5.2×10^{-4}	6.2×10^{-4}
	Mg	7.0×10^{-5}	0
	Ti	5.5×10^{-5}	0

Table 9 (continued)

Analytes, wavelengths, λ, nm	Interferents	$Q_{WJ} (\Delta\lambda_a)$	$Q_{IJ}(\lambda_a)$
U II 367.007 BEC = 0.05 µg ml^{-1} C_L = 1.4 ng ml^{-1}	Al	0	0
	Ca	5.0×10^{-5}	0
	Fe	5.0×10^{-5}	6.0×10^{-4}
	Mg	7.0×10^{-5}	0
	Ti	5.5×10^{-5}	0
U II 263.553 BEC = 0.09 µg ml^{-1} C_L = 2.6 ng ml^{-1}	Al	5.0×10^{-5}	0
	Ca	0	0
	Fe	1.0×10^{-4}	5.0×10^{-4}
	Mg	0	0
	Ti	1.0×10^{-4}	5.0×10^{-3}
U II 409.014 **BEC = 0.2 µg ml^{-1}** **C_L = 6.1 ng ml^{-1}**	**Al**	$\mathbf{1.0 \times 10^{-4}}$	**0**
	Ca	**0**	**0**
	Fe	**0**	**0**
	Mg	**0**	**0**
	Ti	**0**	**0**

(i) The $S_{IJ} (\lambda_a)$ and $S_{WJ} (\Delta\lambda_a)$ values increase with increasing T_{exc} in the presence of iron or aluminium as interferents (Tables 5 and 7);

(ii) The magnitude of $Q_{IJ} (\lambda_a)$ and $Q_{WJ} (\Delta\lambda_a)$ values (Tables 6 and 8) depends on the enhancement factor of S_A (Table 3) and $S_{IJ} (\lambda_a)$ or $S_{WJ} (\Delta\lambda_a)$, respectively (Tables 5 and 7):

- if $S_{A (2)} (\lambda_a) / S_{A (1)} (\lambda_a) > S_{IJ (2)} (\lambda_a) / S_{IJ (1)} (\lambda_a)$ and $S_{A (2)} (\lambda_a) / S_{A (1)} (\lambda_a) > S_{WJ (2)} (\Delta \lambda_a) / S_{WJ (1)} (\lambda_a)$,

then $Q_{IJ (2)} (\lambda_a) / Q_{IJ (1)} (\lambda_a) < 1$ and $Q_{WJ (2)} (\Delta \lambda_a) / Q_{WJ (1)} (\Delta \lambda_a) < 1$ in the case of Tables 6 for Pt I 265.945 nm, B I 249.773 nm and Cd II 214.338 nm and Table 8 for As I 193.695 nm and Pt I 193.670 nm.

- if $S_{A (2)} (\lambda_a) / S_{A (1)} (\lambda_a) \approx S_{IJ (2)} (\lambda_a) / S_{IJ (1)} (\lambda_a)$ and $S_{A (2)} (\lambda_a) / S_{A (1)} (\lambda_a) \approx S_{WJ (2)} (\Delta \lambda_a) / S_{WJ (1)} (\lambda_a)$,

then $Q_{IJ (2)} (\lambda_a) / Q_{IJ (1)} (\lambda_a) \approx 1$ and $Q_{WJ (2)} (\Delta \lambda_a) / Q_{WJ (1)} (\Delta \lambda_a) \approx 1$ in the case of Table 6 for Tl II 190.852 nm and U II 385.958 nm and Table 8 for Tl II 190.852 nm.

- if $S_{A (2)} (\lambda_a) / S_{A (1)} (\lambda_a) < S_{IJ (2)} (\lambda_a) / S_{IJ (1)} (\lambda_a)$ and $S_{A (2)} (\lambda_a) / S_{A (1)} (\lambda_a) < S_{WJ (2)} (\Delta \lambda_a) / S_{WJ (1)} (\lambda_a)$,

then $Q_{IJ (2)} (\lambda_a) / Q_{IJ (1)} (\lambda_a) > 1$ and $Q_{WJ (2)} (\Delta \lambda_a) / Q_{WJ (1)} (\Delta \lambda_a) > 1$ presented in Table 6 for Hg I 194.277 nm and Zn I 213.856 nm.

It should be noted that the increase of Q-values at $T_{exc} \approx 7200$ K is insignificant. This factor is equal to 1.1 in Table 6 for Zn I 213.856 nm and U II 385.958 nm and Table 8 for Tl II 190.852 nm.

The main result from the investigations is that $T_{exc} \approx 7200$ K is an appropriate excitation temperature for determination of traces of elements in environmental samples. The results show that the lowest detection limits in the determination of traces of elements in environmental materials can be obtained under robust operating conditions (Mg II / Mg I = 11.4, which corresponds to $T_{exc} \approx 7200$ K).

3.1.2.3. Line selection at $T_{exc} \approx 7200$ K. The prominent lines of analytes, which are investigated in the present paper, are listed Table 9 (column 1). The data presented under the wavelength of the analysis lines refer to detection limits in pure solvent calculated in accordance with Eq. (4). Column 2 gives matrix elements, columns 3 and 4 show $Q_{WJ} (\Delta\lambda_a)$ values for wing background interference and $Q_{IJ}(\lambda_a)$ values for line interference, respectively. It should be noted that $Q_{WJ}(\Delta\lambda_a)$ values do not enter into the selectivity term in Eq. (3) and affect the true detection limits only via the conventional detection limits (Eq. 2). This implies that the influence of $Q_{WJ} (\Delta\lambda_a)$ values is minor or negligible, as long as $C_{L, true}$ is dictated by line interference, i.e. by the magnitude of $Q_{IJ}(\lambda_a)$ values in the presence of a complex matrix. Hence, the optimum line selection for trace analysis in a variety of multi-component environmental materials without information regarding the concentration of the matrix constituents (Al, Ca, Fe, Mg and Ti) requires the choice of prominent lines free or negligibly influenced by line interference. The selected prominent lines in the presence of complex matrix are printed in bold.

Discussing the results shown in Table 9 it can be seen that in the case of a multi-component matrix containing Al, Ca, Fe, Mg and Ti in the determination of As, Zn, Pt, B, Hg Cd, Tl and U it is not possible to choose the most prominent lines in accordance with the detection limits in pure solvent as analysis lines because these lines are influenced by line interferences, i.e. $\Sigma Q_{IJ}(\lambda_a) > 0$. In this case the second prominent lines of mercury, arsenic and zinc were free of line interferences, i.e. $\Sigma Q_{IJ}(\lambda_a) = 0$ for Hg I 253.652 nm, As I 189.042 nm and Zn II 202.548 nm and were selected as analysis lines. The fourth prominent line of uranium U II 409.014 nm and the third thallium Tl I 276.787 nm were free of line interferences. These lines were selected as analysis lines. For cadmium and platinum no prominent lines free of line interference could be selected. For these elements the following prominent lines were selected as analysis lines: the second prominent line of cadmium (Cd II 214.438) for which $\Sigma[Q_{IAl}(\lambda_a) + Q_{ICa}(\lambda_a) + Q_{IMg}(\lambda_a) Q_{ITi}(\lambda_a)] = 0$, but $Q_{IFe}(\lambda_a) > 0$ - and the fifth prominent line of platinum Pt I 265.945 nm for which $\Sigma[Q_{IAl}(\lambda_a) + Q_{ICa}(\lambda_a) + Q_{IMg}(\lambda_a) Q_{ITi}(\lambda_a)] = 0$ and $Q_{IFe}(\lambda_a) > 0$.

With respect to "zero" values of $Q_{IJ}(\lambda_a)$ values, we will note the following in accordance with [13]: if in Table 3 $Q_{IJ}(\lambda_a)$ are listed as "zero", this implies that $Q_{IJ}(\lambda_a) \times C_{IJ}$ is equal to or smaller than the numerical values of the detection limits (in ng ml^{-1}) shown in Table 3 under the corresponding prominent line.

By using $Q_{IJ}(\lambda_a)$ values and detection limits in pure solvent (Table 9) the maximal interferent concentration C_{IJ} for which $Q_{IJ}(\lambda_a) = 0$ in the presence of matrix constituents can be calculated by equation (5) [13]:

$$C_{IJ} = C_L / Q_{IJ}(\lambda_a) \qquad (5)$$

Table 10 lists the maximal interferent concentrations C_{IJ} for which $Q_{IJ}(\lambda a)=0$ in the presence of aluminium, iron or titanium as interferents (Eq. 5). These matrix constituents determine line interference levels around the most prominent lines of the analytes in accordance with Table 9. The "best" prominent lines are printed in bold. If the concentration of interferents in the sample solution is lower in comparison with the corresponding values shown in Table 10, the most prominent lines can be used as analysis lines. Therefore, Table 10 can be used for additional line selection.

Table 10. Maximum interferent concentration C_{IJ} (µg ml^{-1}) for which $Q_{IJ}(\lambda a) = 0$

Analysis lines, λ, nm	Maximum interferent concentration C_{IJ} (µg ml^{-1}) for which $Q_{IJ}(\lambda a)=0$		
	Al	Fe	Ti
As I 193.695	0.80	-	-
As I 189.042	-	-	-
As I 197.198	0.34	24.0	
As I 200.334	-	-	-
Zn I 213.856	-	140	350
Zn II 202.548	-	-	-
Pt I 203.646	-	0.82	106
Pt II 214.423	35	216	-
Pt I 217.467	6	210	-
Pt I 193.670	2	620	4330
Pt I 265.945	-	2000	-
B I 249.773	-	100	-
B I 249.678	-	112	-
B I 208.959	-	-	-
Hg II 194.277	-	200	105
Hg I 253.652	-	-	-
Cd II 226.502	-	18	-
Cd II 214.438	**-**	**85**	
Tl II 190.852	5.0	6.0	5.0
Tl II 190.876	8.0	10.0	5.0
Tl I 276.787	-	-	-
U II 385.958	-	2.0	-
U II 367.007	-	2.0	-
U II 263.553	-	5.0	1.2
U II 409.014	-	-	-

In conclusion it should be noted that the "best" analysis lines can be used in the determination of the above mentioned trace elements in environmental materials. The optimal operating conditions are shown (Table 2). By using the "best" analysis lines the lowest possible detection limits can be achieved in the presence of the above mentioned matrix constituents. If the concentration of interferents in the sample solution is lower in comparison with the corresponding values shown in Table 10, the most prominent lines in pure solvent can be used as analysis lines in the determination of As, Zn, Pt, B, Hg, Cd, Tl and U in environmental materials with various matrix constituents. Quantification of all significant interferences for the prominent lines ensures the accuracy of measurements by ICP - OES.

3.2. Application of ICP-OES in the determination of As, Zn, Pt, B, Hg, Cd, Tl and U in environmental materials

3.2.1. Determination of As, Zn, Hg, Cd and U in the certified reference material IAEA/ Soil 7. a) Digestion procedure**. Extraction of trace elements soluble in *aqua regia* was used as a decomposition method in accordance with ISO 11466 [22]. 1 g sample was dissolved and the final solution was

collected in 50 ml volume. After the undissolved material has settled, the supernatant solution was subjected to analysis by ICP - OES. The blank sample contains the acids used for digestion.

b) Determination of matrix elements. The concentrations of Al, Ca, Fe, Mg and Ti are as follows: Al – 660 ± 6 (in μg ml^{-1}), Ca – 3160 ± 25 (in μg ml^{-1}), Fe – 500 ± 6 (in μg ml^{-1}), Mg – 210 ± 5 (in μg ml^{-1}) and Ti – 9.6 ± 0.5 (in μg ml^{-1}). Mean values for statistical confidence P = 95 % and six replicates (n =6) are obtained.

c) Determination of As, Zn, Hg, Cd and U. Table 11 shows the contents of As, Zn, Hg, Cd and U obtained by ULTIMA 2 ICP - OES in the analysis of the certified reference material IAEA / Soil 7, as well as the relative standard deviation (RSD %) and the corresponding certified values. Using Student's criterion [25], no statistical differences between the experimental values and certified values were registered. In this way the accuracy of the analytical results can be ensured.

The "best" analysis lines of As, Zn, Hg and U are free of line interferences and true detection limits are equal to conventional detection limits ($C_{L, true} = C_{L, conv}$) (column 3). The conventional detection limits were calculated in the presence of the matrix constituents Al, Ca, Fe, Mg and Ti in the final sample solution by Eq. 2. In case of Cd, the "best" line was influenced by line interference $Q_{IJ}(\lambda_a) > 0$ and $C_{L, true}$ was calculated by Eq.3.

Table 11. Contents of As, Zn, Cd, Hg and U (μg g^{-1}) obtained in the analysis of certified reference material IAEA / Soil 7: mean values [X] for (*n* = 4 replicates) and the confidence interval of the mean value [ΔX] for statistical confidence *P* = 95% and f = *n* - 1= 3 (columns 2); detection limits in the presence of above mentioned matrix constituents (μg g^{-1}) (column 3); relative standard deviation (RSD %) (columns 4); certified values (column 5); maximum permissible concentrations for soils (column 6)

Selected prominent lines, λ, nm	Concentration μg g^{-1} X ± ΔX	True detection limits, μg g^{-1}	RSD, %	Certified values, μg g^{-1}	Maximum permissible concentrations for soils in μg g^{-1}
As I 189.042 BEC = 0.15 μg ml^{-1} C_L = 4.3 ng ml^{-1}	13.2 ± 0.4	$C_{L, true}$ = $C_{L, conv.}$ = 1.58	4.2	13.4	15 ÷ 22 [23]
Zn II 202.548 BEC = 0.06 μg ml^{-1} C_L = 1.7 ng ml^{-1}	103 ± 1.4	$C_{L, true}$ = $C_{L, conv}$ = 0.23	1.8	104	150 ÷ 300 [23]
Hg I 253.652 BEC = 0.07 μg ml^{-1} C_L = 2 ng ml^{-1}	The element is not detected.	$C_{L, true}$ = $C_{L, conv}$ = 0.58	-	0.04	1 ÷1.5 [23]
Cd II 214.438 BEC = 0.06 μg ml^{-1} C_L = 1.7 ng ml^{-1}	1.27 ± 0.06	$C_{L, true}$ = 0.62	4.7	1.3	1 ÷ 3 [23]
U II 409.014 BEC = 0.2 μg ml^{-1} C_L = 6.1 ng ml^{-1}	2.62 ± 0.1	$C_{L, true}$ = $C_{L, conv}$= 0.75	3.8	2.6	0.3 ÷ 11.7 [24]

3.2.2. Determination of platinum in certified reference material BCR-723 (road dust).

a) Digestion procedure: Extraction of traces of Pt by acid mixture (HBr /HNO$_3$) in an apparatus, described in [ISO 11466:1995 (E)] was used for digestion of the certified reference material BCR-723 (road dust). 1 g sample was dissolved and the final solution was collected in 100 ml volume.

b) Determination of matrix elements. The concentrations of Al, Ca, Fe, Mg and Ti are as follows: Al – 220 ± 6 (in μg ml^{-1}), Ca – 550 ± 10 (in μg ml^{-1}, Fe – 350 ± 8 (in μg ml^{-1}), Mg – 250 ± 6 (in μg ml^{-1}) and Ti – 9.0 ± 0.5 (in μg ml^{-1}). Mean values for statistical confidence P = 95 % and six replicates (n =6) are shown.

c) Determination of platinum. The true detection limit for Pt was 19 times higher in comparison with the certified value in the certified reference material BCR-723 - road dust (Table 12). Hence this concentration cannot be detected by direct ICP-OES (without separation or pre-concentration procedure).

The improvement of the detection limits in the determination of Pt in environmental materials by ICP - OES was achieved by developing a new column method with *2-mercaptobenzimidazole* immobilized on activated carbon for separation of the matrix elements Al, Ca, Fe, Mg and Ti and pre-concentration of platinum. The interest in activated

carbons is determined by their unique properties such as large specific surface area, strongly developed micro porosity and the possibility to modify their surface and texture [26 – 32].

Table 12. Contents of Pt (μg g^{-1}) obtained in the analysis certified reference material BCR-723 mean values [X] for (*n* = 4 replicates) (column 2); detection limits in the presence of above mentioned matrix constituents (μg g^{-1}) (column 3); and certified values (column 5)

Selected prominent lines, λ, nm	Concentration μg g^{-1} X ± ΔX	True detection limits, μg g^{-1}	RSD, %	Certified values, μg g^{-1}
Pt I 265.945 BEC = 0.50 μg ml^{-1} C_L = 14.0 ng ml^{-1}	The element is not detected	$C_{L\ true}$ = 1.54	–	0.0813

Table 13. Detection limits with respect to the dissolved solid sample, in μg g^{-1} in the determination of Pt in certified reference material BCR-723, concentration of Pt in μg g^{-1}, RSD of the analytical results and certified values in μg g^{-1}

Analysis line, λ, nm	Detection limits, μg g^{-1}	Concentration, in μg g^{-1}	RSD, %	Certified values, μg g^{-1}
Pt II 203.646	0.0033	0.0809 ± 0.005	3.0	0.0813

2-mercaptobenzimidazole modified activated carbon was prepared by the following steps: first step: the activated carbon was heated in a furnace at 600ºC for 3 h in inert atmosphere. Then the sample was cooled down to room temperature in argon; second step: 3 g of activated carbon were heated for 1 h at 200ºC in vacuum, whereupon 10 ml of a 2 wt % solution of 2-mercaptobenzimidazole in ethanol were added and the mixture was allowed to stand at 20ºC for 2 h to facilitate better penetration of the modifier into the pores of the activated carbon. Then the solvent was evaporated at 90 – 100º C. This procedure was repeated three times. The modified carbon was washed with distilled water and 1M HCl until attaining a constant pH value of the washing water, and then dried at 100ºC for 6 h.

The optimal parameters of the new column method were: column with bore = 3 mm, length = 9 mm, amount of activated carbon = 0. 4 g, flow rate of the solution = 4 ml min^{-1}, pH =1, concentrations of matrix elements were 10 times lower in comparison with the corresponding values shown in Table 4. The column was washed with 0.1 HCl. The experiments were carried out at room temperature. Under these experimental conditions, 100 % of platinum was sorbed on the activated carbon immobilized with *2-mercapto-benzimidazole*. The column with activated carbon was dried in a drying-oven at 90ºC. The activated carbon was transferred to a quartz crucible and the sample was heated at 450 ºC (1 h) and 850 ºC (1 h) in a furnace; the quartz crucible was allowed to cool slowly at room temperature and after that the crucible was put into the reaction flask of an apparatus, described in ISO 11466:1995 (E); an acid mixture HNO$_3$/HBr (3 ml HNO$_3$ + 3 ml HBr) was used for dissolution of the so prepared residue; the sample was heated under reflux until boiling for 1 h and allowed to cool slowly at room temperature. The final sample solution was 10 ml.

The column method with *2-mercapto-benzimidazole* immobilized on activated carbon was applied for pre-concentration/ separation in the determination of Pt in the certified reference material BCR - 723 (road dust.) The final sample solution was introduced into the ICP using an ultrasonic nebulizer (Courtesy of Cetac Technologies, Omaha, Nebraska, USA). Table 13 shows the detection limits in the determination of Pt with respect to the dissolved solid sample, in μg g^{-1} (column 2) by using the above pre-concentration/separation procedure, the content of Pt in the certified reference material BCR-723, obtained by ICP - OES (mean values X, for n = 4 replicates and the confidence interval of the mean value ΔX for statistical confidence P = 95% and f = n − 1 =3 (column 3), as well as the RSD of the analytical results (column 4). Column 5 lists the certified values for comparison. By using the above mentioned pre-concentration/separation procedure the spectral interferences were totally eliminated and the most prominent line Pt II 203.646 nm in pure solvent was used as analysis line. The results obtained by the present pre-concentration / separation method and following ICP-OES determination agree well with the certified values of the reference material BCR-723

and can be successfully used in the determination of platinum in environmental materials.

3.2.3. Determination of As, Zn, Cd, Tl and U in National Water Research Institute (NWRI) certified standard, lake water TMDA-51.2.

Table 14. Determination of As, Zn, Cd, Tl and U in National Water Research Institute (NWRI) certified standard, lake water TMDA-51.2

Selected prominent lines, λ nm	Concentration ng ml^{-1} X ± ΔX	Detection limits in pure solvent, ng ml^{-1}	RSD, %	Certified values, ng ml^{-1}	Maximum permissible concentrations for drinking waters (ng ml^{-1}) [33]
As I 193.695	15.4 ± 0.4	3.0	2.6	15.3	10
Zn I 213.856	107 ± 3	1.4	2.8	106	5 000
Cd II 226. 502	24.8 ± 0.5	1.4	2.0	25.1	5
Tl II 190.852	19.8 ± 0.6	4.0	3.0	20.0	No data
U II 385.958	30 ± 1.0	1.4	3.3	29.3	60
Al	-	-	-	96.0	-
Fe	-	-	-	111.0	-

The concentrations of As, Zn, Cd, Tl and U in NWRI certified standard, lake water - TMDA-51 are collected in Table 14: the results are obtained by ICP - OES, JY ULTIMA 2 equipment (column 2) (n = 6 replicates); detection limits for the analytes in pure solvent (column 3); relative standard deviation (RSD, %) (column 4) and corresponding certified reference values (column 5). It should be noted that the line interference level for the most prominent lines of As, Zn, Cd, Tl and U is determined by aluminium and iron as interferents (Table 9). The concentrations of the interferents in the NWRI certified standard are C_{IAl} (certificate) = 0.096 μg ml^{-1} and C_{IFe} (certificate) = 0.111 μg ml^{-1}, respectively. These concentrations are lower than the corresponding values for which $Q_{I\ Al}\ (\lambda_a) = 0$ and $Q_{I\ Fe}\ (\lambda_a) = 0$ (Table 9). Therefore, the most prominent lines of As, Zn, Cd, Tl and U with $Q_{IJ}(\lambda_a) = 0$ can be used for determination of these elements and the detection limits are equal to the values obtained in pure solvent (column 3). The background can be corrected by a simple off-peak background measurement.

The results obtained by the present ICP-OES method agree well with the corresponding certified values. The detection limits obtained by JY ULTIMA 2 satisfy the requirements from the point of view of maximum permissible concentrations for drinking waters [33].

CONCLUSIONS

This work shows that in the analysis of complex environmental materials, quantitative information on the spectral interferences is essential. The Q-concept, as proposed by Boumans and Vrakking [15], was used for quantification of the spectral interferences in the presence of Al, Ca, Fe, Mg and Ti as interferents. By using a spectrometer with a practical spectral bandwidth of 5 pm it is possible to select the ''best'' analysis lines for As, Zn, B, Hg, Tl and U, which are free of line interferences in the presence of a complex environmental matrix. The "best" prominent lines for Pt and Cd were influenced by line interference (Table 9). The results of Table 11 illustrate the correct background subtraction in the determination of As, Zn, Cd, Hg and U in the analysis of the certified reference material IAEA / Soil 7. Extraction of trace elements in *aqua regia* was used as a dissolution method.

Comparison of the detection limits (Table 11, column 3) by using 40.68 MHz ICP JY ULTIMA 2 with the corresponding maximum permissible concentrations for soils in μg g^{-1} shows that the detection limits are significantly lower in comparison with the given threshold levels. Therefore, this method can be successfully used for real contaminations in soil samples.

The determination of platinum in road dust requires the application of a separation / pre-concentration procedure for improvement of the detection limit. In the present paper a new column method with *2-mercaptobenzimidazole* immobilized on activated carbon was developed for separation of matrix elements Al, Ca, Fe, Mg, Ti and pre-concentration of platinum. The results obtained by the present pre-concentration/ separation method and following ICP - OES determination show that this method can be successfully used in the determination of platinum in environmental materials (Table 13).

The detection limits obtained by JY ULTIMA 2 satisfy the requirements from point of view of maximum permissible concentrations for drinking waters [33] (Table 14).

REFERENCES

1. P.W.J.M. Boumans, Basic concepts and characteristics of ICP - AES, in: Boumans (eds.), Inductively Coupled Plasma Emission Spectroscopy - Part 1, Methodology, Instrumentation, and Performance, John Wiley & Sons, New York, US, 1987, p. 100, Chapter 4.
2. P.W.J.M. Boumans, *Fresenius Z. Anal. Chem.*, **324**, 394 (1986).
3. J. Dennaud, A. Howes, E. Poussel, J.M. Mermet, *Spectrochim. Acta Part B,* **56,** 101 (2001).
4. M. Stepan, P. Musil, E. Poussel, J.M. Mermet, *Spectrochim. Acta Part B*, **56**, 443 (2001).
5. G.C.Y. Chan, W.T. Chan, X. Mao, R.E. Russo, *Spectrochim. Acta Part B*, **56,** 77 (2001).
6. G.C.Y. Chan, G.M. Hieftje, *Spectrochim. Acta Part B*, **61**, 642 (2006).
7. P. Razpotnik, B. Budić, M. Veber, *Appl. Spectrosc.*, **56**, 1000 (2002).
8. G.C.Y. Chan, W.T. Chan, *Spectrochim. Acta Part B*, **58**, 1301 (2003).
9 I. Kolibarska, S. Velichkov, N. Daskalova, *Spectrochim. Acta Part B*, **63**, 603 (2008).
10. P. Petrova, S. Velichkov, I. P. Havezov, N. Daskalova, *Bulg. Chem. Commun.,* **41**, 65 (2009).
11. P. Petrova, S. Velichkov, N. Velitchkova, I. Havezov, N. Daskalova, *Spectrochimica Acta Part B*, **65**, 130 (2010).
12. J.W. McLaren, Applications: Environmental, in: P.W.J.M. Boumans (ed.), Inductively Coupled Plasma Emission Spectroscopy, Part 2: Applications and Fundamentals, Chapter 3, Wiley, New York, 1987, p. 48.
13. N. Velitchkova, S. Velichkov, N. Daskalova, *Spectrochim. Acta Part B*, **62,** 386 (2007).
14. N. Daskalova, L. Aleksieva, G. Gentsheva, S. Velichkov, *Spectrochim. Acta Part B,* **57**, 755 (2002).
15. P.W.J.M. Boumans, J.J.A.M. Vrakking, *Spectrochim. Acta Part B,* **43**, 69 (1988).
16. P.W.J.M. Boumans, Introduction to atomic emission spectrometry, in: P.W.J.M. Boumans (eds.) - Inductively Coupled Plasma Emission Spectroscopy - Part 1, Methodology, Instrumentations and Performance, John Wiley & Sons, New York, US, 1987, Chapter 1, p. 1
17. J.M. Mermet, Spectroscopic diagnostics: basic concepts, in: P.W.J.M.Boumans (eds.), Inductively Coupled Plasma Emission Spectroscopy - Part 1, Methodology, Instrumentation and Performance, John Wiley & Sons, New York, US, 1987, Chapter 10, p. 353.
18. M.W. Blades, G. Horlick, *Spectrochim. Acta Part B*, **36**, 861 (1981)
19. G.R. Harrison, M.I.T. Wavelength Tables, M.I.T. Press, Cambridge, MA, 1969.
20. A.N. Zaidel, V.K. Prokofèv, S.M. Raiskii, V.A. Slavnyi, E.Ya. Shreider, Tables of spectral lines, IFI / Plenum, New York, 1970.
21. P.W.J.M. Boumans, Line Coincidence Tables for inductively coupled plasma atomic emission spectrometry, Pergamon, Oxford, 1980.
22. International Organization for Standardization, Soil Quality, Extraction of Trace Elements Soluble in Aqua Regia, ISO 11466, 1995.
23. Maximum permissible concentrations of potentially toxic elements in sludge-treated soils (mg kg^{-1} dry soil) in EC Member States and US, Millieu, WRc and RPA, 2010.
24. S.C. Sheppard, M.I. Sheppard, M. Gallerand, B. Sanipelli, *J. Environ. Radioactivity*, 79, 55 (2005).
25. K. Doerffel, Statistik in der Analytischen Chemie, VEB Deutscher Verlag für Grundstoffindustrie, Leipzig, 1960.
26. K.Jankowski, A. Jackowski, P.Łukasiak, *Analytica Chimica Acta,* **540,** 197 (2005).
27. H.H. Someda, R.R. Sheha, *Radiochemistry*, **50**, 56 (2008).
28. B. Mikuła, B. Puzio, *Talanta* **71**, 136 (2008).
29. M.Ghaedi, A. Shokrollahi, A.H. Kianfar, A.Pourfarokhia, N. Khanjaria, A.S. Mirsadeghia, M. Soylak, *Journal of Hazardous Materials*, **162**, 1408 (2009).
30. A.A. Ensafi, T. Khayamian, M. Karbasi, *Analytical Sciences* **19,** 953 (2003).
31. A.C. Ferreira, M.A. Korn, S.L.C. Ferreira, *Microchim. Acta*, **146**, 271 (2004).
32. G. Gentsheva., P. Vasileva, P. Tzvetkova, L. Lakov, O. Peshev, E. Ivanova, *J. Porous Mater.*, **15**, 331 (2008).
33. Regulation No. 9, /2001, Quality Requirements for Drinking waters.

ОПРЕДЕЛЯНЕ НА As, Zn, Pt, B, Hg, Cd, Tl И U В ПРОБИ ОТ ОКОЛНАТА СРЕДА ЧРЕЗ ОПТИЧНА ЕМИСИОННА СПЕКТРОМЕТРИЯ С ИНДУКТИВНИ СВЪРЗАНА ПЛАЗМА С РАДИАЛНО НАБЛЮДЕНИЕ И ВИСОКО РАЗДЕЛЯНЕ

Н. Величкова [1], О. Велева [1], С. Величков [2], П. Марков [2], Н. Даскалова [2*]

[1] *Геологически институт, Българска академия на науките, Акад. Г. Бончев, бл. 24, 1113 София*
[2] *Институт по обща и неорганична химия, Българска академия на науките, Акад. Г. Бончев, бл. 11, 1113 София*

(Резюме)

Показани са възможностите и ограниченията на оптичната емисионна спектрометрия с радиална 40.68 MHz индуктвно свързана плазма и спектрометър с високо разделяне при определяне на As, Zn, Pt, B, Hg, Cd, Tl и U в проби от околната среда. Подобряване на границите на откриване е постигнато чрез оптимизирането на работните условия. Най-ниски граници на откривне бяха получени при твърди работни условия (температура за възбуждане около 7200 K) както в присъствие на чист разтворител, така и в присъствие на Al, Ca, Fe, Mg или Ti като комплексна матрица за пробите от околната среда. Границите на откриване за As, Zn, B, Hg, Cd, Tl и U задоволяват изискванията за максимално допустими концентрации за почви и питейни води. Подобряването на границите на откриване при определяне на платина в пътен прах беше постигнато чрез разработване на нов колонен метод с активен въглен, имобилизиран с *2*-меркаптобензимидазол за отделяне на матричните компоненти и концентриране на платината.

Survey of the mineral content and some physico-chemical parameters of Bulgarian bee honeys

K. Nikolova[*], G. Gentscheva[1], E. Ivanova[1]

University of Food Technologies, 4002 Plovdiv, Bulgaria
[1] Institute of General and Inorganic Chemistry, Bulgarian Academy of Sciences, 1113 Sofia, Bulgaria.

The quality control of honey requires a number of physical and chemical parameters to be determined in order to provide evidence of the origin and environmental purity of the product. 14 types of Bulgarian bee honeys were analyzed and the following parameters were determined: refraction index, thermophysical characteristics, color characteristics, lightness L^* and chroma C^*_{ab}. The contents of water, β-carotene, glucose, fructose, saccharose, oligosaccharides, essential and toxic trace elements were also found. The correlation between the refractive index and the water content of honey was determined as a criterion for the quality of honey. The fructose-glucose ratio was determined as a parameter related to the crystallization of honey. The criteria used were applied for the first time to Bulgarian honeys.

Relatively high content of potassium was found in the analyzed Bulgarian bee honeys, which makes them an important source of this essential element. No traces of the toxic elements As, Cd, Ni and Pb were found.

Key words honey, mineral content, sugar content, thermophysical and optical parameters

INTRODUCTION

Honey is a natural sweet substance that bees produce by transforming natural nectar of plants. It is well known for its valuable nutritional and medicinal qualities. Honey composition depends on its type and origin. Honey contains monosaccharides, macro- and micronutrients, antioxidants, free amino acids, organic acids, vitamins, enzymes and minerals [1].

The contents of water, glucose, fructose, saccharose, essential and toxic metal ions, as well the refractive index are major parameters in assessing the quality of honey. On the other hand, parameters with stronger impact for the consumers are the color, the crystallization state and the fermentation grade [2]. Trace element levels in honey are of particular importance as an indicator of environmental pollution [3], owing to the fact that bees are in contact with air, waters and plants. The determination of trace elements such as Ca, Mg, Zn, Mn is widely used in food authenticity studies [4].

The purpose of the present work was to determine several physical and chemical characteristics of samples of bee honey harvested from different regions in Bulgaria. Classical physico-chemical methods available in most laboratories dealing with food control were used. Parameters were looked for permitting an unequivocal differentiation between natural honeys and those adulterated by addition of sweeteners. The criteria used were applied for the first time to Bulgarian honeys.

MATERIALS AND METHODS

Samples

14 honey samples, harvested in 2008 and 2009, were purchased from supermarkets or directly from beekeepers and stored at room temperature in dark. The geographical and botanical origin of samples is indicated in Table 1.

The contents of glucose, fructose, saccharose, water, oligosaccharides, β-carotene, trace elements, the refractive index and the color parameters were determined according to methods proposed by the International Honey Commission [5].

Methods

The content of carbohydrates in honey was determined by high performance liquid chromatography (HPLC) using a Refractive Index detector, Waters. Peaks were identified on the basis of their retention times using an Aminex HPX-87H column. The temperatures of both column and detector (differential refractometer R401, Waters) were 30°C; the sample volume was 10 μl.

---

* To whom all correspondence should be sent:
E-mail: *kr.nikolova@abv.bg*

Table 1. Geographical and botanical origin of honey samples.

Sample N	Geographical origin (town in Bulgaria)	Predominant botanical origin	Year of harvesting
1	Triavna	Honeydew	2009
2	Elena	Honeydew	2009
3	Asenovgrad	Lime (*Tilia*)	2009
4	Asenovgrad	Acacia (*Robinia pseudoacacia*)	2008
5	Asenovgrad	Thistle (*Cardus nutans*)	2008
6	Karlovo	Honeydew	2009
7	Galabovo	Multifloral	2009
8	Asenovgrad	Multifloral	2009
9	Sliven	Multifloral	2008
10	Montana	Sunflower (*Helianthus annuus*)	2009
11	Montana	Sunflower (*Helianthus annuus*)	2009
12	Montana	Sunflower (*Helianthus annuus*)	2008
13	Samokov	Multifloral	2009
14	Troian	Multifloral	2009

The refractive indexes of the samples were measured at 20ºC at λ=589 nm on an Abbé refractometer, Carl Zeiss Jena, Germany, calibrated with distilled water. Constant temperature in the refractometer was maintained using a thermostat. The water content was determined from the refractive indexes using the Wedmore table [6].

The honey samples were heated at a temperature of 30÷35°C to dissolve the sugar crystals and then were poured into a 10-mm thick dish. The *β*-carotene content was determined on a Lovibond PFX 880 instrument (Tintometer Ltd., UK). A standard light source was used and wavelengths from 420 to 710 nm were selected by means of 16 narrow-band interference filters of 20 nm bandwidth. The measuring system was programmed to interpolate peak wavelengths at 5 nm intervals.

The color parameters (index of lightness L^* and color coordinates x, y, a^*, b^* corresponding to the uniform color space CIELab [7], were determined on the Lovibond PFX 880 instrument as well. The parameter chroma (C^*) was calculated according to the formula $C^* = [(a^*)^2+(b^*)^2]^{1/2}$.

The differential scanning calorimeter SETARAM 141, (France) was used for thermal scanning of the honey samples cooled to –60ºC. Nitrogen was used as a purge gas at a flow rate of 50 ml min⁻¹. Samples were accurately weighed into hermetically sealed polymer-coated aluminium pans. An empty aluminium pan was used as a reference. The test was made in the following way: (i) Cooling the sample to –60ºC with a cooling rate of 5ºC/min; (ii) Holding for 5 min at –60ºC; (iii) Heating to 150 ºC with a heating rate of 5ºC/min; (iv) Holding for 5 min at 150 ºC.

The content of Li, Na, K, Ca, Mg, Cu, Fe, and Mn in the honey samples was determined by flame atomic absorption spectrometry using the Thermo M5 instrument (UK) in an air-acetylene flame under standard conditions. 3 g of honey were dissolved in 100 ml of distilled water and the obtained solutions were subjected to analysis. For calibration, aqueous standard solutions of the analytes at the mg l⁻¹ level, prepared from titrisols (Merck, Germany), were used.

RESULTS AND DISCUSSION

The examined honey samples may be divided in three groups: multifloral honeys, blossom honeys of predominant botanical origin and honeydew honeys.

The color of bee honey is affected by the harvesting method and the storage duration. It depends on the content of pigments such as chlorophylls, carotenoids, flavonoids. The color parameters (L^*, a^*, b^*), established in CIELAB system, *x, y* parameters and chroma (C^*_{ab}) are presented in Table 2.

Table 2. Color parameters of the examined bee honey samples

	x	y	L^*	a^*	b^*	C^*_{ab}
Max value	0.61	0.5	87.29	29.67	84.26	85.54
Min value	0.35	0.38	3.47	-4.47	1.39	1.41
Average value	0.44	0.44	65.33	2.83	54.51	55.49

As can be seen, ten of the examined honey samples have negative values of the color parameter a^*. This indicates the presence of a large proportion of green color. Only four of the samples – 1, 6 (honeydew) and 7, 14 (multifloral) have positive values of the parameter a^*, indicating the presence of red color. Similar results have been obtained for orange honey from Greece [8].

Table 3. Values of fructose/glucose ratio (F/G), refractive index (n) and content of carbohydrates, water and β-carotene for the investigated honey samples

	Carbohydrates				Parameter			
	Fructose	Glucose	Saccharose	Oligo-saccharides	F/G	n	W, %	β-carotene,
	g/100 g	g/100 g	g/100 g	g/100 g				ppm
Max value	52.26	45.27	11.59	8.81	1.49	1.497	19	65.23
Min value	44.64	31.14	7.56	1.74	0.99	1.489	15.8	8.21
Average	48.68	37.88	9.56	3.54	1.29	1.4937	17.09	35.07

All honeys examined in the present work showed positive values of the parameter b^*, characteristic of the yellow colors. The value was highest for honeydew samples and lowest for sunflower and lime honey.

Linear dependences between chroma C^*_{ab} and the color parameter b^*, as well as between the content of β-carotene and the color parameter x were found as follows:

$$C^*_{ab} = 0.99b^* + 1.54 \qquad R^2 = 0.99$$
$$\beta = 351.3x - 120.7 \qquad R^2 = 0.97$$

Upon increasing the value of the color parameter x, the content of β-carotene also increases.

The results for the content of water, carbohydrates (glucose, fructose, saccharose and oligosaccharides), the refractive index (n) and the crystallization index (fructose/glucose ratio F/G) of the examined honey samples are presented in Table 3.

The content of oligosaccharides in the examined honey samples is between 2.1 and 8.81 g/100 g honey. Some authors have reported that honeydew honeys have about 35–40 g fructose per 100 g dry matter, while flower honeys show about 40–50 g fructose per 100 g dry matter [9]. In contrast, the flower honeys and honeydew honeys in our investigation have 40–53 g fructose per 100 g dry matter. All investigated samples satisfy the condition of EC Directive 110/2001 – the sum of glucose and fructose contents to be above 60 g/100 g of honey [9].

The fructose/glucose ratio (F/G) was calculated for all samples. From this parameter information about the crystallization state of honey may be derived: the crystallization ability of honey is low if the content of fructose exceeds that of glucose. Only one of the examined samples had a crystallization index equal to 1 and it was partially crystallized. The other samples had F/G>1 and they were fluid. The F/G ratio depends on the nectar source. Monofloral blossom honeys contain more glucose than honeydew honeys while multifloral and honeydew honeys have close glucose contents.

The moisture content of honey samples depends on the botanical origin of the sample, on the degree of ripeness, on the processing techniques and on the storage conditions. The water content is an important characteristic of honey quality: the high water content promotes the separation of a crystallized phase at the bottom and a liquid phase on top of the honey sample [10]. Moreover, the high water content leads to higher risk for spoilage of honey *via* fermentation [11]. According to EC Directive 110/2001, the water content of pure honey should be below 20 % [9].

All examined samples had water content between 15.8 % and 17.6 %, except for samples 2 and 6, having water contents of 18.25 and 19 %, respectively. The low water content of most of the samples points to an extremely low rate of the fermentation process. The higher water content of the latter samples may be attributed to (1) honey extraction in humid weather; (2) immaturity of the extracted honey or (3) adulteration of the honey sample with glucose. The glucose/water (G/W) ratio could be a better indicator for predicting honey crystallization. G/W values lower than 1.7 are typical for slowly crystallizing honeys. The G/W values of honeydew honeys are about 1.7 while those of multifloral and monofloral honeys are about 2.2 and 2.3, respectively.

In Table 4 the color parameters, the contents of water, glucose, fructose, saccharose and oligosaccharides of three commercial brands of bee honey containing sweeteners (isosweet or glucose-fructose syrup) are presented. By color parameters and β-carotene content these samples do not differ from the other examined honey samples.

The addition of isosweet to honey does not essentially increase the water content and consequently, does not affect the fermentation ability of the honey sample. This sweetener is enzyme-hydrolyzed saccharose – laevorotating mixture of glucose and saccharose. Its addition to honey leads to a considerable increase in the glucose content, so that the F/G index of honey

Table 4. Physico-chemical parameters of natural honey and honeys containing different sweeteners

Honey sample	n	W, %	β-carotene, ppm	x	Y	a^*	b^*	L^*	Oligo-saccharides, g/100 g	Saccha-rose, g/100 g	Fructose, g/100 g	Glucose, g/100 g	F/G
Natural honey (sample 9)	1.4970	15.8	21.44	0.41	0.43	-2.21	50.87	72.25	2.10	10.22	48.24	39.44	1.07
Commercial (Pepino) containing isosweet	1.4920	17.8	34.49	0.45	0.46	-0.17	49.51	48.18	3.75	13.77	35.23	47.26	0.75
Commercial (Orfeo) containing glucose-fructose syrup purchased	1.4907	18.2	17.47	0.40	0.42	-4.29	40.47	74.23	27.32	10.91	32.03	29.74	1.08

Table 5. Mineral composition of some Bulgarian honey samples (mean ± standard deviation, n=3)

Sample N	K, mg g^{-1}	Na, µg g^{-1}	Ca, µg g^{-1}	Mg, µg g^{-1}	Fe, µg g^{-1}	Cu, µg g^{-1}	Mn, µg g^{-1}	Li, µg g^{-1}
1	1.23±0.05	34.6±1.5	76.8±1.0	36.1±1.0	3.05±0.05	0.97±0.02	1.34±0.05	0.10±0.02
2	1.21±0.05	22.3±1.2	84.2±1.0	35.6±1.0	3.24±0.05	0.96±0.02	1.79±0.05	<0.05
3	0.29±0.02	13.6±1.2	46.4±1.0	11.5±0.5	3.47±0.05	0.42±0.02	<0.15	<0.05
4	0.25±0.02	62.1±2.0	46.9±1.0	13.1±0.5	0.31±0.05	0.34±0.02	<0.15	<0.05
5	0.36±0.02	11.8±1.2	94.6±1.0	17.4±0.5	1.89±0.05	<0.05	<0.15	<0.05
6	1.64±0.05	22.3±1.5	127.7±1.5	109.1±1.5	5.01±0.05	0.99±0.02	15.6±1.0	0.57±0.05
7	1.82±0.05	25.4±1.5	99.3±1.0	32.6±1.0	<0.15	0.19±0.01	0.36±0.05	<0.05
8	0.40±0.02	15.0±1.2	82.1±1.0	21.4±1.0	0.93±0.05	<0.05	<0.15	<0.05
9	0.38±0.02	15.8±1.2	64.7±1.0	11.9±0.5	3.28±0.05	1.29±0.02	0.27±0.05	<0.05.
10	0.21±0.02	9.8±1.0	42.2±1.0	6.9±0.2	2.22±0.05	0.90±0.02	<0.15	<0.05
11	0.28±0.02	9.5±1.0	50.9±1.0	9.6±0.3	0.31±0.05	0.76±0.02	<0.15	<0.05
12	0.26±0.02	10.2±1.0	56.8±1.0	11.0±.0.5	3.33±0.05	1.06±0.02	<0.15	<0.05
13	0.30±0.02	20.6±1.5	33.1±1.0	7.5±0.2	1.05±0.05	2.26±0.03	<0.15	<0.05
14	0.26±0.02	15.3±1.2	22.8±1.0	5.2±0.2	0.56±0.05	1.74±0.02	<0.15	<0.05

becomes less than unity (Table 4), which favors the crystallization ability of the sample.

The addition of glucose-fructose syrup does not influence the crystallization ability of honey, but elevates its water content and reduces the refraction index. Such honey samples are characterized with a higher content of oligosaccharides (up to 27.6 g per 100 g of honey).

Differential scanning colorimetry was used for the first time for the identification of the composition of Bulgarian honeys. As a criterion the glass transition temperature (T_g) was used. The thermograms of pure bee honey and honey adulterated with glucose-fructose syrup or isosweet are presented in Figures 1a, b, c. Sample 9 was chosen as a representative of pure bee honey. Fig. 1 shows that T_g of natural honeys is about –37ºC, while for those adulterated by glucose/frucrose syrup it is –48ºC. The lack of glucose adulterant in this sample was checked by comparing its parameters with those of pure lime honey obtained by private producers (own production, guaranteed free from added glucose syrup).

The addition of glucose-fructose syrup to honey results in a decrease in the glass transition temperature T_g. T_g of a sample containing glucose-fructose syrup is by about 10ºC beneath that of pure honey. T_g of the isosweet containing sample, however, is close to that of pure honey, which is in the range between –33 and – 42ºC [12]. Isosweet addition leads, however, to a considerable change in ΔC_p (ΔC_p=-43.60) while samples of pure bee honey and those containing glucose-fructose syrup have ΔC_p values of -12.83 and 12.13, respectively.

The content of Li, K, Na, Ca, Mg, Fe, Cu and Mn in the examined honey samples is presented in Table 5. As can be seen, the content of potassium is at the mg g^{-1} level in most of the analyzed samples

(a)

(b)

(c)
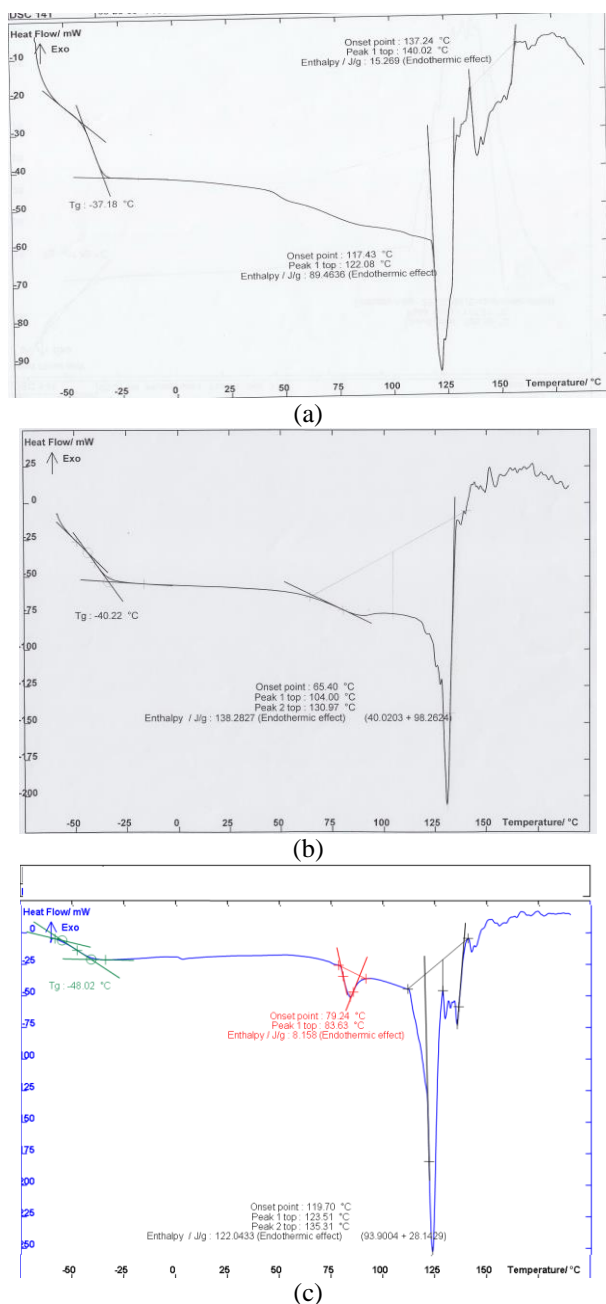
Fig. 1. Thermophysical parameters of pure and adulterated bee honey; a) pure bee honey (sample 9); b) bee honey containing isosweet; c) bee honey containing glucose-fructose syrup

and exceeds that of the other elements by approx. one order of magnitude. Its content is between 0.2 and 0.4 mg g^{-1} for the blossom honeys. Similar potassium content was registered by Madejczyk for rape honey [13]. The honeydew samples displayed a higher content of potassium – between 1.2 and 1.6 mg g^{-1}. Similar results were reported for honeydew honeys from Poland [14]. Hence, bee honey and particularly honeydew honey may be considered is an important source of the essential element K. Na, Mn, Ca, Cu and Fe are present at the μg g^{-1} level. The Mg content (between 7 and 110 μg g^{-1}) is

similar to that of Macedonian bee honeys (12–117 μg g^{-1}) [15]. The Ca content is close to that in honey from other European regions, *e.g.,* Poland and Czech Republic [16–17], while the Cu and Mn contents are similar to those of Turkish honeys [18]. Li was detected in two of the honeydew samples only (1 and 6). The concentrations of the toxic trace elements As, Cd, Ni and Pb in the honey were below the corresponding limits of detection.

CONCLUSIONS

All examined Bulgarian honey samples correspond to the EC regulations. The honey samples collected from different regions of Bulgaria display similar characteristics; moreover, there are no significant differences between commercial honeys and honeys from private producers. The examined honey samples have a low water content, hence a low tendency for fermentation. The addition of glucose-fructose syrup to honey can be established by an increase in the water content and a decrease in the refractive index. The content of oligosaccharides in these samples is about 4 times higher than that in pure bee honey. The presence of isosweet in bee honey accelerates the crystallization of the honey samples and lowers the crystallization index.

The glass transition temperature of honey containing over 25% of glucose-fructose syrup is below –40ºC, which hampers its crystallization. Bulgarian bee honeys have a relatively high content of the essential element potassium and do not practically contain toxic trace elements**.** It follows from the obtained results that Bulgarian bee honeys are a high-quality environmentally pure product with excellent characteristics.

REFERENCES

1. M.L. Conzalez-Mizet, A.Terrab, D. Hernandez, M.A. Fernandez-Recamales, F. J.Heredia *J. Agric. Food Chem.*, **53,** 2574 (2005).
2. L. Juszczak, R. Socha, J. Roznowski, T. Fortuna, K. Nalepka, *Food Chemistry*, **113**, 538 (2009).
3. P. Przybylowski, A. Wilcrynska, *Food Chemistry*, **74**, 289 (2001).
4. E. Crane: in*:* Honey: A Comprehensive Survey, Heinemann, London , 1975, p. 375-378
5. S. Bogdanov, P. Martin, C. Lullmann, *Apidologie*, **997**, 1 (1998).

6. AOAC. *(Association of Official Analytical Chemists)* Official Methods of Analysis, 15th ed. AOAC, Arlington, VA: 1170, 1990.

7. Commission Internationale de l'Elairage Recommendations on uniform color spaces, color difference equations, psychometric color terms. CIE publication no 15 (F. 1. 3. 1.) 1971, supplement 2, Bureau central de la Commission Internationale de l'Elairage, Vienna, 1978.

8. A. Lazaridou, C. Billaderis, A. G. Sabatini, *J. Food Eng.,* **64**, 9 (2004) .

9. Council Directive 2001/110 EU of 20 December 2001 relating to honey. Decree on requirements to bee honey. *Official Journal of the European Communities*, **10,** 2002.

10. K. Bauer, in: Bestimmung des Zuckerspektrums in Honigen unterschiedlicher Sorte und Herkunft mit Hilfe der HPLC, (Master Thesis), University of Hohenheim, Germany, 2001, p. 347-350.

11. H. Horn, C. Lullmann, in: *Das grosse Honigbuch: Entstehung, Gewinnung, Zusammensetzung, Qualität.* Gesundheit und Vermarktung, Ehrenwirth Verlag, München, 1992, p. 743-745.

12. J. Ahmed, S. T. Prabhu, G. S. Raghavan, V. M. Ngadi, *J. Food Eng.,*, **79**, 1207 (2007).

13. M. Madejczyk, D. Baralkiewicz, *Analytica Chimica Acta* , **617**, 11, (2008).

14. C. O. Chichester in : Advances in food research. Academic Press, New York, 1978, p. 24.

15. E. Stankovska, T. Stafilov, Šajn Robert, *Environ. Monit. Assess.*, **142**, 117 (2008).

16. M. Chudzinska, D. Baralkiewicz, *Food Chem. Toxicol.*, **48**, 284 (2010).

17. J. Lachman, D. Kolihova, D. Miholova, J. Kosata, D. Titera, K. Kult, *Food Chemistry*, 101, 973 (2007).
M. Tuzen, S. Silici, D. Mendil, M. Soylak, *Food Chemistry*, **103**, 325 (2007)

ПРЕГЛЕД НА МИНЕРАЛНОТО СЪДЪРЖАНИЕ И ФИЗИКО-ХИМИЧНИТЕ ПАРАМЕТРИ НА БЪЛГАРСКИ ПЧЕЛЕН МЕД

К. Николова, Г. Генчева[1], Е. Иванова[1]

Университет по хранителни технологии, Пловдив,
[1]Институт по обща и неорганична химия, БАН, София

(Резюме)

Качественият контрол на пчелния мед изисква определянето на редица физични и химични параметри с цел оценка на натуралността и екологичната чистота на продукта. Анализирани са 14 типа български пчелен мед от различни области на България и са определени техните параметри като показател на пречупване, цветови параметри, светлост L^*. В изследваните образци е определено също така съдържанието на β-каротен, глюкоза, фруктоза, захароза, олигозахариди, водното съдържание, както и съдържанието на основни и токсични елементи. Като критерий за качеството на пчелния мед е определена корелацията между водното съдържание и показателя на пречупване. Фруктозо-глюкозното отношение е определено като параметър, свързан с кристализацията на пробите. В изследваните български медове е установено сравнително високо съдържание на калий, което ги прави важен източник на този есенциален елемент. Медовете практически не съдържат токсични елемент.

Spectrophotometric determination of sildenafil citrate drug in tablets. Spectroscopic characterization of the solid charge transfer complexes

M.S. Refat[1,2*], G.G. Mohamed[3], A. Fathi[3]

[1]Department of Chemistry, Faculty of Science, Taif University, 888 Taif, Kingdom Saudi Arabia
[2]Department of Chemistry, Faculty of Science, Port Said 42111, Suez Canal University, Egypt
[c]Chemistry Department, Faculty of Science, Cairo University, Egypt.

The purpose of this study is to propose sensitive, accurate and reproducible methods for the determination of sildenafil citrate in pure pharmaceutical preparations. Sildenafil citrate is determined spectrophotometrically *via* charge-transfer complex formation. This includes the use of some π-acceptors as 2,3-dichloro-5,6-dicyano-p-benzoquinone (DDQ) and 3,6-dichloro-2,5-dihydroxy-p-benzoquinone (p-CLA). The proposed methods can be used for routine analysis of the suggested drugs in pharmaceutical preparations. The solid ions of the CT complexes from the reaction of DDQ and p-CLA as π-acceptors with sildenafil citrate as donor are isolated and the formed CT complexes are characterized *via* elemental analyses, IR, ^{1}H NMR and mass spectrometric studies.

Keywords: Sildenafil citrate, DDQ, p-CLA, Spectrophotometry, Charge transfer complexes.

1. INTRODUCTION

Sildenafil (S) (1-[4-ethoxy-3-(6,7-dihydro-1-methyl-7-oxo-3-propyl-1H-pyrazolo-[4,3-d] pyrimidin-5-yl) phenylsulphonyl]-4-methylpiperazine) (Formula 1) has been widely prescribed for treating erectile disfunction [1–4] and its bioavailabilty, metabolism, elimination route and pharmacokinetics have been reported in details [3,5]. The maximum sildenafil plasma concentrations measured after a single oral dose of 100 mg to healthy male volunteers is 450 ng/mL. The lower therapeutic concentrations in human plasma after a 25 mg single oral dose are approximately 7 ng/mL [5]. Many analytical methods, using high performance liquid chromatography (HPLC), have been published for quantification of the parent drug sildenafil in plasma, but not for its active metabolite, using ultraviolet visible (UV–vis) detector [6,7], or a liquid chromatography system combined with a triple quadrupole mass spectrometric detector [8], as well as in oral fluids using a liquid chromatography single mass spectrometry system [9]. Lewis and Johnson [10] reported the detection of both sildenafil and N-desmethylsildenafil in *post-mortem* fluids and tissues, while a liquid chromatography tandem mass spectrometry (LC–MS/MS) system was reported for their detection in

urine and tissue samples [11] or in *post-mortem* human blood [12]. Al-Ghazawi *et al*. [13] developed a method for the determination of both analytes in plasma using electrochemical detection; Cooper *et al*. [14] used a UV–vis detector for their determination in plasma; and Saisho *et al*. [15] determined them in human hair by GC–MS. On the other hand, the detection of these compounds without a derivatisation step leads to a higher sensitivity limit. These findings seem to be confirmed not only by the absence of GC–MS methodology for the simultaneous detection of these compounds in the literature, but also by the contradictory results on the parent drug [16, 17].
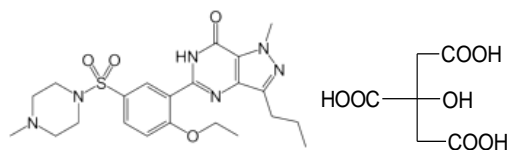
Formula 1. Structure of sildenafil citrate.

In the present study DDQ and p-CLA reagents are utilized as π-acceptors for the spectrophotometric determination of sildenafil citrate (SILC) drug in raw materials and in some commercial pharmaceutical preparations. Different experimental conditions are checked in order to select the optimum conditions suitable for CT complexes formation and hence quantitative determination of sildenafil citrate (SILC). Statistical treatment of the data obtained, like SD, RSD, Sandell sensitivity, ε, relative error, t- and F-tests are also made.

* To whom all correspondence should be sent:
E-mail: msrefat@yahoo.com

2. EXPERIMENTAL

2.1. Materials

All chemicals and reagents were of analytical reagent grade and were used without further purification. Sildenafil citrate (SILC) was provided by EVA Pharma Company for Pharmaceutical Industry. 2,3-Dichloro-5,6-dicyano-1,4-benzoquinone (DDQ) was supplied from Arcos-USA. 2,5-Dichloro-3,6-dihydroxy-1,4-benzoquinone (p–CLA) was supplied from BDH chemicals, UK. Absolute ethanol and sodium hydroxide were supplied from ADWIC. Acetonitrile (AR) was supplied from Fisher chemicals and methanol was supplied from Sigma. Chloroform, acetone, 1,4–dioxane, methylene chloride, 1,2-dichloroethane and dimethyl formamide were supplied from El-Nasr Company.

The SILC pharmaceutical preparations were purchased from Silden capsules, 25 mg/cap. (EIPICO) and Virecta, 100 mg/cap. (EVA pharma).

2.2. Solutions

2.1×10^{-3} M SILC solutions were prepared by dissolving accurately weighed amounts of the drugs in warm methanol. 0.1 % (w/v) of 2,3-dichloro-5,6-dicyano-1,4-benzoquinone (DDQ) and 0.1 % (w/v) of 2,3-dichloro-5,6-dihydroxy-1,4-benzoquinone (p-CLA) reagents were prepared by dissolving 100 mg of each reagent in 100 ml acetonitrile. All solutions had to be protected from light by keeping them in dark colored quickfit bottles during the whole work. 0.1 M NaOH solution was prepared by dissolving 400 mg of NaOH in 100 ml methanol. Redistilled water from an all-glass equipment was used. Redistillation was carried out from alkaline permanganate solution.

Ten tablets of SILC were accurately weighed and the average weight of one tablet was calculated. The tablets were crushed to a fine powder. A portion of the powder equivalent to 100 mg SILC was dissolved in 75 ml methanol, and then filtered on a dry filter paper in a 100 ml volumetric flask. The volume was brought up to the mark with methanol.

2.3. EQUIPMENTS

All absorption spectral measurements were made using the Perkin Elmer automated spectrophotometer ranged from 200-900 nm with scanning speed 400 nm/min and band width 2.0 nm, equipped with 1 cm matched quartz cells.

Elemental analyses (C, H, N) were made at the Microanalytical center of Cairo University using CHNS-932 (LECO) Vario Elemental analyzers. Infra Red measurements (KBr discs) of the isolated CT complexes were carried out on a Perkin Elmer 1430 ratio recording infrared spectrometer (400–4000 cm^{-1}). ^1H NMR spectra in d_6-DMSO (200 MHz) were recorded on a Varian spectrophotometer Gemini 200 using solvent signals as a reference. ^1H NMR data are expressed in parts per million (ppm). The mass spectra of the CT complexes were recorded at 70 eV by using EI-MS 30 mass spectrometer.

2.4. General procedure for spectrophotometric determination of SOLC

1 ml of 0.1% (w/v) DDQ or p-CLA was added to solutions containing different amounts of 2.1×10^{-3} M SILC. The mixtures were brought up to 10 ml with acetonitrile. The absorbance of the colored CT complexes was measured at the specific wavelengths against reagents blank prepared similarly without drugs.

2.5. Day – by – day measurements:

In order to prove the validity and the applicability of the proposed method and the reproducibility of the results obtained, four replicate experiments at different concentrations of SILC were carried out. Using the above mentioned procedures, the absorbance of the four samples was measured daily for four days and the results were recorded to make statistical calculations.

2.6. General procedure for spectrophotometric determination of SILC in some pharmaceutical preparations:

Different concentrations of SILC drug (10–70 µg ml^{-1}) were added to 1 ml of 0.1 % (w/v) DDQ or p-CLA. The volumes were made up to the mark with acetonitrile in 10 ml calibrated measuring flasks. The absorbance was measured at $\lambda_{max} = 460$ and 510 nm for SILC using DDQ and p-CLA reagents, respectively, against reagents blank.

2.7. Synthesis of the charge transfer complexes

The solid CT complexes of SILC with DDQ and p-CLA were prepared by mixing a saturated solution of the drug in chloroform (10 ml) and a saturated solution of DDQ or p-CLA in methanol (10 ml) with continuous stirring for about 1 h at room temperature. The colored complexes were developed and the solution was allowed to evaporate slowly at room temperature. The colored

solid complexes formed were filtered, washed several times with little amounts of methanol, and dried under vacuum over anhydrous calcium chloride.

3. RESULTS AND DISCUSSION

Charge transfer complex is the name that is given to a stable molecular system formed in solution between an electron donating molecule, having sufficiently low ionization potential, and an electron accepting molecule having high electron affinity. The main feature of this type of complex formation is the appearance of new intense absorption bands in the ultra-violet or visible region of the spectrum. Absorption bands of this type are known as charge transfer bands, since they involve electronic transitions from an orbital on the donor to a vacant orbital on the acceptor. Many explanations were given to the phenomenon based on the quantum mechanical theory of Mülliken. The formation of molecular complexes from two aromatic molecules could arise from the transfer of an electron from a π–molecular orbital of the donor (Lewis base) to a vacant π–molecular orbital of the acceptor (Lewis acid), i.e. π-π* electronic interaction [18,19].

3.1. Absorption spectra

The absorption spectra of the SILC-DDQ CT complex in acetonitrile solvent (Figure 1) show three maxima at $\lambda = 460$ nm ($\varepsilon^1 = 2.50 \times 10^3$ L.mol^{-1} cm^{-1}), 510 nm ($\varepsilon^2 = 1.86 \times 10^3$ L.mol^{-1} cm^{-1}) and 550 nm ($\varepsilon^3 = 2.13 \times 10^3$ L.mol^{-1} cm^{-1}) while the absorption spectrum of DDQ shows no absorption peaks in the scanned spectral region. The peak at $\lambda = 460$ nm was selected because it gives the highest absorption intensity, as indicated by the ε values. Polar solvents such as acetonitrile and methanol were reported to promote the complete transfer of electron from a donor (D) to the π-acceptor (A), DDQ resulting in complete formation of DDQ radical anion (A$^-$) as a predominant chromogen.

Figure 1 shows the absorption spectra of the SILC-p-CA CT complex in methanol. A solution of drug and p-CLA in acetonitrile and methanol solvents has an intense pink color with characteristic wavelength absorption bands, frequently with one maximum at $\lambda = 510$ nm ($\varepsilon = 0.83 \times 10^3$ L.mol^{-1} cm^{-1}), while the p-CLA solution showed a peak at $\lambda = 440$ nm ($\varepsilon = 0.23 \times 10^3$ L.mol^{-1} cm^{-1}).
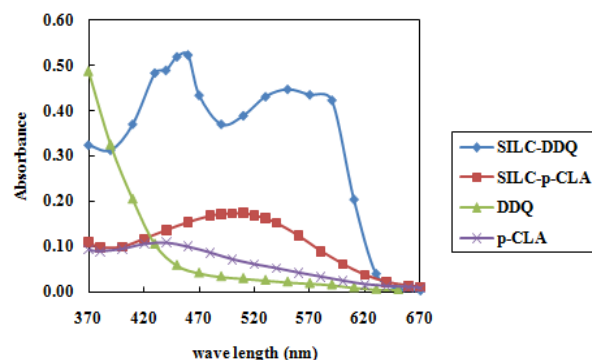
Fig. 1. Absorption spectra of DDQ and p-CLA in acetonitrile and their charge transfer complexes with SILC drug.

3.2. Effect of solvents

In order to select the suitable solvent for CT complex formation, the reaction of DDQ and p-CLA with SILC drug was performed in different solvents. These solvents include acetonitrile, chloroform, ethanol, methanol, acetone, 1,4–dioxane, dichloromethane, 1,2-dichloroethane and dimethyl formamide. The results obtained are shown in Figures (2,3) and Table (1). The DDQ
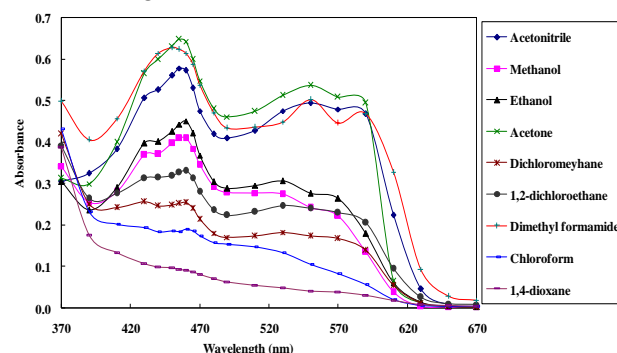
Fig. 2. Effect of organic solvents on the absorption spectra of SILC-DDQ CT complex.
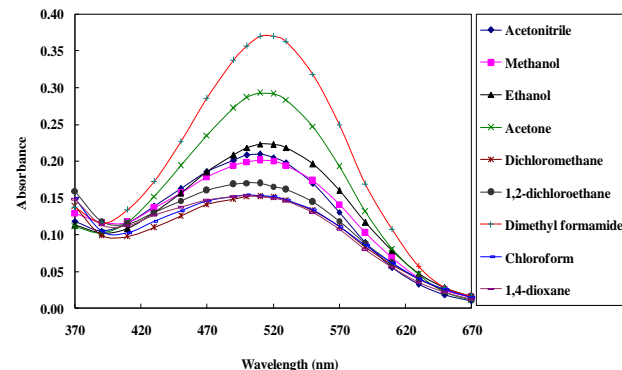
Fig. 3. Effect of organic solvents on the absorption spectra of SILC–p-CLA CT complex.

reagent, acetone and dichloromethane display higher molar absorptivity than acetonitrile. The p-CLA reagent, dimethyl formamide, acetone and ethanol display higher molar absorptivity than

Table 1. The molar absorptivity values of SILC-DDQ and SILC-p-CLA CT complexes in different solvents.

Solvent	Absorbance		ε (L.mol^{-1}. cm^{-1}) * 10^3	
	λ= 460nm	λ= 510nm		
	DDQ	p-CLA	DDQ	p-CLA
Acetonitrile	0.573	0.209	2.73	1.00
Methanol	0.410	0.201	1.95	0.96
Ethanol	0.451	0.223	2.15	1.06
Acetone	0.643	0.292	3.06	1.39
Dichloromethane	0.254	0.151	1.21	0.72
1,2-dichloroethane	0.330	0.269	1.57	1.28
DMF	0.615	0.369	2.93	1.76
Chloroform	0.190	0.153	0.91	0.73
1,4-dioxane	0.090	0.152	0.43	0.72

Table 2. Spectral characteristics of sildenafil citrate CT coloured reaction products and the analytical characteristics (accuracy and precision) of these reactions.

Parameters	Results	
	DDQ method	p-CLA method
λ_{max}, nm	460	510
Molar absorptivity, L. mol^{-1}. cm^{-1}	2.50×10^3	0.83×10^3
Sandell Sensitivity, μg cm^{-2}	0.035	0.043
Beer's law limit, , μg mL^{-1}	10.00 – 100.0	5.00 – 250.0
Percentage recovery, %	98.90 – 100.7	97.80 – 100.1
Range of error, %	0.09 – 1.10	0.01 – 2.20
Standard Deviation (SD)	0.14 – 0.42	0.13 – 0.68
Relative Standard Deviation, (RSD) %	0.20 – 0.84	0.12 – 0.78
Regression equation *, slope (b)	0.0063	0.0016
Intercept (a)	-0.0115	0.0050
Correlation coefficient (r^2)	0.9882	0.9974
LOD, μg mL^{-1}	11.74	12.19
LOD, μg mL^{-1}	9.13	10.63

*A = a + bC; where C is the concentration in μg mL^{-1}.

acetonitrile. But in all cases the best stability and reproducibility of the CT reaction is registered in acetonitrile as a solvent. From these results it follows that acetonitrile can be considered as the ideal solvent for the color reaction, as it offers solvent capacity for DDQ and gives the highest yield of radical anions, as indicated by the high ε values. This is because it possesses the highest dielectric constant among all solvents examined; a property which is known to promote the dissociation of the original CT complex to radical ions, i.e., the dissociation of the donor–acceptor complex is promoted by the high ionizing power of the solvent.

3.3. Effect of reagents concentration

It is found that upon adding various concentrations of DDQ or p-CLA solutions to a constant concentration of ALB, APN and SILC drugs, 1000 μg mL^{-1} of a DDQ or p-CLA solution are sufficient for the quantitative determination of the drug under study, as mentioned above. Maximum and reproducible color intensities are obtained and higher concentration of reagents does not affect the color intensity.

3.4. Effect of time and temperature

The optimum reaction time is determined spectrophotometrically at different time intervals at λ_{max} = 460 and 515 nm for SILC-DDQ and SILC–P-

Table 3. Between – day precision of the determination of SILC drug using DDQ and p-CLA reagents under optimum conditions

Drug	[Drug] Taken, $\mu g\ mL^{-1}$	[Drug]* Found, $\mu g\ mL^{-1}$	Percentage Recovery (%)	SD	RSD (%)
DDQ	20.00	19.59	98.00	0.42	2.16
	30.00	30.58	102.0	0.22	0.72
	50.00	50.54	101.1	0.31	0.61
	90.00	89.86	99.80	0.39	0.44
p-CLA	20.00	19.66	98.31	0.60	2.06
	50.00	50.20	100.4	0.60	1.21
	90.00	90.00	100.0	0.67	0.74
	150.0	149.8	99.87	0.47	0.32
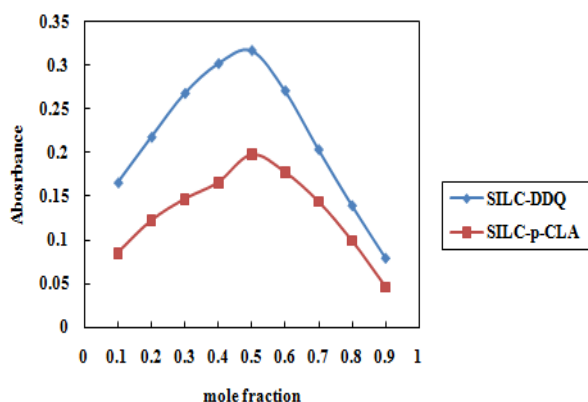
Fig. 4. Job's method for sildenafil citrate CT complexes with DDQ and p-CLA in acetonitrile.

Fig. 5. Molar ratio of sildenafil citrate CT complexes with DDQ and p-CLA in acetonitrile.

CLA CT complexes, respectively. It is found that complete color development is attained after 30 minutes and the color remains stable for one day at least using these reagents.

The effect of temperature in the range from 5 to 60 °C on DDQ or p-CLA reactions with SILC drug is studied using 100 $\mu g\ mL^{-1}$ SILC. It is shown that the maximum color is attained at a temperature of 10±1 or 30±2 °C for SILC-DDQ and SILC-p-CLA CT complexes, respectively. The color of the CT complexes remained constant for at least 24 h.

3.6. Stoichiometry of the CT complexes

Molar ratio and Job's continuous variation methods [20,21] are applied in order to determine the suitable ratio between SILC drug and DDQ or p-CLA reagents. Figures 4, 5 show that the interaction between these drugs and the reagents occurs on equimolar basis, i.e. the two straight lines are intersected at an 1:1 [Drug]:[Reagent] ratio. This means that 1:1 complexes were formed between the drug and the DDQ or p-CLA reagent. CT complex formation between DDQ or p-CLA and SILC drug takes place through the transfer of electron from a donor (drug) to the π-acceptor reagent (DDQ or p-CLA) [20].

3.7. Validity of Beer's law

Table 2 shows the results of studying the quantitativeness of the reaction between SILC drug and DDQ and p-CLA reagents under the selected optimum conditions. It is found that Beer's law is valid over the concentration ranges from 10 – 100 and 5 - 250 $\mu g\ mL^{-1}$ of SILC using DDQ and p-CLA reagents, respectively.

Table 2 shows the slope, intercept, correlation coefficient, Sandell sensitivities, molar absorptivity (ε), range of error, standard deviation, relative standard deviation, limits of detection (LOD) and quantification (LOQ). The low values of Sandell sensitivity indicate the high sensitivity of the proposed method in the determination of the drugs under investigation.

Four to six replicate measurements are performed at different concentrations of ALB, APN and SILC drugs using DDQ and p-CLA reagents. The relative standard deviation and the range of error are calculated. The low values obtained indicate the high accuracy and high precision of the proposed spectrophotometric method. The low values of the limits of detection (LOD) and quantification (LOQ) indicate the possibility of

254

applying DDQ and p-CLA reagents in routine analysis of the drugs under investigation.

3.8. Between-day precision

In order to prove the validity and applicability of the proposed method and the reproducibility of the results obtained, four replicate experiments at four concentrations of SILC are carried out. Table 3 shows the values of the between-day relative standard deviations for different concentrations of the drugs, obtained from experiments carried out over a period of four days. It is found that within-day relative standard deviations are less than 1%, which indicates that the proposed method is highly reproducible and DDQ and p-CLA reagents are successfully applied to determine SILC *via* the charge transfer reaction.

3.9. Spectrophotometric microdetermination of SILC drug in different pharmaceutical preparations

The spectrophotometric microdetermination of SILC drug in preparations from EPICO and EVA Pharma Companies are carried out. The results obtained are given in Table 4. These data show that the determined concentration of SILC drug by the proposed methods is close to that obtained by the applied standard method [22, 23]. On screening pharmacopoeia (e.g. USP, BP or EP) it is found that there is no official method related to the determination of SILC in tablet dosage forms or bulk drugs, so we used the standard addition method for testing the proposed method.

Table 4. Spectrophotometric determination of SILC drug in different pharmaceutical preparations with DDQ and p-CLA using the standard addition method.

Sample	[Drug] taken, $\mu g\ mL^{-1}$	Amount of standard added, $\mu g\ mL^{-1}$	[Drug] found, $\mu g\ mL^{-1}$	SD	RSD
Using DDQ: SILC	25.00	--	25.42	0.42	0.89
	50.00	--	49.43	0.31	0.62
	75.00	--	76.43	0.39	0.44
D1	25.00	25.00	50.50	0.71	1.40
	50.00	25.00	75.17	0.43	0.57
	75.00	25.00	100.29	0.50	0.50
D2	25.00	25.00	50.57	0.46	0.91
	50.00	25.00	75.44	0.67	0.89
	75.00	25.00	100.3	0.96	0.95
Using p-CLA: SILC	25.00	--	25.00	0.51	0.31
	50.00	--	50.33	0.60	0.12
	75.00	--	74.67	0.48	0.32
D1	25.00	25.00	50.42	0.88	1.47
	50.00	25.00	75.17	0.51	0.57
	75.00	25.00	99.58	1.00	0.99
D2	25.00	25.00	50.50	1.00	1.75
	50.00	25.00	74.83	0.33	0.89
	75.00	25.00	100.1	0.67	1.00

No. of replicates (n) = 4.
D1 Silden tablets (25 mg/ cap.), EPICO, Cairo, Egypt.
D2 Virecta tablets (100 mg/cap.), EVA Pharma Co., Cairo, Egypt.

Table 4 shows the results obtained by determining the different concentrations of SILC drug using DDQ and p-CLA reagents. It is obvious from these results that the percent recoveries are 98.86 – 101.9 and 99.56 – 100.7 % with DDQ and p-CLA, respectively. These values indicate the accuracy and precision using DDQ and p-CLA reagents.

3.10. Characterization of charge-transfer (CT) complexes

CT complexes formed between SILC drug as donor and DDQ or p-CLA as acceptor were isolated in solid form. The synthesis and characterization of SILC CT-complexes of DDQ and p-CLA were described. These complexes are readily prepared from the reaction of SILC with

DDQ and p-CLA with chloroform and/or methanol solvents. IR, ^{1}H NMR, mass spectra and elemental analyses (C, H, N) were performed to characterize the charge-transfer complexes.

3.10.1. Composition and solubility of the CT-complexes

Results of elemental analysis for the SILC CT complexes are listed in Table (5). From the table it can be seen that the values found are in a good agreement with the calculated ones, and the composition of the CT-complexes matches the stoichiometry (1:1; drug: reagent) of the charge transfer complexes, which is determined by applying continuous variation and molar ratio obtained from a series of solutions of DDQ or p-CLA to SILC. All CT-complexes are insoluble in cold and hot water, but easily soluble in dimethyl formamide and dimethyl sulfoxide.

3.10.2. IR spectral studies

The IR spectra of 1:1 CT-complexes formed from the interaction of the donor and the corresponding acceptor with the general formula SILC-acceptor, together with the corresponding free acceptor (DDQ and p-CLA) and SILC donor, are shown in Figure (6 a-e). Full assignments concerning all infrared bands located in the spectra are listed in Table 6.

A comparison of the relevant IR spectral bands of the free donor; SILC, and acceptors; DDQ and p-CLA, with those of their corresponding isolated solid CT-complexes clearly indicates that the characteristic bands of SILC show some shift in the frequencies (Table 6), as well as some change in bands intensities. This could be attributed to the expected symmetry and electronic configuration changes upon the formation of the CT-complex. The explanation will follow separately for each CT-complex to give an idea about the position of complexation.

SILC-DDQ CT-complex

The bands distinguished for the SILC donor in SILC-DDQ CT-complex display small changes in band intensities and frequency values (Figure (6) and Table (6)). For example, the ν(O-H) vibration occurring at 3473 cm^{-1} for the free donor is shifted to 3439 cm^{-1} with broadening in the IR spectrum of the CT complex. The vibration frequency of the C≡N group for DDQ observed at 2250 cm^{-1} is shifted to 2210 cm^{-1} in the charge transfer complex. The other observation is the blue shift in the δ(NH) deformation from 1581 cm^{-1} in the free donor to 1563 cm^{-1}. From the three mentioned items we can

conclude that the charge transfer complexation occurs through interaction between the –NH group of the donor and one of the cyano groups of the DDQ acceptor (Scheme 1).
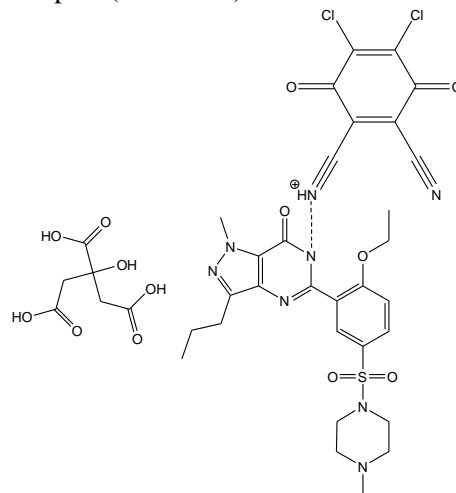
Scheme 1. Structure of the SILC-DDQ CT-complex.

SILC-p-CLA CT-complex

The infrared spectra of SILC along with its charge-transfer complex SILC-p-CLA are presented in Figure (6), and their band assignments are given in Table (6). The presence of the essential infrared bands of the donor and acceptor in the spectra of the resulting CT-complex, strongly support the formation of a CT complex. Small shifts in both wavenumber values and band intensities between free donor and the CT-complex are registered. This fact is due to the structure configurations upon complexation. For example:

(i) The ν(N-H) vibration of the donor is observed as a medium strong band at 3473 cm^{-1} in the spectrum of the free donor. This band disappears in the spectrum of the complex and so the band due to δ_{def}(N-H) at 1581 cm^{-1} in case of free donor is shifted to 1549 cm^{-1}. This assumption gives an image about the speculative CT complex structure and implies that an –NH group from the donor participated in the complexation.

(ii) The IR spectrum of the SILC-p-CLA CT complex is characterized by two bands (2702 and 2635 cm^{-1}) which are not present in the spectra of the free donor. These bands are assigned to the intermolecular hydrogen bonding [22] between the -NH group (lone pair of electron on nitrogen atom) of the donor SILC with a phenolic OH group in case of p-CLA. Electron-withdrawing groups (chloro groups) attached to the benzene ring increase the acidic property of the phenolic groups present in the p-CLA reagent, accordingly, the phenolic group plays an effective role in the

Table 5. Elemental analysis (C, H, N) and physical parameters of the CT-complexes formed from the reaction of the SILC drug with DDQ and p-CLA reagents.

Complexes(FW)	M wt g/mol		C%		H%		N%		Physical data	
	Found	Calculated	Found	Calculated	Found	Calculated	Found	Calculated	Color	Mp (°C)
SILC-DDQ $(C_{36}H_{38}N_8O_{13}SCl_2)$	929.0	893.7	48.27	48.34	4.23	4.25	12.44	12.53	Yellow	235
SILC-p-CLA $(C_{34}H_{43}N_6O_{15}SCl_2)$	865.0	874.7	46.52	46.65	4.90	4.92	9.44	9.60	Red	225

Table 6. Infrared frequencies[a] (cm^{-1}) and tentative assignments for DDQ, p-CLA, SILC-DDQ and SILC-p-CLA CT-complexes.

DDQ	p-CLA	SILC	Assignments[b]		
			SILC-DDQ	SILC-p-CLA	
3325 w 3218 br	3237 s, br	3615 s 3473 ms 3298 vs 3028 vw	3439 m, br 3305 s 3075 vw 3019 vw	3497 vw 3312 w 3235 ms	$\nu_{(O-H)}$ $\nu_{(N-H)}$ NH_2^+
--	--	2962 w 2869 w 2732 w 2562 w	2970 w	2971 ms	$\nu_{s(C-H)} + \nu_{as(C-H)}$; $-CH_3 + CH_2$
--	--	--	2825 sh 2731 m, br	2702 w 2635 w, br	Hydrogen bonding
2250 vw 2231 ms	--	--	2210 s	--	$\nu_{(C\equiv N)}$
1673 vs	1664 vs	1702 vs	1696 vs 1637 mw	1700 ms	$\nu_{(C=O)}$
--	--	1581 s	1563 vs	1659 w 1631 ms	$\delta_{def}(N-H)$ Ring breathing bands
1552 vs 1451 s	1630 vs	1489 w 1461 ms	1460 ms	1549 ms 1458 ms	$\nu_{(C=C)} + \nu_{(C=N)}+$ -COO- C-H deformation+NH_2^+ Ring breathing bands
1358 w 1267 s 1172 vs 1072 w	1366 s 1267 s,br	1361 ms 1278 vw 1245 mw 1172 ms 1100 w 1086 w	1394 m 1345 m 1273 mw 1243 w 1193 w 1160 ms 1102 w 1072 vw	1370 ms 1268 s, br 1188 s, br 1162 s, br 1077 sh	$\nu_{(C-C)} + \nu_{(C-N)} +\nu_{(C-O)} +\nu_{(C-S)}$
1010 vw 893 s	980 vs 847 vs	1026 s 937 vs 810 vs	1024 w 938 s 884 m 816 s	1025 sh 979 vs 941 ms 879 vw 837 s	δ_{rock}; NH CH, in-plane bend CH-deformation $\nu_{(C-Cl)}$
800 vs 720 s 615 ms 527 vw 457 ms 432 mw	753 s 688 s 566 s	735 vs 689 ms 658 s 615 s 587 s 560 s 485 s 436 ms	730 ms 688 w 647 w 611 w 580 ms 498 vw 449 vw	750 s 690 s 646 m 615 m 566 vs 494 mw 408 vw	skeletal vibration CH bend CH out-of- plane bend Skeletal vibration $\nu_{(C-S)}$ CNC def. NH_2 rock

(a): s = strong, w = weak, m = medium, sh = shoulder, v = very, br = broad.

(b): ν, stretching; δ, bending

behavior of the acceptors. The proposed mechanism of the interaction between acid and base means that the acidic proton of the acceptor has a tendency to be transferred to the donor (base). This fact can be applied herein in our study of the reaction of p-CLA with SILC as a donor. Such assumption is strongly supported by the existence of new bands of weak intensity (hydrogen bonding) in the spectra of each complex prepared.

(iii) The main stretching vibrations of ν(C=O) and ν(C=C) of the donor are not affected upon complexation, this clearly demonstrating that the lone pair on the nitrogen atom of the –NH group in the pyrimidine ring participates in the complexation process between donor and acceptor. Based on the molar ratio between donor and acceptor which yields 1:1, only one –OH group from the acceptor (p-CLA) is involved in the complexation, as given in Scheme 2.
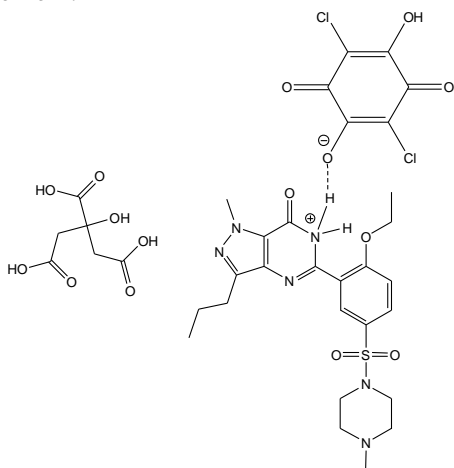
Scheme 2. Structure of the SILC-p-CLA CT-complex.

3.10.3. ¹H NMR spectral studies

¹H NMR spectra of ALB, APN, SILC drugs and their six CT- complexes in DMSO are measured and given in Figure (7). The assignments of the spectral data are listed in Table (7). The chemical shifts (ppm) of proton NMR for the defined peaks are determined and listed in Table (7). Evidently, the results obtained from elemental analysis, infrared spectra, and molar ratio titrations met in the same point with ¹H NMR spectra to interpret the mode of interaction between donor and acceptor. It is found that the 1H; NH of pyrimidine ring, was up field shifted from 4.11 ppm incase of free donor to 3.83 ppm for SILC-DDQ and 3.99 ppm for SILC-p-CLA, respectively. These suggestions prove the participation of the –NH group of the pyrimidine ring in the CT interaction with one CN group for DDQ and one OH group for

p-CLA acceptors *via* intermolecular hydrogen bond.
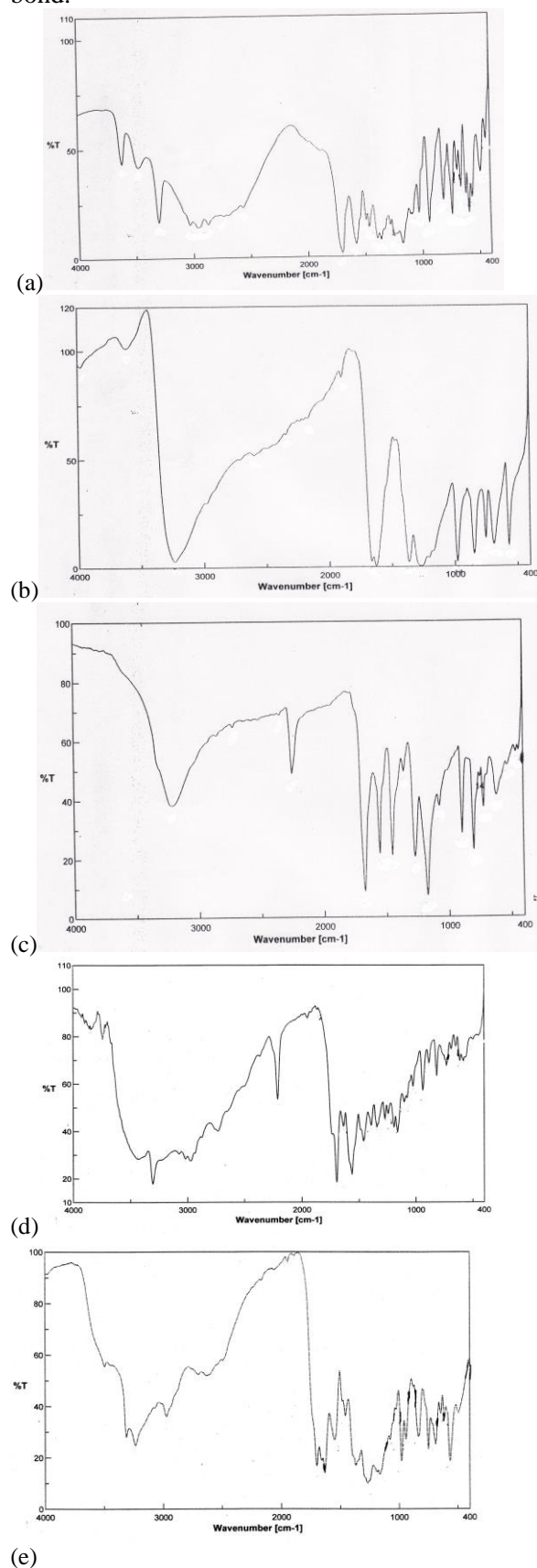
Fig. 6. Infrared spectra of (a) SILC, (b) DDQ, (c) p-CLA,(d) SILC-DDQ, and (e) SILC-p-CLA complexes.

258

Table 7. ^{1}H NMR spectral data of SILC, DDQ, p-CLA, SILC-DDQ and SILC-p-CLA complexes.

Compound	Chemical shift δ (ppm)	Assignments
SILC	0.873 (m)	3H; CH_3 (Pyrazole-(CH_2)-**CH**$_3$)
	1.305 (m)	3H; CH_3 (O-CH_2-**CH**$_3$)
	1.664 (m)	2H; Pyrazole-CH_2-**CH**$_2$
	2.441-2.616 (m)	2H; Pyrazole-**CH**$_2$-CH_2 + CH_2 of Piprazine ring
	2.668 (m)	CH_2 and CH_3 of Piprazine ring + CH_2 of citric acid
	2.832 (s)	CH_2 of Piprazine ring + CH_2 of citric acid
	3.065 (s)	CH_2 of Piprazine ring + CH_2 of citric acid
	3.978 (s)	3H; N-**CH**$_3$ (pyrazole ring) + 2H; CH_3 (O-**CH**$_2$-CH_3)
	4.105 (s)	1H; NH of pyrimidine ring
	7.337 –7.899 (m)	3H; aromatic ring
DDQ	--	--
p-CLA	8.90 (br)	2H; 2(OH)
SILC-DDQ	0.870 (m)	3H; CH_3 (Pyrazole-(CH_2)-**CH**$_3$)
	1.341 (m)	3H; CH_3 (O-CH_2-**CH**$_3$)
	1.734 (m)	2H; Pyrazole-CH_2-**CH**$_2$
	2.495-2.664 (m)	2H; Pyrazole-**CH**$_2$-CH_2 + CH_2 of Piprazine ring
	2.678 (m)	CH_2 and CH_3 of Piprazine ring + CH_2 of citric acid
	2.869 (s)	CH_2 of Piprazine ring + CH_2 of citric acid
	3.145 (s)	CH_2 of Piprazine ring + CH_2 of citric acid
	4.123 (s)	3H; N-**CH**$_3$ (pyrazole ring) + 2H; CH_3 (O-**CH**$_2$-CH_3)
	3.833 (s)	1H; NH of pyrimidine ring
	7.375 –7.927 (m)	3H; aromatic ring
SILC-p-CLA	0.924 (m)	3H; CH_3 (Pyrazole-(CH_2)-**CH**$_3$)
	1.341 (m)	3H; CH_3 (O-CH_2-**CH**$_3$)
	1.690 (m)	2H; Pyrazole-CH_2-**CH**$_2$
	2.493-2.614 (m)	2H; Pyrazole-**CH**$_2$-CH_2 + CH_2 of Piprazine ring
	2.666 (m)	CH_2 and CH_3 of Piprazine ring + CH_2 of citric acid
	2.782 (s)	CH_2 of Piprazine ring + CH_2 of citric acid
	3.065 (s)	CH_2 of Piprazine ring + CH_2 of citric acid
	4.126 (s)	3H; N-**CH**$_3$ (pyrazole ring) + 2H; CH_3 (O-**CH**$_2$-CH_3)
	3.987 (s)	1H; NH of pyrimidine ring
	7.339 –7.924 (m)	3H; aromatic ring

Table 8. Mass fragmentation of SILC, SILC-DDQ and SILC-p-CLA complexes.

Compound	M/z (%)[a]
SILC	691(12%), 404(30%), 291(14%), 218(14%), 99(100%), 56(79)
DDQ	227(53%), 200(64%), 165(15%), 137(37%), 110(45%), 87(100%), 52(55%)
p-CLA	209(49%), 188(49%), 145(23%), 123(12%), 105(43%), 87(56%), 69(100%), 52(43%)
SILC-DDQ	865(5%), 827(7%), 765(3%), 730(7%), 663(6%), 625(7%), 506(7%), 409(7%), 376(7%), 341(6%), 304(7%), 271(7%), 227(7%), 193(9%), 157(9%), 120(10%), 58(100%)
SILC-p-CLA	929(12%), 569(15%), 185(20%), 129(12%), 87(100%)

[a] Intensities expressed as % of base peak.

3.10.4. Mass spectral studies

Mass spectrometry was applied to study the purity and the main fragmentation routes of SILC charge-transfer complexes. The differentiation in fragmentation was caused by the nature of the attached acceptors through the intermolecular hydrogen bond between donor/acceptor, while the molecular ion peaks assigned to DDQ m/z = (M+1) 228 (53%), p-CLA m/z = 208(49%), and SILC m/z = 666(12%) are detected in the fragmentation of their CT-complexes. The corresponding mass spectra are given in Table (8). The different competitive fragmentation pathways of the donors give the peaks at different mass numbers listed in Table 8. The intensities of these peaks reflect the stability and abundance of the ions [23].
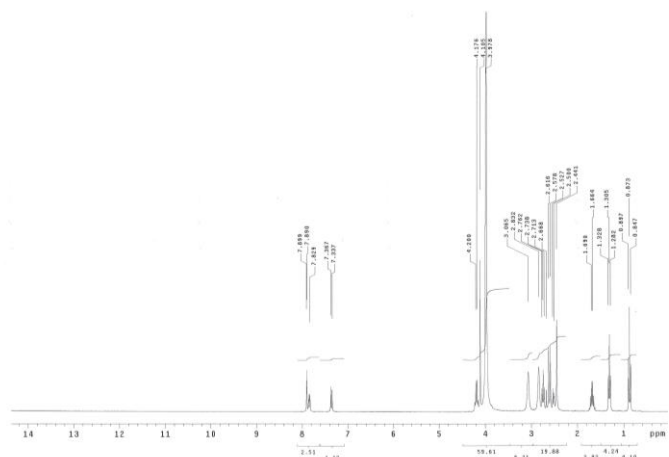
(a)
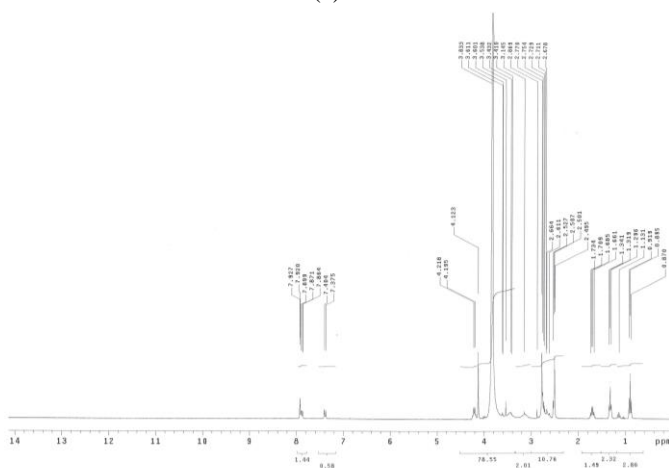
(b)
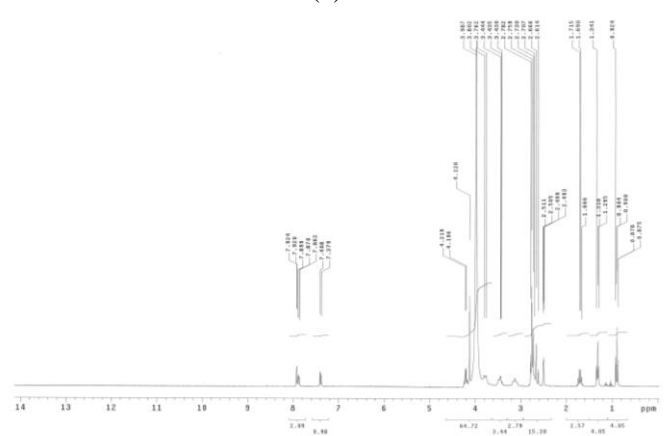
(c)

Fig. 7. ^{1}H NMR spectra of (a) SILC, (b) SILC-DDQ and (c) SILC-p-CLA CT complexes.

4. CONCLUSION

A simple, rapid and reliable spectrophotometric method was adopted for the microdetermination of ABZ drug *via* CT complex formation with DDQ or p-CLA reagents. The effect of different parameters was studied. The results obtained by the suggested procedure were compared with those obtained by the standard method. The data obtained by both procedures were found to be very close to each other and very close to those given by the pharmaceutical companies. The calculated F- and t-tests at the 95% confidence level do not exceed the theoretical values. Also, the formed CT complexes were studied using elemental analyses, IR, ^{1}H NMR and mass spectrometry in order to elucidate the structure of these CT complexes. The results obtained confirmed the results of previous stoichiometric studies and suggested that 1:1 reaction between donors and acceptors takes place; in addition it helped in elucidating the site of interaction between donors and acceptor.

REFERENCES

1   I. Goldstein, T.F. Lue, H. Padma-Nathan, R.C. Rosen, W.D. Steers, P.A. Wicker, *N. Engl. J. Med.* **338** (1998) 1397–1404.

2   R.B. Moreland, I. Goldstein, A. Traish, *Life Sci.* **62** (1998) PL309–PL318.

3   M. Boolell, M.J. Allen, S.A. Ballard, S. Gepi-Attee, G.J. Muirhead, A.M. Naylor, I.H. Osterloh, C. Gingell, *Int. J. Impot. Res.* **8** (1996) 47–52.

4   C.G. Stief, S. Uckert, A.J. Becker, M.C. Truss, U. Jonas, *J. Urol.* **159** (1998) 1390–1393.

5   Viagra/Clinical Pharmacology/Pharmacokinetics and Metabolism, May 2007. http://www.rxlist.com/cgi/generic/viagra.htm,

6   M. Lee, D. Min, *Ther. Drug Monit.* **23** (1) (2001) 21–26.

7   M. Thau Sheu, A.B. Wu, Y.G. Cheng, A. Hsia, H. Ho, *J. Chromatogr. B* **791** (2003) 255–262.

8   Y. Wang, J. Wang, Y. Cui, J.P. Fawcett, J. Gu, *J. Chromatogr. B* **828** (2005) 118–121.

9   A. Tracqui, B. Ludes, *J. Anal. Toxicol.* **27** (2003) 88–94.

10 J.R. Lewis, R.D. Johnson, L.C. Blank, *J. Anal. Tox.* **30** (2006) 14–20.

11 W. Weinmann, M. Bohnert, A. Wiedemann, M. Renz, N. Lehmann, S. Pollak, Int. J. Legal Med. **114** (2001) 252–258.

12 C. Pistos, I. Papoutsis, A. Dona, M. Stefanidou, S. Athanaselis, C. Maravelias, C. Spiliopoulou, *Forensic Science International* **178** (2008) 192–198.

13 M. Al-Ghazawi, M. Tutunji, S. Aburuz, *J. Pharm. Biomed. Anal.* **43** (2007) 613–618.

14 J.D. Cooper, D.C. Muirhead, J.E. Taylor, P.R. Baker, J. *Chromatogr. B* **701** (1997) 87–95.

15 K. Saisho, K.S. Scott, S. Morimoto, Y. Nakahara, *Biol. Pharm. Bull.* **24** (12) (2001) 1384–1388.

16 S. Pagani, D. Mirtella, R. Mencarelli, D. Rodriquez, M. Cingolani, *J. Anal. Toxicol.* **29** (2005) 254–257.

17 P. Van Hee, H. Neels, W. Lambert, V. Coucke, M. Dedoncker, Comment on: J. Anal. Toxicol. **29** (2005) 254–257: Postmortem distribution of sildenafil in histological material, *J. Anal. Toxicol.* **30** (2006) 403–404;

18 K. A. Kover, W. Mayer, *Pharm. Uns. Zeit*, **8** (1979) 46-53

19 R. Foster, Organic Charge-Transfer Complex, pp. 4, 23, Academic Press, London, **1969**.

20 M.S. Refat, A.A. Hamdy, I. Grabchev, L.A. El-Zayat, *Spectrochimica Acta*, Part A, **70** (2008) 907-915.

21 W.C. Vosburg, G.R. Cooper, *J. Am. Chem. Soc.*, **63** (1941) 437.

22 L. J. Bellamy, The Infrared Spectra of Complex Molecules, Chapman & Hall, London, **1975**.

M. Hamming, N. Foster, "Interpretation of mass spectra of organic compounds", Academic press: New York, USA, **1972**.

СПЕКТРОФОТОМЕТРИЧНО ОПРЕДЕЛЯНЕ НА СИЛДЕНАФИЛ ЦИТРАТ В ТАБЛЕТКИ. СПЕКТРОФОТОМЕТРИЧНО ОПРЕДЕЛЯНЕ НА ТВЪРДИ КОМПЛЕКСИ С ПРЕНОС НА ЗАРЯДА

М. С. Рефат[1,2*], Г. Г. Мохамед[3], А. Фатхи[3]

[1] Катедра по химия, Факултет по науки, Университет Таиф, 888 Таиф, Кралство Саудитска Арабия
[2] Катедра по химия, Факултет по науки, Порт Саид 42111, Университет Суецки канал, Египет
[3] Катедра по химия, Факултет по науки, Университет в Кайро, Египет

(Резюме)

Целта на това изследване е да се предложат чувствителни, точни и възпроизводими методи за определянето на силденафил цитрат в чисти фармацевтични препарати. Силденафил цитратът се определя спектрофотометрично чрез образуването на комплекси с пренос на заряда. Това включва използването на някои π-акепторикато 2,3-дихлоро-5,6-дициано-p-парабензохинон (DDQ) and 3,6-дихлоро-2,5-дихидрокси-p-бензохинон (p-CLA). Предложеният метод може да се използва за рутинен анализ на предлаганото лекарство във фармацевтични препарати. Твърдите йони в комплексите от реакциите с DDQ и p-CLA като π-acceptors и силденафил цитрат като донор са изолирани и образуваните комплекси са охарактеризирани чрез елементен анализ, ИЧ-, [1]H ЯМР and мас-спектрометрия.

Photocatalytic degradation of malachite green by zinc oxide sprayed films

V.N. Blaskov[1], I.D. Stambolova[1], S.V. Vassilev[2], C.D. Dushkin[3]

[1] *Institute of General and Inorganic Chemistry, Bulgarian Academy of Sciences, Acad. G. Bonchev St, bl.11, 1113 Sofia, Bulgaria*

[2] *Institute of Electrochemistry and Energy Systems, Bulgarian Academy of Sciences, Acad. G. Bonchev St, bl. 10, 1113 Sofia, Bulgaria*

[3] *Laboratory of Nanoparticle Science and Technology, Faculty of Chemistry and Pharmacy, University of Sofia, James Bourchier Blvd. 1, 1164 Sofia, Bulgaria*

Nanocrystalline porous ZnO films are deposited by spray pyrolysis of polyvinyl alkohol (PVA) modified zinc acetate solutions. The effect of polyvinyl alcohol on the structural, morphological and photocatalytical properties of ZnO sprayed films was studied. The X-ray diffraction patterns revealed the formation of wurtzite phase. Compact granular morphology was observed for the ZnO samples grown from zinc acetate solutions. Addition of PVA to zinc acetate leads to the formation of ganglia-like morphology. The crystallite sizes are about 10-11 nm (XRD), regardless of the type of the solvent. It was observed that PVA plays an important role in modifying the surface morphology and the photocatalytic properties of the ZnO films. The films obtained from PVA containing zinc acetate solutions showed better degradation of malachite green dye than the films deposited from solutions without polymer modifier.

Keywords: ZnO, films, photocatalysis, PVA, dye degradation

1. INTRODUCTION

Zinc oxide has been applied in solar cells [1], optoelectronic systems [2], transparent conductive oxides [3], gas sensors [4], and so forth, owing to its versatile properties. ZnO has an increasingly important status in the field of environmental protection. Zinc oxide powders and thin films are low cost and non-toxic photocatalysts for degradation of toxic organic compounds and industrial effluents under UV and visible light [5–7]. It is important to find ways for the preparation of films with porous, developed structure taking into account that the efficiency of the photocatalytic processes is attributed to the presense of more active sites.

The introduction of polymers into a zinc precursor solution can affect the films morphology and develop their surface due to a strong interfacial reaction between the inorganic metal ions and the organic polymer. This approach is mainly used in sol-gel deposition of ZnO films. Various non-ionic and polymer-type surfactants, such as polyethylene glycol (PEG) [8] and poly(vinylpyridine) (PVP) [9] were applied for preparation of nanosized ZnO films.

The spray pyrolysis offers an elegant approach to produce ZnO films with desired morphology *via* spraying a polymer-modified precursor solution. The polymer complex starts to decompose on the heated substrate and subsequent thermal treatment leads to the oxidation of the decomposition products, which ensures the formation of ZnO films with porous structure.

Recently we have successfully prepared porous sprayed ZnO films with enhanced photocatalytic activity to malachite green dye using ethylcellulose as a polymer modifier in the precursor solution [10]. It seems to be promising to proceed with the investigation in order to study the effect of other types of polymers on the structural and photocatalytic properties of ZnO films.

In this work we have chosen polyvinyl alcohol as a functional, water soluble and linear polymer, whose hydroxyl (–OH) groups at the side chains could form complexes with inorganic ions. In the process, the zinc salt was mixed with a PVA solution to issue the complex reaction between the Zn^{2+} ions and the –OH group of the PVA precursor. The cross-linking between the linear chains forms small cages which prevent the particle growth. A few investigators have used polyvinyl alcohol as a surfactant in the chemical preparation of bulk ZnO [11]. Two type of polymers (PVA and PVP) and

* To whom all correspondence should be sent:
E-mail: vblaskov@abv.bg

zinc nitrate were used to obtain ZnO nanoparticles [12]. To our knowledge, ZnO thin films have not been prepared by spray pyrolysis using PVA additive in the precursor solution.

The aim of the present paper was to obtain photocatalytic active ZnO films with developed surface morphology using PVA-modified solution *via* simple and low cost spray pyrolysis method. The effect of the solvent on the morphological and photocatalytic characteristics was investigated.

2. EXPERIMENTAL

Zinc acetate ($Zn(CH_3COO)_2.2H_2O$) was dissolved in water or ethanol-water mixture to obtain 0.4 M/L solutions of Zn which were called *sol AcW* and *sol AcE,* respectively. To prevent the high velocity hydrolysis a few drops of HNO_3 were added to each sol. The solution of polyvinyl alcohol (PVA, Mw=40,000) in ethanol-water mixture was prepared by 5 h stirring and heating at a constant temperature of 40ºC until the final solution was clear, homogeneous, and free from precipitate (*sol C*). A defined quantity of sol C was added to the zinc acetate sols in order to obtain a final spray solution with 30 wt% PVA relative to the zinc concentration. The mixtures were vigorously stirred for 1 h and then used for the spray procedure. The alumina foil plates (80 × 25 mm) were cleaned successively in hot ethanol and acetone. The aerosol of the precursor solution was generated by a pneumatic glass nebulizer and was transported to the substrate heated at 300-400°C. Afterwards, the films were treated at 350ºC for 45 min for pyrolization of the organics and oxide formation.

The crystalline phase composition of the samples was studied by X-ray diffraction (XRD) using a X-ray diffractometer Philips PW 1050 with CuK_α-radiation. The crystallite size was estimated from the XRD spectra. X-ray diffracton line broadening (XRD-LB) measurements were carried out in order to estimate the crystallite size. Calculation was performed using Scherrer's equation:

$$D=k\lambda /B.\cos\Theta$$

where D is the crystallite size (nm), λ is the wavelength of CuK_α radiation (nm), θ is the Bragg angle (º), K is a constant (0.89) and B is the calibrated width of a diffraction peak at half-maximum intensity (rad).

The average crystallite size of the thin films is determined from the half width of full maximum (HWFM) intensity of the (100) peak. A scanning electron microscope (SEM) JSM‑5510 of JEOL,

operated at 10 kV of acceleration voltage was used for morphology observations of the films. The investigated samples were coated with gold by JFC-1200 fine coater (JEOL) before observation. Fourier transform infrared (FTIR) spectra were taken with a Nicolet Avatar 360 spectrometer (Nicolet, Madison, USA) spectrometer at a spectral resolution of 2 cm^{-1} and accumulation of 64 scans by the KBr tablet technique. The spectra were scanned in the 4000 – 400 cm^{-1} range. The treatment and the analysis of the spectra were made using the OMNIC advanced software.

The photocatalytic experiments were conducted using an ultraviolet source (UV lamp) with light intensity of 5.10^{-5} W/cm^2 located in the centre of a vessel. The latter contained 5 ppm aqueous solution of the dye, which was constantly agitated with a magnetic stirrer (400 rpm). The photocatalytic degradation of 5 ppm malachite green (MG) oxalate (Chroma Gesellschaft) was evaluated by taking aliquots of the solution and measuring the residual concentration on a spectrophotometer type Jenway 6400 at regular time intervals. The actual dye concentration was determined by comparison of the measured absorbance at the wavelength of the spectral maximum with the absorbance of solutions of known dye concentration.

3.RESULTS AND DISCUSSIONS

Figure 1 shows the XRD spectra of ZnO layers obtained from zinc acetate. The results show that the ZnO films obtained possess a wurtzite structure (space group P63mc) and the diffraction peaks (100), (002) and (101) can be indexed to hexagonal ZnO (JCPDS no. 36–1451). The mean size of the crystallites (calculated by Scherrer's equation) is in the range 10–20 nm.

The films obtained from $Zn(CH_3COO)_2.2H_2O$ dissolved in ethanol-water mixture (*sol AcE*) are crack-free with homogeneous, very fine grained surface (Fig 2-a). When water was used as a solvent for the zinc acetate precursor (AcW sol), the films morphology became rougher and porous, with sections of undistinguishable grain boundaries and the specimen had a net-like morphology. The crystallite sizes are slightly larger (21 nm) than those in the case of films made from AcE sol (15 nm) (Fig. 2-b). We observed significant evolution of the morphology of the samples obtained from polyvinyl alcohol-modified acetate solutions. As can be seen from Fig. 2, the addition of PVA leads to the formation of ganglia-like structure. The crystallite sizes are about 10–11 nm (XRD)
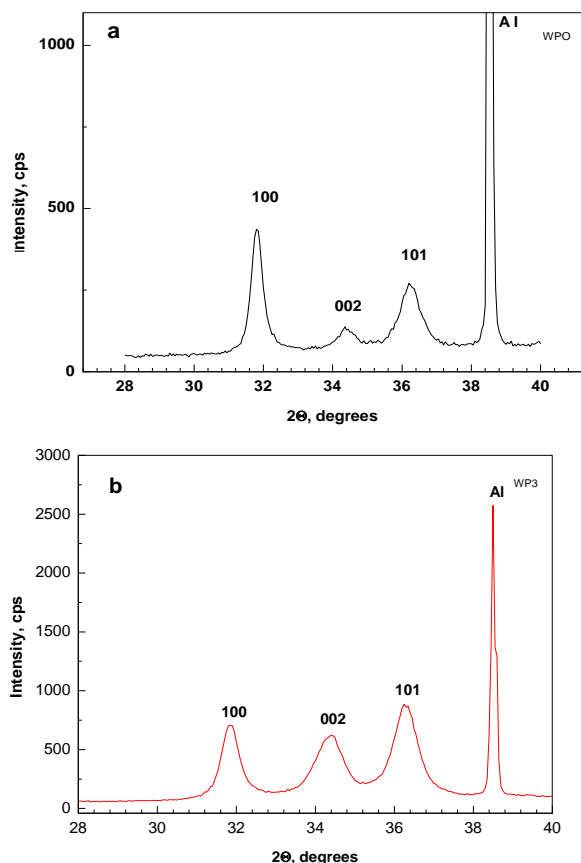
Fig 1. XRD of the films obtained from zinc acetate solution (a), PVA modified zinc acetate solution (b).

regardless of the type of the solvent. The small dimensions of the crystallite sizes could be explained taking into account the mechanism proposed in [13]. Polyvinyl alcohol adsorbs nonspecifically on the oxide surface because its molecule has no charge. It remains with a conformation similar to that of a free molecule, acting as a bridge between the particles. The cross-linking between the linear chains of PVA in aqueous medium provides small tails and loops, wherein the reactant sol is trapped and converted to small particles of ZnO during thermolysis.

It is interesting to point out that the films obtained from PVA-modified zinc acetate possess quite different morphology compared to those from the ethylcellulose-acetate solutions presented in our previous study [10]. Probably, when zinc acetate is used as a precursor for ZnO sprayed films, the nature of the added polymer modifier defines the films morphology.

The FTIR spectrum of the precursor xerogel is shown on Fig. 3. The absorption bands at 3400 and 3094 cm^{-1} (wide maximum) can be ascribed to the OH vibration stretching [14], the bands at 2929 and 2856 cm^{-1} are attributed to CH and CH$_2$ vibration
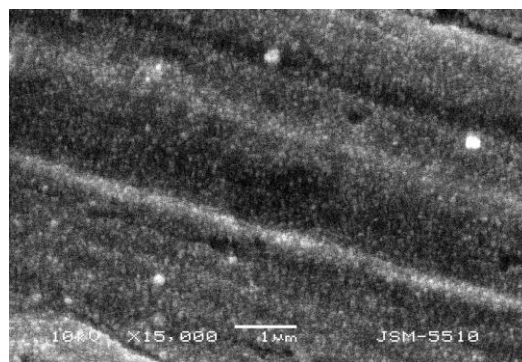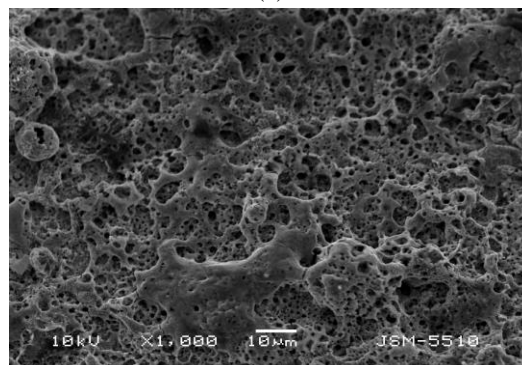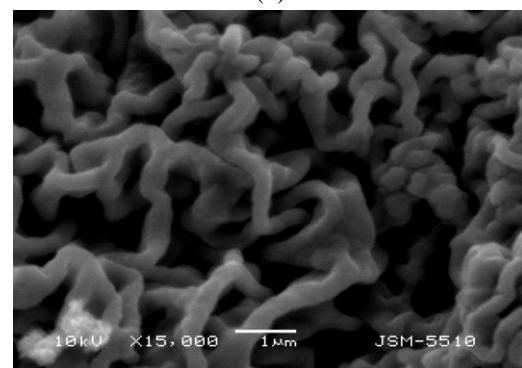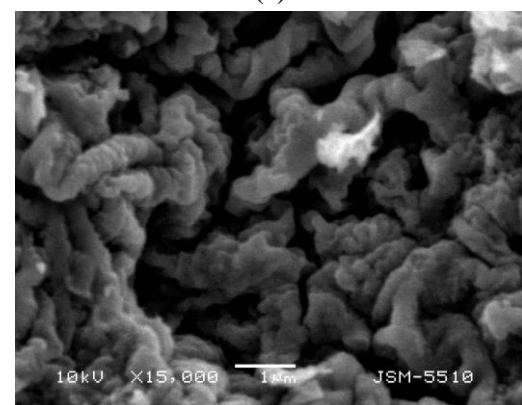
Fig 2. SEM of ZnO films deposited from ethanol-water solution (a), from aqueous solution (b), from PVA modified ethanol-water solution (c), PVA modified aqueous solution (d).

265
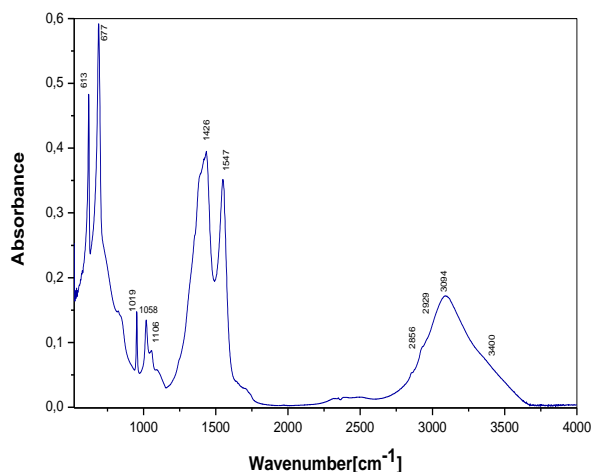
Fig 3. Fourrier transform infrared (FTIR) spectra of ZnO precursor solution with PVA modifier, dried at 80ºC.

Fig.4. Photocatalytic degradation of Malachite Green on ZnO films deposited from:-AcW solution - curve1; PVA modified AcW solution-curve 2; AcE solution –curve 3 and PVA modified AcE solution of $Zn(CH_3COO)_2.2H_2O$ - curve 4.

stretching and are typical of PVA [15,16]. The band at 1714 cm^{-1} is characteristic of C=O and C–O stretching [17]; the intensive bands at 1547 and 1426 cm^{-1} are also related with C=O and C-O stretching, where the peak at 1547 cm^{-1} can be assigned to C=O bridging type metal acetate bonding. Both bands are characteristic of zinc acetate [18,19]. The bands in the range 950-1110 cm^{-1} are identified as CH_3 bending modes [14]. The stretching at 842 cm^{-1} can be referred to CH_2 and is characteristic of PVA [35]. The latter two bands at 677 and 613 cm^{-1} belong to zinc acetate [14].

The photocatalytic activity of the obtained films was evaluated under illumination with UV light. The change of the relative concentration C/C_o (where C_o is the initial concentration of MG) of the dye on ZnO films deposited from $Zn(CH_3COO)_2.2H_2O$ (*sols AcW, AcE*) with and without PVA addition with the time of UV radiation is shown in Fig. 4. As can be seen on the figure, the addition of PVA in the spray solution of zinc acetate strongly enhances the degradation rate of the malachite green dye (curves 2,4 *vs* curves 1,3). Curves 2 and 4 show a similar course of photocatalytic degradation for both modified sprayed ZnO films. Malachite green dye undergoes 50 % decomposition within 1 hour of UV irradiation. One can conclude that the enhancement in the photocatalytic activities can be attributed to the well developed structure of the films obtained by PVA modified AcE and AcW solutions, which ensures a larger amount of active sites for the photocatalytic process.

The films obtained from unmodified solutions possess lower activities probably due to both the more compact structure and the slightly larger crystallites (Fig. 4, curves 1,3). The best photocatalytic activity is achieved for the films obtained from PVA-modified ethanol-water solutions of zinc acetate.

4. CONCLUSIONS

Nanosized thin ZnO films were prepared by spray pyrolysis from polyvinyl alcohol modified solutions. The films obtained form zinc acetate solutions have relatively compact structure with crystallite size of 15–20 nm. The addition of PVA leads to a smaller crystallite size (about 10–11 nm), regardless of the type of the solvent and ganglia-like structure. The well developed surface structure with fine grains determines the better photocatalytic properties of the films from polymer-modified solutions.

REFERENCES

1. S. Rani, P. Suri, P.K. Shishodia, R.M. Mehra, *Solar Energy Mater. Solar Cells*, **92,** 1639 (2008)
2. S. Liang, H. Sheng, Y. Liu, Z. Huo, Y. Lu, H. Shen, , *J. Cryst. Growth*, **225,**110 (2001)
3. S Park, T. Ikegami, H. Ebihara, P.K. Shin, *Appl. Surf. Sci.*, **253,** 1522 (2006).
4. X.J.Huang and Y.K.Choi, *Sens. Actuators B: Chem.,* **122,** 659 (2007)
5. G. Kenanakis, Z. Giannakoudakis, D. Vernardou, C. Savvakis, N.Katsarakis. *Cat.Today*, **151**, 34(2010).

6. S. Sakthieval, B. Neppolian, M.V. Shankar, B. Arabindoo, M. Palanichamy, V. Murugeshan, *Sol. Energy Mater. Solar Cells,* **77,** 65(2003).

7. N. Kaneva**,** I. Stambolova**,** V. Blaskov**,** Y. Dimitriev**,** S. Vassilev**,** C. Dushkin, *J. Alloys Comp*., **500,** 252 (2010).

8. T. Du, H. Song, O.J. Ilegbusi, *Mater. Sci. Eng. C* **27,** 414 (2007).

9. Zh. Liu, Zh. Jin, W. Lei, J. Qin, *Mater. Lett.*, **59**, 3620 (2005).

10. I. Stambolova, V. Blaskov, S. Vassilev, M. Shipochka, C. Dushkin, Y. Dimitriev, *Mater. Chem Phys*., **121,** 447 (2010).

11. Z. Wang, B.Huang, X. Liu, X. Qin, X. Zhang, J.Wei, P.Wang, Sh. Yao, Qi Zhang, X. Jing, *Mater. Lett.*, **62,** 2637 (2008).

12. P.R**.** Patil, S.S. Joshi, *Mater. Chem. Phys.*, **105,** 354 (2007).

13. Kirk–Othmer, Encyclopedia of Chemical Technology, **23** (John Willey and Sons, New York, 1983).

14. C.Liewhiran, S.Seraphin, S.Phanichaphant, *Current Appl. Physics*, **6**,499 (2006).

15. N. Sangkhaprom, P. Supaphol, V. Pavarajan, *Ceram. Intern*., **36**, 357 (2010).

16. S.Gandi, R.H.H. Subramani, T. Ramakrishnan, A. Sivabalan, V. Dhanalakshimi, M.R.G. Nair, R. Anbarasan, *J. Mater. Sci*., **45,** 1688 (2010).

17. M.N. Kamalasanon, S.Chandra, *Thin Solid Films***, 288,** 112 (1996).

18. S. Suwanboon, *Science Asia*, **34** , 031 (2008).

19. I. Uslu, B. Baser, A. Yayli, M.L. Aksu, e- *Polymers,* art.no.145 (2007).

20. (http://www.e-polymers.org)

ФОТОКАТАЛИТИЧНО РАЗГРАЖДАНЕ НА МАЛАХИТОВО ЗЕЛЕНО ЧРЕЗ СПРЕЙВАНИ СЛОЕВЕ ОТ ZnO

В.Н. Блъсков[1,*], И.Д. Стамболова[1], С.В. Василев[2], Ц.Д. Душкин[3]

[1]) Институт по обща и неорганична. химия, БАН, ул. "Акад. Г. Бончев", бл.11, 1113 София
[2]) Институт по електрохимия и енергийни системи, БАН, ул. "Акад. Г. Бончев", бл. 10, 1113 София
[3]) Лаборатория за на наночастици наука и технологии на Факултета по химия, Софийски университет, бул. "Джеймс Баучер" 1, 1164 София

(Резюме)

Нанокристални порести филми от ZnO бяха отложени чрез спрей пиролиза на модифициран с поливинилов алкохол (PVA) разтвор на цинков ацетат. Изследван е ефектът на поливиниловия алкохол върху структурните, морфологични и фотокаталитични свойства на спрейвани филми от ZnO. Рентгеновата дифракция разкри образуването на чиста вюрцитна фаза. Наблюдавана е компактна гранулирана морфология за слоевете от ZnO, получени от цинков ацетат. Добавянето на поливинилов алкохол към цинков ацетат води до формиране на ганглии. Размерите на кристалите са около 10-11 нанометра (XRD), независимо от вида на разтворителя. Беше установено, че PVA играе важна роля в промяната на морфологията и на фотокаталитичните свойства на филмите от ZnO. Слоевете, получени от модифицирани с поливинилов алкохол разтвори на цинков ацетат, провяват по-висока активност за разграждане на багрилото малахитово зелено, отколкото филмите, отложени от разтвор без полимерен модификатор.

BULGARIAN CHEMICAL COMMUNICATIONS

Instructions about Preparation of Manuscripts

General remarks: Manuscripts are submitted in English by e-mail or by mail (in duplicate). The text must be typed double-spaced, on A4 format paper using Times New Roman font size 12, normal character spacing. The manuscript should not exceed 15 pages (about 3500 words), including photographs, tables, drawings, formulae, etc. Authors are requested to use margins of 3 cm on all sides. For mail submission hard copies, made by a clearly legible duplication process, are requested. Manuscripts should be subdivided into labelled sections, e.g. **Introduction, Experimental, Results and Discussion**, *etc*.

The title page comprises headline, author's names and affiliations, abstract and key words.

Attention is drawn to the following:

a) **The title** of the manuscript should reflect concisely the purpose and findings of the work. Abbreviations, symbols, chemical formulas, references and footnotes should be avoided. If indispensable, abbreviations and formulas should be given in parentheses immediately after the respective full form.

b) **The author**'s first and middle name initials, and family name in full should be given, followed by the address (or addresses) of the contributing laboratory (laboratories). **The affiliation** of the author(s) should be listed in detail (no abbreviations!). The author to whom correspondence and/or inquiries should be sent should be indicated by asterisk (*).

The abstract should be self-explanatory and intelligible without any references to the text and containing not more than 250 words. It should be followed by key words (not more than six).

References should be numbered sequentially in the order, in which they are cited in the text. The numbers in the text should be enclosed in brackets [2], [5, 6], [9–12], etc., set on the text line. References, typed with double spacing, are to be listed in numerical order on a separate sheet. All references are to be given in Latin letters. The names of the authors are given without inversion. Titles of journals must be abbreviated according to Chemical Abstracts and given in italics, the volume is typed in bold, the initial page is given and the year in parentheses. Attention is drawn to the following conventions:

a) The names of all authors of a certain publications should be given. The use of "*et al.*" in the list of references is not acceptable.

b) Only the initials of the first and middle names should be given.

In the manuscripts, the reference to author(s) of cited works should be made without giving initials, e.g. "Bush and Smith [7] pioneered...". If the reference carries the names of three or more authors it should be quoted as "Bush *et al*. [7]", if Bush is the first author, or as "Bush and co-workers [7]", if Bush is the senior author.

Footnotes should be reduced to a minimum. Each footnote should be typed double-spaced at the bottom of the page, on which its subject is first mentioned.

Tables are numbered with Arabic numerals on the left-hand top. Each table should be referred to in the text. Column headings should be as short as possible but they must define units unambiguously. The units are to be separated from the preceding symbols by a comma or brackets.

Note: The following format should be used when figures, equations, *etc*. are referred to the text (followed by the respective numbers): Fig., Eqns., Table, Scheme.

Schemes and figures. Each manuscript (hard copy) should contain or be accompanied by the respective illustrative material as well as by the respective figure captions in a separate file (sheet). As far as presentation of units is concerned, SI units are to be used. However, some non-SI units are also acceptable, such as °C, ml, l, etc.

The author(s) name(s), the title of the manuscript, the number of drawings, photographs, diagrams, etc., should be written in black pencil on the back of the illustrative material (hard copies) in accordance with the list enclosed. Avoid using more than 6 (12 for reviews, respectively) figures in the manuscript. Since most of the illustrative materials are to be presented as 8-cm wide pictures, attention should be paid that all axis titles, numerals, legend(s) and texts are legible.

The authors are asked to submit **the final text** (after the manuscript has been accepted for publication) in electronic form either by e-mail or mail on a 3.5'' diskette (CD) using a PC Word-processor. The main text, list of references, tables and figure captions should be saved in separate files (as *.rtf or *.doc) with clearly identifiable file names. It is essential that the name and version of

the word-processing program and the format of the text files is clearly indicated. It is recommended that the pictures are presented in *.tif, *.jpg, *.cdr or *.bmp format, the equations are written using "Equation Editor" and chemical reaction schemes are written using ISIS Draw or ChemDraw programme.

The authors are required to submit the final text with a list of three individuals and their e-mail addresses that can be considered by the Editors as potential reviewers. Please, note that the reviewers should be outside the authors' own institution or organization. The Editorial Board of the journal is not obliged to accept these proposals.

EXAMPLES FOR PRESENTATION OF REFERENCES

REFERENCES

1. D. S. Newsome, *Catal. Rev.–Sci. Eng.*, **21**, 275 (1980).
2. C.-H. Lin, C.-Y. Hsu, *J. Chem. Soc. Chem. Commun.*, 1479 (1992).
3. R. G. Parr, W. Yang, Density Functional Theory of Atoms and Molecules, Oxford Univ. Press, New York, 1989.
4. V. Ponec, G. C. Bond, Catalysis by Metals and Alloys (Stud. Surf. Sci. Catal., vol. 95), Elsevier, Amsterdam, 1995.
5. G. Kadinov, S. Todorova, A. Palazov, in: New Frontiers in Catalysis (Proc. 10th Int. Congr. Catal., Budapest, 1992), L. Guczi, F. Solymosi, P. Tetenyi (eds.), Akademiai Kiado, Budapest, 1993, Part C, p. 2817.
6. G. L. C. Maire, F. Garin, in: Catalysis. Science and Technology, J. R. Anderson, M. Boudart (eds), vol. 6, Springer-Verlag, Berlin, 1984, p. 161.
7. D. Pocknell, *GB Patent* 2 207 355 (1949).
8. G. Angelov, PhD Thesis, UCTM, Sofia, 2001.
9. JCPDS International Center for Diffraction Data, Power Diffraction File, Swarthmore, PA, 1991.
10. CA **127**, 184 762q (1998).
11. P. Hou, H. Wise, *J. Catal.*, in press.
12. M. Sinev, private communication.
13. http://www.chemweb.com/alchem/articles/1051611477211.html.

CONTENTS

СЪДЪРЖАНИЕ